DETECTION OF JOINT INFLAMMATION IN RHEUMATOID ARTHRITIS USING MULTISPECTRAL DIFFUSE OPTICAL IMAGING

by

DANIEL LIGHTER

A thesis submitted to
The University of Birmingham
for the degree of
DOCTOR OF PHILOSOPHY

Physical Sciences for Health Doctoral Training Centre
College of Engineering and Physical Sciences
The University of Birmingham
September 2019

Abstract

Rheumatoid arthritis is a chronic autoimmune disease, characterised by joint inflammation, which if untreated causes disability. A clinical need exists for novel, low-cost and non-invasive imaging tools capable of detecting inflammation in the joints for the diagnosis and monitoring of patients with rheumatoid arthritis. Diffuse optical imaging provides information about the underlying functional properties of biological tissue and previous studies have reported an optical contrast between inflamed and non-inflamed joints, with former displaying localised increases in absorption and scattering attributed to underlying pathophysiological changes. In this work, a novel, multispectral diffuse optical imaging system for imaging human hand joints was presented, which combined surface imaging and optical transmission imaging in a single work-flow to reconstruct maps of clinically relevant parameters such as oxygen saturation, total haemoglobin, water and scattering amplitude in three dimensions. The system was designed to provide accurate, robust and rapid data acquisition, particularly through the novel application to joint imaging of a galvanometer-based unit for fast source repositioning allowing full datasets to be acquired in ≈2mins per joint, such as to be sufficient for implementation in a clinical setting. This clinical prototype system was then comprehensively studied through experiments involving biological tissue mimicking optical phantoms, to assess performance against a ground truth set of known parameters.

Preliminary studies involving healthy volunteers gave useful insight into the systems *in vivo* performance and provided a good understanding of baseline values in healthy subjects, with significantly greater variability observed between subjects than when comparing joints within the same subject. A pilot clinical study was then carried out, involving 144 joints from 21 rheumatology patients with ultrasound imaging and clinical examination as reference comparisons, to assess the systems diagnostic accuracy capabilities. A degree of sensitivity was observed from three dimensional maps of total haemoglobin and scattering amplitude to pathophysiological changes in the joint during longitudinal monitoring of either recovery from acute injury in a single healthy subject or the response to therapy in rheumatoid arthritis patients. From single time-point examination data, classification accuracies when considering the entire cohort were limited, with areas under the receiver operator curve of up to 0.657 achieved, with similar conclusions reached to those in comparable single-wavelength, continuous-wave studies previously reported despite the multiple wavelength acquisition. A normalised Fourier transform methodology was then presented, engineered to extract features related to the spatial signature of the transmitted light through the joint that were less sensitive to inter-subject variability in total flux for

the assessment of optical transmission images. For the first time within the academic community, to the authors knowledge, the impact on diffuse optical imaging signals of the spatially asymmetrical prevalence of inflammation in hand joints of rheumatoid arthritis patients was addressed. In distinction from previous work, optical images were acquired from the dorsal side with illumination on the palmar side and results when using the proposed normalised fast Fourier transform methodology demonstrated accurate detection of inflamed joints from single time-point examinations, with of area under the receiver operator curve values up to 0.888 together with sensitivities and specificities of up to 77.9% and 90.9% respectively achieved for this specific dataset. This work-flow may enable future development of clinically viable, low-cost devices for assessing inflammation in arthritis patients, without the need for cuff occlusion or comparison to baseline. It will be important to assess the generalisation of these accuracies in future work, using a larger patient cohort and testing different machine learning classification schemes.

ACKNOWLEDGEMENTS

I would like to express my deepest gratitude to my supervisors. Iain Styles for his depth of understanding on the most intricate problems and eye for detail in manuscript preparation. Andrew Filer for his wealth of expertise in rheumatology and guidance on clinic applications. A very special thanks to Hamid Dehghani for his unresolving support throughout the project, acting as a fountain of knowledge for all his students within the field of Biomedical optics. Our weekly meetings have provided me with an invaluable space to explore new ideas and directions of work. I would like to thank all my colleagues, both in the PSIBS and Sci-Phy-4-Health doctoral training centres, and the Medical Imaging Lab, for creating such an inspiring scientific community to work within. A particular thanks to Stanislaw Wojtkiewicz, Matthaios Doulgerakis and Kamlesh Patel for their engaging scientific discussions and friendship throughout my studies.

I would like to acknowledge Hector Basevi for being so generous with his time and assistance in integrating the surface imaging technology, and Bertram Dandy for his guidance in system construction. I would also like to thank all the staff at University of Birmingham Research Laboratories for their fantastic work supporting patients throughout clinical studies, including Ilfita Sahbudin and Jeanette Trickey for carrying out ultrasound scanning, and all the nurses Joanne Dasgin, Alexandra Newton-Cox, Jaqueline Cobb, Charlotte Sabine and Karen Horton. I must also gratefully acknowledge all the volunteers who kindly participated during imaging studies, without whom none of this work would have been possible.

Finally, I would like to thank my loving wife and beloved sister for always supporting me in everything I do. I would like to dedicate this thesis to my beautiful baby boy, Samuel.

This work was financially supported by a Engineering and Physical Sciences Research Council grant (EP/L016346/1) through a studentship from the Physical Sciences for Health Centre for Doctoral Training.

PUBLICATIONS RESULTING FROM THIS WORK

Journal Papers

A set of deep neural network models for rheumatoid arthritis (RA) classification were applied to simulated diffuse optical tomography images of inflamed and non-inflamed joints, demonstrating an improvement in diagnostic accuracy when compared to more traditional machine learning algorithms.

Feng Y., **Lighter, D.**, Zhang L., Wang Y., and Dehghani H., 2020, Application of deep neural networks to improve diagnostic accuracy of rheumatoid arthritis using diffuse optical tomography. Quantum Electronics, 50(1), pp.21-32.

A novel Fourier transform based methodology was presented, capable of detecting inflammation from single time point assessment in 21 patients with inflammatory arthritis, with values for the area under the curve of up to 0.888. Results from this pilot study are reported in Chapter 6 of this thesis.

Lighter D., Filer, A. and Dehghani H., 2019, Detecting inflammation in rheumatoid arthritis using Fourier transform analysis of dorsal optical transmission images from a pilot study. Journal of Biomedical Optics, 24(6), pp.066008.

A study involving 11 healthy subjects demonstrated a significantly greater inter-subject variability in physiological parameters recovered using multispectral, non-contact diffuse optical tomography than compared to the variability seen between individual finger indices or repeat measurements, contributing to Chapter 5 of this thesis.

Lighter D., Hughes, J., Filer, A. and Dehghani H., 2018, April. Multispectral, non-contact diffuse optical tomography of healthy human finger joints. Biomedical Optics Express, 9(4), pp.1445-1460.

A proposed L1-based regularisation method was evaluated using experimental phantom data acquired using the presented multispectral, non-contact diffuse optical tomography

system, presented in Chapter 4 of this thesis.

Lu, D., **Lighter, D.** and Styles, I. B., L1-norm Based Nonlinear Reconstruction Improves Quantitative Accuracy of Spectral Diffuse Optical Tomography, 2018, Biomedical Optics Express, 9(4), pp.1423–1444.

Conference proceedings

Investigation into the potential benefits of using deep neural networks for classifying arthritic joints applied to a simulated DOT dataset.

Dehghani, H., Feng, Y., **Lighter, D.**, Zhang, L. and Wang, Y., 2019, July. Deep neural networks improve diagnostic accuracy of rheumatoid arthritis using diffuse optical tomography. In Diffuse Optical Spectroscopy and Imaging VII (p. 110741I). Society of Photographic Instrumentation Engineers.

Proceedings were submitted reporting physiological responses in healthy joints during arm cuff occlusion, which contribute to Chapter 5 of this thesis.

Lighter, D., Styles, I. B., Filer, A. and Dehghani, H., 2018, January. 3D pathophysiological changes in healthy finger joints during cuff occlusion. In European Conference on Biomedical Optics (p. 104120N). Optical Society of America.

Initial study reporting data from three healthy subjects was presented in a conference proceedings.

Lighter, D., Filer, A. and Dehghani, H., 2017, June. Multispectral diffuse optical tomography of finger joints. In European Conference on Biomedical Optics (p. 104120N). Optical Society of America.

CONTENTS

LIST OF ACRONYMS

ACPA	Anti-Citrullinated Protein Antibody
ACR	American College of Rheumatology
AMCC	Automatic Multiple Camera Calibration
AUC	Area Under the Curve
BOLD	Blood Oxygen Level Dependent
CCD	Charge-Coupled Device
CE	Clinical Examination
CGAL	Computational Geometry Algorithms Library
CMOS	Complementary Metal-Oxide-Semiconductor
CT	Computed Tomography
CTE	Clinical TEnderness
CSW	Clinical SWelling
CW	Continuous Wave
DA	Diffusion Approximation
DAQ	Data AcQuisition
DMARD	Disease Modifying Anti-Rheumatic Drug
DMD	Digital Micro-mirror Device
DOI	Diffuse Optical Imaging
DOT	Diffuse Optical Tomography
EF	EFfusion
EULAR	European League Against Rheumatism
FD	Frequency Domain
FEM	Finite Element Method
FLS	Fibroblast-Like Synoviocytes
FOI	Fluorescence Optical Imaging
FFT	Fast Fourier Transform

GS	GrayScale
GUI	Graphical User Interface
IA	Inflammatory Arthralgia
IL	InterLeukin
KW	Kruskal-Wallis
MC	Monte Carlo
MCP	MetaCarpal Phalangeal
ML	Machine Leaning
MRI	Magnetic Resonance Imaging
MSE	Mean Squared Error
MWU	Mann-Whitney U
NIR	Near Infra-Red
NIRS	Near Infra-Red Spectroscopy
OA	OsteoArthritis
PA	Palindromic Arthritis
PAT	PhotoAcoustic Tomography
PD	Power Doppler
PL-LOOCV	Patient Level Leave One Out Cross-Validation
PIP	Proximal InterPhalangeal
PV	ParvoVirus arthritis
RA	Rheumatoid Arthritis
RC	Recovered Contrast
RF	Rheumatoid Factor
ROC	Receiver Operator Curve
ROI	Region Of Interest
ROS	Reactive Oxygen Species
RTE	Radiative Transport Equation
SC	Spectrally Constrained
SH	Synovial Hypertrophy
SHS	Sharp/van der Heijde Score

SNR	Signal to Noise Ratio
SI	Surface Imaging
SVM	Support Vector Machines
TD	Time Domain
TNF	Tumour Necrosis Factor
UA	Unclassified Arthritis
US	UltraSound
VEGF	Vascular Endothelial Growth Factor
VOI	Volume Of Interest
VR	Volume Ratio

LIST OF FIGURES

LIST OF TABLES

CHAPTER 1

INTRODUCTION

Rheumatoid arthritis (RA) is an inflammatory, autoimmune disease of the joints. In humans it is particularly frequently seen in the hands, and if untreated can cause disability. Two treatment paradigms are becoming increasingly important in the clinical management of RA; aggressive therapy during the first three months of symptoms has been shown to improve long-term patient outcomes, and stratified treatment strategies are required to prescribe medications with the greatest efficacy in that specific patient. These two paradigms place an importance on sensitive imaging techniques capable of early diagnosis and monitoring response to therapy. In the modern rheumatology clinic, diagnosis and monitoring is carried out through a combination of patient history, clinical examination, blood tests, questionnaires and medical imaging, however well-established imaging modalities are each subject to specific disadvantages for detecting joint inflammation. Radiography suffers from low sensitivity to the soft tissue changes occurring early in RA, while both ultrasound and magnetic resonance imaging require highly trained staff, leading to high cost and limited availability [1], creating a clinical need for novel, low-cost and non-invasive imaging tools capable of quantifying inflammatory changes in human joints. Multispectral, diffuse optical imaging (DOI) is a highly sensitive, low-cost technique, in which near infrared (NIR) light (650 - 930nm) is injected into the tissue and subsequently measured at the tissue boundary. DOI has been widely used to measure pathophysiological changes *in vivo*, applied for example to; whole animal imaging in arthritis models [2], osteoarthritis in

finger joints [3], or state of the art, non-contact, frequency domain imaging of RA joints [4]. Tomographic joint imaging of RA patients has, up to now, been limited to single wavelength data acquisition, preventing the detection of pathophysiological changes known to occur in inflamed joints, such as localised tissue hypoxia or elevated blood volume fraction.

In the work presented, the design and evaluation of a DOI imaging system is covered and its efficacy as a clinical imaging modality for diagnosing early RA is explored, both through simulation and experimentation. The final prototype system presented in Chapter 3 has several novel aspects compared to previous joint imaging devices, including a rapid, fully non-contact approach for optical transmission imaging based on galvanometer-based light source control coupled to camera-based measurement, and integrated surface imaging technology to produce spatial *a prior* information about the joint geometry, both of which were integrated into a single system to collect all data required for tomographic reconstruction during a single workflow. The performance of this system was then assessed in controlled phantom studies and *in vivo* preliminary healthy subject studies, in Chapters 4 and 5 respectively. Finally, the diagnostic accuracy for detecting inflammation in patients with inflammatory arthritis, using either recovered tomographic images or optical transmission images, was assessed during a clinical study reported in Chapter 6, with relevant conclusions and future work discussed in Chapter 7. As the nature of this work was highly interdisciplinary, this thesis has been written to include the fundamental knowledge needed, such that the significance of this work can be understood by readers from backgrounds in rheumatology or biomedical optics. This first chapter focuses on presenting the clinical context behind motivations for the development a DOI system to image joints of patients with RA.

1.1 Rheumatoid Arthritis

The primary goal of a medical imaging systems is to create a visual representation of the interior of the body which provides clinically useful information during patient care. In the modern rheumatology clinic, medical imaging devices such as ultrasound (US) and magnetic resonance imaging (MRI) play a crucial role in assisting clinical decision making when diagnosing a condition or administering treatment. In order to assess the potential benefits of DOI for assessing the inflammatory status of joints in RA patients, it is first important to understand the pathophysiological changes which occur in diseased tissue. This chapter reviews the latest understandings in RA pathogenesis and the current clinical approaches for diagnosis and monitoring of patients, with a particular focus on the established imaging modalities.

1.1.1 Epidemiology

RA is a common, immune-mediated disease characterised by chronic inflammation in the peripheral joints. RA is not the only type of inflammatory arthritis, but it is the most common, with a prevalence of ≈1% in the UK [5]. Disease severity can vary from mild to complete disability and its social impact includes: reduced quality of life for patients, increased health-care costs and working life reduction, with around one third of those diagnosed stopping work on medical grounds within 5 years of initial symptom onset [6]. In 2009, the economic impact of RA in the UK was estimated to be ≈ £560 million per year in healthcare costs and a total additional cost to the economy from sick leave and work-related disability of ≈ £1.8 billion a year [7]. Extra-articular impacts of the disease result in increased prevalence of other comorbidities compared to the general population including; cardiovascular disease, malignancies, lung disease, bone and muscle wasting, premature aging and neuropsychiatric disease [8, 9].

A complex interplay of genetic susceptibility together with environmental factors contributes to an increased risk of developing RA, as illustrated in Figure 1.1. Evidence of

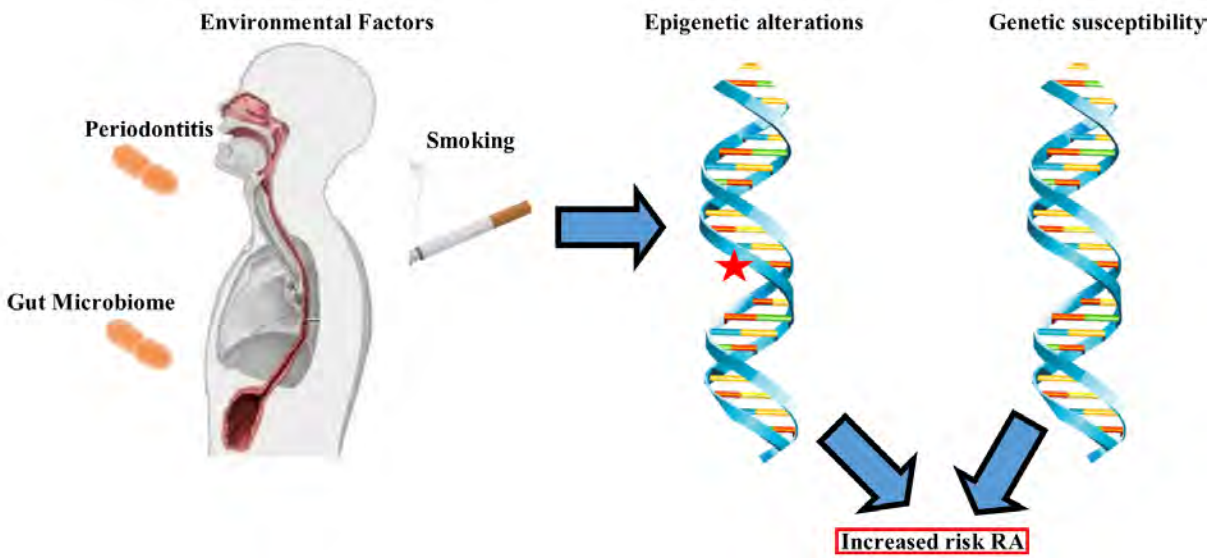

Figure 1.1: Chart illustrating the combination of risk factors, including environmental influences that can trigger epigenetic alterations such as methylation or histone modifications to DNA, or an inherited genetic predisposition within the DNA sequence, which together contribute to an increased risk of developing RA.

genetic predispositions include studies in twins revealing a 5% rate of concordance amongst dizygotic twins and 30% in monozygotic twins, with an overall disease heritability of around 60% [10], a gender imbalance with around three times as many women as men with RA [11], and a family history of RA in first degree relatives contributing to increased risk, where a greater susceptibility is passed on from a mother than a father [12]. A number of the genes that predispose to seropositive RA have been identified [13], such as HLA-DR, PTPN22 etc. Environmental risk factors include a perturbed gut microbiome [14], the presence of porphyromonos gingivalis, a Gram-negative bacteria in periodontitis (commonly known as gum disease) [15] and being a smoker [16], all of which have been reported to have an influence on the likelihood of developing RA. Epigenetic alterations occurring as a result of these environmental factors together with any genetic predispositions can lead to disruption of the typical post-transcriptional regulation, such as modification of autoantigens by citrullination, and ultimately increase the risk of developing RA [17].

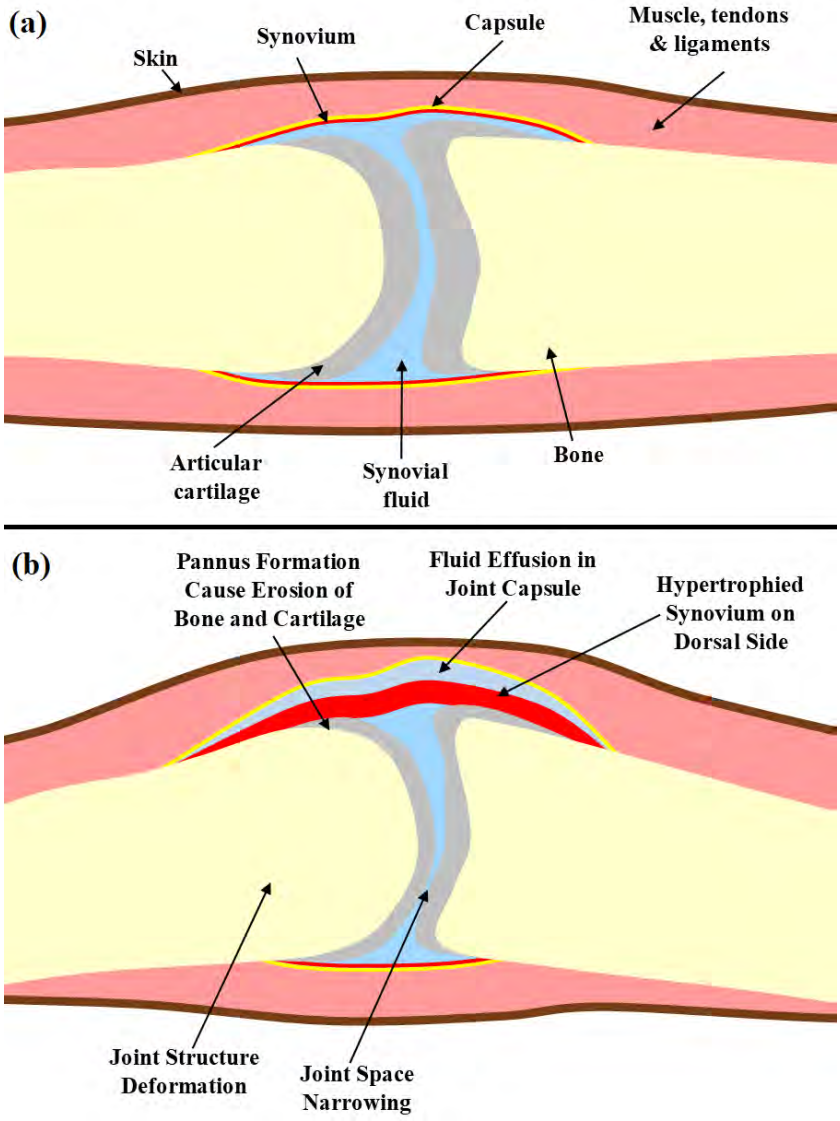

Figure 1.2: Simplified diagram of structure of (a) a healthy joint and (b) an inflamed joint of a patient with RA, with a hypertrophied synovium and formation of a pannus resulting in erosion of bone and cartilage.

1.1.2 Pathophysiology

The physiology of the human finger joint is highly heterogeneous in structure, consisting of 5 main tissue types: bone, cartilage, synovial membrane, synovial fluid and other soft tissues, as shown in Figure 1.2. Articular surfaces of the opposing bones either side of the joint are covered in a layer of cartilage. The non-articular surfaces of both bones are connected by a capsule, lined on its inner surface by a two layer synovial membrane, which is made up of a highly specialised, inner lining layer, normally only 1-3 cells thick, and an

outer more vascular (sub-lining) layer in which immune cells accumulate. In the proximal interphalangeal (PIP) and metacarpal phalangeal (MCP) joints in the hand, this membrane envelops a volume of around 100μl of highly viscous, non-Newtonian, synovial fluid in the joint cavity which provides lubrication to articulating joint surfaces, and finally soft tissues, including tendon, muscle and skin surround the joint structure [18]. The synovium is a highly specialised tissue, with a primary function of supporting healthy lubrication and nutrition of the joint. In afflicted joints of RA patients, a series of signalling pathways stimulate increased vascular permeability and encourage the migration of immune cells to the joint through adhesion molecules, resulting in an abnormal influx of inflammatory cells into the synovium. Furthermore the increased permeability of the synovium leads to localised oedema and an increase in synovial fluid volume, which manifests as joint swelling.

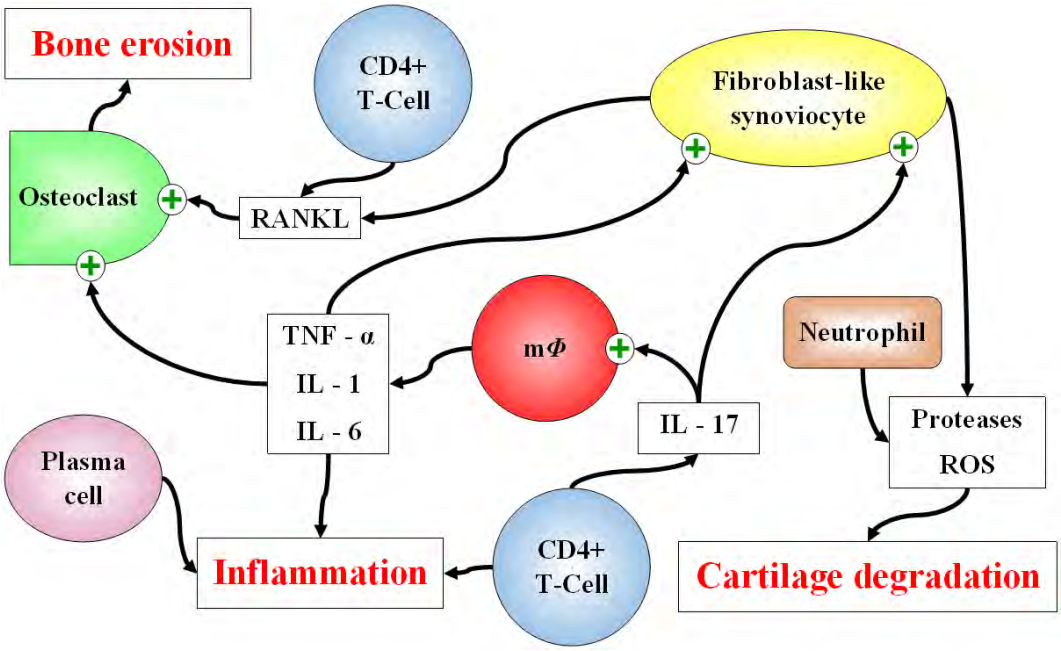

Figure 1.3: Illustration of the cells (coloured shapes) and their corresponding cytokines (white boxes) involved in some of the key pathways in RA pathology. Auto-immune response is initiated in the lymph nodes via the production of CD4+ T helper cells by APCs, that trigger the activation of other immune cells such as macrophages and fibroblast-like synoviocytes. Together, these autoimmune cells cause both the over-stimulation of osteoclasts that result in excessive bone erosion and the release of proteases and reactive oxygen species that lead to cartilage degradation.

The progression to persistent synovial inflammation in RA is driven by over expression

of multiple cytokines, which stimulate biological inflammatory cascades outlined in Figure 1.3. Abnormal post-transcriptional modifications result in modified autoantigens, that are recognised by the body's immune system. These activate antigen presenting cells which initiate an immune response in the lymph nodes, activating CD4+ T helper cells, and driving B-cells to become plasma cells that secrete autoantibodies. Two antibodies involved include rheumatoid factor (RF) and anti-citrullinated protein antibodies (ACPA), which can be detected in the serum. CD4+ T-helper cells make up around 50% of the immune cells in the joint and activate macrophages (mϕ) and fibroblast-like synoviocytes (FLS) through cytokines including interleukin (IL)-17. Tumour necrosis factor (TNF), IL-1 and IL-6 are all macrophage synthesized cytokines, known to play a key role in driving synovial inflammation and joint destruction in RA [19]. These cytokines up-regulate FLS cells, which subsequently proliferate resulting in a dramatic increase in size of the synovium (hyperplasticity of stromal cells) [20]. Systemic increases in these inflammatory cytokines in the blood are also one cause of extra-articular involvement in other organs.

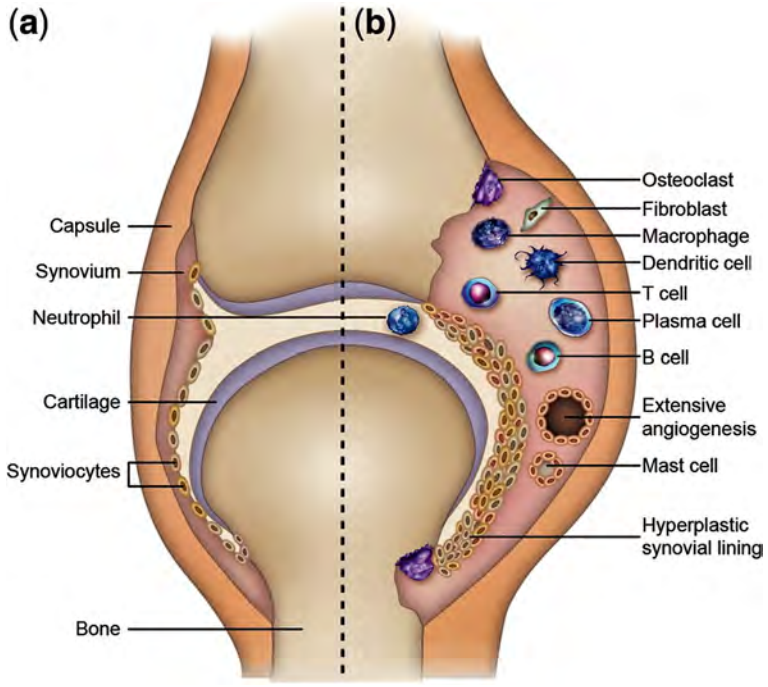

Figure 1.4: Illustration depicting the anatomy of (a) a healthy joint in the left half, and (b) an inflamed joint of a patient with RA in the right half together with the associated immune cells involved in the underlying inflammatory pathways. Figure reproduced with permission from [21].

CD4+ T cells, FLS and B cells secrete receptor activator of nuclear factor kappa−B ligand (RANKL), which stimulates both the differentiation of monocyte precursors into osteoclasts and their release of enzymes which erode the bones of the joint. Proteases and reactive oxygen species (ROS) are also produced by FLS and neutrophils located in the synovial fluid, which cause the degradation of cartilage. FLS cells can migrate via the vasculature to other joints, potentially providing an explanation for symmetrical affliction of joints in RA. Immune complexes and plasma cells are other drivers of inflammation. At later stages of the disease, the formation of a pannus as shown in Figure 1.2(b) occurs, which erodes the articular cartilage and bone and leads to deformation of the joint structure [22].

A joint space naturally has a lower oxygen tension than surrounding tissue in healthy cases. In inflamed joints, an increased metabolic demand associated with the elevated number of inflammatory cells results in further abnormal reductions in joint oxygenation (hypoxia) compared to healthy joints [23]. Evidence of hypoxic conditions in RA has been demonstrated by comparing 103 synovial fluid samples from knee joints, displayed in Table 1.1, with mean oxygen tensions of RA patients found to be considerably lower than either patients with osteoarthritis (OA) or exudates from patients with traumatic joint damage, representing the healthy group in this study for ethical reasons [24]. This localised hypoxia is thought to play an important role in upregulating inflammation, oxidative stress and damage, via for example fibroblast expression of hypoxia-inducible molecules such as vascular endothelial growth factor (VEGF) [25, 26]. Angiogenesis is a natural process in healthy joints, with the vascular structure constantly being remodelled. In an inflamed rheumatoid joint, TNF and IL-1 upregulate an abnormal increase in regional blood flow and blood volume fraction via synovial angiogenesis [27], in an attempt to meet the increased metabolic oxygen demands. Evidence has been shown of another profound change in the joint space, with a 10 to 50 fold increase in quantity of leukocytes and the tripling of protein content observed in the synovial fluid [28, 29], both of which will have an impact for optical transmission due to their micrometre length scales on a similar order

to scattering lengths in biological tissue .

Group	Oxygen tension (mmHg), mean ± S.D.	StO_2 (%), mean
RA	26.53 ± 19.29	49
OA	42.92 ± 15.09	78.5
Healthy	63.00 ± 19.20	91.7

Table 1.1: Synovial fluid oxygen tensions obtained by aseptic puncture of knee joint *(ex vivo)*, as reported by [24]. Extrapolated values for oxygen saturation are shown, which can be used for optical modelling, estimated using the simplified Severinghaus equation for the oxygen saturation curve of a healthy subject [30] (it must be noted that this equation is for blood samples, not tissue and CO_2 concentrations are not taken into account).

1.2 Clinical Management of RA

Treatment

A cure for RA does not currently exist [31]. Despite an incomplete understanding of aetiology [31], significant progress in the knowledge of underlying biological mechanisms in recent decades has meant that a wide range of disease modifying anti-rheumatic drugs (DMARDs) are now available to RA patients for managing disease progression. These include either biological agents such as TNFα-blockers; infliximab, etanercept and adalimumab, or synthetic treatments including; methotrexate, sulfasalazine and hydroxychloroquine [32]. Many of these medications work by targeting and disrupting the inflammatory pathways discussed in Section 1.1.2. Patients are commonly also treated with glucocorticoids, naturally occurring steroid hormones known to suppress inflammation, which can be administered either locally through intra-articular injections in the inflamed joint or in the form of oral tablets for systemic delivery. Associated with these immunosuppressive therapies are potentially harmful side effects, such as an increased risk of infection or liver damage, making accurate diagnosis and prescription of correct treatments vitally important.

Stages of Disease

RA is a dynamic disease. For example, patients can experience acute flare ups, where inflammation and associated symptoms severely worsen, or can go into sustained remission, where no inflammatory symptoms occur for long periods. Achieving sustained remission is the ultimate aim in all clinical management of RA through prescription of DMARDs. The stages of development of RA which precedes fulfilment of the criteria for RA diagnosis, has been categorised into several clinical phases by the European League Against Rheumatism (EULAR): (1) presence of genetic and environmental risk factors for RA, (2) systemic autoimmunity associated with RA, (3) symptoms without clinical arthritis, (4) unclassified arthritis (UA) and finally (5) RA [33]. This process can be an acute, rapid onset or a gradual deterioration, in which patients with UA who will go on to develop RA will nearly always do so within around 2 years. The symptomatic phase (3) is the one of earliest opportunities to clinically recognise patients who are at risk of progressing to RA preceding clinical arthritis.

1.2.1 Current Diagnostic and Monitoring Procedures

At present, there is unfortunately no single, definitive feature capable of accurately diagnosing RA. Initial symptoms frequently reported by patients at presentation include joint swelling, morning stiffness and swelling, with the small joints in the hands and feet most commonly afflicted, often with a high degree of symmetry [34]. Typically onset of symptoms such as pain and stiffness precedes onset of joint swelling. Additionally other joint diseases often present with similar symptoms to RA, such as OA [35], gout, polymyalgia and lupus, making diagnosis sometimes a complex and challenging task. A questionnaire survey of 10,161 patients attending their primary care practitioner highlighted the challenge faced by GPs when identifying patients at-risk of RA, in which complaints of inflammatory symptoms typical of RA were commonly reported by non-musculoskeletal related consulters also, at 42%, 36% and 18% for joint pain, joint stiffness and joint swelling

respectively, whilst reported rates in patients truly afflicted by musculoskeletal conditions were only marginally higher at 62%, 50% and 24% respectively [36]. A multifaceted approach is therefore often required to improve diagnostic accuracy, by combining patient history, clinical examination, which involves physically examining all joints for swelling and tenderness, laboratory tests and imaging modalities.

1.	Morning stiffness	Morning stiffness in and around the joints, lasting at least 1 hour before maximal improvement.
2.	Arthritis of 3 or more joint areas	At least 3 joint areas simultaneously have had soft tissue swelling or fluid (not bony overgrowth alone) observed by a physician. The 14 possible areas are right or left PIP, MCP, wrist, elbow, knee, ankle, and MTP joints.
3.	Arthritis of hand joints	At least 1 area swollen (as defined above) in a wrist, MCP, or PIP joint.
4.	Symmetric arthritis	Simultaneous involvement of the same joint areas (as defined in 2) on both sides of the body (bilateral involvement of PIPS, MCPs, or MTPs is acceptable without absolute symmetry).
5.	Rheumatoid nodules	Subcutaneous nodules, over bony prominences, or extensor surfaces, or in juxtaarticular regions, observed by a physician.
6.	Serum rheumatoid factor	Demonstration of abnormal amounts of serum rheumatoid factor by any method for which the result has been positive in 4% of normal control subjects.
7.	Radiographic changes	Radiographic changes typical of rheumatoid arthritis on posteroanterior hand and wrist radiographs, which must include erosions or unequivocal bony decalcification localized in or most marked adjacent to the involved joints (osteoarthritis changes alone do not qualify).

Table 1.2: The ACR 1987 revised criteria used by clinicians for diagnosing RA. A patient is said to have RA if they have satisfied at least 4 of these criteria, with criteria 1 through to 4 having been present for a minimum 6 weeks and patients with two clinical diagnoses not excluded. [34].

The American College of Rheumatology (ACR) 1987 revised criteria, as shown in Table 1.2, is a commonly used set of classification criteria [34], which involves the fulfilment of a combination of different scoring approaches for RA diagnosis and has a reported sensitivity (S_E) 91.2% and specificity (S_P) of 89.3% for diagnosing RA. A systematic literature review into diagnosis at early stages (within first year from presentation) using these criteria reported however a pooled S_E and S_P of both only 77% [37], indicating it to be a poor diagnostic tool for early RA. Recently in 2010 a new set of criterion was published [38], designed to increase S_E for classification of RA earlier in disease.

Laboratory Studies

A set of laboratory tests on blood samples are typically carried out for systemic biomarkers indicative of RA. Higher than normal levels of erythrocyte sedimentation rate, the rate at which red blood cells settle, is reported in 85-90% of subjects with RA, or elevated C-reactive protein, which is acute-phase reactant, both indicate the potential presence of underlying inflammation [39]. Additionally, the detection of autoantibodies including RF or ACPA using enzyme-linked immunosorbent assay methods is present in the blood of 65% of patients [38]. RF has poor specificity for patients with RA, however, as elevated titres are also observed in sarcoidosis, systemic lupus erythematosus, endocarditis, chronic liver disease and chronic pulmonary disease including tuberculosis [111].

1.2.2 Significance of Early Diagnosis

The existence of a window of therapeutic opportunity [40] in the first three months of symptoms is widely acknowledged, during which aggressive therapy using a combination of DMARDs improves long-term patient outcomes [41]. Results from a study monitoring outcomes in 598 patients over 6 years [42] demonstrated statistically significantly lower Sharp/van der Heijde scores (SHS), a scoring system of erosion and for joint space narrowing in radiographs, over a 6 year follow up as displayed in Figure 1.5. These studies indicated that early interventions during the initial phases of RA can reduce the risk of disease persistence and the development of structural damage. It has been argued that this increased amenability to treatment may be due to the underlying inflammatory feedback processes not yet having become established, with evidence of distinct synovial fluid cytokine profiles in these early stages compared to established RA [43]. Although rapid referral from GP surgeries to rheumatology clinics is vital, many doctors first carry out blood tests that are only useful in a proportion of patients, leading to a risk of missed disease in seronegative patients, and can lead to costly time delays. For example, the median time between symptom onset and consultant appointment was reported to be 27.2

weeks in a recent study involving 822 patients, with only 20% of these patients seen during the first 3 months [44]. These delays create a clinical need for cheap, non-invasive tools capable of quantifying joint changes during the early stages of the disease, for widespread screening of patients with clinically suspect arthralgia (joint pain).

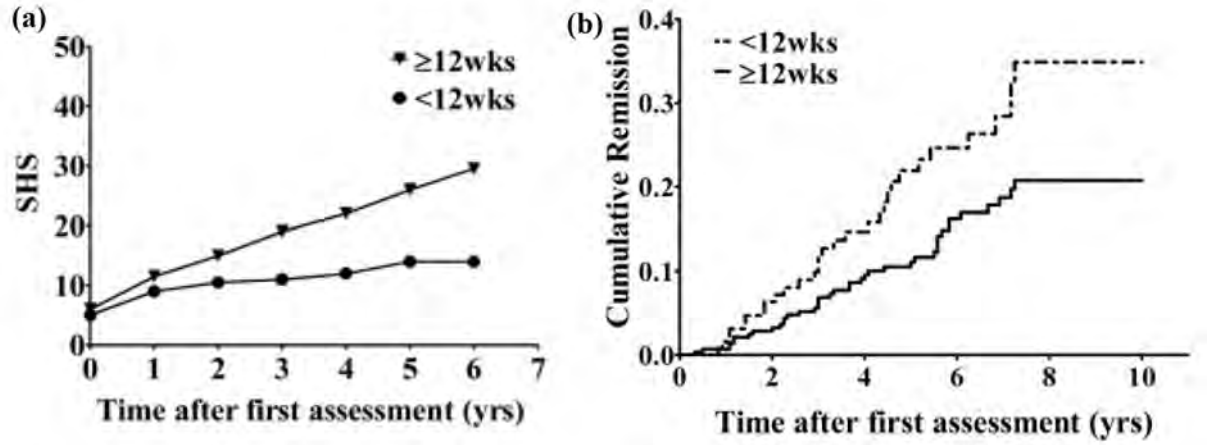

Figure 1.5: Plots of (a) the median Sharp/van der Heijde Scores (SHS), a measure of radiographic deterioration, and (b) the probability of achieving sustained DMARD free remission, defined as the persistent absence of synovitis for at least 1 year. Both plots are shown for groups with either greater than 12 weeks (late diagnosis) or fewer than 12 weeks (early diagnosis) delay in time to initial assessment by a rheumatologist, followed up over 6 years since this initial assessment. Figure reproduced with permission from [42]

1.2.3 Longitudinal Monitoring

RA is a highly heterogeneous disease, both clinically and pathologically, meaning patient responses to specific DMARDs are diverse across patients, with the efficacy of a specific treatment higher some patients than others, making stratified treatment strategies desirable [45]. For example, some reported non-responder rates are 45% by 2 years for methotrexate, 25% by 6 months for anti-TNF and 40% by 6 months for rituximab[46, 47, 48]. Following diagnosis, an example of a typical DMARD treatment pathway is outlined in Figure 1.6, where the patients start with a synthetic treatment, followed by more expensive biologics, which are genetically engineered proteins, to treat non-responders. Delays in identifying the treatment effective to a specific individual causes significant burden on patient outcomes and leads to a financial cost by funding of drugs that are not benefiting

that individual. This places a critical importance on imaging modalities capable of safely and sensitively monitoring response to therapy for improved disease management.

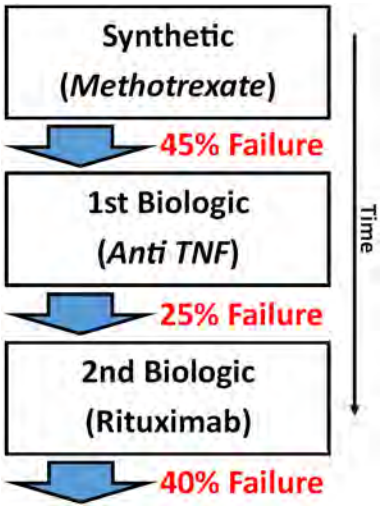

Figure 1.6: An example of a typical DMARD treatment pathway for RA patients with reported failure rates of non-responders annotated at each stage. Patients typically are first prescribed a low-cost synthetic treatment, from which any non-resoponders then progress to more expensive biologic treatments [46, 47, 48].

1.3 Established imaging modalities

Medical imaging is becoming a crucial tool in modern Rheumatology clinics, with modalities such as MRI and US revolutionising how clinicians diagnose patients and monitor response to therapy. Two image characteristics are of interest in RA; early pathophysiological changes, such as increased vascularisation, and structural changes typically occurring at a later stage in the disease, such as hypertrophied synovium or bone erosion.

1.3.1 Radiography

Conventional 2D X-ray imaging has been a vital tool for clinicians assessing joint damage over many decades [49]. Very low scattering in biological tissue for the 10^{-9} - 10^{-12}m range of the electromagnetic spectrum along with a high absorptivity by heavier elements, namely calcium in the bone, allows skeletal structure to be captured with excellent spatial

resolution. Diagnostic features of interest for RA include narrowing of the joint space, bone erosion and periarticular osteopenia (mild thinning of the bones surrounding the joint) [50], as shown in Figure 1.7. Computed tomography (CT) is the three-dimensional extension of radiography, where X-ray images taken from multiple angular projections around the joint are used to build a 3D picture of hard tissues. CT is not routinely implemented in rheumatology, due to its greater ionization exposure than conventional 2D radiography, increased expense due to more complex technology and algorithms, and limited additional useful information compared to its 2D equivalent. Radiography is commonly used as a disease progression outcome measure, but is not useful for current disease activity [51]. Furthermore, a lack of contrast to any soft tissue changes in the early stages of RA and its inherent ionisation risk are the main drawbacks of X-ray / CT imaging for early diagnosis and routine monitoring in rheumatology. Crucially, X-ray changes are rare in early disease, as significant bone loss has to occur before these are visible.

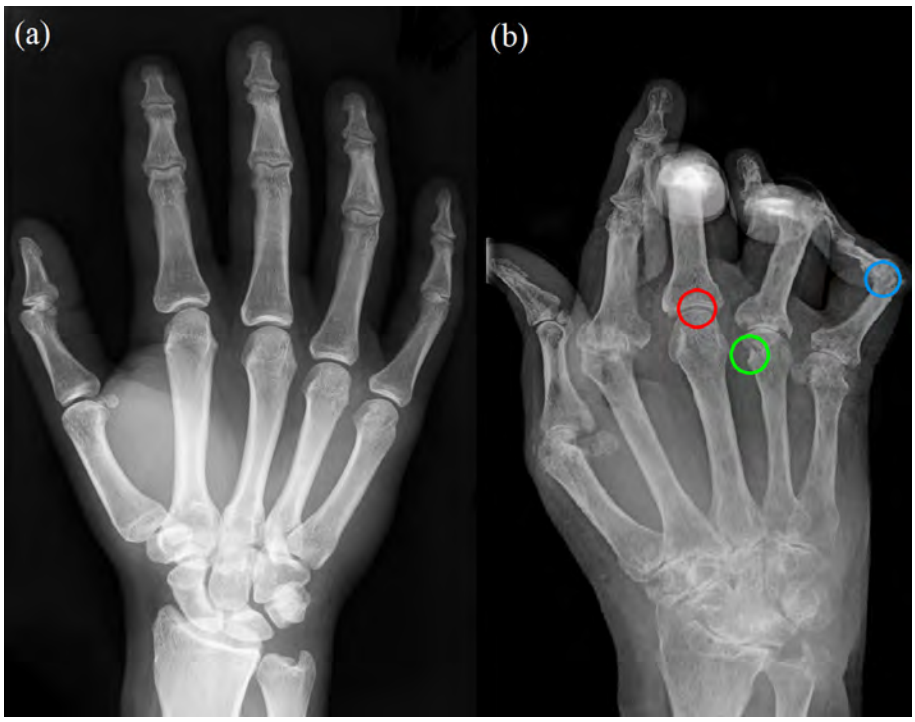

Figure 1.7: X-ray of (a) a healthy hand and (b) a hand from a patient with severely progressed rheumatoid arthritis. Typical characteristic features observed in RA patients include joint space narrowing (red), bone erosion (green) and severely deformed joints (blue). (Image courtesy of freely available wikimedia commons - last accessed 25 August 2016).

1.3.2 Ultrasound

During ultrasound (US) imaging, high frequency (10 to 15MHz) acoustic waves are propagated into the tissue. Upon encountering a boundary with significant variation in acoustic impedance, ie. between tissue and bone, these acoustic waves are reflected and subsequently measured upon return to the boundary, so that structural images can be generated using knowledge of the speed of sound. Power Doppler (PD) mode is an additional mode in US, in which net vascular motion can be measured by taking advantage of the Doppler effect of acoustic waves and is used to quantify blood flow in vessels.

Musculoskeletal US is becoming an essential tool for diagnostics and monitoring of joint synovitis in patients with inflammatory arthritis, being more sensitive and reliable than clinical examination alone and less expensive and more widely available than MRI [52, 53, 54]. Measures of vascular flow using PD-US are closely related to activity of synovial inflammation and subsequent damage to the joints in patients with RA [55, 56, 57] and have emerged as independent predictors of diagnostic outcome in undifferentiated arthritis [58]. Although US examinations are increasingly being used in clinics for early RA diagnosis, they can only be performed by clinicians trained in sonography and can take up to 30 minutes, leading to high cost and limited availability. Additionally a degree of subjectivity in interpretation of US images is a concern and can lead to interobserver variability [59].

1.3.3 Magnetic Resonance Imaging

Magnetic resonance imaging (MRI) systems use powerful magnets (1.5 - 7 Tesla) to image biological tissue. These magnets are used to induce a net alignment of molecules with an uneven number of neutrons and protons, which gives them a physical property termed spin. Spin can then be perturbed using radio frequency pulses, and their relaxation times measured to generate an image.

MRI can be used to assess intrinsic biological properties, where the presence of hydrogen

provides contrast in either just water or both water and fat levels in T1-weighted or T2-weighted images respectively. In the context of RA, MRI is the gold standard, with good soft tissue contrast, high resolution and no ionising radiation. One early sign of bone deterioration is the build-up of fluid (oedema) in the bone marrow, which MRI images are able to detect, helping in predicting future bone erosion [60]. Blood oxygen level dependent (BOLD) and dynamic contrast enhanced signals in MRI have been shown capable of tracking functional changes associated with inflammation including decreased intra-articular oxygen pressure and increased vascularity [61, 62]. Additionally, the intravenous injection of contrast agents such as gadolinium (Gd), which enhance signal due to their paramagnetic properties and can target specific molecules of interest, has been shown to be a highly accurate approach in the context of RA diagnosis [63], as shown in Figure 1.8 (b). Despite its utility, extremely high costs ($> £200$ per scan) and a poor tolerance by some patients, for example with metal implants, pacemakers or claustrophobia, prevent the widespread routine clinical use of MRI in rheumatology.

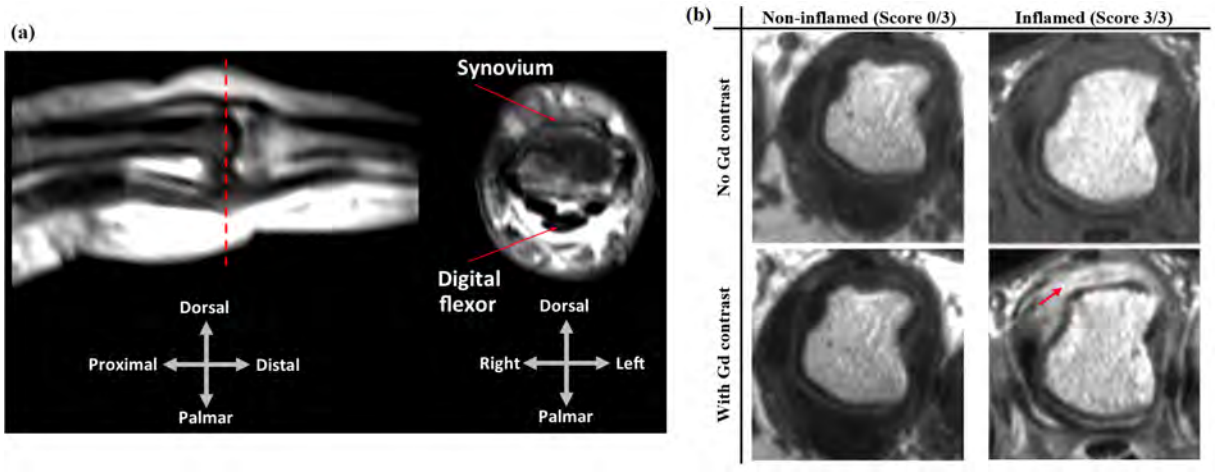

Figure 1.8: (a) Example sagittal and coronal T1-weighted MRI images showing the structure of a healthy PIP joint. (b) Example T1-weighted MRI images of non-inflamed or inflamed MCP joint with corresponding semiquantitative RAMRIS scores, shown either without or with Gd contrast, reproduced with permission from the EULAR−OMERACT RA magnetic resonance imaging reference image atlas [64]. The red arrow in (b) indicates significant Gadolinium (Gd) enhancement on the dorsal side, corresponding to severe synovitis.

1.4 Conclusion

Extensive research into the underlying biological mechanisms of RA in recent decades has meant that a wide range of DMARDs are now available to be prescribed for RA. The paradigms in administering these treatments are shifting towards; 1. earlier, more aggressive therapy and ; 2. stratified, person specific therapies, placing importance on sensitive imaging techniques suitable for both early diagnosis and monitoring response to therapy. Well established imaging modalities utilised in modern rheumatology clinics are each subject to specific disadvantages in these regards, with radiography suffering from low sensitivity to the soft tissue changes occurring early in RA, whilst both ultrasound and magnetic resonance imaging require highly trained staff, leading to high cost and limited availability. Together these factors create a clinical need for novel, low-cost and non-invasive imaging tools capable of quantifying functional pathophysiological changes in inflamed human joints. The use of optical techniques to image biological tissue is an emerging and exciting new imaging candidate to meet this clinical need. An introduction to the physics governing diffuse optics in biological tissue and the potential utility for monitoring patients with RA will be covered in detail in the next chapter.

CHAPTER 2

DIFFUSE OPTICAL IMAGING

As electromagnetic waves propagate through space they carry both energy and information, making light a powerful tool for studying our environment. By analysing incident waves, an observer can deduce information about either the origin of their source or the medium through which they have passed. The path of light in free space is accurately described in the field of modern optics, where in a vacuum and ignoring relativistic effects, light will travel in a straight line at the speed of light ($c = 299\ 792\ 458\ ms^{-1}$). In DOI, the path of light through the medium, such as biological tissue, is more complex and two principle interactions are of interest; absorption and scattering.

The focus of this chapter is to present the fundamental physical models describing light propagation in biological tissue and the algorithms required to reconstruct an image of the underlying pathophysiology. This background knowledge is essential for understanding the motivations behind the design of the presented system and associated algorithms used to produce joint images in 3D, and is also useful to effectively interpret the relationship between the recovered functional images and the diseased state of underlying tissue. A review of relevant previous joint imaging studies using optical techniques is also presented, with a focus on the technical details of the systems and their reported efficacies in clinical studies, to provide a context from which the performance of the developed system can be compared. As all referenced devices were aimed for use with patients, their respective advantages or limitations for clinical translation will also be discussed.

2.1 Theory

2.1.1 Spectroscopy

A photon encountering an atom or molecule with quantised energy gaps matching the photon energy can get absorbed, elevating an electron to a higher energy state. The wavelength dependency of a photon, $E = \frac{\hbar c}{\lambda}$ where $\hbar$ is the Dirac constant and λ is the wavelength in nm, means that spectral analysis of any absorbed photons will infer some information about the chemical composition of the illuminated material. In a non-scattering medium, the probability of absorption events occurring means incident light intensity (I_0) decays exponentially with pathlength L through the medium, a relationship commonly described as the Lambert-Bouguer law. This behaviour was first observed in essays by French Physicist Pierre Bouguer in 1729 and later outlined in *Photometria* by Johann Heinrich Lambert, and can be summarised by the following equation,

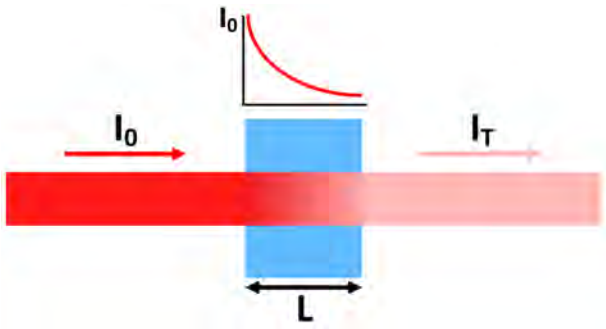

$$I_T = I_0 e^{-\mu_a L}, \qquad (2.1)$$

Figure 2.1: Illustration of exponential decay in intensity in a non-scattering medium according to the Lambert-Bouguer law.

with decay constant μ_a known as the absorption coefficient having units mm^{-1}, commonly chosen as such within the literature in place of their SI unit equivalent as they provide a sensible numerical scaling of values. In 1852, August Beer expanded this relationship to a more general description commonly described as the Beer-Lambert law that considers the dependence of μ_a on the mediums individual constituent chromophores, which can be expressed according to the equation,

$$\mu_a(\lambda) = \sum_{i=1}^{n} \varepsilon_i(\lambda) c_i, \tag{2.2}$$

where λ is the wavelength in nm, ε_i is the wavelength dependent extinction coefficient for the ith chromophore with units mm^{-1} mMol^{-1} and c is chromophore concentration in mMol for n number of chromophores.

2.1.2 Diffuse Behaviour

As light travels through biological tissue, photons may also change direction due to either an inelastic scattering event, which is the theoretical basis of Raman spectroscopy and occurs around once in every 10^6 interactions [65], or an elastic scattering interaction, which can be either with particles smaller than λ (Rayleigh scattering) or atoms / molecules larger than λ (Mie scattering), the second of which is predominantly of interest in DOI. The origin of these elastic scattering events in biological tissue is attributed to a combination of refractive index mismatches between the cellular membrane and the extracellular fluid [66], and the presence of organelles with similar length scales to the wavelength of NIR light, such as the nuclei, mitochondria and lysosomes [66, 67, 68]. The resulting behaviour of light transport is described as diffuse, where scattering dominates over absorption ($\mu_s' >> \mu_a$) and the paths of individual photons can be described as a random-walk, as illustrated in a finger in Figure 2.2.

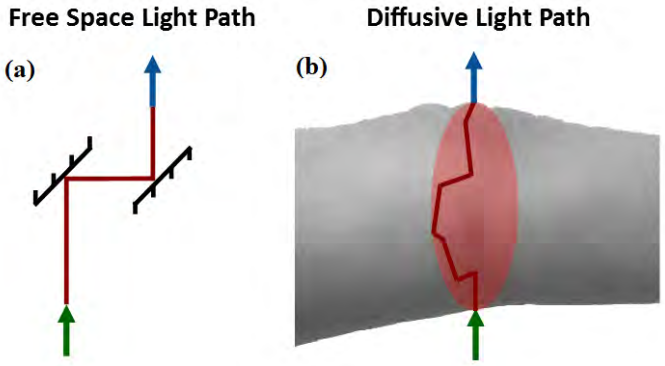

$$\mu_s' = (1 - g)\mu_s, \tag{2.3}$$

Figure 2.2: Illustrations of (a) the easily predictable path of light in free space reflected off two mirrors and (b) the random-walk nature of a diffusive photon transmitted through the finger.

The degree of scattering is described by the reduced scattering coefficient μ_s', where $\frac{1}{\mu_s'}$ represents the average distance travelled by a photon into a medium after which any initial directional information is diminished, and the scattering coefficient μ_s, where $\frac{1}{\mu_s}$ is the average distance travelled by a photon into a medium until a scattering event occurs, both of which are in units mm^{-1}. Equation 2.3 describes the relationship between these two coefficients, where g is the unitless anisotropy factor indicating the asymmetry of scatter that ranges between -1 and 1, corresponding to either highly backward or forward scattering respectively, with $g = 0$ therefore denoting isotropic scattering. Soft tissues in mammals are typically highly forward scattering, with g ranging between 0.8 and 0.98 [69]. Modelling tissue as a collection of spherical scattering particles, the wavelength dependence of scattering interactions with photons can be accurately described according to Mie theory, where λ is comparable to size of the scatterers [70, 71],

$$\mu_s' = S_A \left(\frac{\lambda}{\lambda_{ref}} \right)^{-S_P} . \tag{2.4}$$

Equation 2.4 can be used to calculate the scatter amplitude, S_A, which has units of mm^{-1}, and dimensionless parameter scatter power, S_P, which depend on either the particle scatter centre size or scatter density respectively [72]. λ_{ref} is the reference wavelength, also in nm, arbitrarily chosen throughout the literature, with the effect of scaling S_A values, meaning caution must be taken when comparing these values between studies [73]. For the remainder of this work, λ_{ref} was chosen as 1000nm, as this is the default value in the finite element method (FEM) package NIRFAST [72] used throughout this work.

2.1.3 Imaging Biological Tissue using Light

The principal aim of biomedical optical imaging is to use light to examine the human body. In microscopy, high resolution images of cells can be achieved by restricting the sample thickness ($< 100\mu$m), and recent super resolution developments, such as structured illumination [74] and stochastic optical reconstruction microscopy [75], have even enabled

the diffraction limit to be overcome. The potential for *in vivo* clinical monitoring using near-infrared (NIR) light was first proposed by Franz Jöbsis in 1977 [76], where he identified that a relatively higher transparency of biological tissue in the NIR spectrum can enable transmitted signals to be usefully measured. This wavelength range, commonly known as the NIR optical window, occurs approximately between 650nm and 930nm, and is a result of the comparatively low absorptivity for the predominant biological chromophores; oxyhaemoglobin (HbO), deoxyhaemoglobin (Hb) and water (H_2O), as shown in Figure 2.3, in addition to melanin and lipids.

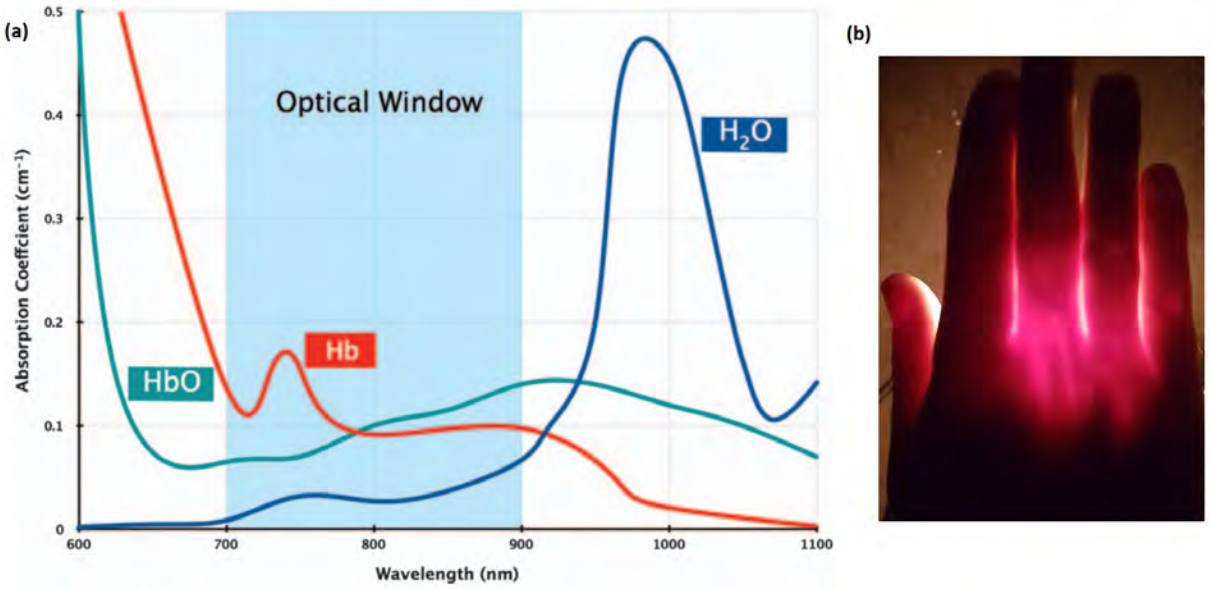

Figure 2.3: (a) Absorption coefficient spectral variation for the most prevalent biological chromophores; water, oxyhaemoglobin and deoxyhaemoglobin, highlighting the NIR optical window of low absorptivity. Reproduced with permission from [77]. (b) Simple experiment illuminating the hand with a broadband white light source and imaged using an RGB CMOS camera, illustrating that red light is predominantly transmitted.

Haemoglobin is a relatively complex, water soluble globular protein, consisting of two alpha and two beta polypeptide chains. Importantly, when bound to oxygen, its spectral absorption profile is altered, as shown in Figure 2.3(a), with the isosbestic point defined as where the absorption coefficients of HbO and Hb are equal, at around 800nm. The use of multispectral measurements at two or more wavelengths permits the spectral decoupling of chromophore contributions to the total attenuation and therefore the underlying concentrations can be estimated. This concept underpins a technique called near

infrared spectroscopy (NIRS), and allows two clinically useful parameters in biomedicine, total haemoglobin (tHb) and oxygen saturation (StO_2), to be calculated using Equations 2.5 and 2.6, both of which can be strong indicators of underlying pathophysiological behaviour, such as the severity of a cancerous tumour [78] or degree of inflammation in RA [25].

$$tHb = Hb + HbO, \qquad (2.5) \qquad\qquad StO_2 = \frac{HbO}{tHb}, \qquad (2.6)$$

2.1.4 Diffuse Optical Tomography

Diffuse optical tomography (DOT) is an imaging technique in which NIR light is injected into biological tissue at multiple locations on its boundary and then subsequently measured at multiple other distinct boundary locations when exiting the tissue. This enables tomographic reconstruction of the underlying spatial distribution of optical properties (absorbers and scatterers) within the biological tissue, in either 2D or 3D. Image contrast can either be extrinsic, in which exogenous fluorescent or bioluminescent agents that target molecules of interest are injected, or intrinsic, in which light interacts with the discriminative indigenous biological chromophores and scatterers. Two areas where DOT has been successfully applied for *in vivo* monitoring include functional imaging of cerebral activations [79, 80] and breast cancer diagnosis [81, 82], examples of which are shown in Figure 2.4. Several groups have previously explored the application of DOT to assess disease in the peripheral joint, a full review of which will be discussed in Section 2.5.

2.2 Modes of Data Acquisition

Three potential modes of data acquisition are employed in DOT; continuous wave (CW), the simplest approach where only the amplitude of the transmitted light intensity exiting the tissue is measured [83]; frequency-domain (FD), where the mean phase shift for a modulated source is additionally measured [4]; and time domain (TD), which requires

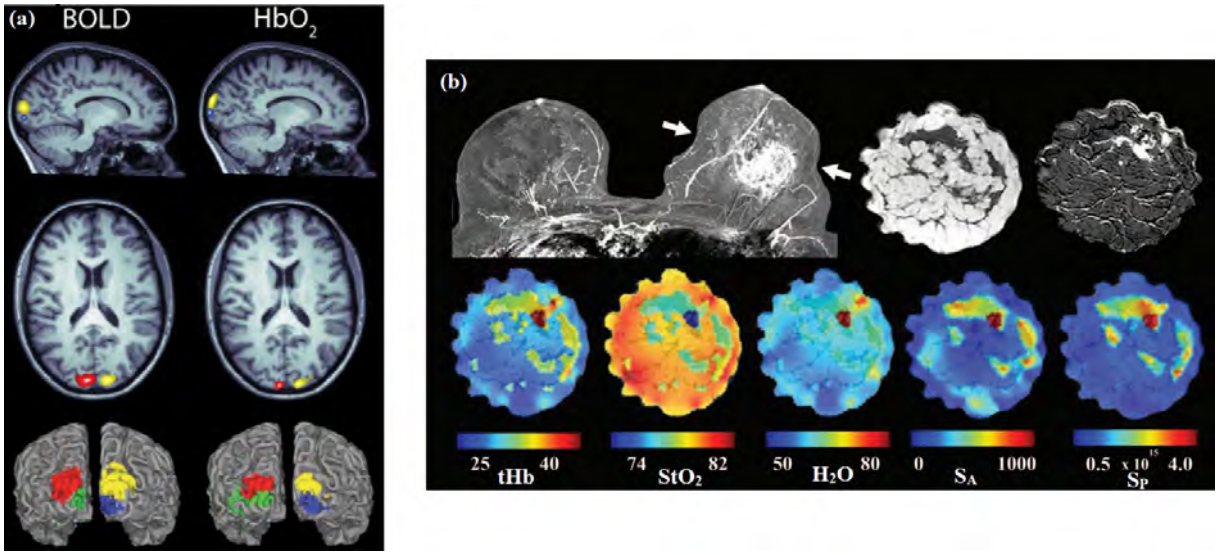

Figure 2.4: Examples of successful applications of DOT such as (a) a correlation between fMRI BOLD signal and high-density DOT functional activations, where each colour represents different visual stimuli, reproduced with permission from [80] and (b) reconstructed distributions of water, oxygenation, total haemoglobin and scatter for MRI guided DOT of breasts for cancer tumour detection, reproduced with permission from [82].

measurement of the flight time of individual photons [84]. FD and TD data provides additional information compared to CW about the probabilistic mean pathlength of photons, improving the ability to separate scattering and absorption events, however the hardware required for these modes is significantly more expensive than in CW systems. Two of these modes of data acquisition have been investigated for joint imaging, CW [85, 86, 87], and FD [4, 88], however the high associated cost has limited clinical translation of FD joint imaging systems in the past, making the development of CW systems of interest.

Additionally, the orientation of source and detector positions are typically described as either reflectance measurements, when both the sources and detectors are placed on the same boundary of the imaged object, or transmission, in which the sources and detectors are on opposing sides of the imaged object. The later has been commonly implemented in joint imaging, presumably as it should provide a better dynamic range for this application as a result of a smaller variation in the pathlength when considering source-detector pairs for an array of detectors on an opposing boundary of a cylindrical-like object when compared to reflectance mode, when sources and detectors are placed on a common

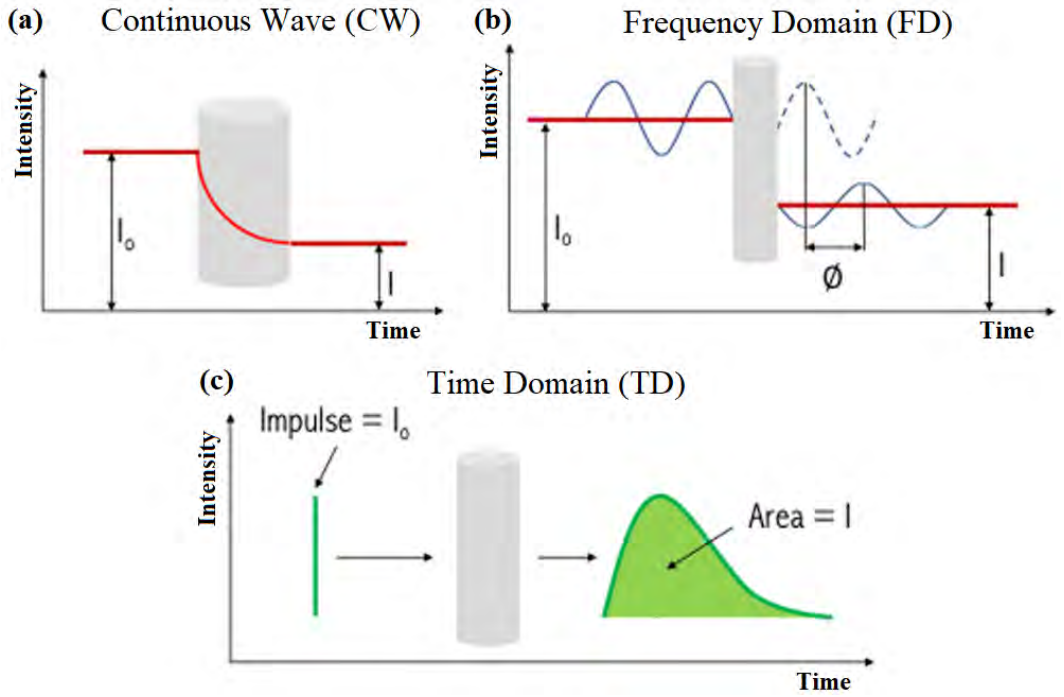

Figure 2.5: Illustrations of the three modes of data acquisition employed in DOT, with plots of intensity over time of transmitted light through tissue. I_0 is the input intensity which is either unmodulated, modulated at ≈MHz or as a picosecond pulse for either (a) continuous wave (b) frequency domain or (c) time domain, respectively. Measurement of the phase shift (ϕ) or the temporal spread point function requires additional hardware and therefore adds to system total cost. Figure adapted from [89] with no permissions required.

boundary.

2.2.1 Non-Contact DOT

To enable tomographic reconstruction in DOT, light must be both injected and measured at multiple boundary locations. Measurement of the boundary fluxes is typically achieved using either optical fibres in contact with the surface of the tissue [90] or a highly sensitive, non-contact imaging device such as a charge-coupled device (CCD) camera [91]. One advantage in the latter case is that camera pixels provide a high density array of detectors, measuring the flux at a many locations on the boundary simultaneously in a single image. Illumination can also be either contact-based, using optical fibres, or non-contact based, using mechanical devices to redirect light to the desired tissue boundary locations. The

advantages of a non-contact approach, for both illumination and flux measurement, are a greater flexibility in the shape of the object being imaged and significantly shorter set-up times, without the need for time consuming attachment of optical fibres. Examples of applications where non-contact approaches have successfully been used for DOT include foot imaging for monitoring peripheral arterial disease [92], small animal imaging [93, 94] and finger imaging [91].

Three different implementations of non-contact illumination have been previously proposed in the literature for a variety of optical imaging applications, including; stepping motor-driven translation stages [91, 95, 96, 97], digital micro-mirror devices (DMDs) [93], or galvanometer-based systems [98, 99], with schematics of these three approaches in the context of joint imaging illustrated in Figure 2.6. Translation stages can be used to mechanically adjust the position of an optical fibre to control the source position, however this approach is inherently slow at switching source positions. DMDs consist of an array of mirrors which can be selectively switched into either an "on" or "off" state to spatially adjust the incident illuminating pattern. These devices are particularly useful for structured illumination [100], where the tissue is illuminated with a set of spatial patterns, however for point source illumination this requires the majority of mirrors to be in an "off" state thus sacrificing a large proportion of the source flux. Finally, galvanometer-based systems have also been previously used for source position control, in both DOT [98] and diffuse correlation spectroscopy [99], where a collimated beam of light is redirected by controlling the axial rotation of a pair of mirrors.

2.3 Modelling Light Propagation in Tissue

In order to recover a distribution of optical properties μ within a tissue from fluence measurements at the boundary ϕ, the process of which is commonly called the *inverse problem* $\mathfrak{F}^{-1}$, a mathematical construct or model commonly known as the *forward problem* $\mathfrak{F}$ must first be defined that accurately predicts how light will propagate through biological

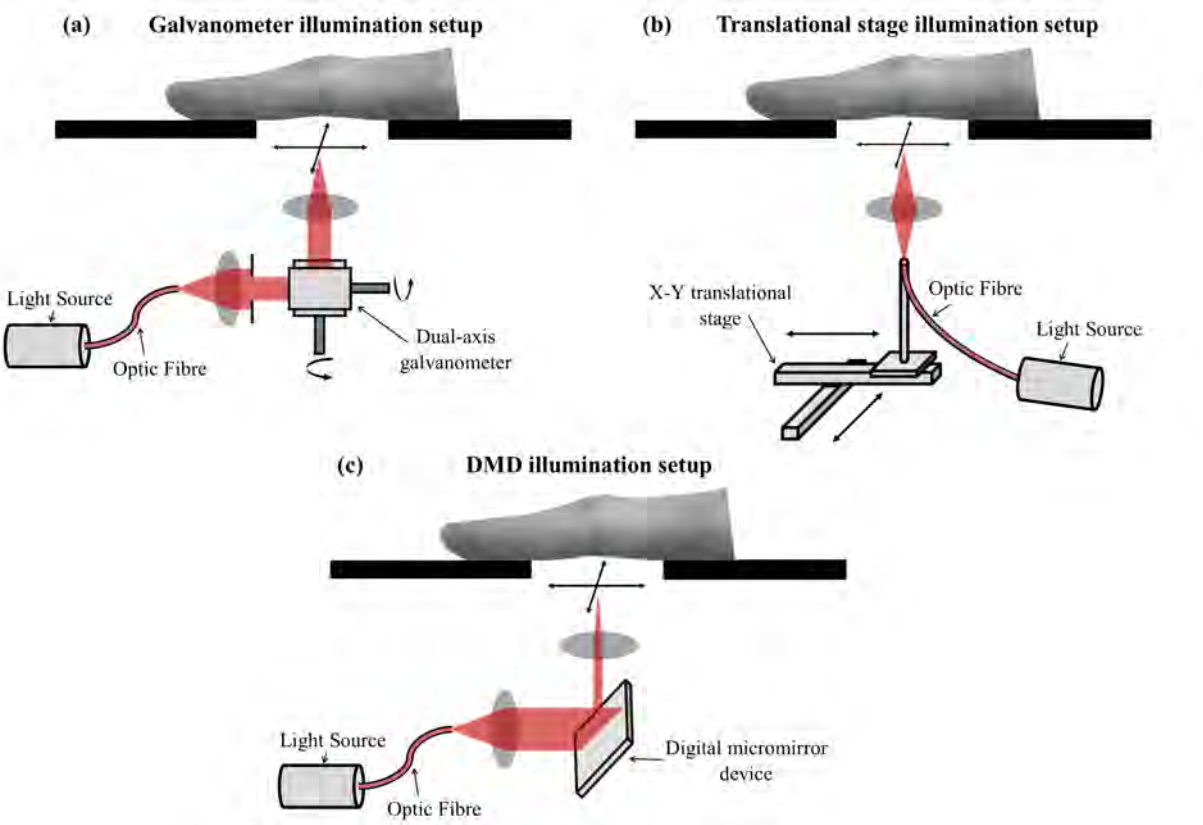

Figure 2.6: Schematics of three different approaches for non-contact optical illumination previously proposed in the literature, in the context of joint imaging.

tissue, accounting for both scatter and absorption interactions as shown in Equations 2.7 and 2.8.

$$\mathfrak{F}\{\mu\} = \phi, \tag{2.7}$$

$$\mathfrak{F}^{-1}\{\phi\} = \mu, \tag{2.8}$$

The physical properties behind the propagation of light in biological tissue have been extensively studied over the last 50 years and are well understood. In classical electromagnetism, light is described as an interaction of electric and magnetic waves governed by Maxwell's equations. By considering energy conservation from these equations and ignoring the non-sphericity and orientation of particles, depolarization or any coherence effects, the most general time dependent form of the Radiative Transport Equation (RTE) can be derived [101],

$$\frac{1}{c}\frac{\delta R(\mathbf{r},\hat{s},t)}{\delta t} + \nabla . R\left(\mathbf{r},\hat{s},t\right)\hat{s} = -\mu_t R\left(\mathbf{r},\hat{s},t\right) + \mu_s \int_{4\pi} R\left(\mathbf{r},\hat{s},t\right) P\left(\hat{s},\hat{s}'\right) d\Omega' + Q\left(\mathbf{r},\hat{s},t\right), \tag{2.9}$$

with radiance R, total absorption $\mu_t = \mu_a + \mu_s'$, speed of light c, energy of photon flux from light source Q and probability of changing direction due to scatter P, all defined anisotropically at position $\mathbf{r}$ and time t, in the direction $\hat{s}$. The RTE is a highly accurate, deterministic model for light travelling through a homogeneous turbid media and this integro-differential equation can be solved numerically using, for example, Monte-Carlo (MC) simulation, where probability density functions can help calculate the trajectories of a large number of simulated photons [102]. Implementation of MC methods, however, are challenging and come with high computational expense, as both spatially and angularly discretised degrees of freedom are needed. Higher order approximations to the RTE exist that rely on more complex integral-differential equations to incorporate both directional and spatial components of light propagation. Examples include spherical harmonics $\mathrm{P_N}$ or discrete ordinates method $\mathrm{S_N}$, in which the angular components of fluence in each method are either expanded into spherical harmonics [103] or discretised into a number of directions respectively [104], however implementation of these forward models is challenging and very computationally expensive, making reconstruction times undesirably long for the proposed clinical prototype device in which multiple joints are imaged during a single imaging session. A less computationally expensive, simplified spherical harmonics ($\mathrm{SP_N}$) approximation to the RTE has been proposed [105], in which the 3D $\mathrm{SP_N}$ forward model consists of coupled diffusion equations for composite moments of fluence, the derivation and full implementation of which has been discussed in detail in the referenced works. These equations in full define the $\mathrm{SP_7}$ model, however they can be further simplified to either $\mathrm{SP_5}$, $\mathrm{SP_3}$ or $\mathrm{SP_1}$. Integration of the $\mathrm{SP_N}$ forward model into FEM package NIRFAST was previously reported [106], however limitations of this implementation include a more under-determined inverse problem from a greater number of Nth order unknowns and an inability

to experimentally measureme individual composite moments using CW systems such that the total fluence must be approximated by summing the individual composite moments [107], meaning this forward model requires significantly more testing and verification before any clinical applications.

The diffusion approximation (DA) is a first order, P_1 spherical harmonic approximation to the RTE, derived through a series of assumptions about dominance of scatter over absorption $\mu_s' >> \mu_a$ and isotropy of scatter,

$$\frac{1}{c}\frac{\delta\phi(\mathbf{r},t)}{\delta t} + \mu_a\phi\left(\mathbf{r},t\right) - \nabla.\left[D\nabla\phi\left(\mathbf{r},t\right)\right] = S\left(\mathbf{r},t\right) \tag{2.10}$$

with fluence rate ϕ, isotropic source S and diffusion coefficient D defined as $\frac{1}{3(\mu_a+\mu_s')}$. The time dependent version is shown in Equation 2.10, although this can be simplified to time independent and frequency dependent equivalents depending on the mode of data acquisition chosen. Analytical solutions of the DA exist for regular homogeneous geometries, such as infinite [108] or semi-infinite [109] mediums, yet for more complex, arbitrarily shaped geometries, where analytical solutions are often not possible, numerical methods can be used to solve the forward problem. In the FEM formulation, the problem is discretised over an area or volume, dividing it into a set of nodes connected by triangular elements, an example of which is shown in Appendix A.10. Detailed description of implementation of the forward problem and construction of the Jacobian using a FEM framework are beyond the scope of this thesis, but excellent reviews of this are available [110, 111]. An index-mismatched type III condition, commonly known as the Robin boundary condition, is used to represent the tissue-air boundary in this work, where at the tissue boundary flux exits but does not return [112, 113].

The presence of regions of low scattering such as cerebrospinal fluid in the brain or very short source-detector separations can invalidate assumptions used in the derivation of the DA about isotropic fluence or the dominance of scatter over absorption $\mu_s' >> \mu_a$, and lead to errors in image reconstruction [114, 104]. Although in this sense the DA sacrifices some accuracy compared to alternative forward models of the RTE, it is significantly easier

and therefore faster to solve, meaning it is commonly used as a forward model due to its robustness, flexibility and computation speed [115, 93, 116]. The DA was therefore selected in this work for several reasons, 1. it provided fast reconstruction times preferential for the extensive testing during system development and joint imaging during pilot studies, 2. it was well-integrated into the readily available open-source FEM package NIRFAST [72], and 3. this implementation had been extensively tested and verified during comparative studies with both analytical solutions or phantom measurements [113, 115].

2.3.1 Reconstruction Algorithm for Inverse Problem

When recovering absolute values using DOT, the inverse problem is solved by minimising the difference between the measured data, ϕ^M, and the modelled (forward) data, $\mathfrak{F}\{\mu\}$, in a least squared sense over a number of source and detector pair measurements. The resulting *inverse problem* $\mathfrak{F}^{-1}$ is highly ill posed, owing to the non-linearity of the forward model, and to commonly being under-determined, where there are a larger number of unknowns than measurements. As this inverse problem cannot be solved accurately in a single step, this is achieved using nonlinear iterative reconstruction algorithms involving either optimisation schemes where the gradient of the objective function is calculated directly [117, 118] or Newton-like approaches implemented in a Levenberg-Marquardt procedure [119, 72], the latter of which was implemented in this work. The objective function in the least squared sense is defined as,

$$\psi = \min_{\mu} \|\phi^M - \mathfrak{F}\{\mu\}\|_2^2 + \tau\|\mu\|_2^2, \tag{2.11}$$

where τ is the regularisation parameter equal to $r * max(J^T J)$, with r a predefined constant. An initial estimate for the optical properties, μ_0, is typically obtained using a global, homogeneous fitting procedure [115] or based on prior knowledge from the literature. By considering the Taylor expansion of ψ around μ_0 it is possible to derive the generalized Moore-Penrose update [120], which is used to update optical properties at each iteration,

$$\delta\mu = (J^T J + \tau I)^{-1} J^T \delta\phi, \tag{2.12}$$

where $\delta\mu$ is the update vector and $\delta\phi$ is the difference between the measured data and forward data. The natural logarithm of the boundary intensity $ln(I)$ is commonly used to represent ϕ, as this has been shown to significantly improve reconstruction quality compared to absolute intensity values [121]. J is known as the Jacobian or sensitivity matrix, constructed using the adjoint method and calculated using the reciprocity approach, which has been validated using the perturbation method [122]. As the Hessian ($J^T J$) is typically ill-conditioned, inclusion of regularisation is required to make it more diagonally dominant and stabilise the update by damping very small singular values, such as L2-based (Tikhonov) regularisation [123] in Equation 2.11 implemented in this work and results in a smoother final solution. An alternative regularisation scheme to Tikhonov (L2) is L1-norm implementation, has been investigated in DOT for its abilities to preserve edges in images and robustness against noise, as a consequence of its sparsity-promoting properties. In the L1-norm scheme, the objective function becomes,

$$\psi = \min_{\mu} \|\phi^M - \mathfrak{F}\{\mu\}\|_2^2 + \tau\|\mu\|_1, \tag{2.13}$$

however to solve this equation requires more complex approaches compared to the L2 equivalent, due to its non-differentiable properties, such as iteratively reweighted least square algorithm, alternating directional method of multipliers, or fast iterative shrinkage-thresholding algorithm [124]. An initial value for τ is commonly chosen empirically in DOT, and reduced at each iteration by a factor of 10^q, where q = 0.125 in this work. The termination criteria κ was set to allow convergence of the solution to sufficient accuracy, pre-defined in these studies as when as a change in optical properties of less than 2% from the previous iteration.

All modelling of light propagation in this thesis was carried out using open-source FEM package NIRFAST [72]. Previous investigations have been carried out to validate

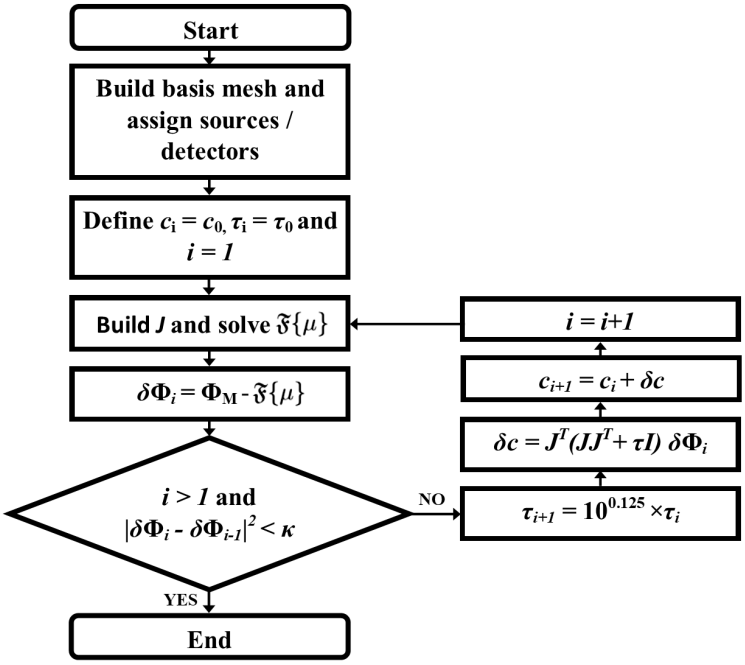

Figure 2.7: Simplified flow diagram illustrating the Levenburg - Marquardt based iterative algorithm implemented to solve the regularised inverse problem, by directly updating chromophore concentrations (c) using the spectrally constrained approach to minimise in the least squared sense the difference between measured and forward boundary data.

the accuracies of both the forward model and the iterative reconstruction algorithm implemented in this software either in comparison with MC simulations [113] or with phantom data [115] respectively. Figure 2.7 displays a flow diagram summarising the reconstruction algorithm used to solve the inverse problem, in which chromophore concentrations are updated directly using a spectrally constrained approach, which will be discussed in the next section.

2.4 Spectrally Constrained Multiwavelength Approach

Single wavelength measurements only permit the recovery of maps in μ_s' and μ_a corresponding to the measurement wavelength. Acquiring optical data at multiple wavelengths is advantageous as it permits the spectroscopic decoupling of contributions from individual biological chromophores, which in turn can be used to derive clinically relevant parameters such as tHb and StO_2. In early multiwavelength DOT studies when solving the inverse

problem, values of μ_s' and μ_a at multiple wavelengths were first recovered, from which chromophore concentrations could be calculated using the Beer-Lambert law or S_A and S_P fitted for using Mie theory, an approach referred to here as conventional spectral (CONV)-DOT. In CONV-DOT, it has been shown that small errors in μ_s' and μ_a for a given wavelength are amplified in these resulting values for chromophore concentrations, S_A or S_P [125]. A spectrally constrained (SC)-DOT approach was previously proposed, where corresponding extinction coefficients and scattering values were directly incorporated into J, such that chromophore concentrations, S_A and S_P are instead updated directly using the Moore-Penrose update at each iteration, making the structure of J and $\delta\mu$,

$$\mathrm{J} = \begin{bmatrix} \mathrm{J}_{\lambda_1,C_1} & \mathrm{J}_{\lambda_1,C_2} & \mathrm{J}_{\lambda_1,C_3} & \mathrm{J}_{\lambda_1,S_A} & \mathrm{J}_{\lambda_1,S_P} \\ \mathrm{J}_{\lambda_2,C_1} & \mathrm{J}_{\lambda_2,C_2} & \mathrm{J}_{\lambda_2,C_3} & \mathrm{J}_{\lambda_2,S_A} & \mathrm{J}_{\lambda_2,S_P} \\ \mathrm{J}_{\lambda_3,C_1} & \mathrm{J}_{\lambda_3,C_2} & \mathrm{J}_{\lambda_3,C_3} & \mathrm{J}_{\lambda_3,S_A} & \mathrm{J}_{\lambda_3,S_P} \\ \mathrm{J}_{\lambda_4,C_1} & \mathrm{J}_{\lambda_4,C_2} & \mathrm{J}_{\lambda_4,C_3} & \mathrm{J}_{\lambda_4,S_A} & \mathrm{J}_{\lambda_4,S_P} \\ \mathrm{J}_{\lambda_5,C_1} & \mathrm{J}_{\lambda_5,C_2} & \mathrm{J}_{\lambda_5,C_3} & \mathrm{J}_{\lambda_5,S_A} & \mathrm{J}_{\lambda_5,S_P} \end{bmatrix}, \qquad (2.14)$$

$$\delta\mu = \begin{bmatrix} C_1 \\ C_2 \\ C_3 \\ S_A \\ S_P \end{bmatrix}, \qquad (2.15)$$

where $\mathrm{J}_{\lambda_i,C_j} = (\delta\phi_{\lambda_i}/\delta\mu_{aC_j}) \cdot \varepsilon_{\lambda_i,C_j}$, $\mathrm{J}_{\lambda_i,S_A} = (\delta\theta_{\lambda_i}/\delta D) \cdot (-3D^2)(\lambda_i^{-S_P})$ and $\mathrm{J}_{\lambda_i,S_P} = (3D^2)(\mu_s' ln(\lambda_i))$. The advantage of SC-DOT approach is that the number of unknowns remain constant, irrelevant of any increase in the number of wavelengths measured, whilst in CONV-DOT, an increase in number of measurement wavelengths results in a proportional increase in the number of unknowns, in this case $\mu_a(\lambda)$ and $\mu_s'(\lambda)$ at each node. By reducing the parameter space of the inversion in this way when spectral *a priori* information is incorporated, SC-DOT has been shown to significantly improve reconstruction quality [126], with evidence that in certain cases spectral *a priori* information can be more beneficial than spatial *a priori* information to reconstruction [127]. An example plot for the HbO sensitivity profile within a homogeneous finger model for a single source detector pair is shown in Figure 2.8, with the diffusive nature of light transport resulting in the so called 'banana shaped' profile of J, displaying hypersensitivity close to the sources and detectors. This hypersensitivity can cause systematic and random error to propagate to these regions, with reconstruction artefacts close to the boundaries commonly reported in the literature [127, 128].

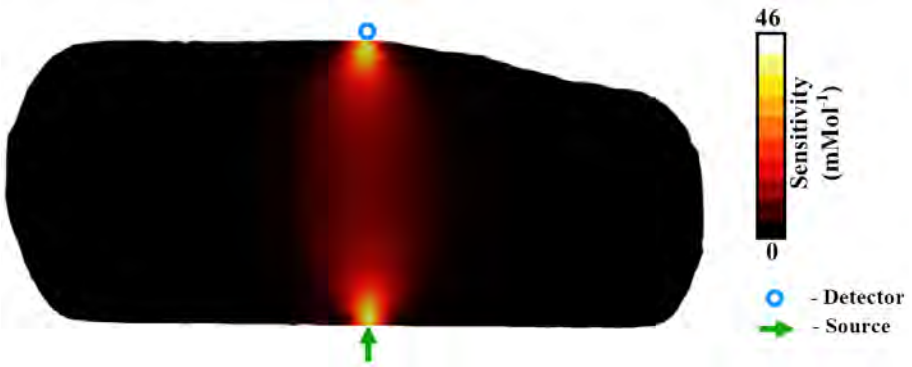

Figure 2.8: Example sensitivity for HbO at 650nm for a single source detector pair, illustrating the increased sensitivity closer to the boundary. Slice shown through homogeneous finger model with values assigned for HbO, Hb, H_2O, S_A and S_P of 0.012mMol, 0.005mMol, 30%, 1.4mm^{-1} and 1.47 respectively.

2.4.1 Optimum Wavelength Selection

A fundamental non-uniqueness in the DOT inverse problem has been proven theoretically when using the DA as a forward model and single wavelength, CW data [129, 130]. In this work the authors show the solutions to the non-linear forward problem lie in the null space ie. there exist an infinite set of optical parameters, μ_a and μ_s', which give rise to identical boundary data. This results in an excessively ill-posed inverse problem and can lead to crosstalk between μ_a and μ_s' values at different wavelengths. Nevertheless, a solution can still be attained in DOT by solving a regularised inverse problem through the optimisation schemes such as that already discussed in Section 2.3.1. It has also been demonstrated that with multispectral data, the degree of non-uniqueness and crosstalk can be minimised by choosing an optimal set of wavelengths, through constraining two parameters derived from the DA. The first is the residual (R), a measure of the solutions uniqueness ranging from 1 (unique) to 0 (non-unique),

$$R = \|1 - \mathbf{E}\left(\mathbf{E}^T\mathbf{E}\right)^{-1}\mathbf{E}^T 1\|, \qquad (2.16) \qquad \mathbf{E} = \begin{bmatrix} \frac{\varepsilon_1(\lambda_1)}{(\lambda_1)^{S_P}} & \cdots & \frac{\varepsilon_N(\lambda_1)}{(\lambda_1)^{S_P}} \\ \vdots & \ddots & \vdots \\ \frac{\varepsilon_1(\lambda_M)}{(\lambda_M)^{S_P}} & \cdots & \frac{\varepsilon_N(\lambda_M)}{(\lambda_M)^{S_P}} \end{bmatrix}, \qquad (2.17)$$

where N is the number of chromophores and M is the number of wavelengths. The second is the condition number κ,

$$\kappa = \frac{max\,(\epsilon)}{min\,(\epsilon)} \tag{2.18}$$

where ϵ is the matrix of all extinction coefficients, which acts as a measure of the crosstalk between chromophores and should therefore be minimised. Through optimising a wavelength set selecting a combination that simultaneously minimise κ and maximise R, evidence of successful recovery of heterogeneities in S_A, in addition to recovery of the HbO, Hb and H_2O, have been demonstrated when using CW measurements with SC-DOT [130, 131].

2.5 Diffuse Optical Imaging of RA

The pathological changes occurring in an inflamed joint of an RA patient, which include localised hypoxia, angiogenesis and scattering changes as discussed in Section 1.1.2, lead to spectral alterations of optical properties of the synovium and synovial fluid compared to healthy tissue. This has motivated several research groups to investigate the utility of this intrinsic optical contrast for diagnosis and monitoring of inflammatory arthritis [91, 132, 133, 134]. All the systems developed in these referred works were designed to image the hand, with the PIP, MCP and wrist joints some of the most commonly afflicted in RA [135] and logistically being a relatively straightforward part of the anatomy to image.

2.5.1 Early Studies

Interest in the detection of inflammatory disease in the peripheral joints using DOI was first reported in the mid-1990s, with an intra-lipid based joint phantom experiment [136] and a small *in vivo* pilot study comparing transillumination images of joints from four patients with rheumatic conditions and four healthy participants [137]. In both these studies, the total intensity, standard deviation, relative skewness and relative kurtosis

of the transmitted intensity profile through the joint were used as features to assess inflammation.

Tissue	Healthy		RA	
	μ_a (mm^{-1})	μ_s' (mm^{-1})	μ_a (mm^{-1})	μ_s' (mm^{-1})
Skin	0.02	1.95	0.02	1.95
Bone	0.08	2.1	0.08	2.1
Cartilage	0.17	1.8	0.17	1.8
Articular Capsule	0.15	0.6	0.24	1.1
Synovia	0.004	0.006	0.011	0.012

Table 2.1: Optical properties of different (*ex vivo*) tissue samples from the joint at 685nm, for both healthy subjects and patients with RA, as mean values for 10 and 14 samples, respectively, reproduced from [133].

Further work analysing extruded samples of both the synovium and synovial fluid *in vitro* using a double-integrating-sphere technique revealed a difference in μ_a and μ_s' between healthy and diseased tissue [138, 139], as shown in Table 3.1. The authors of this work reported an optical difference in the extruded synovial fluid samples was evident from visual inspection alone, as it changed from a clear yellow substance in healthy joints to a more opaque, greyish yellow colour in RA patients, alterations that were attributed to the pathophysiological changes associated with proliferation of leukocytes infiltrated into the synovium as discussed in Chapter 1. Furthermore, the degree of distinction in optical properties between diseased and healthy tissue was shown to spectrally vary [140], as shown in Figure 2.9, with the greatest discrepancy observed between the 600-700nm range.

2.5.2 Transillumination Imaging

These initial findings motivated the development of a non-tomographic, single wavelength, CW transillumination device, in which a light source was focused on the dorsal side of the finger and images were collected using a CCD camera on the palmar side [141, 86, 142, 87], as shown in Figure 2.10. The captured images of flux transmitted through the joint

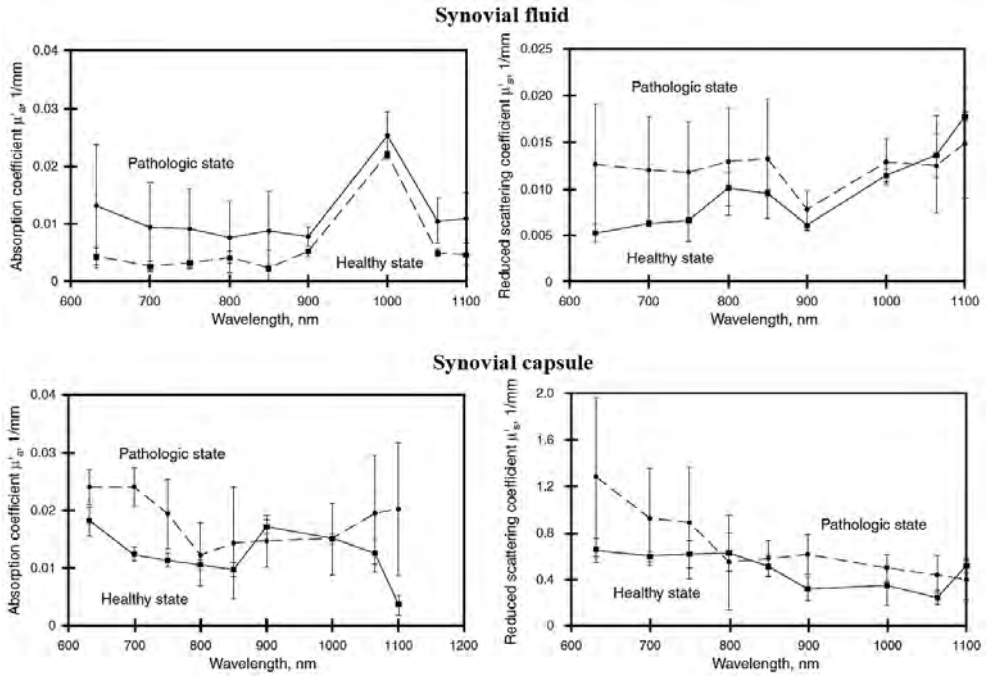

Figure 2.9: μ_a and μ_s' measured experimentally for extruded samples of both the synovial capsule and synovial fluid using a double-integrating-sphere technique, for both healthy and diseased participants. Reproduced with permission from [132].

were analysed using a range of features including average intensity, maximum intensity, a Gaussian density function fit and second derivative curvature of the light intensity. Longitudinal studies involving a total of 136 PIP joints from 22 RA patients and 8 healthy controls, reported up to 80% S_E and 89% S_P for correctly classifying changes in the inflammatory status over time when comparing baseline and follow-up examinations, by using use advanced classification tools such as, a generalized linear model, Gaussian progress regression, Gaussian process classification or support vector machines (SVM) [86, 87]. Despite these promising results for monitoring disease progression, the authors describe an inability to accurately determine the inflammatory status using this dataset from a single examination alone without reference baseline, attributed due to "high inter-individual variability of joint structure and optical characteristics" [86].

Two image processing algorithms were presented with the aim of increasing the difference between the healthy and inflamed transillumination images, including; a methodology for the deconvolution of non-useful contributions from the skin, where the point spread function was accurately estimated using MC simulations [143], and a non-local image

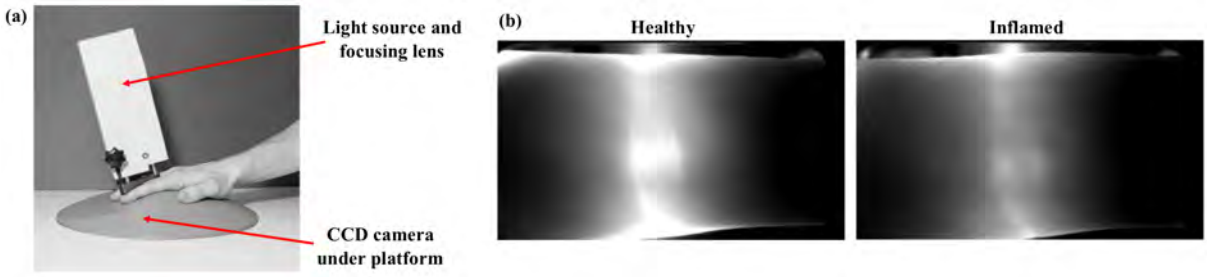

Figure 2.10: (a) Non-tomographic, CW transillumination finger imaging device. (b) Examples of typical transmission images acquired using the system for both a healthy and an inflamed joint. Adapted from [87], no permission needed.

segmentation algorithm to characterize light transmission distributions [133]. This device was then developed to include multiple light emitting diodes at different wavelengths, from which images were combined to create false colour images for optimum visualisation by the human eye [144]. A clinical study using this device that included 38 RA patients and 28 healthy subjects demonstrated 65.8% S_E and 92.9% S_P when classifying the already confirmed diagnosis of each subject [145], however results in this are limited to a patient level, with no attempt to classify on an individual joint basis.

2.5.3 DOT of Rheumatoid Arthritis

The feasibility for tomography to study rheumatic human joints was first investigated in numerical simulations using either TR [146] or CW [147] data for joint models created by segmenting an MRI image of a human PIP finger in each of these respective studies and assigning realistic optical properties for the synovial capsule, synovial fluid and bone. Promising results from these initial simulations motivated the development of a state of the art, single wavelength, FD system for imaging RA joints capable of recovering 3D maps of absorption and scattering coefficients [91, 148]. This device was assessed in a large clinical study, involving 120 healthy and 99 inflamed fingers, revealing an elevated scattering and absorption in the joint space of RA patients compared to healthy volunteers [4], examples of which are shown in Figure 2.11. From this study, values for S_E and S_P of up to 91% and 86% respectively were attained when using multivariate machine learning (ML) with

basic statistical features from these images, such as the maximum, minimum and variance. Improvements in S_E and S_P were demonstrated, with values between 93.8 - 100% [88] using the same dataset through a combination of more complex heuristic feature extraction about the spatial distribution of these maps, including a Gaussian mixture model or fast Fourier transform (FFT) analysis, and implementation of more advanced ML techniques including; k-nearest-neighbours, linear and quadratic discriminant analysis, self-organizing maps, and support vector machines (SVM) [149]. The associated hardware required to measure phase for FD data for this system introduces additional complexity and cost [148], which can make imaging systems prohibitively expensive for clinical translation. Although a CW approach is significantly cheaper, when considering only the amplitude of measurements for reconstruction using the same dataset and techniques, the authors report a dramatically reduced S_E and S_P of up to 64% and 55% respectively [88].

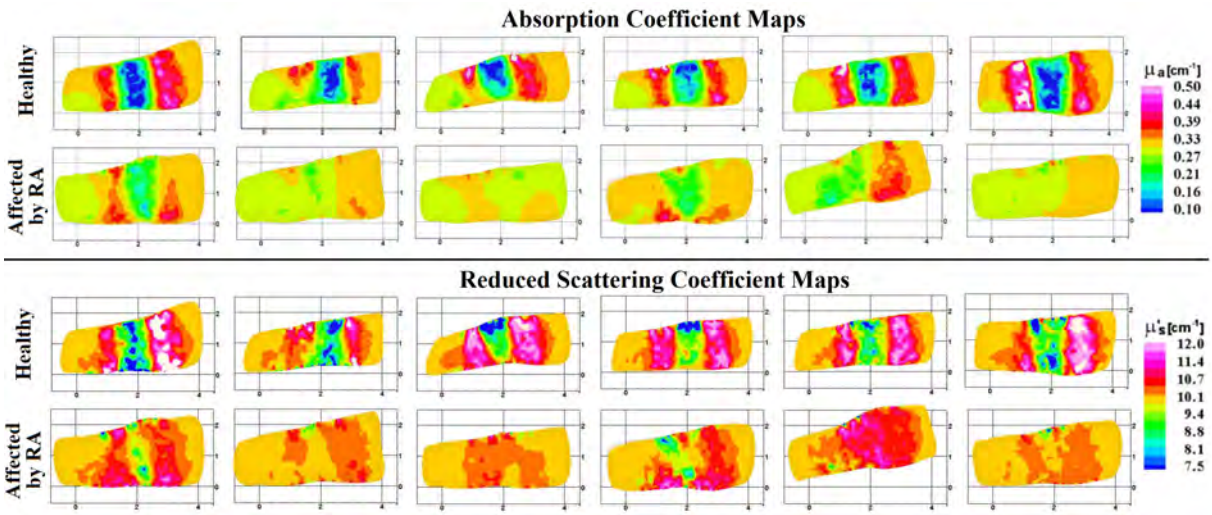

Figure 2.11: Absorption and scattering coronal cross-sectional images of PIP joints from subjects without or with RA, acquired using a single wavelength (670nm), FD system with 600 MHz source modulation. Reproduced with permission from [4].

Some limitations of this work include (1) data acquisition at a single wavelength (670nm), with a multiwavelength approach required to deduce pathophysiological changes that are known to occur in RA such as hypoxia or angiogenesis, as outlined in Chapter 2, and (2) a separate laser scanning device was required to measure the surface geometry for mesh generation, which was then registered to the optical data using an fiducial marker

added to the skin surface.

2.5.4 DOT of Osteoarthritis

OA is another common joint disease, where age-related changes, genetic predisposition, and abnormal biomechanical force result in degeneration of the joint and cartilage. In distinction from RA, OA is described as a prototypical non-inflammatory condition, although a degree of localised stress-induced proinflammatory mechanisms is associated [150]. One group have investigated the potential of DOT for monitoring OA, with initial studies showing it was feasible to obtain cross-sectional images of bone structure for both a chicken bone phantom and a human finger using 2D DOT with only CW data and employing reconstruction algorithm based on the DA in a FEM construct [83]. Extension of this approach to 3D reconstruction with FD data revealed the benefits of volumetric images, with even further detail of the joint structure and composition visible [151, 152]. In a small clinical study involving two patients with OA and three healthy volunteers, structural changes in OA patients such as a narrowing of the joint space could be detected using this device [3].

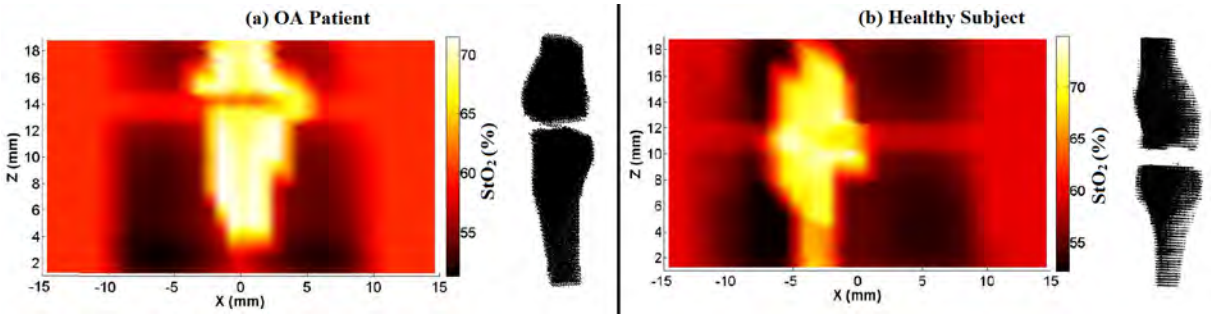

Figure 2.12: Image slice color heatmaps maps of StO_2 in colour together with the corresponding volumetric X-ray tomosynthesis bone structure for joints from etiehr (a) an OA patient and (b) a healthy subject. Characteristic joint narrowing in X-ray tomosynthesis images and localised hypoxia in the joint space of StO_2 heatmaps can be seen for the joint of the OA patient compared with the healthy subject. Adapted with permission from [153].

The inclusion of spatial *a priori* information about the tissue's layered structure by constraining the iterative reconstruction algorithm has been shown to dramatically improve

the spatial resolution and quantitative accuracy of recovered optical properties in DOT [154, 155]. X-ray tomosynthesis imaging was incorporated into this joint imaging system to allow a multi-modal approach, where X-ray images were acquired at multiple slices and combined to build a 3D map of the bone structure to be used as spatial *a priori* information for a hybrid regularization-based algorithm [156]. This resulted in dramatic enhancement of spatial resolution of the structure of the joint, as shown in Figure 2.12 and a clinical study imaging the distal inter-phalangeal joints from 22 subjects with OA and 18 healthy controls, OA could be diagnosed with 91% S_E and 100% S_P using multispectral CW data [153]. Although results from this approach are impressive, limitations of this device in a clinical context include the associated high ionisation exposure when acquiring volumetric X-ray images in a multi-modal approach, the requirement of 128 coupling fibres making the system extremely bulky, and its long acquisition times, at 27 minutes for a single joint at 8 wavelengths. These studies also raise a challenging issue regarding the capability of optics to distinguish between inflammatory changes in RA and other joint diseases, such as in OA, a subject which is beyond the scope of the presented work, but will require investigation in future studies.

2.5.5 Dynamic DOI

An alternative approach for detecting inflammation is to induce a physiological change using an external stimulus and measure the corresponding change in optical properties. One way to achieve this in the joint is through the restriction of arteriole or ventricular blood flow using a Sphygmomanometer across the arm, with optical changes during this haemodynamic response providing information more reflective of the underlying vascularity than static optical images. In this dynamic approach, a number of systematic errors and calibration factors are shared at all time points and are therefore eliminated from this differential measurement, which is taken advantage for example when measuring functional activations within the brain for cerebral DOT.

In a study directly comparing static and dynamic joint imaging using a dual-wavelength,

tomographic contact imaging system, contrast and maximum quantitative percentage difference between RA and healthy joint images were found to be greater when using dynamic measurements [157]. Further results from three case studies provided evidence that maps of dynamic changes in HbO and Hb during cuff occlusion are distinct between a healthy subject and two patients with RA [158]. Another imaging system was developed measuring non-tomographic, bulk changes in the hyperspectral transmission spectra (500 - 1000nm) for the joint during cuff occlusion. In a clinical study involving 67 patients, by applying partial least-squares discriminant analysis to the changes in these spectra during occlusion, optical scores were shown to agree well with severity of inflammation, as measured by CE (area under the receiver-operater curve (AUC) = 0.88) [134], with wavelengths between 810 - 830 nm most significant in contributing to regression analysis. Based on these initial findings, a non-tomographic, whole hand imaging system was commercially developed (Handscan, Hemics, Eindhoven, The Netherlands), in which an optical score is assigned to each joint. An initial pilot study showed the system performed moderately for RA diagnosis compared to ultrasound (AUC=0.79) [159] and a much larger study involving 1003 joints from 44 patients, showed improved AUC 0.85 all joints of 0.88, 0.83 and 0.74 for the MCPs, PIPs and wrists respectively, attributed to the replacement of the light emmiting diode light source with a laser [160]. One obvious drawback of a dynamic methodology is this approach can potentially introduce additional discomfort for patients already experiencing a degree of pain.

2.5.6 Higher Order Solutions to the RTE

Reports of comparable levels of μ_s and μ_a for the synovial fluid [136], together with the relatively small geometry of the finger, have motivated efforts to utilise higher order approximations to the RTE for more accurate light propagation modelling in the finger [161, 162]. Several groups have previously implemented SP_N forward models for joint imaging, with single wavelength, FD imaging reporting improvements from 66.7% to 87.9% in S_P and from 81.1% to 92.9% in S_E when using the SP_3 model instead of SP_1 to classify

inflamed RA joints [162]. For single wavelength, CW imaging for osteoarthritis diagnosis, a discrepancy of between 4-15% in recovered parameters between SP_1 and SP_3 models [161] was observed, although the difference between the two models was much less substantial when X-ray information was incorporated into the reconstruction as a spatial prior.

2.6 Related Optical Techniques

2.6.1 Photoacoustic Tomography

Photoacoustic tomography (PAT) is a relatively novel, hybrid imaging modality that combines the two physical wave modalities of light and sound. When biological tissue is optically illuminated, localised thermal expansions and compressions create a series of acoustic waves, which can be measured at the tissue boundary using US transducers. Knowledge of the physics behind acoustic wave propagation in biological tissue, together with multi-wavelength illumination, allows tomographic reconstruction of endogenous chromophore concentrations. The principal advantage of the PAT over DOI is its superior, sub-millimetre spatial resolution, a consequence of the linearity of US wave propagation, although recovering quantitatively accurate chromophore concentrations using PAT is more challenging.

PAT was first demonstrated as a promising technique for RA monitoring in studies of joints from animals and human cadaver finger [163]. The effectiveness of PAT for joint imaging was further explored using a series of phantom experiments, showing its ability to differentiate between phantom "cartilage" and phantom "bone" [164] and the ability to recover absorption coefficient maps *in vivo* in human finger joints [165]. The technique is particularly effective at resolving blood vessel formation, useful for indicating angiogenesis in RA, with vessels detected as small as 0.2mm whilst simultaneously providing a measure of StO_2 [166]. Furthermore, a multimodal approach, where photoacoustic imaging and ultrasonography were combined in a single probe, has been shown capable of detecting

functional biomarkers for statistical differences in hyperaemia and oxygenation between healthy subjects and RA patients [167, 168].

2.6.2 Fluorescence Optical Imaging

Fluorescence optical omaging (FOI) involves the intravenous injection of fluorescent contrast agents which are illuminated at some excitation wavelengths and then any re-emitted light at some higher, Stokes-shifted wavelength is then measured at the tissue boundary. The contrast agents used can be either non-specific markers or markers conjugated with molecules specific for a target, for example a folate-targeted fluorescent marker has been used for whole animal imaging in arthritis models [169]. Indocyanine green is currently the only fluorescent dye approved by the European Medicines Agency for usage *in vivo* in humans, and has been shown to enhance visualisation of increased vascularisation within inflamed joints [170], as shown in Figure 2.13. Based on these findings, a commercial, non-tomographic system for human FOI (Xiralite X4; Mivenion GmbH, Berlin, Germany) was developed, with the performance of this system demonstrated in a clinical trial involving 90 joints from 18 patients with RA, found to be 67% S_E and 77% S_P for detecting MRI-confirmed synovitis [171]. A FOI system for tomographic reconstruction of indocyanine green in 3D has also been developed, revealing increased concentrations in inflamed joints of RA patients compared to healthy joints [172]. Although FOI is effective at detecting arthritis related vascular changes in joints, from a clinical perspective, its invasive nature makes it difficult to justify for routine monitoring and unsuitable for patients allergic to contrast agents.

2.7 Advantages and Limitations of DOI

In the context of RA diagnosis and monitoring, non-invasive DOI holds many distinct advantages compared to more well-established imaging modalities discussed in Chapter 1 being; (1) comparatively low cost, (2) highly tolerated by patients with an impeccable

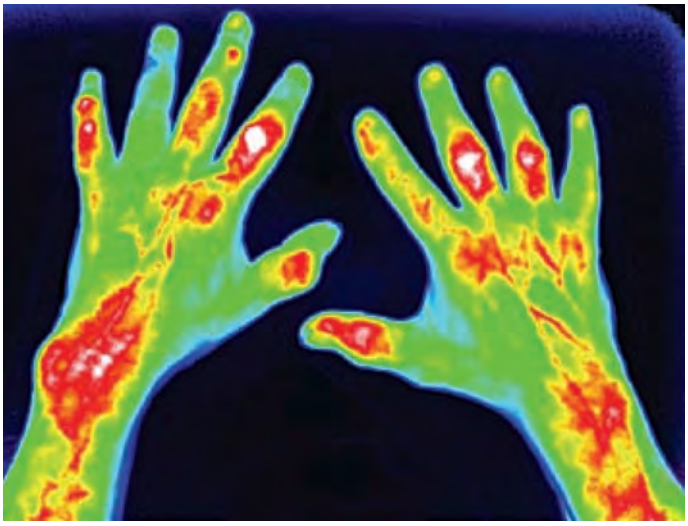

Figure 2.13: An example FOI image for both hands of an RA patient. FOI signal enhancement can be seen for example in the right PIP II, left PIP III and IV and left wrist. Figure reproduced with permission from [170].

safety profile and no associated ionisation exposure, (3) no exclusion criteria such as those encountered with MRI, (4) can be operated by non-clinicians and (5) multi-wavelength measurements can provide functional information, with a high sensitivity to any underlying pathophysiological changes. These factors combined make DOI a promising candidate for applications when a large quantity of scanning is often required, such as wide-scale screening of patients suspected to be afflicted with disease or longitudinal monitoring to assess responses to therapy. The pathophysiological changes associated with inflammation in RA will occur at an earlier stage than subsequent structural bone damage, the only change detected by radiography, making the functional measurements obtained from DOI therefore a good candidate for early diagnostics. Furthermore, compared to more well-established applications of DOT such as the brain or breast, the hand joints are comparatively small at approximately 2-3cm in thickness, making then ideal for achieving good signal to noise ratios (SNR) with transmission imaging in comparatively short times. From these range of implementations

There are some limitations of DOI compared to other modalities. An intrinsically low spatial resolution resulting from the diffuse nature or light transport, means that without spatial *a priori*, many details of from the highly heterogeneous anatomy of the human joint,

which consists of skin, muscle, tendon, bone and a capsule containing synovial fluid cannot be accurately spatially resolved. Additionally an ill-posed and underdetermined inverse problem means there is potential for crosstalk between parameters, impacting quantitative accuracy. Overall however, the advantages of DOI make it a promising candidate as a potential tool for joint imaging to differentiate between inflamed and healthy tissue in RA [1].

2.8 Conclusion

The physical principles describing the propagation of light in biological tissue have been extensively studied and are now well understood within the community. This chapter has outlined the fundamental concepts essential for understanding the remainder of this work and the image reconstruction algorithm used to recover 3D pathophysiological images of the joint was presented.

DOI provides distinctive advantages over the more established modalities discussed in Chapter 1, including being comparatively low cost, well-tolerated by patients, extremely safe with no exposure to ionizing radiation, and can be operated by a non-clinician. The use of multi-wavelength measurements can provide functional information about the current pathophysiological state of diseased tissue and through tomographic data acquisition a degree of structural information can also be attained. This provides opportunity for the development of novel tools that are highly sensitive to underlying pathophysiological changes for clinical monitoring. Optical techniques have already proved useful in applications such as breast cancer and cerebral monitoring, however widespread application in rheumatology clinics has yet to be realised and in the subsequent chapter, a review of previous work relating to joint imaging using optics in the context of inflammatory disease was presented, including a critical assessment of methodologies and performance in the context of RA, from which any benefits or limitations in system design were drawn. These previously reported studies have demonstrated evidence of optical contrast between healthy,

non-inflamed joints and inflamed arthritic joints, when either invasive contrast agents were used or from indigenous optical properties. A number of distinct optical-based techniques were presented as potential candidates for imaging RA patients. Despite PAT and FOI both demonstrating the capability to detect inflammation with a high spatial resolution, DOT provided a unique combination of strengths that made it the most desirable approach in the context of diagnostics and monitoring. DOT is a more economically viable solution for widespread clinical implementation in comparison to PAT, with additional, expensive hardware needed in the latter for US measurement, whilst the ability to provide contrast to endogenous pathophysiological properties of DOT is highly preferable when compared to the reliance on intravenous contrast agents for FOI, particularly given the regularity of which patients are monitored for disease progression.

The promising results from the academic research community discussed in this chapter highlight the exciting potential of DOI in the context of RA, providing motivation for the work carried out in this thesis. Despite these successes in benchtop investigations, widespread application of optical techniques in rheumatology clinics has yet to be realised, with only two optical systems having undergone successful translation to commercially available devices approved for clinical use, to the authors knowledge (Xiralite X5, Xiralite GmbH, Berlin, Germany and Handscan, Hemics, Eindhoven, The Netherlands). One area not explored until now though is the use of CW, multispectral measurements for recovery of pathophysiological information of RA joints in 3D. The following chapter will outline details of the stand alone, non-contact multispectral DOT system developed to carry this out.

CHAPTER 3

IMAGING SYSTEM

In this chapter a new multispectral, non-contact DOT imaging system and its associated software used for recovering pathophysiological parameters in 3D from human hand joints are presented. Their development has been based on a previously described first-generation system [95], with a number of modifications, which are described in this work. The system contains multiple off-the-shelf components, each of which is justified for its selection and discussed in detail to allow reproduction of the system, with experiments characterising more specific, technical aspects of the system covered in the Appendices and experiments assessing the systems accuracy using ground truth phantoms discussed in Chapter 4. Various data post-processing steps are also covered in this chapter, in which 2D optical image data and raw surface imaging point clouds are combined to reconstruct a 3D image of the pathophysiological properties using DOT. As the system has been used to image patients, several requirements had to be considered during its design, such that the system was comfortable and safe to use, had a short total imaging time and was aesthetically professional. An image of the resulting clinical-prototype system in the rheumatology clinic is shown in Figure 3.1, which was fully non-contact and had a mean total imaging time of $\approx$2 minutes per joint.

Figure 3.1: Final clinical system set-up in the rheumatology clinic.

3.1 System Hardware

For joint imaging, a non-contact approach was chosen as it provided several practical advantages over equivalent contact-based systems, as outlined in Section 2.2.1. The system was designed to carry out two workflows of data acquisition during a single joint imaging protocol; (1) surface imaging (SI) of the hand, where projected structured light was captured using a webcam-projector unit, and (2) multispectral, transmission DOI where one side of the hand was illuminated with a high-pass filtered, broadband light source whilst the other side was imaged using a highly sensitive CCD camera, with a schematic of the final system design shown in Figure 3.2. The integration of SI and DOI within

a single system has been demonstrated before in both bioluminescence tomography for preclinical murine studies [93] and the first-generation hand imaging DOT system [95], however both these systems used the CCD camera to capture SI data, leading to slow SI acquisition times which was undesirable for this clinical application.

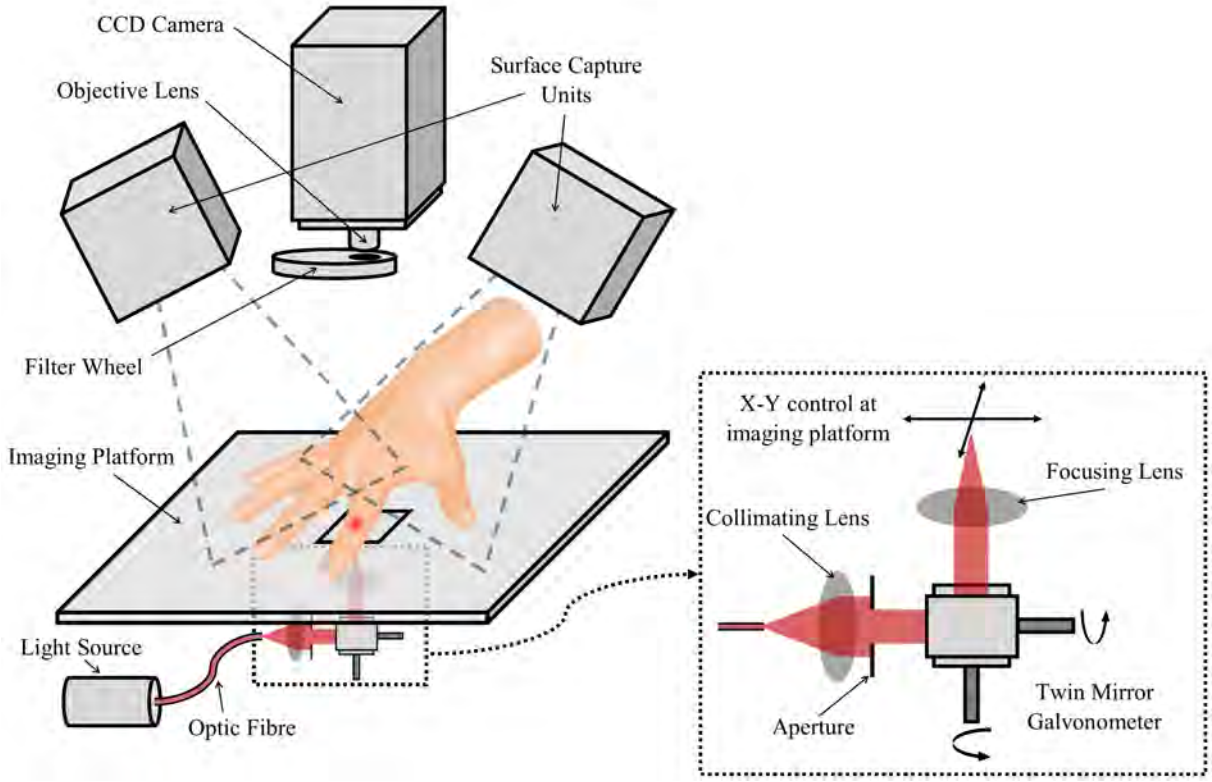

Figure 3.2: Multispectral DOT imaging system schematic, with insert outlining the non-contact, scanning illumination unit design.

3.1.1 System Frame and Casing

Construction of a structurally solid, stable frame was important for two reasons, (1) participant safety making certain no parts could fall and injure a subject, and (2) to ensure the positions and orientations of all system components were fixed so that geometric calibrations were not invalidated by any relative movements.

The aluminium frame illustrated in Figure 3.3 was constructed using Bosch Rexroth 45×45 mm aluminium strut with 10mm grooving (RS Components, Corby, UK). These were cut to the desired length using a circular saw and connected at corners using Bosch

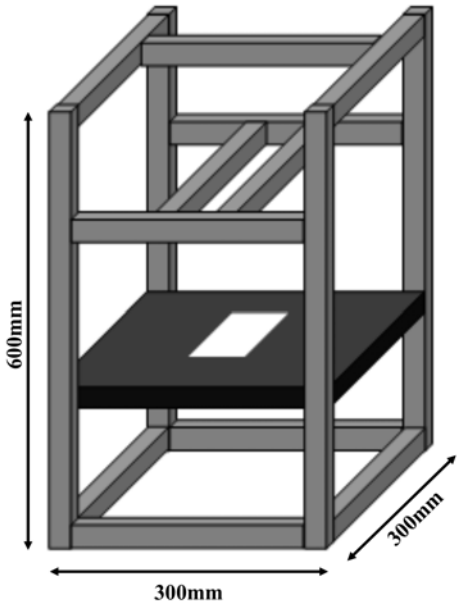

Figure 3.3: Aluminium frame on which the system components were fixed.

Rexroth strut profile angle bracket, strut profile 20 mm (RS Components, Corby, UK). This structure was designed such that the heights of the stage, platform and cameras could all be easily adjusted to provide flexibility when optimising the relative positioning of components during construction. An imaging platform, upon which the subject rested their hand during imaging, was machined from 10mm thick, black acetal sheeting (343mm×416mm), which included an overhanging front ledge to provide arm support for subject and a 60mm×60mm opening allowing light to pass for non-contact illumination of the hand. Dark blue, 3mm thick acrylic sheets were used to create an ambient light shielding box, as shown in Figure 3.1, for eliminating unwanted external light from being detected by the CCD, which would contribute noise to the measurements, and hiding all interior components from the view of the participant, with the interior of this box spray painted matte-black to ensure opaqueness and minimise internal reflectivity. Opaque, black-out cloth was draped at the front entrance of the platform to provide further ambient light shielding whilst still allowing patients to insert their hand. At its base, the system was secured on a 300×300×10mm optical breadboard (Thorlabs, Cambridgeshire, UK), containing a 12×12 array of M3 threads from which the non-contact illumination set-up could be fixed. This entire system was supported by an all-steel table (590mm× 890mm×727mm) as shown

in Figure 3.1, which included casters and levelling feet, to allow ease of transport and storage within the hospital. On the remaining half of the table, a workstation desk was constructed for the monitor, keyboard and mouse used by the system operator.

3.1.2 Optical Transillumination Measurement

In the presented system, the subjects placed their hand on the imaging platform and transillumination optical images were collected, with an illuminating source on one side and images collected from the other side of the finger to provide DOI data for DOT image reconstruction.

Figure 3.4: Photograph of the light source with the 600nm high pass filter added.

Illumination of the hand was achieved using a 20W Tungsten Halogen lamp light source (HL2000-FHSA, Ocean Optics, Oxford, UK), coupled to a premium grade, 1000μm diameter, acrylate coated optical fibre (QP1000-2-VIS-BX, Ocean Optics, Oxford, UK) as shown in Figure 3.4(a). The lamp had a broadband illumination spectrum, ranging

from 360 nm to 2400 nm, however a 600nm long pass, dielectric filter (FEL0600, Thorlabs, Ely, UK), was inserted into the aluminium casing as measurements were not acquired in this range and this minimised any unnecessary heating effects on the tissue. Stability and initialisation studies detailed in Section 4.4.1 indicated that the lamp required a 20min minimum stabilisation period once it had been switched on before each imaging session, to allow the bulb to warm up for optimum performance. Transistor-transistor logic gate control for switching the light source shutter open or closed was driven using a data acquisition (DAQ) device (USB-6002, National Instruments, Newbury, UK) to supply voltages to the bulb via its 15-point serial input, useful for providing rapid and automated control of the light source during data acquisition.

3.1.3 Non-Contact Illumination

Three distinct approaches for non-contact illumination were explored for use within the system, as discussed in Section 2.2.1. In preliminary studies, an X-Y motorized translational stage (MTS50-Z8, Thorlabs, Ely, UK) was used, which controlled the source position focussed at the imaging plane by mechanically moving the optical fibre [173], however this approach suffered from long total acquisition times as the mechanical translations were slow, making it unsuitable for patient imaging in a clinical setting. A galvanometer-based, twin mirror scanning illumination set-up was then implemented, chosen over the use of a DMD due to its superior conservation of flux for single point source illumination, to allow a rapid, versatile, and accurate methodology of re-positioning the source. The design and construction of this unit was completed during a collaboration between the author of this thesis and MSc student James Hughes [85], reducing the total acquisition time by a factor of $\approx$2 compared to the preliminary motorized set-up. The final optical set-up is shown in the insert of Figure 3.2. Light exiting the optical fibre was collimated using a 25mm/f0.98 plano-convex lens and the numerical aperture of the optic fibre was measured to be 0.21, resulting in a collimated beam diameter of 10.7mm. To ensure the entire beam was incident on both galvanometer mirrors, this diameter was reduced using an

adjustable aperture to approximately 5mm. The direction of this collimated beam was controlled using an off the shelf, small beam diameter, dual-axis scanning, mirror system (GVS002, Thorlabs, Ely, UK), with silver-coated mirrors selected to maximise reflectance in the NIR range, as shown in Figure 3.5(b). This device consisted of two optical mirrors mounted on shafts, the angles of which were controlled by galvanometer-based stepper motors each of which was driven by individual servo-driver boards connected to heat sinks. Control of the mirror angle was achieved through a feedback response of the mirrors position supplied to the control board by an on-board detector, allowing very accurate and rapid (300μs small-angle step response) mirror repositioning. The DAQ device used for transistor-transistor logic control of the light source was also used to supply voltages for controlling both mirror angles.

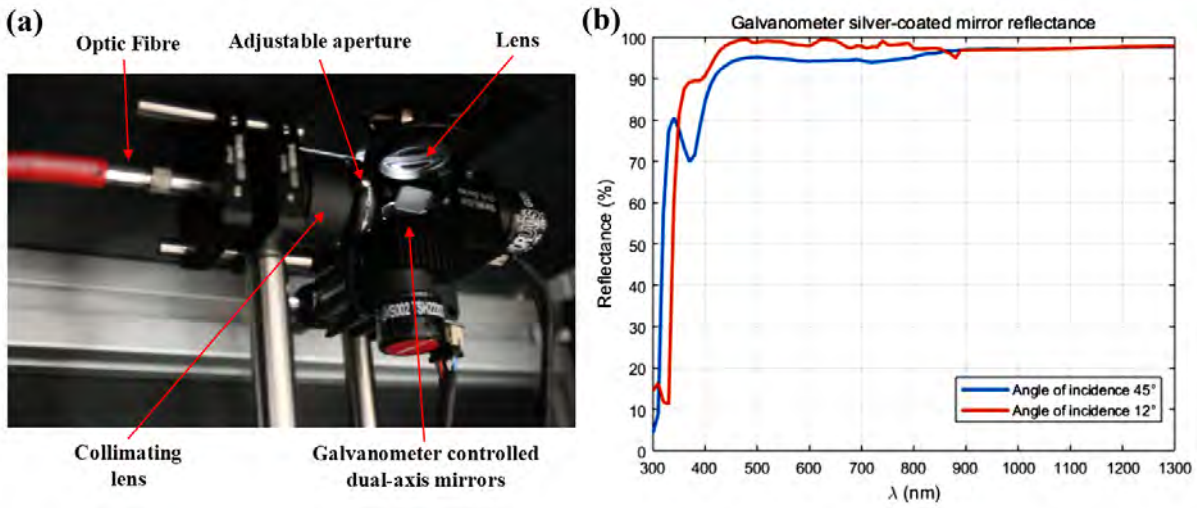

Figure 3.5: (a) Image of dual axis galvanometer mirror construction. (b) Spectral variation in reflectance for the galvanometer silver-coated mirrors.

After exiting the twin mirror setup, the collimated beam was subsequently focussed using a 50mm/f1.97 plano-convex lens, to create a point source at the plane of the imaging platform. The conversion factor of the servo-driver boards was set to 0.8V/° and the DAQ device has a 0 - 10V range, making the maximum scanning angle of the mirrors ±12.5°, with a 0.0008° resolution. This allowed the source position to be set to any arbitrary point within an approximately 40mm×40mm region on the plane of the imaging platform, as shown in Figure 3.6 (a).

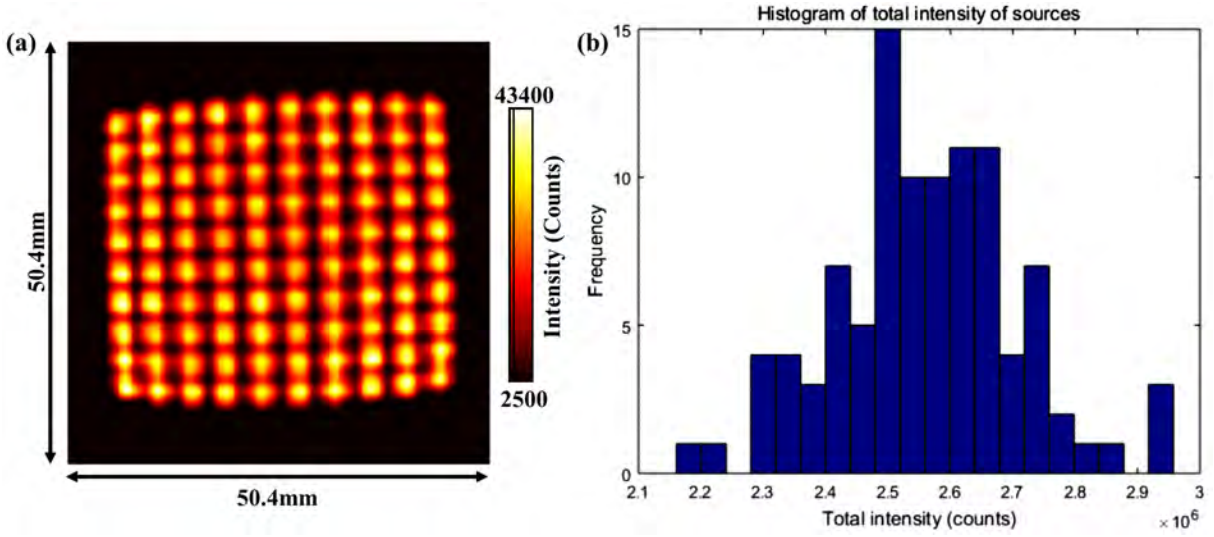

Figure 3.6: (a) Pre-defined 10×10 array of source positions demonstrating the range of using the galvanometer set-up, projected onto a white sheet of paper and (b) a corresponding histogram of the total intensity for all 100 sources.

To assess the distribution of the light source positioning, a 10×10 array of sources was imaged sequentially, ranging between ±12° at 1.33° intervals, whilst a piece of plain white paper was placed on the stage. A degree of optical aberration was visible, expected to be resulting from a combination of barrel type distortion from the focussing lens and the inherent cosine dependence of in the y direction when implementing a dual-axis mirror design. In practice during imaging, source positions were only considered in a central rectangular region of interest of around 15×40mm where optical aberration was less significant as the locations of these source positions were determined during calibration before acquisition, a perfectly regular grid was not needed for this application. The relative strength of each of these source positions was assessed by measuring the total intensity for these source images, displayed as a histogram in Figure 3.6(b), with an average total intensity of 212,000 ± 98,000 counts, corresponding to a coefficient of variation 46.5%. The reflectance of the mirrors according to the manufacturers was dependent on the angle of incidence, with higher reflectance at 12° than 45° in the NIR region as shown in Figure 3.5(b), which will contribute to this variation in the source strength at different positions and highlights the importance of a calibration procedure to account for variation in source coupling for all wavelengths. For joint imaging, 14 source positions in a straight, central

line were used along the underside of the finger with ≈3mm equal spacing, which provided less variation in intensity and hence good SNR across the finger surface, compared to the possible use of lateral source positions. Additionally, as the underside of the finger was not covered by SI, the assumption that the finger base is at the plane of the imaging platform was most accurate for these chosen central sources.

3.1.4 Non-Contact Imaging

A non-contact imaging set-up was constructed to capture optical transmission images of the joint at multiple wavelengths, which could be used as boundary data for imaging reconstruction in DOT. One advantage of camera-based data measurement over alternative contact based acquisition was the image pixels provided a high density array of detectors that could all be captured in a single acquisition.

Camera

A Hamamatsu ORCA II charged couple device (CCD) camera (C4742 - 98, Hamamatsu Photonics, Hamamatsu City, Japan) was chosen for optical image acquisition, selected based on its high resolution (1024 × 1024 pixels), digital output, low noise specifications and high quantum efficiency (Q_E) across the NIR-range, as shown in Figure 3.8. The CCD camera was securely fixed to the aluminium frame, resting approximately 300mm directly above the platform opening.

The purpose of the camera was to convert a spatial distribution of the incident photons into digital counts, which can be interpreted as an image. In brief, the CCD chip consisted of an array of pixels, each containing photosensitive silicon semiconductors. Incident photons on each chip were converted to electrons which were read out, in this case one line at a time using the interline transfer CCD register and converted by a series of amplifiers into digital voltages, which were then transferred to the computer interface via a firewire connection. The resolution of the chip in this model was 1024×1024 pixels, with an

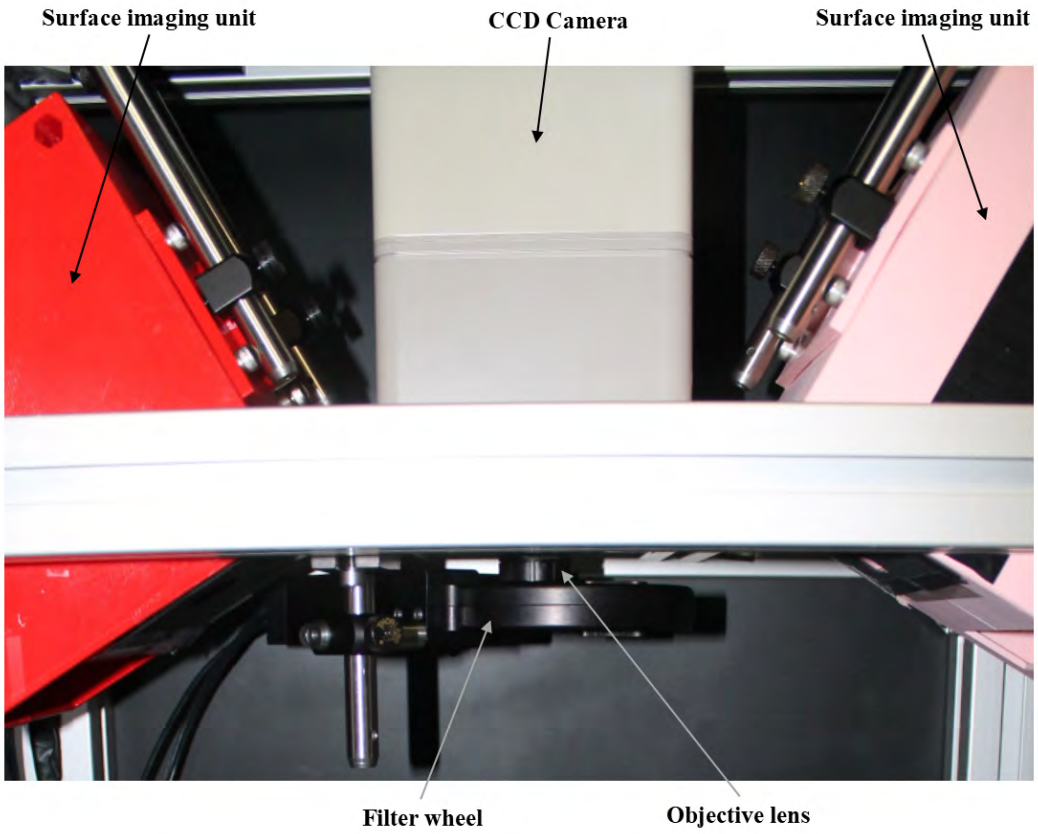

Figure 3.7: A photograph of the non-contact imaging setup positioned directly above the hand. The objective lens was coupled directly to the aperture of the CCD camera and preceded by a six-position filter wheel to enable acquisition of multispectral DOI transmission images of the joint, whilst two surface imaging units were placed either side each containing an optical projector and CMOS camera to acquire dual view SI data of the joint, all of which were fixed to a solid, aluminimum strut frame using Thorlabs components.

individual pixel size of 13×13 μm making the total chip area 177.2mm^2 or 13.3×13.3mm in dimensions. The back-thinned chip was cooled using a Peltier element, in which a current stimulates heat flow away from the chip. This set-up was encased in hermetic vacuum-sealed technology, helping to maintain a stable, high vacuum housing over a long period of time, which together with an air-cooling system in the casing of the camera, enabled the model to achieve very low dark noise characteristics. An optimal operating temperature of -65°C was stated by the manufacturer, however during operation, the minimum temperature achieved by the camera was in fact ≈ -40°C. This could potentially be a result of the age of the camera (≈6 years), making it no longer within warranty

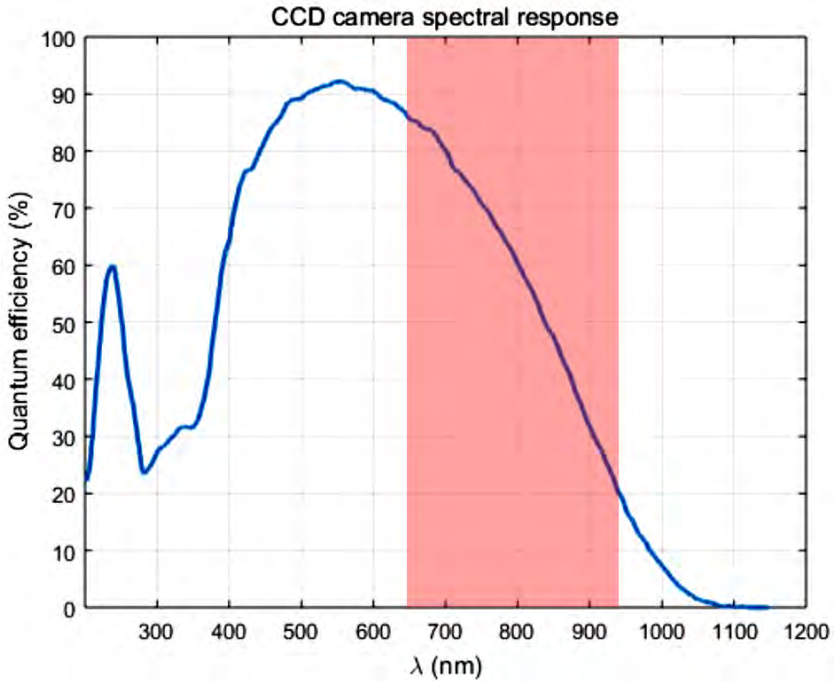

Figure 3.8: Nominal CCD camera Q_E spectral response from its manual, with the spectral range collected by the system of 650-930nm highlighted in red.

and assessment of its impact on the dark noise is discussed further in Appendix A.2.2. The addition of the light box casing, restricted the airflow through the camera, further increasing the attained temperature to ≈ -30°C. To circumvent this lack of airflow, a fan was added to the side of the casing as shown in Figure 3.1, which resolved the issue and restored the temperature to ≈ -40°C.

Camera Settings

A range of operating modes and settings were available for the camera, which could be controlled using an IEEE1394 interface via the firewire cable. Acquired CCD images will always be subject to a variety of noise types, including readout, dark and shot noise as described in Appendix A.2, all of which will depend on these chosen camera settings. When considering the optimal mode of operation or value for these settings, a careful balance had to be found between minimising total frame time for patient imaging, whilst at the same time maintaining image quality for DOT reconstruction.

The dynamic range of a CCD indicates its ability to measure both very low light signals

Readout mode	High-precision (14-bit or 16-bit); High-speed (12-bit)
Binning	Normal readout; 2×2; 4×4; 8×8
Gain	Super high dynamic range; High dynamic range; High sensitivity range
Exposure (ms)	20 - 3000

Table 3.1: IEE1394 setting options available for the CCD camera

alongside bright signals simultaneously, typically defined as the full-well capacity divided by the camera read noise. For non-contact DOT measurements, a large dynamic range is highly desirable as a single image will include intensity data from large sections of the tissue boundary which will greatly vary depending on the distance of the source and the underlying optical properties. The readout mode was always set to 16-bit high precision to provide the greatest dynamic range, with nominal values of full-well capacity and read out noise at this setting of 80,000 e^- / pixel and 6 e^- r.m.s. respectively, corresponding to a dynamic range of ≈13300:1. During the process of converting incident photons to digital counts, the signal is typically amplified by analogue charge-to-voltage amplifier (in the CCD chip itself) and an analogue-to-digital amplifier, defined by the amplification gain transfer coefficient. The latter of these could be defined in the camera settings, with a higher gain setting providing a greater digital signal for the same number of photons. As any noise would also be amplified and the dynamic range would be reduced at higher gain settings, the lowest available gain setting was used throughout this work, which in this case is "super high dynamic range" mode.

A simple way to reduce the total frame time was to reduce the number of pixels and lines read from the chip, achieved in two ways. Firstly, on-chip binning enabled adjacent pixels to be read out simultaneously which both dramatically reduced the required exposure time to achieve good SNR and at the same time lowered readout time, with only marginal increases in readout noise, characterised in Appendix A.2.4. Binning was therefore set at 8×8, resulting in effective pixel dimensions of 1.26×1.26mm at the tissue surface, for which the image pixel array density at the hand surface was still greater than the detector array density used in DOT reconstruction. Secondly, a rectangular 64×32 pixel sub-array was

defined to only be read from the chip for a region of interest (ROI) containing the joint, so that any pixels containing non-useful information outside this ROI were ignored, again dramatically reducing the readout time further by a factor of ≈6. Finally, the exposure time could also be set, which is the length of time photons are incident on the chip before readout. This was adjusted using an auto-exposure routine to achieve the optimum SNR, which will be discussed further in Section 3.4.

Lens

A VIS-NIR coated lens with 25mm fixed focal length (Edmund Optics, York, UK) was coupled to the C-mount of the CCD. The adjustable aperture of this lens was set to its maximum value of f=1.4, ensuring as much incident light as possible on the chip. The working distance ≈300mm was required to allow adequate fields of view for both the SI units and the CCD camera simultaneously and the lens was adjusted manually to be in focus with the imaging platform at this distance.

3.2 Spectral Decoupling

To obtain multispectral data, a method was necessary for spectrally decoupling the broadband light ejected from the tissue surface. Optical bandpass filters provided a low-cost and easy to implement option to achieve this, which reject light from unwanted wavelengths using thin film Fabry-Perot interferometry. A six position, motorized filter wheel (FW102c; Thorlabs, Ely, UK) was mounted directly in front of the lens as shown in Figure 3.7, which housed five circular, 1" diameter bandpass filters (Thorlabs, Ely, UK) all with a peak transmission of around 55%, chosen as a compromise between narrow spectral resolution and high transmission required for DOT. The final available slot contained a 1" diameter 2.0 neutral density filter, required for producing image masks. This filter wheel provided a simple and automated way of changing the wavelength of the acquired image, with added flexibility that if required, filters could easily be removed from the housing for

cleaning or replaced if different wavelengths were to be tested.

3.2.1 System Specific Optimum Wavelengths

The importance of an optimum set of wavelengths for minimising non-uniqueness and crosstalk when recovering HbO, Hb, H_2O and S_A has been presented in the literature, outlined in Section 2.4.1, together with a methodology for selecting this set based on maximising the residual, R and minimising the condition number, κ. A system specific combination of five optimum wavelengths, for each of the available positions in the filter wheel, was therefore calculated according to this criterion, from a range of possible vales in the NIR window, between 650nm to 930nm in 10nm intervals, giving a total of $C_5^{29} = 118755$ possible combinations to be tested. The derivation of the constraining parameters relies on a constant value for S_P, this case was set to the same value as that used in finger reconstructions of 2.145. Values for the chromophore extinction coefficients for HbO and Hb were taken from data compiled by Prahl at the Oregon Medical Laser Center (OMLC) [174] and for H_2O from data collected by Hale and Querry [175].

The resulting optimisation space is shown as a plot of R against κ in Figure 3.9, with the top left corner corresponding to the optimum region. To compare the performance from different regions of this optimisation space, three example sets wavelength combinations were selected from the extreme corners of this plot, either with (1) high κ and high R, (2) low κ and low R or (3) low κ and high R values, the final of which is theoretically optimum. Simulated data for a 2D circular test mesh, as described in Appendix A.5, with backgrounds values of 10mMol, 10mMol, 40% and $1mm^{-1}$ and with four 20mm diameter anomalies values of either 20mMol, 20mMol, 80% or $0.5mm^{-1}$ for HbO, HB, H_2O and S_A respectively as shown in Figure 3.10, were used to compare the performance of these wavelength combinations.

The reconstructions for all four parameters when using data simulated for each of the wavelength sets are shown in Figure 3.10, with all three recovering good contrast in the S_A anomaly, set 1 failing to accurately recover the HbO and H_2O anomalies, whilst set 2

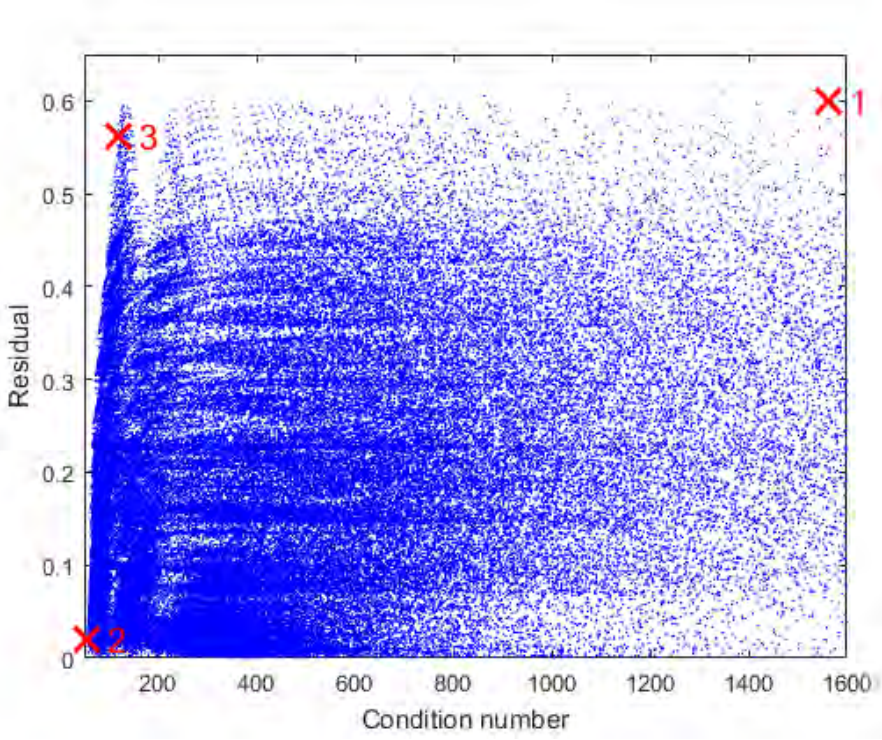

Figure 3.9: Scatter plot of the R versus κ for all combinations of five wavelengths from between 650nm to 930nm in 10nm intervals.

	Wavelengths (nm)	κ	R	HbO (μMol)	Hb (μMol)	H_2O (%)	S_A (mm^{-1})
Target	N/A	N/A	N/A	20.0	20.0	80.0	0.5
Set 1	650, 720, 730, 770, 900	0.592	1540	11.6	15.9	48.1	0.55
Set 2	730, 810, 820, 830, 930	0.0206	56.4	13.6	13.7	66.6	0.55
Set 3	650, 710, 730, 830, 930	0.562	119	13.1	16.1	63.5	0.55

Table 3.2: Wavelength sets from three regions of the solution space. Sets 1 and 2 are suboptimal with either high condition number or low residual respectively, while set 3 is from an optimal region with both a low condition number and a high residual. Mean values from the corresponding anomaly regions for each recovered parameter for the reconstructions in Figure 3.10 for all three wavelength sets are also displayed.

demonstrated a poor reconstruction of the Hb anomaly. The most consistent performance was observed using set 3, with all four anomalies resolved well, which was from the optimal region with both a low condition number and a high residual, a conclusion which is quantitatively supported by the mean values recovered from each corresponding anomaly region displayed in Table 3.2. Based on this, set 3 was chosen for the bandpass filters; 650, 710, 730, 830 and 930nm.

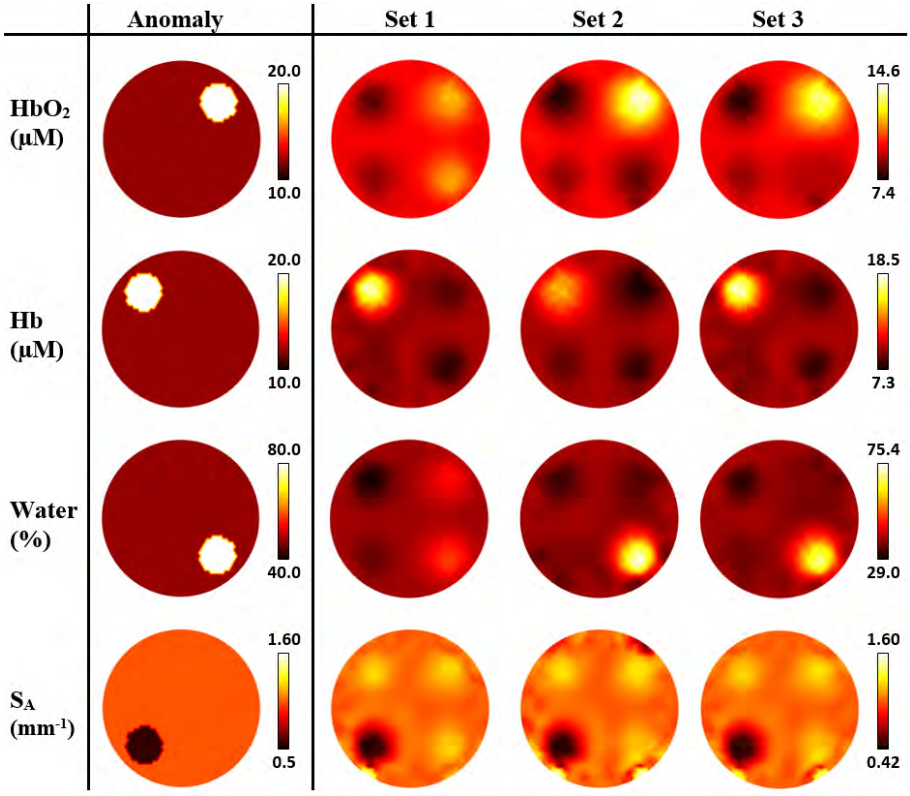

Figure 3.10: Simulated 2D circular test mesh and corresponding reconstruction using the three wavelength sets in Table 3.2.

3.2.2 Instrument Response Function

The relative total sensitivity of the system to optical flux at distinct wavelengths was represented by the instrument response function (R_F), defined in Equation 3.1 as the linear convolution of all components involved in the optical measurement, including the Q_E spectral response of the CCD camera, the emission spectra of the light source (E) and the relative total integration of the transmission spectra for the filter (F). It was important to first characterise R_F so that its spectral impact on the measured flux by the CCD camera could be removed, making boundary data used for DOT reconstruction comparable between wavelengths.

$$RF(\lambda) = Q_E(\lambda) \otimes E(\lambda) \otimes F(\lambda) \tag{3.1}$$

The R_F was measured through 100 repeat images of the 99% reflectance standard at each of the 5 wavelengths of interest whilst the light source fibre end was placed at a

sufficiently large distance to achieve an even illumination of the standard. Due to physical limitations when setting up this experiment, the spectral variation in the galvanometer mirror could not be incorporated in this measurement and its variation was assumed to be negligible based on the nominal values in Figure 3.5(b). The resulting relative sensitivity plotted in Figure 3.11 was significantly lower at 650 and 930nm compared to 710, 730 and 830nm, in agreement with the spectral profiles of the individual components such as the Q_E and E in Figures 3.8 and 3.4(b) respectively.

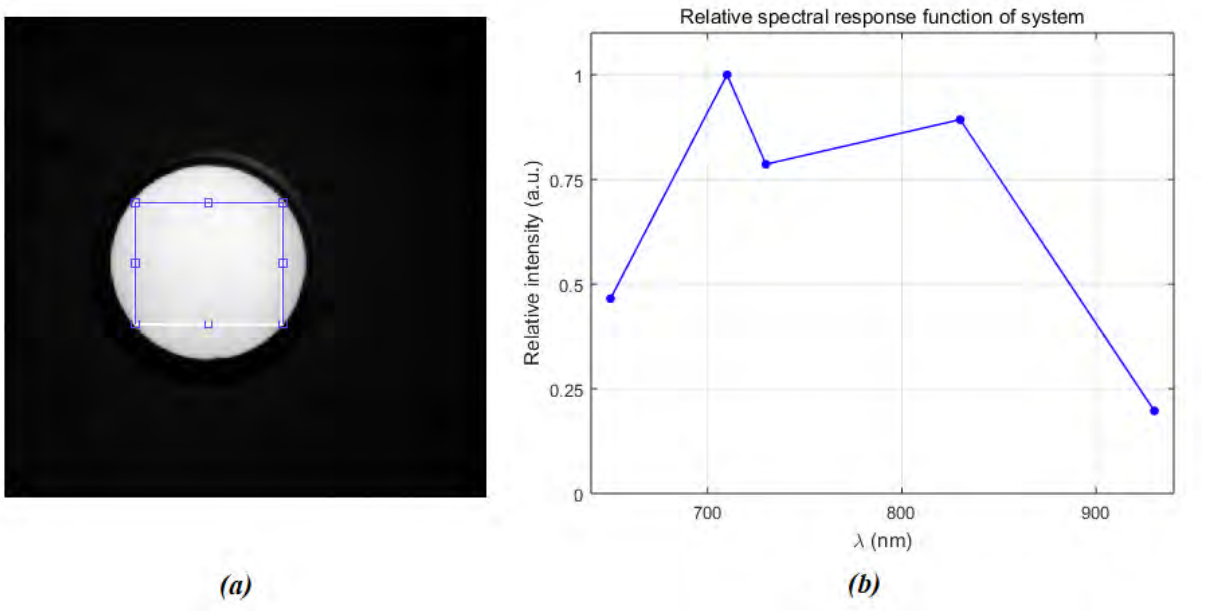

Figure 3.11: (a) 99% reflectance standard imaged with region of interest displayed. (b) Relative spectral response function

3.3 Surface Imaging

The aim of SI technology is to measure a 3D point cloud which accurately describes the surface profile of some object, in this case of the hand. There are many methodologies for achieving this, some examples of which include, light detection and ranging (LIDAR), time of flight cameras, stereophotogrammetry and laser point/line scanning. Digital fringe projection profilometry is another SI approach, in which the object of interest is illuminated with structured fringe patterns and simultaneously imaged using a camera [176]. These

patterns act as light-based reference, which appear deformed compared to the apparent distribution that would be observed on a plane orthogonal from the axis of the projector in the frame of reference of the camera. The object height from the camera pupil can be calculated for each pixel, provided the relative positions and intrinsics of the camera and projector are known [177]. For the specific application of imaging hands, digital fringe projection profilometry is an attractive solution due to its high accuracy, feasibility to work at short focal distances, low implementation cost and functionality when the camera and projector remain static.

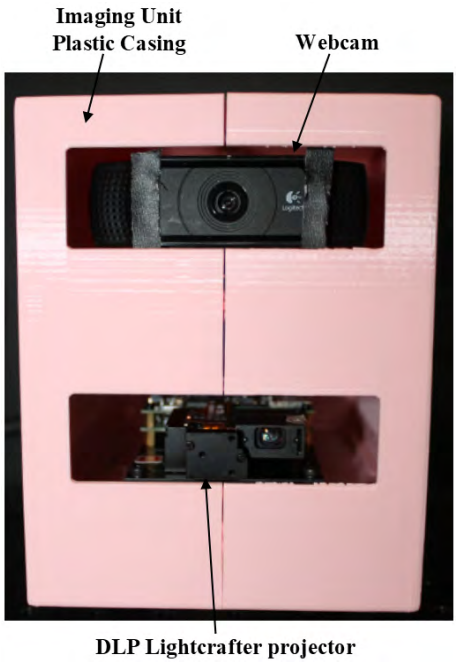

Figure 3.12: Front view of a SI unit.

The SI units used in this system are projector-camera systems, each consisting of a DLP Lightcrafter Evaluation Module projector (Texas Instruments, Texas, USA) and an off-the-shelf webcam (C920, Logitech, Lausanne, Switzerland), both fixed in 3D printed plastic casing, as shown in Figure 3.12, both chosen due to their low cost and high speed. The projectors included an RGB-LED based light engine, a digital micro-mirror device and were powered by an independent supply, with the pattern and colour of the projections controlled via USB. The design and construction of the SI units together with their associated algorithms for 3D point cloud recovery are the work of Basevi et al. [178].

The author of this thesis was responsible for integrating the SI units into the system and adapting the source code kindly provided by the developer for optimal application within the developed joint imaging system. Both SI units were fixed to the uppermost part of the aluminium frame using aluminium posts either side of the CCD camera, as shown in Figure 3.7 and the units were orientated to point roughly towards to the centre of the imaging platform, providing view points from either side of the hand with some overlap. The focal planes of both the projectors and webcams were manually adjusted to be in line with the imaging platform. Although the projectors could be set to black, the projected power could not be programmatically turned to zero so there was always some residual light. To overcome this, 600nm short pass dielectric filters were inserted in front of both projectors, to minimise cross-talk with multispectral optical data, which was for 650nm or higher, characterised in Appendix A.3.2, allowing multiple finger acquisitions to be carried out sequentially without the need for switching off and rebooting the projectors for every acquisition, which would have taken several minutes.

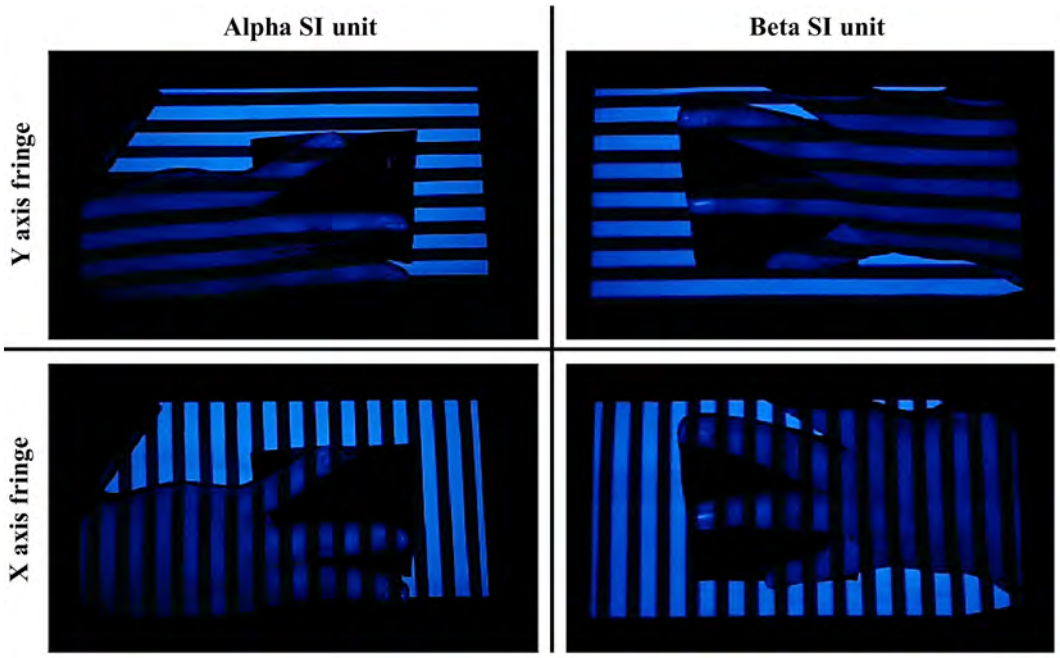

Figure 3.13: Example images of fringe patterns acquired using the SI units for the left IV PIP, for both SI units and projected at both orientations.

During SI, a predefined set of 36 fringe patterns, made up of a combination of either sinusoidal or square wave fringes at either X or Y axis orientation, were projected onto the

surface of the hand by each SI unit, whilst both webcams continuously acquired images, examples of which are shown in Figure 3.13. Default settings for the number of waves per projection were used, at either 0.78, 1.1, 1.6, 2.2, 3.1, 4.4, 6.3, 8.8, 13, 18, 25, 35, 50 or 70 in each image, with further optimisation of these values beyond the scope of this work. Dark and brightfield images were also acquired, to be utilised for background subtraction and masking respectively. The projectors were set to project in blue only, as transmission in biological tissue and therefore any blurring of the reflected patterns would have been greater with green or red light. All the SI data was saved and removed from memory at the end of each acquisition, before the imaging next joint.

3.3.1 Safety and Comfort

The safety of participants using the system was of highest priority, particularly as RA patients can typically have some degree of disability. All electronic devices where off the shelf, complying to CE standards and were portable appliance tested by the medical engineering team in the hospital. A draughtsman chair on castors with arms was purchased, which allowed patients to sit at a comfortable height of the imaging system whilst remaining secure. All corners were covered with baby safe protective covers and any sharp edges of the system were filed to be smooth. Ethical approval was obtained for both healthy subject and patient imaging, as discussed in Sections 5.2 and 6.1.

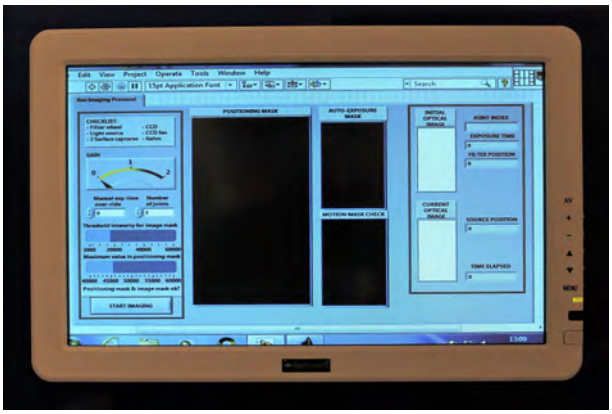

Figure 3.14: Patient visualisation monitor for finger positioning.

A touchscreen monitor (10TS2W, Beetronics, Park Royal, London, UK) was added to

the front of the system, as shown in Figure 3.14, which displayed a duplicate of the system control screen and served two functions; (1) it allowed the patient to visualise the finger position and adjust it accordingly such that it was in line with the source positions and (2) it provided visualisation of the imaging process to reduce anxiety in the patient. This benefit has been demonstrated for example during US guided injection [179]. Tests were carried out using reflective standards either with or without the screen switched on to ensure there was negligible cross talk with the optical measurement, detailed in Appendix A.3.2.

3.4 System Control

The data acquisition routine is summarised in a flow chart in Figure 3.15. All system components were first initialised and CCD settings defined including the readout mode, analogue gain, binning level, and sub-array in this order, which was important as the range of options for latter parameters were dependant on the setting of previously used parameters. At the same time, an anonymised hospital reference number was requested from the operator as a folder name, in which all relevant data files could be written.

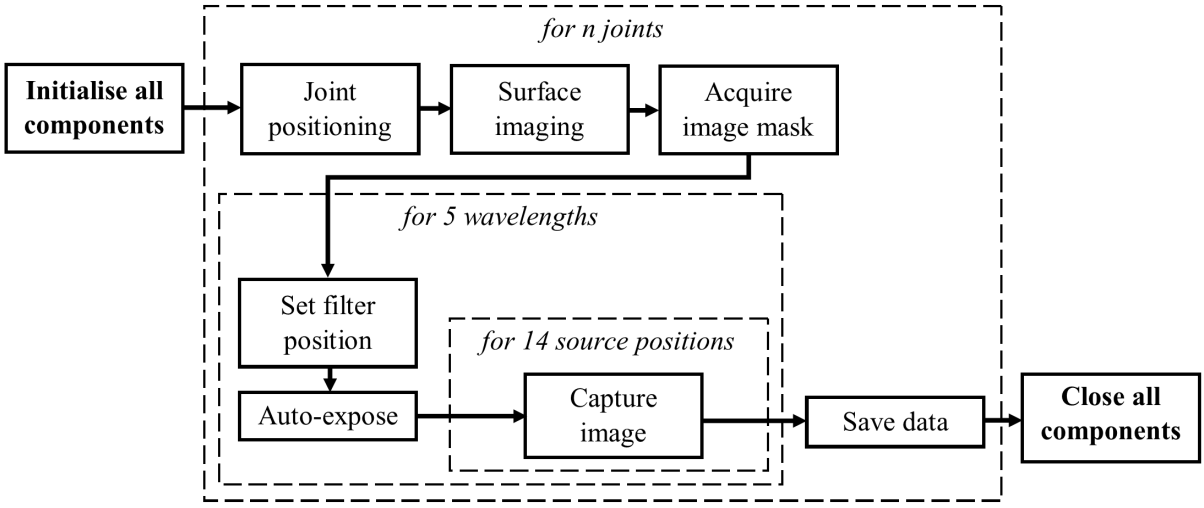

Figure 3.15: Flow-chart illustrating the data acquisition implemented by the GUI.

Participants were briefly explained how the system worked and asked to place their

hand flat on the imaging platform in a relaxed position. The position of the finger was then readjusted using a live feed of the CCD camera preceded by the neutral density filter, whilst a white screen was projected from the SI units, to align the PIP joint with a set of crosses which indicated the source positions visible in Figure 3.17. An image mask was also created from this live feed image by the operator manually adjusting the threshold until the boundary for the finger could be clearly visualised. The surface profile of the hand was then measured, with each SI unit sequentially projecting fringe patterns onto the hand, after which both SI unit projectors were set to black. This was followed by adjustment of the filter wheel position to 650nm and an initial optical image was acquired using the CCD camera with the source position at most distal end of the finger. Variability in both the optical properties and finger thickness resulted in a dramatic variation in the transmitted intensity at the surface, both between participants and at different wavelengths. In order to maximize the dynamic range and SNR in all optical images, an auto-exposure routine was implemented in which an initial exposure image was acquired and used to calculate the scaling factor for the exposure time adjustment such that the maximum signal within this image mask region was ≈50,000 counts, sufficiently below the saturation limit of 65,535 counts for 16-bit data format. Optical images were then collected at the remaining thirteen source positions in a straight line along the sagittal direction of the finger as illustrated in Figure 3.16, following which the light source was turned off for a dark image acquisition, all using this new exposure time. This was then repeated for the four remaining wavelengths and the corresponding exposure time was accounted for during data processing, as discussed in Section 3.6.

At the end of imaging each joint, both the optical and SI data were saved as .mat files, which provided an efficient and lossless compression scheme, after which the data was cleared from the virtual memory. The whole protocol, with the exception initialisation, was then repeated for the remaining joints. All hardware was controlled via standard computer ports including USB, DVI, HDMI and firewire, using a custom-made graphical user interface (GUI) was built in LabVIEW (National Instruments, Newbury, UK), displayed

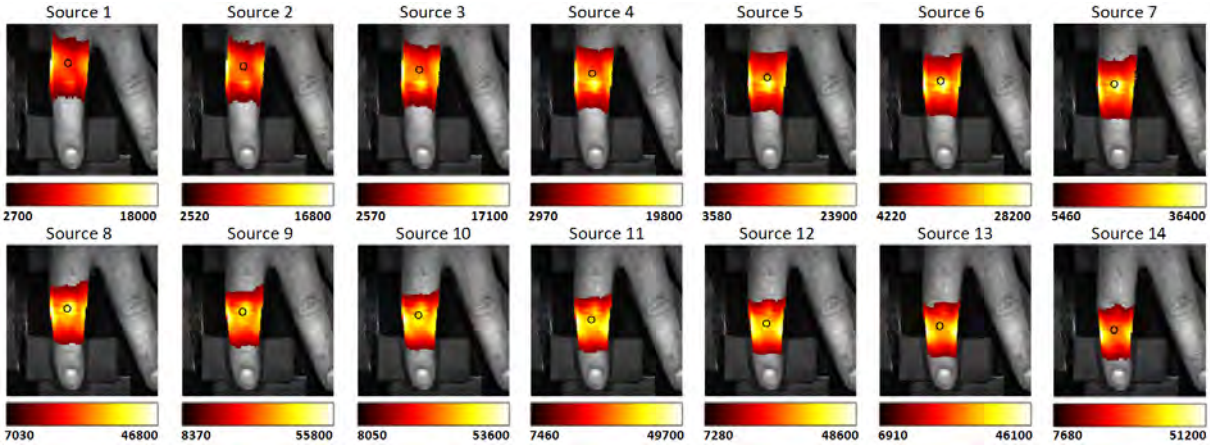

Figure 3.16: Transillumination images of the finger at 14 source positions at 650nm overlaid on greyscale image with widefield illumination using the projectors. Colour bars display the range in CCD counts (a.u.) and the source locations below the finger are displayed as black circles. Note: These are displayed in reverse order of acquisition, with the most distal source 14 being the first image acquired and used to auto-expose.

in Figure 3.17, which operated on a desktop computer (Stones, UK) with 8GB RAM and an Intel Core i7 CPU 860 at 2.80 GHZ, running 64-bit Windows 7 (Microsoft, Redmond, WA). A significant advantage of DOI, particularly compared to US, is the lack of a need for any specialist clinical training to carry out a scan. With this in mind, the GUI and data acquisition were designed to be as simple and automated as possible, to such a degree that following only one hour of training, one of the nurses in the clinic was able to use the system to successfully acquire data from a human subject.

3.4.1 Cosmic Ray Artefacts

Cosmic rays are extremely energetic subatomic particles constantly passing through the atmosphere which can lead to unwanted bright artefacts in CCD images [180]. This issue could be problematic during the initial image acquisition for the auto-exposure routine, which relied on the maximum intensity of this initial image within the image mask. To circumvent this, the difference between the image and a median filtered version was considered and any values above a threshold of 500 were replaced using the median filtered value at this pixel, chosen based on histograms for three images impacted by cosmic rays,

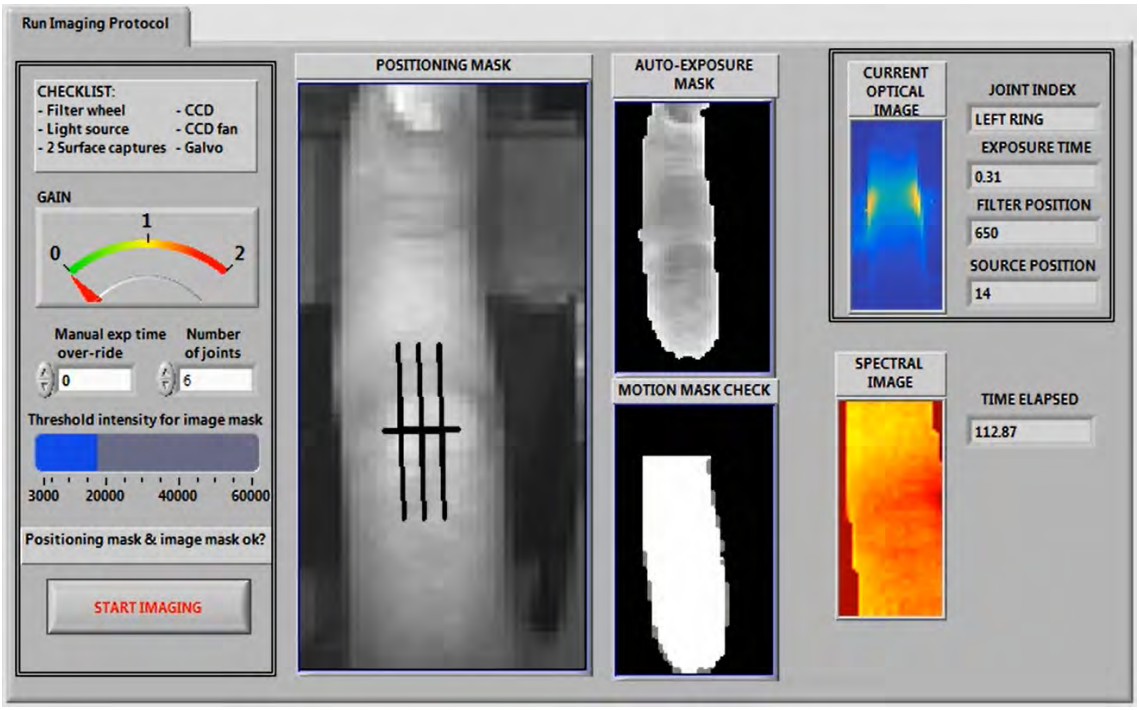

Figure 3.17: Graphical user interface for data acquisition

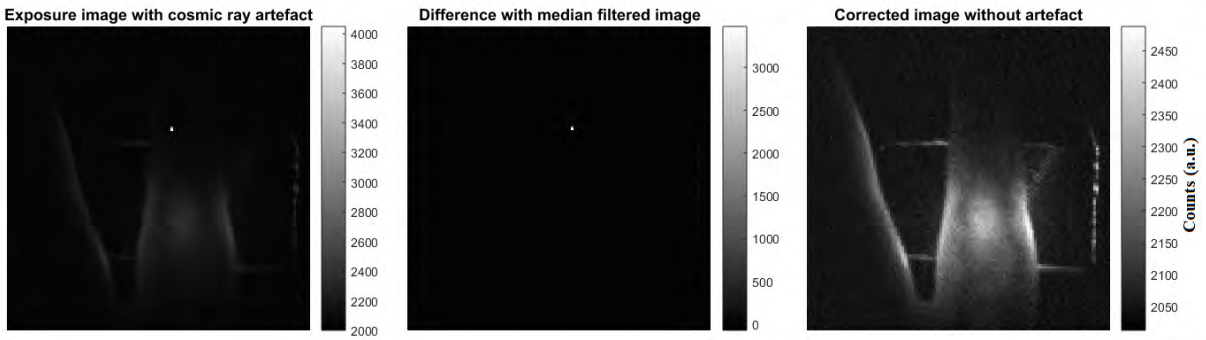

Figure 3.18: Example of the protocol for removal of cosmic ray artefacts in the initial image.

an example of which is shown in Figure 3.18. Due to the risk of discarding useful signals in the auto-exposed image, this processing was only carried out on initial images used for auto-exposure.

3.4.2 Acquisition Time

When imaging human subjects, it was important to minimise the acquisition time whilst at the same time maintaining the quality of the acquired data for a number of reasons. (1)

to prevent errors resulting from motion (assessed with subjects in further detail in Section 5.1.2), (2) to reduce the impact of any drift in the system (characterized in Section 4.4.1) and (3) from a patient comfort perspective. A breakdown of mean imaging times for each stage of data acquisition from all 21 subjects in the clinical study in Chapter 6 are shown in Table 3.3.

	Positioning	Surface imaging	Optical imaging	Writing to disk	Total
Time (s)	30.69 ± 28.7	29.11 ± 0.164	37.77 ± 2.88	17.18 ± 0.288	114.75 ± 15.30

Table 3.3: Acquisition times for each section of data acquisition (mean ± S.D.) per joint for 21 patients in the final clinical study.

Unsurprisingly, the greatest variability in imaging time was seen for finger positioning, with patients sometimes asking further questions during this stage or patients with limited dexterity struggling to accurately orientate their finger using the visualisation screen. The optical imaging time was also slightly variable, as exposure times needed to achieve the required SNR depended on finger thickness, optical properties, skin pigment etc. To not exceed virtual memory, SI data had to be saved and cleared following each joint acquisition. Writing this data to the hard drive was time consuming, although the patient could temporarily remove their hand and rest during this stage before imaging the next joint. The raw images were cropped such that pixels with non-useful information were not written to the disk, which slightly reduced writing time, but the addition of a solid-state drive to the system control desktop in future would be beneficial in this regard. The mean total imaging time for a complete imaging session of all six joints with this dataset, including initialisation of the system components, was 12.6 ± 1.2 mins, meaning scanning could be carried out without interfering with the rest of the clinic schedule for the US room.

3.5 Volumetric Mesh Generation

The 3D surface point cloud acquired using the SI units was used to generate two volumetric, tetrahedral meshes, one high density, irregular mesh used as a basis for numerical modelling of light propagation, as outlined in Chapter 2, and a second low density, regular mesh used as a basis for the inverse problem when updating chromophore concentrations using a number of pre-processing, data cleaning and meshing tools which will now be outlined.

3.5.1 Surface Point Cloud Processing

Prior to data acquisition, each SI unit required a one-time calibration of the intrinsics and relative extrinsics for both the webcam and projector as *a priori* for calculating the surface height map. This was achieved using open source software package Procamcalib [181], which implemented a geometric protocol involving both the projector and the webcam. A predefined printed pattern was fixed onto a rigid board and was held in the field of view of the webcam, whilst the optimal fit for a corresponding pattern projection was found, which was repeated 30 times at a number of different orientations and distances. The SI data for the hand consisted of a set of fringe pattern images which were processed using the SI associated software [178] and the resulting output from each SI unit was a 3D surface point cloud in each of their respective fields of view. By ensuring a degree of overlap in their fields of view, this algorithm was capable of automatically coregistering the two individual point clouds by calculating correspondences in the phase maps from each unit and applying a rigid transposition on the secondary surface point cloud from unit (Beta) into the frame of reference of the primary SI unit (Alpha), an example of which is shown in Figure 3.19.

3.5.2 FEM Meshing

Typically, the structure of an FEM mesh can be either uniform, with cuboid shaped elements, or non-uniform with tetrahedral elements. The forward problem is more straight-

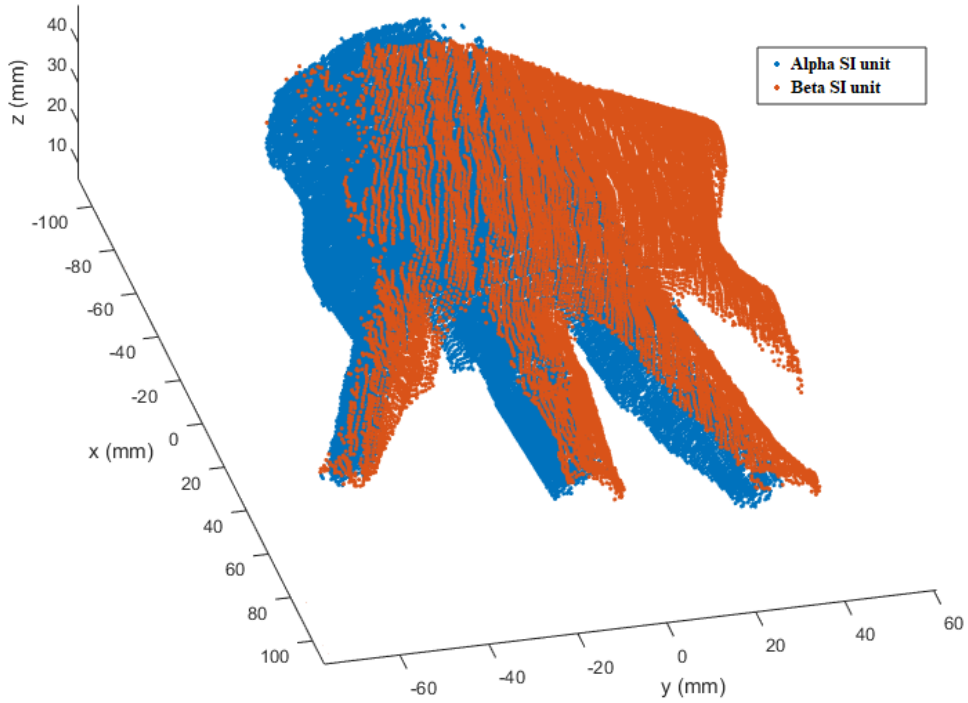

Figure 3.19: Co-registered surface point clouds of an example hand from both SI units.

forward to solve numerically when using a uniform mesh as a basis [162], however in cases where the surface geometry is complex and curved, such as for a joint, the boundaries are more accurately described when using a non-uniform, tetrahedral mesh, which was chosen throughout this work. The Computational Geometry Algorithms Library (CGAL) meshing engine 4.14 [182] was selected as it has been shown to rapidly produce FEM meshes of higher or comparable quality to other propriety software tools [183]. The CGAL tool discretizes the mesh in an optimal way for solving the DA by using a finite set of surface points to approximate one-dimensional curved features using restricted Delaunay triangulation, thus ensuring that node density and numerical accuracy are not biased to regions of greater surface complexity. A work-flow was developed for generating these volumetric meshes of the joint from the surface point cloud, as depicted in Figure 3.20.

The geometric location of the imaging platform was attained by SI a piece of white A4 paper fixed flat on the platform and fitting a plane to the recovered point cloud, with any points in the hand SI point cloud falling within 5mm perpendicular distance from this plane removed. It was necessary to ensure that only the surface of the finger joint was

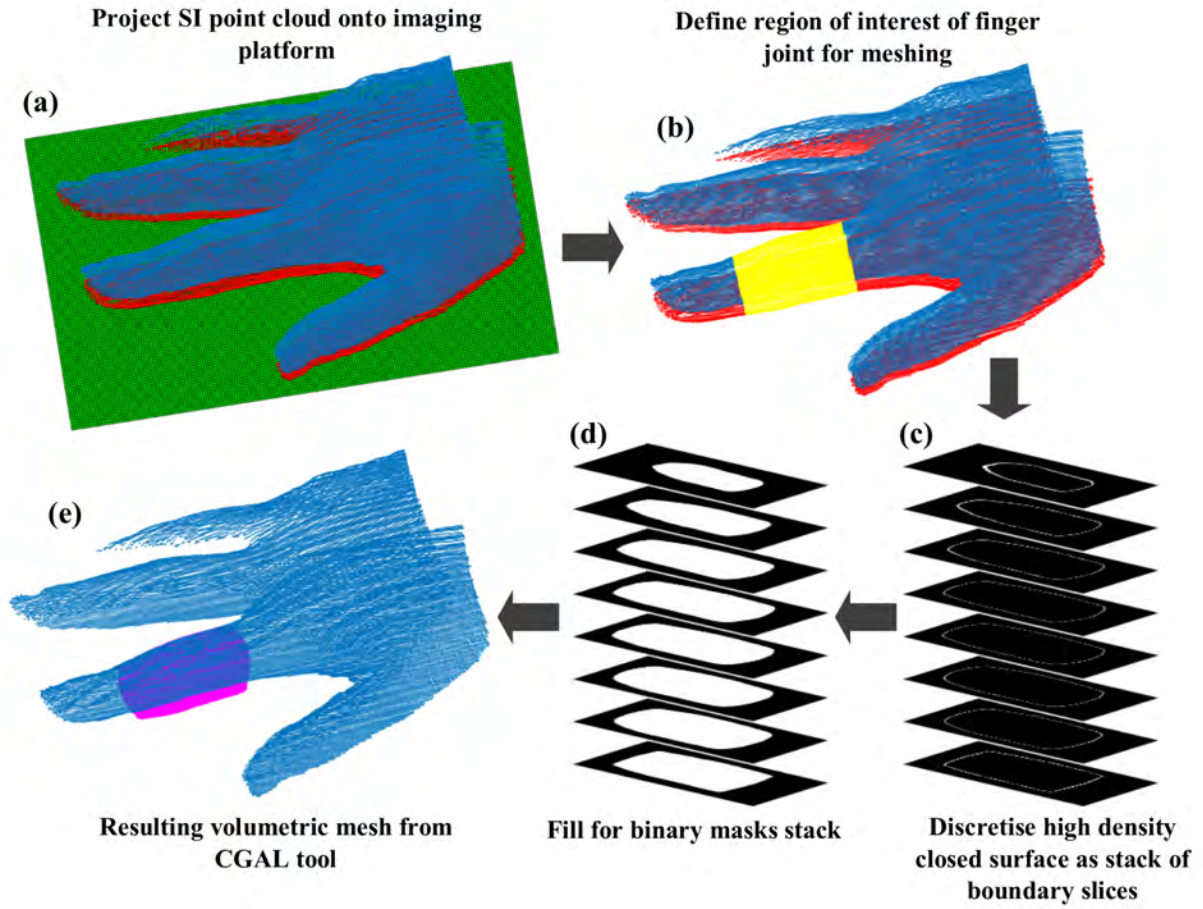

Figure 3.20: Diagram outlining the workflow used for volumetric FEM mesh generation on an example joint, illustrating: (a) The plane fitted to the imaging platform (green), with the acquired SI point cloud (blue) and its projection onto the platform along the plane normal. (b) The region of interest of the mesh (yellow) defined from the source positions within which points were considered for generating the mesh of the finger joint. (c) A sample of 8 slices from the stack of boundary slices outlining the boundary of the high density closed surface for the joint. (d) Corresponding slices filled to create binary masks for CGAL meshing tool. (e) Resulting volumetric mesh with the original SI point cloud overlaid (magenta).

used to create the volume mesh, instead of the entire hand, to avoid allocating memory to unimportant regions during FEM meshing and therefore allowing a higher density mesh of the joint alone to be generated. Based on the maximum expected joint width and region of interest for FEM mesh creation, 45×30 mm bounding square was defined along the finger with its centre based around the source positions centroid, outside of which the SI points were ignored as shown in Figure 3.20(b). Due to the lack of SI for the underside of the hand, all remaining surface points were projected onto the plane of the imaging platform

to represent the base of the joint and combined with the original mesh. The MATLAB function MyRobustCrust, which performs a manifold extraction based on a ball pivoting method, was used to generate triangular elements connecting these nodes, forming a closed surface mesh from this 3D point cloud. This mesh was saved as a .ply file and then using freely available meshing software Meshlab [184], several repairing and cleaning steps were executed programmatically within the MATLAB script, in the following order;

1. select non-manifold edges and delete of all associated faces and vertices,
2. re-orientate all face normals coherently,
3. Poisson surface reconstruction,
4. Laplacian Smooth $\times$ 2, and
5. resample surface with 200,000 nodes.

These steps were all chosen heuristically using Meshlab, designed to maximize robustness by smoothing out noise or anomalous points in the point cloud, to create a closed, high density surface mesh required for generating 3D volumetric meshes of imaged objects. The high density closed surface from Poisson resampling was discretised onto a regular grid of with pixel dimensions of $0.0625mm^3$, with binary assignment of 1 for pixels containing at least one point and 0 for the remaining pixels, effectively producing a stack of 2D transverse slices outlining the boundary within the point cloud surface, as shown in Figure 3.20 (c). These were filled using the MATLAB function imfill to produce a stack of binary masks defining the volume encapsulated within the joint, which could be used as an input for the CGAL meshing engine. The cell size parameter in CGAL was adjusted such that mean nodal separation distance achieved approximately 1mm, resulting 3D tetrahedral mesh which typically consisted of around 195,000 linear triangular elements which connected around 35,000 nodes, depending on finger dimensions. As can be seen in Figure 3.20 (e), the original coordinate system of the primary SI unit was preserved during this volume mesh generation process.

The 3D location of the sources in the same frame of reference (Alpha SI unit) were ascertained using a one-time protocol, similar to those implemented in previous non-contact DOT systems[185, 186]. In brief, an A4 white, plain piece of card placed on the imaging platform and the source strength was adjusted as to not saturate the webcam. At each source position the card was imaged using the webcam and a 2D Gaussian was fitted to accurately locate the source positon in each image, which were then mapped onto the imaging platform plane using the SI units intrinsic parameters. Sources were moved $\frac{1}{\mu_s'}$mm within the joint FEM mesh boundary, to reflect a spherically isotropic source within the assumptions of the DA model [72]. A grid of 43 virtual detectors was defined with its centroid identical to that of the sources at plane with 50mm perpendicular distance from the platform positioned directly above the joint. This grid was then incrementally translated by 0.01mm in the direction of the unit vector perpendicular to the imaging platform, such that each detector was assigned directly on top of the finger joint as it came into contact with the mesh, at which point they were moved directly to the closest point on the mesh boundary. This process resulted in a FEM volumetric model of the joint, as shown in Figure 3.21 (a), which was used as a basis to solve the forward problem.

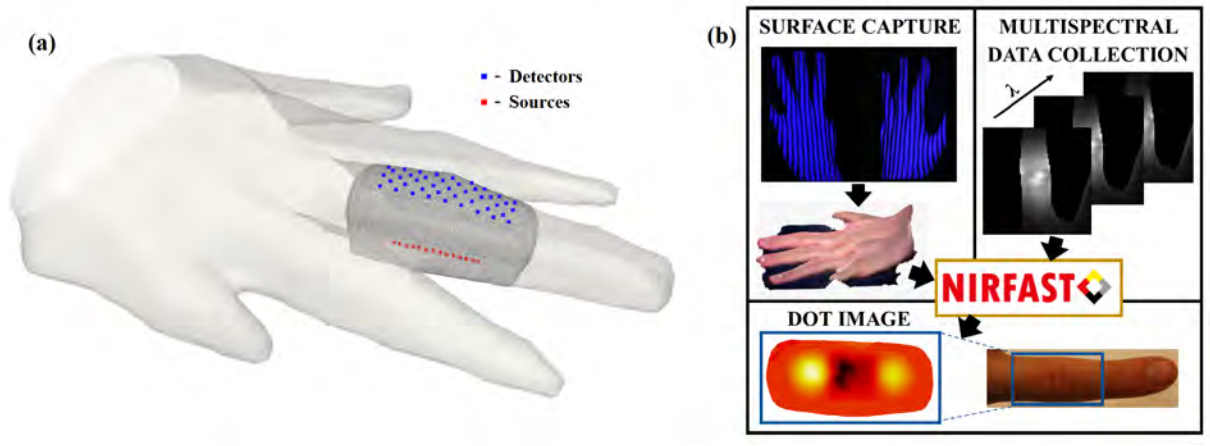

Figure 3.21: Example of imaged surface profile with corresponding FEM mesh of the finger joint of interest with positions of 14 sources and 43 virtual detectors assigned. (b) Overall work flow for acquiring and processing data.

3.5.3 Mesh Quality

The accuracy of predicted flux using FEM numerical modelling will depend on the quality of the mesh. A volumetric FEM mesh will ideally consist of all element volumes, nodal separation distances and internal angles to be all uniform, such that the discretised set of linear equations representing the forward problem are all equal in importance. This maximises the conditioning of the forward problem and prevents the solution to the DA from being spatially biased to any particular region, hence the distribution of these parameters were therefore used as metrics of mesh quality.

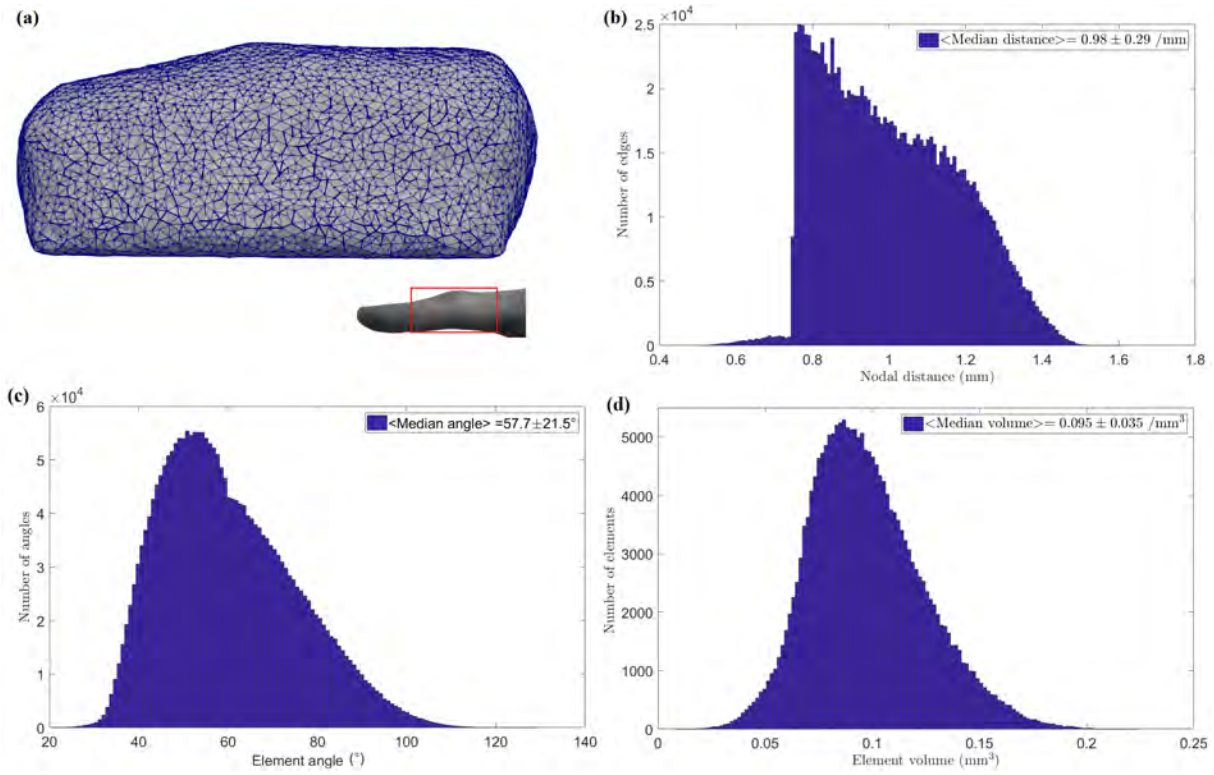

Figure 3.22: (a) Example of typical tetrahedral mesh generated using CGAL meshing engine used as a basis in FEM modelling to solve the DA, with finger image shown for orientation reference. Corresponding histograms of mesh quality metrics for (b) nodal distance, (c) element angle and (d) element volume, with median ± interquartile range.

A typical example of the tetrahedral FEM mesh of the joint produced by the CGAL meshing engine is displayed in Figure 3.22(a). The corresponding histograms indicated a high quality basis, indicating a Gaussian distribution in element volume and slightly skewed distribution of internal element angles. The distribution of nodal distance is more

asymmetrical, with a majority of distances between 0.8mm and 1.4mm, but very few below this range. The median distance achieved was close to the target 1mm, resulting in a median volume $\approx$0.01mm^3 and a median angle close to the optimum value of 60° for an equilateral tetrahedron. Importantly there are no extreme outliers for nodal distance or element angle, making the minimum element volume equal to 0.0085mm^3, which at 10% of the median was deemed to be acceptable.

3.5.4 Basis for Inverse Problem

At each iteration of the inverse problem, as described in Section 2.4, optical parameters were linearly interpolated onto a coarser, 3D regular tetrahedral mesh to be used as a basis when building the spectrally constrained Jacobian in the inverse problem. A coarser basis provides additional spatial smoothing of the recovered chromophore maps, so the node spacing was defined based on a reasonable estimate of the maximum resolvable distance with the proposed imaging set-up of 1.5mm, resulting in mesh typically made up of $\approx$35,000 linear tetrahedral elements which connect $\approx$6500 nodes. When generating this mesh, occasionally elements of negligible volume would occur when all four nodes happened to be positioned close to the surface. As the optical property update at each node was normalised by the mean volume of connected elements, these tiny elements would drastically bias the update to this region. Any nodes linked to these elements were therefore ignored. A threshold was applied to the Jacobian matrix, in which columns corresponding to nodes with a sensitivity less than 0.01% of the maximum sensitivity were removed, as any update in chromophore concentration from these nodes were assumed to be negligible, based on the reduced sparse sensitivity matrix representation [187, 188]. The benefits of utilising this coarse basis mesh and thresholded Jacobian included a reduction in the number of unknowns and therefore ill-conditioning of the inverse problem, and a limiting of the time and memory allocated to building the Jacobian matrix, which was particularly relevant for the spectrally constrained implementation, with the Jacobian size multiplied by both the chromophore number and the wavelength number compared to the

equivalent single wavelength case (see Section 2.4).

Initial estimates for the inverse problem were chosen based on literature values, as shown in Table 3.4, with chromophore extinction coefficients for HbO and Hb taken from data compiled by Prahl at the Oregon Medical Laser Center [174] and for H_2O from data collected by Hale and Querry [175]. Haemoglobin concentrations in reconstructed images were then converted to the more physiologically interpretable parameters StO_2 and tHb. In this work, S_P was fixed as a homogeneous constant and not updated due to known difficulty in separation with Hb in CW [130]. Tikhonov regularisation τ was initially set to value of $100 \times \max(J^T J)$ and reduced by a factor of $10^{0.25}$ every iteration, to speed up convergence and make the inverse problem more robust to the initial choice. Convergence was achieved when the change in total projection error (the least squared difference between the forward and measured data) was less than 2% as compared to the previous iteration.

Parameter	Value
Initial HbO	0.014mMol
Initial Hb	0.006mMol
Initial H_2O	30%
Initial S_A	0.77
Initial S_P	2.145 mm^1
Refractive index of tissue	1.33
Refractive index of air	1.00
Speed of light	3×10^8
Initial regularization	100
Inverse tolerance	2%

Table 3.4: Parameters defined for modelling light propagation and the inverse problem, with initial estimates for S_A and S_P based on the average of values for bone and muscle [189], and chromophore concentrations based on previous multispectral images of finger joints [153].

3.6 Optical Data Processing

Each acquired optical image, I_A, measured by the CCD camera underwent the same data processing steps. A corresponding dark image D at the same exposure time was subtracted, which was then divided by both acquisition exposure time, T_A and the instrument response function, $R_F(\lambda)$ at the measured wavelength from Section 3.2.2, according to the following equation,

$$\psi = \frac{(I_A - D)}{T_A R_F(\lambda)}. \tag{3.2}$$

to give a fluence image ψ in arbitrary units. For comparable fluence values between acquisitions, the use of this auto-exposure method and subsequent normalisation by exposure relied on a linear response of the CCD camera in digital counts within the dynamic range utilised, which was verified to be true for this high specification camera in Appendix A.3.1.

A cylindrical, homogeneous, plastic phantom, as described in Appendix A.1.1, whose optical properties were known *a-priori*, was imaged using the system and used to calibrate for the model/data mismatch and any source coupling coefficient variation. A three-step calibration protocol similar to that proposed in previous breast imaging DOT studies [115] was implemented: 1. global values for μ_a were calculated at each wavelength first using a analytical fit for an infinite medium based on the source-detector separation, followed by a numerical fit using the FEM model (with constant homogeneous values assumed) with μ_s' known *a priori* 2. using these global values, the data-model offset was calculated as the difference between the measured and modelled data for the homogeneous cylinder, which was averaged for each source position over all detectors, 3. this offset was subtracted from the measured finger data on a source by source basis to produce a calibrated data set. The conversion from number of incident photons in the signal to digital counts will depend on both the electron conversion gain (G_E) and Q_E of the camera and it was appropriate to assume for this high specification CCD camera that digital counts were

proportional to incident intensity, verified using reflectance standards in Appendix A.3.1. Although J/cm^2 are commonly used the units of fluence, as G_E and Q_E were identical for both phantom and finger data, these factors were eliminated during the model-data mismatch calibration process meaning units of digital counts could be used for boundary fluence during reconstruction, an approach that is widely utilised throughout the literature. Finally, optical images were processed by a 5×5 pixel Gaussian kernel with a standard deviation of 0.793, estimated based on the numerical aperture of an equivalent a 1mm diameter optical fibre in contact with the boundary to make SNR comparable with contact based systems commonly used in DOT, as demonstrated in Section 4.2.1.

3.6.1 Registration of Optical Data to Mesh

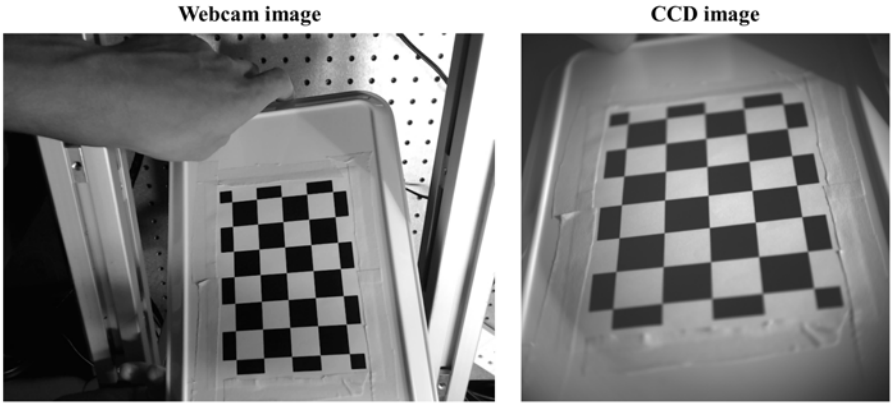

Figure 3.23: Example of images acquired using both the webcam of the primary SI unit and CCD camera simultaneously with the chequerboard at a single orientation.

To enable FEM modelling of light propagation in the workflow displayed Figure 3.21, accurate mapping was needed to combine the optical transmission data acquired using the CCD camera to the captured surface geometry boundary acquired in the frame of reference of the primary SI unit (Alpha). Registration of two or more cameras with overlapping fields of view is a common problem in computer vision, typically found in stereo imaging systems [190], and requires measurements of both the intrinsics of each camera and relative rotational and translational extrinsics between cameras. To register the detector points assigned on the volumetric FEM mesh to the DOI data, a one time calibration

protocol was carried using MATLAB-based automatic multiple camera calibration (AMCC) toolbox [191]. A checker-board pattern was printed and fixed to a rigid, flat board, and simultaneously imaged by both the primary webcam of the Alpha unit and the CCD camera using an in house LabVIEW script, as shown in Figure 3.23, repeated at 200 random orientations and distances. From these corresponding images, the AMCC toolbox used the automatically localised checker-board corners together with the a priori spatial dimensions of the chequerboard, to fit the respective intrinsic (focal length, principal point and distortion) and relative extrinsic parameters (rotation, translation) of these two cameras using a Levenberg-Marquart algorithm based on Zhang's camera calibration methodology [192], with their relative positions rendered in Figure 3.24.

A process for fine tuning the resulting optical data mapping function was devised to improve accuracy. A computer vision tool shown in Figure 3.25(a) was constructed by painting matt white 48 circles on a black LEGO block, which was imaged using both the CCD camera and using the SI protocol. A threshold was manually set to separate these circles from the background in the CCD image and MATLAB function bwlabel was used to assign a unique label to each, as shown in Figure 3.25(b). Any points not originating from the circles in the recovered 3D surface point cloud were removed by thresholding at a distance from the imaging platform, and the remaining points were clustered into 48 separate clusters using manually seeding and a k-means algorithm, allowing the 3D location of the centroid of each circle in the frame of reference of SI unit Alpha to be computed, as shown in Figure 3.25(c). The point cloud centroids were then projected onto the CCD chip using the mapping function, producing two corresponding grids of reference points in both the 2D CCD image and the 3D point cloud in the SI for registration. A rigid, affine transformation (translation and scaling) was then iteratively applied to this projection to ensure the circle centroids in the surface profile aligned sufficiently with the CCD circle centroids, such that the average distance between these corresponding centroids was minimised in a least squared sense, with this fine tuned transformation then applied to all future SI point cloud projections.

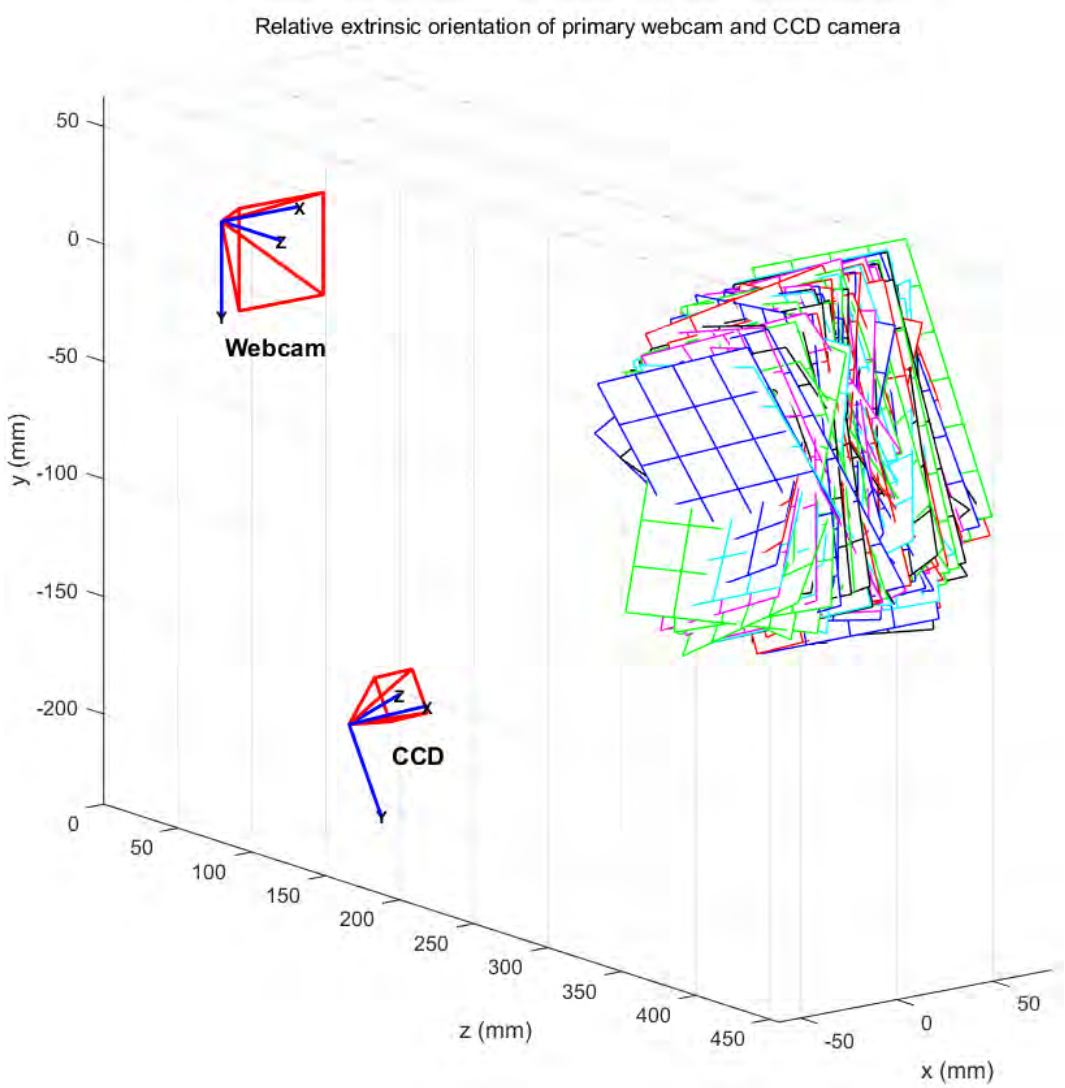

Figure 3.24: The resulting extrinsic transformation in the frame of reference of the webcam, with all 200 chequerboard orientations.

The accuracy of this mapping function was assessed through comparison between the spatial distribution of transmitted flux through plastic phantoms and the predicted fluence in light propagation models, as discussed in Chapter 4, with an example of the alignment between the SI point cloud rendered onto the CCD chip and the corresponding greyscale image shown in Figure 3.26. Although this approach relied on the assumption that the original rotational transformation was correct, the overall work-flow was deemed sufficiently accurate for this application.

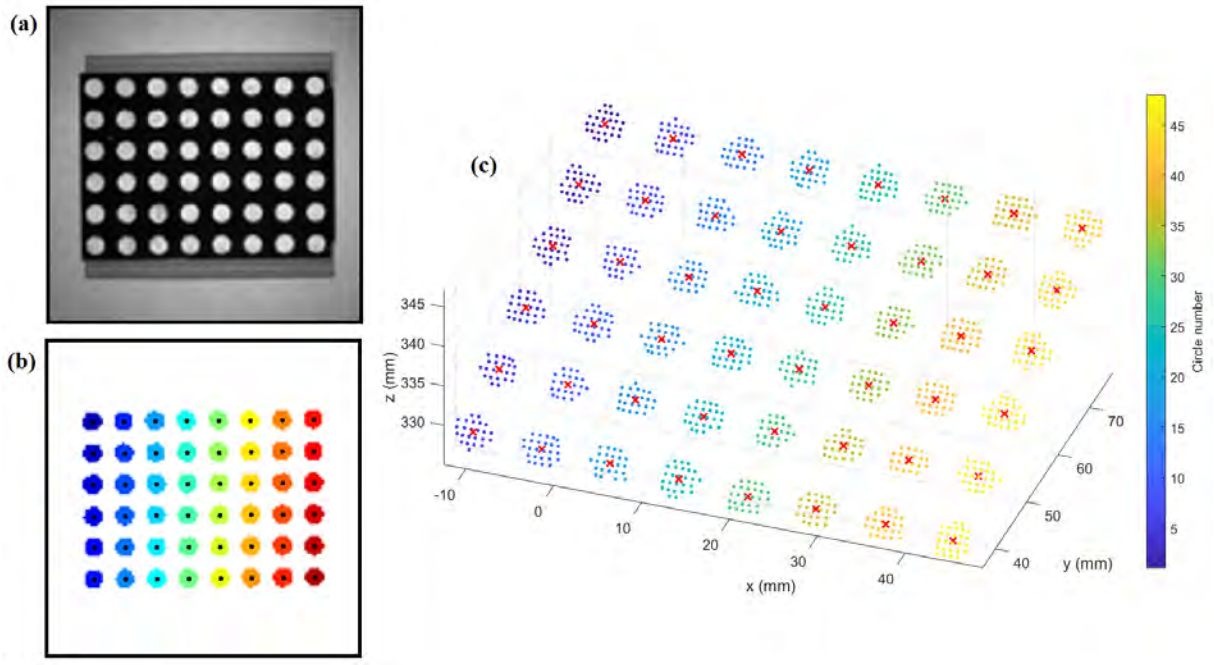

Figure 3.25: (a) Grayscale image with the neutral density filter of the LEGO based computer vision tool. (b) Corresponding circles of each labelled in a unique colour with their corresponding centroids shown as a black dot. (c) Clusters for each of 48 circles in the 3D point cloud, labelled as unique colours and their respective centroids displayed as a red cross.

3.6.2 Processing System

A separate desktop computer to that used for data acquisition (Stones, UK) with 16GB RAM and an Intel Core i7 CPU 4790 at 3.60 GHZ, running 64-bit Windows 7, was used for data processing and 3D image reconstruction, all of which was executed in MATLAB (The MathWorks, Natick, Massachusetts, USA). For clinical devices, it is important to be able to process datasets rapidly to enable clinicians to interpret results and provide feedback to patients as quickly as possible. To minimise the time required to solve the forward problem or build the Jacobian, both these operations were implemented in parallel [116] either on a GeForce GTX 970 GPU or on the CPU respectively, with reduction in time by a factor of $\approx$10 for typical meshes. There is potential for further optimisation of the processing times in the SI processing, FEM mesh generation and inverse basis generation stages, beyond the scope of this current work, whilst reconstruction times could be slightly reduced by using a more powerful GPU.

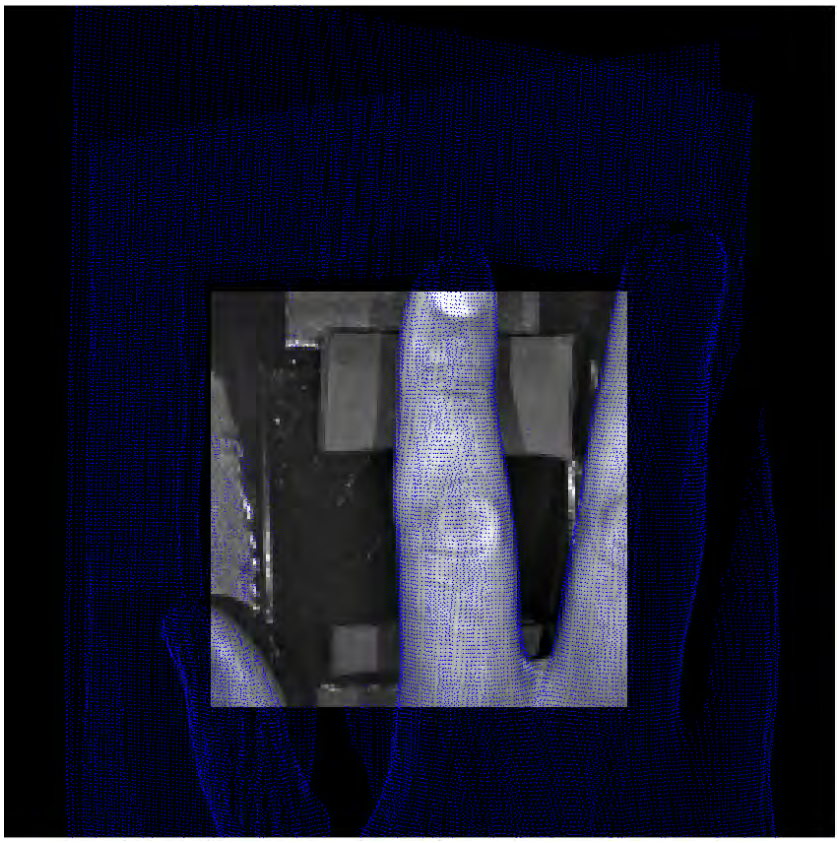

Figure 3.26: Example of registered SI point cloud rendered onto the CCD chip (blue) overlaid onto corresponding greyscale CCD image of the joint following the calibration protocol.

3.7 Conclusion

In this chapter, a novel work-flow was presented that combined multispectral, optical transmission data with surface imaging to facilitate light propagation modelling of the hand joint. A series of data processing steps incorporated into the associated software were also presented for the production of high quality FEM meshes and the registration of optical data for numerical modelling. A number of design elements were incorporated into the final clinical prototype system that were novel in the context of joint imaging and provided unique benefits for patient imaging. The fully non-contact nature of the system, in which both SI and DOI were combined within the same imaging session, allowed for easy transition between imaging different hand joints, particularly relevant in RA patients where hand shape variation resulting from bone deformation is common. The combination of galvanometer-based illumination and complementary metal-oxide-semiconductor (CMOS)

based SI technology, allowed rapid total imaging times, of ≈2 minutes per joint, important for both reducing time pressure in clinics and to minimise the likelihood of motion artefacts occurring. The use of multispectral data provided intrinsic contrast in clinically relevant indicators, based on chromophore concentrations and scattering parameters, without the need for invasive, endogenous contrast agents. Finally the CW nature of the system resulted in a comparatively low total cost, as outlined in Appendix A.6, making it commercially viable for future development.

The resulting system was safe, fast, fully-automated and straightforward to operate, such that an examination could be easily carried out by a trained non-clinician. The entire data processing pipeline described in this chapter, including mesh generation, optical data filtering and reconstruction, was implemented in an automated fashion with identical algorithm parameters and initial conditions chosen for all participants. This produced maps of the joint pathophysiology that were quantitatively comparable between subject groups and made the algorithm objective in the sense that the same outcomes would be reached if it were repeated by multiple users when using the same raw data. Some aspects of the data acquisition workflow that would benefit from further automation or computer-aided guidance in future included the joint positioning process and the thresholding to produce the image mask used during the auto-exposure routine, in order to ensure any operator subjectivity is minimised. There were a number of potential further optimisations beyond the scope of this current work. These included adjustment of the optical set-up to increase the scanning range of the galvanometer, such that multiple joints could be imaged in a single workflow, addition of further SI units to cover the underside of the joint to ensure source positions were accurately reflected in 3D, and system miniaturisation is desirable to make the device more portable and user friendly through, for example, reducing the working distance of the SI units. Finally the inclusion of more expensive, premium optical filters, available with nearly twice the transmission, at 650 and 930nm would also be beneficial for producing a more even R_F and thus reducing the comparatively longer exposure times required at these wavelengths to achieve sufficient SNR. In the subsequent

chapter, the performance of the presented prototype system will be extensively tested and characterised through a series of phantom experiments.

CHAPTER 4

SYSTEM CHARACTERISATION

Prior to *in vivo* subject imaging, it was important to first evaluate the performance of the constructed system against a number of ground truth reference measures. To achieve this, several studies were carried out in which a variety of objects and custom-made optical phantoms were imaged, with the aim of assessing the performance of individual elements of the acquisition work-flow, such as surface imaging, optical imaging data quality and validating the overall capabilities of the system for carrying out DOT to recover optical contrast, the results of which are presented in this chapter.

4.1 Surface imaging

To facilitate 3D tomographic reconstruction of pathophysiological parameters in the joint, knowledge of the boundary is required. Accurate recovery of the joint surface geometry was important for realistically defining the boundary of the generated volumetric FEM mesh. The capability of the SI technology implemented for recovering surface profiles in 3D has been validated in previous studies [178, 185], with the accuracy of the recovered point cloud from the ground truth surface mesh reported to be 50% of points within 0.1mm, 82% of points within 0.2mm and 96% of points within 0.4mm error when imaging a mouse phantom. Further assessment of the SI algorithm within the context of the presented system was carried out by imaging a number of objects, including two plastic phantoms of

cuboid or cylindrical geometries, and a stepped model at distinct heights, with 3D point clouds acquired using the same protocol as outlined in Section 3.3.

4.1.1 Phantom Geometries

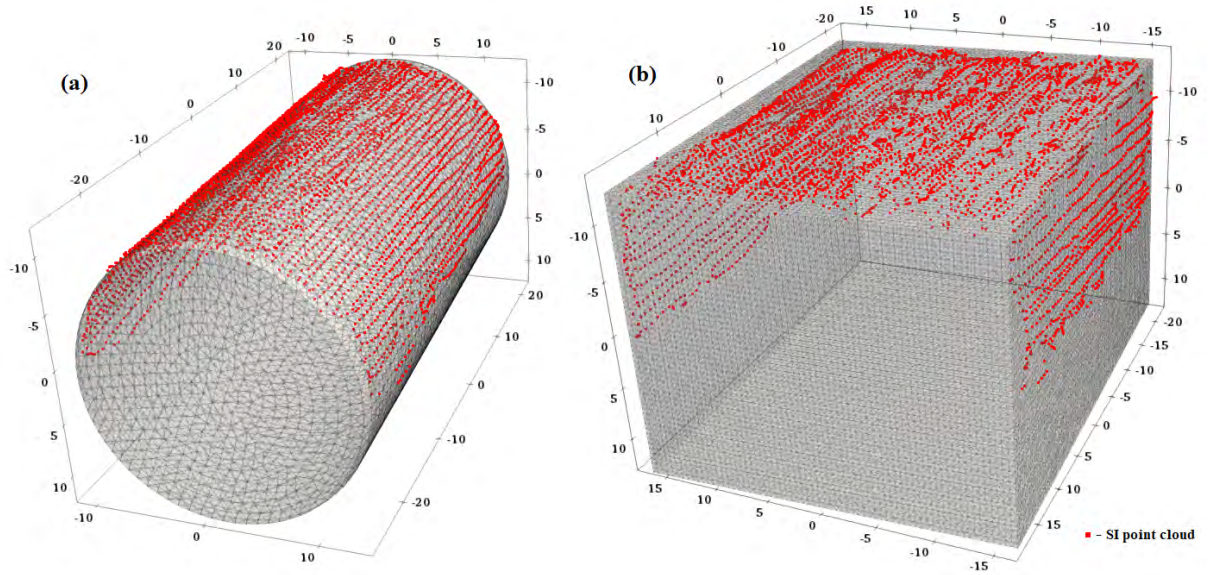

Figure 4.1: SI point cloud in red overlaid on registered, geometrically accurate surface meshes in grey for both (a) the cylindrical phantom or (b) the cuboid phantom.

The first set of SI validation studies involved imaging two biological tissue-mimicking optical phantoms, details of which are outlined in Appendix A.1.1. The dimensions of these phantoms were measured using Vernier callipers to be 26.0 × 33.0 × 40.0mm for the cuboid version and 24.6 × 50.0mm for the respective diameter and length of the cylindrical version. These measurements were used to generate geometrically accurate surface meshes, representing the ground truth against which the accuracy of the SI methodology could be assessed, as shown in Figure 4.1. Registration of the ground truth reference surface to the recovered point cloud was achieved using a three-step process; the centroids of both meshes were translated to the origin, an approximate global alignment of the meshes was achieved using principal component analysis and then finally a finite iterative closest point algorithm was used to align both meshes, in which all vertices in the surface mesh were fixed and paired to their nearest neighbour in the reference 3D point cloud from SI. These

reference vertices were then iteratively transformed and rotated to minimise the average distance between pairs, solved using finite difference methods [193]. The perpendicular distance of each point in the SI point cloud to their closest location on the surface of the registered reference mesh was calculated and both the distribution and the median of these distances were used as metrics to assess the accuracy of the SI methodology.

Distance threshold (mm)	1.0	0.7	0.4	0.2	0.1	(mm)
	% of points from surface					Median distance
Cylinder	99	97	88	68	52	0.194
Cuboid	98	93	80	51	30	0.197
Mouse Phantom*	-	-	96	82	50	-

Table 4.1: SI accuracy metrics for both the cylindrical and cuboid phantoms. This includes the percentage of points within the defined distance threshold and the corresponding median of minimum perpendicular distances of the 3D point cloud recovered using SI from a registered *a priori* surface mesh. * Corresponding values for a mouse shaped phantom reproduced from [178] are also displayed for comparison.

The percentage of points within a perpendicular distance from the reference surface for the cylindrical phantom were comparable to those reported previously in the literature for the mouse phantom at a 0.1mm threshold, as displayed in Table 4.1, but slightly inferior at thresholds of 0.2mm or 0.4mm. One distinction between the SI methodology utilised in this work and the one used in these comparative previously reported studies is the implemented hardware, with the CCD camera used in the latter case to acquire fringe images requiring significantly longer total acquisition times ≈180s, making this approach undesirable for this clinical joint imaging prototype. Nevertheless, further comparative studies would be beneficial to determine whether the lower noise characteristics, improved dynamic range or greater sensitivity of this CCD camera approach can explain the superior accuracies previously reported over video-rate CMOS technology used in this work. The SI accuracy in Table 4.1 was superior when imaging the cylinder compared to the cuboid phantom, with a lower median and higher comparative fraction of points at each distance metric. This may be explained by the SI point cloud of the cuboid struggling to accurately recover the abrupt changes at the corners, as can be seen in the non-existent curvature introduced

in Figure 4.1, reflected as a positive skew of the corresponding histogram in Figure 4.2. Any discrepancies in shape such as this may also potentially introduce systematic errors during the registration process. These issues should not, however, be applicable to joint imaging, with the smooth surface curvature of the finger much more similar to that of the cylinder.

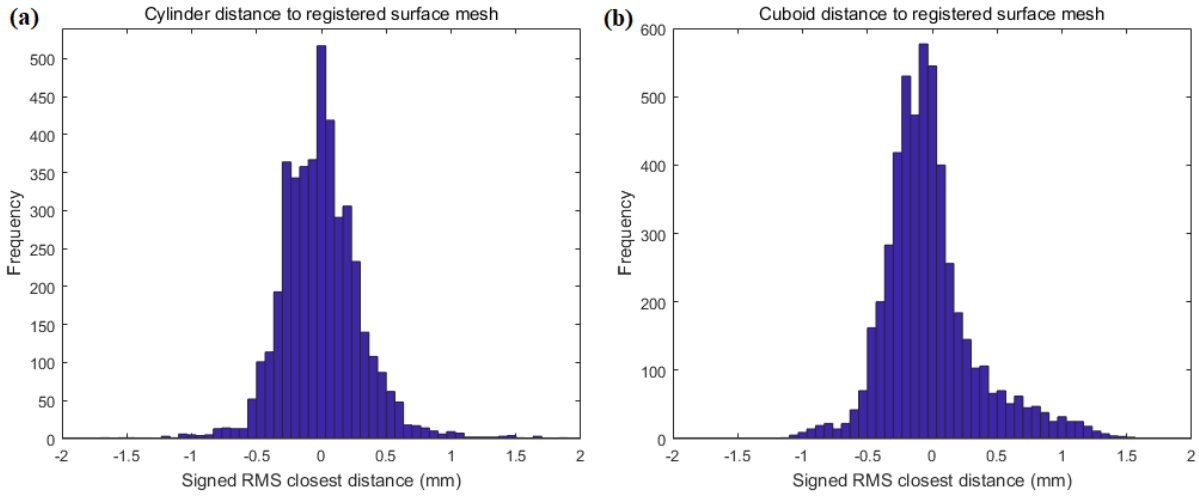

Figure 4.2: Corresponding histograms of signed distance to registered, geometrically accurate surface meshes for both (a) the cylindrical phantom an (b) the cuboid phantom displayed in Figure 4.1.

4.1.2 Displacement From Platform

To assess the linearity of changes in displacement from the platform in the point cloud recovered using the SI, a model was constructed using LEGO with white panels creating three distinct heights, as shown in Figure 4.3(a), measured to be 12.7, 22.2 and 31.7mm from the base using Vernier callipers.

The resulting point cloud from SI is plotted in both Figure 4.3(c) and (d), illustrating the three distinct steps. The point clouds at each step were distinguished by thresholding, and the mean heights at each step (± S.D.) were found to be 13.04±0.41, 21.99±0.39 and 31.37±0.40. These mean values displayed a high correlation with true height (R^2 = 0.99986), as shown in Figure 4.3(b), indicating that that the distances measured from the platform were linear up to ≈ 32mm in height from the platform.

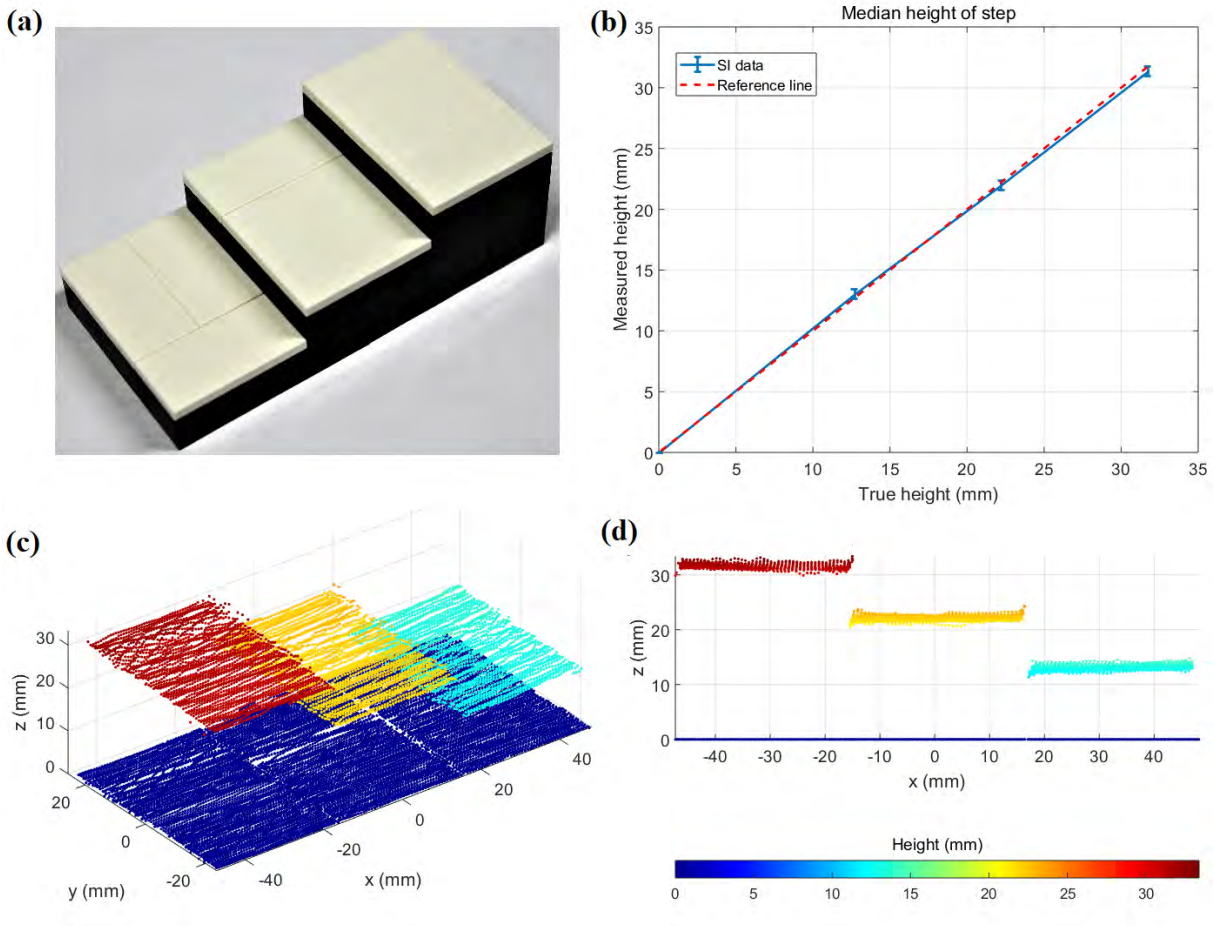

Figure 4.3: (a) A photograph of the stepped model constructed from LEGO, (b) a plot of median height in the point cloud against true height of each step and images of the 3D point cloud coloured by height at either (c) isometric or (d) side views.

4.2 Phantom Validation Studies

To evaluate the ability of the constructed system for performing DOT against a ground truth, the two custom-made solid plastic phantoms (Biomimic, INO, Quebec, Canada) were imaged in a variety of experiments, one cuboid in shape and one cylindrical version approximately similar in size to a human finger. Both phantoms contained two bored cylindrical 6mm diameter tunnels at depths of 5mm and 15mm, which are illustrated together with dimensions in Figure 4.4. Cylindrical plastic rods constructed from the same material, 6mm diameter and 50mm in length, could be inserted with a tight fitting into these tunnels, with optical properties either equal to the background for homogeneous phantoms, or with distinct optical properties to create spatial heterogeneities. For the cuboid

phantom, a separate homogeneous phantom with identical background optical properties was available, whilst in the case of the cylindrical phantom, a spatially homogeneous version was made by adding background matching rods. Due to tendency of the cylindrical phantom to roll, it was held in position using blue tack attached to its base at one of its ends far from the source illumination, as to have minimal impact on the boundary conditions.

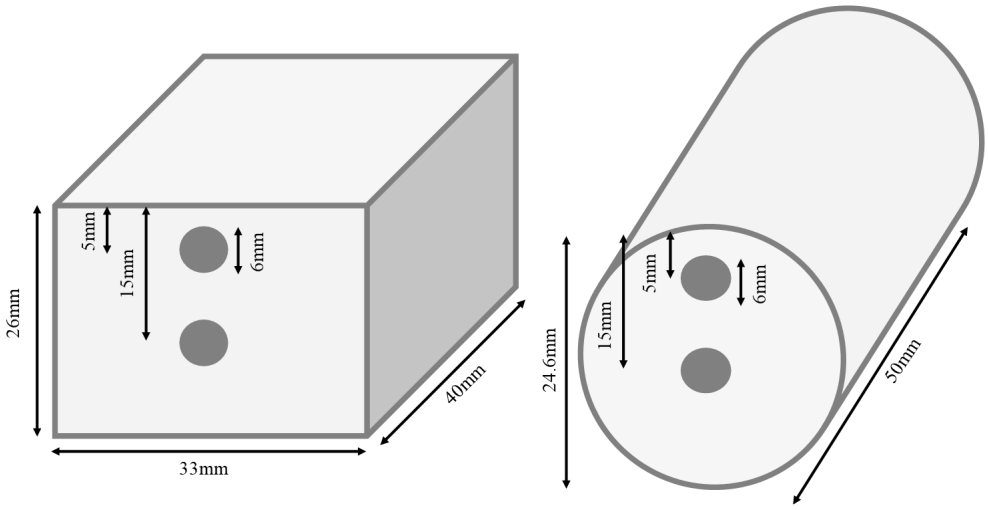

Figure 4.4: Dimensions with tunnel locations of (a) the cylindrical phantom and b) the cuboid phantom.

The absorption and reduced scattering coefficients of both phantoms were spectrally varying, with the wavelength dependence of these optical properties characterized during time resolved spectroscopy experiments previously in the literature [194], outlined in Appendix A.1.1. To enable the implementation of SC-DOT, in which chromophore concentrations are recovered using measurements at multiple wavelengths, two non-existent chromophores were invented referred to as either cylinder dye concentration (Dye-Conc-Cyl) or cuboid dye concentration (Dye-Conc-Cub) for each respective phantom. These chromophores were defined as having extinction coefficients equal to the *a priori* absorption coefficients of the phantoms, resulting in both homogeneous phantoms effectively having a background concentration of 1 for their respective chromophores. Further technical details of these phantoms are outlined in Appendix A.1.1.

Due to a lack of SI on the underside of the phantoms, geometrically accurate pre-

generated FEM meshes were used as spatial *a priori* information and registered to the SI data, following the same transformation approach as outlined when assessing the SI accuracy in Section 4.1.1, consisting of either 63,049 nodes and 304,334 linear tetrahedral elements for the cuboid or 85,205 nodes and 451,821 linear tetrahedral elements for the cylinder. This approach allowed for off centre sources to be used in these phantom studies, such that a 7 × 5 grid of source positions could be chosen for illuminating the underside of the phantoms to fully evaluate the performance of the system, whilst a 11 × 9 grid of virtual detector positions was assigned on the opposing side, as illustrated in Figure 4.5.

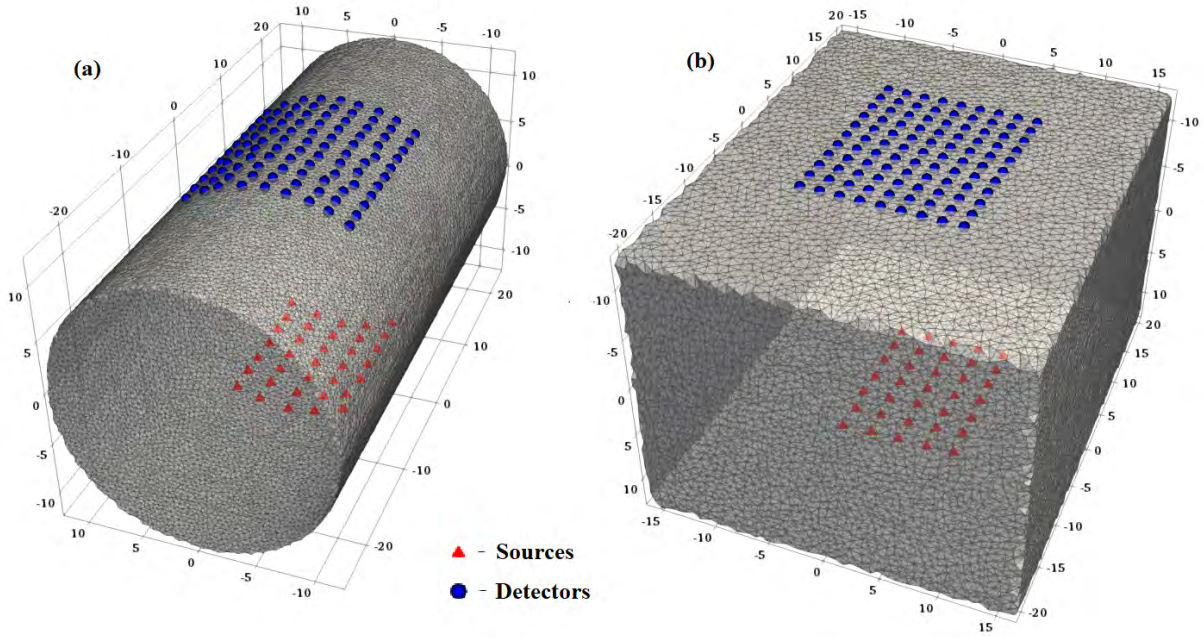

Figure 4.5: FEM meshes of (a) the cylindrical phantom and (b) the cuboid phantom, assigned as a spatial *a priori* to the SI data, with the corresponding 35 source positions and 99 detector positions used for optical transmission imaging.

4.2.1 Optical Data Pre-Processing

Prior to any fitting or reconstruction of optical anomalies, a crucial additional post-processing step was to first clean the optical data by filtering out any measurements with high levels of noise, as their inclusion will have a detrimental impact on reconstructed image quality. In DOT systems, this is typically achieved by excluding source-detector pairs expected to exhibit poor signal quality, based on either source-detector separation distance

or another measure of signal quality such as SNR, as defined in Appendix A.2.5. To assess the typical SNR achieved by the optical imaging protocol outlined in Section 3.4, 20 repeat acquisitions were collected at each source position for the homogeneous cylindrical phantom in a static position. A desired threshold was established based on absolute signal corresponding to a SNR of 100 and any source-detector pairs below this value were disregarded when solving the inverse problem, which corresponded to a coefficient of variation in noise at 1%.

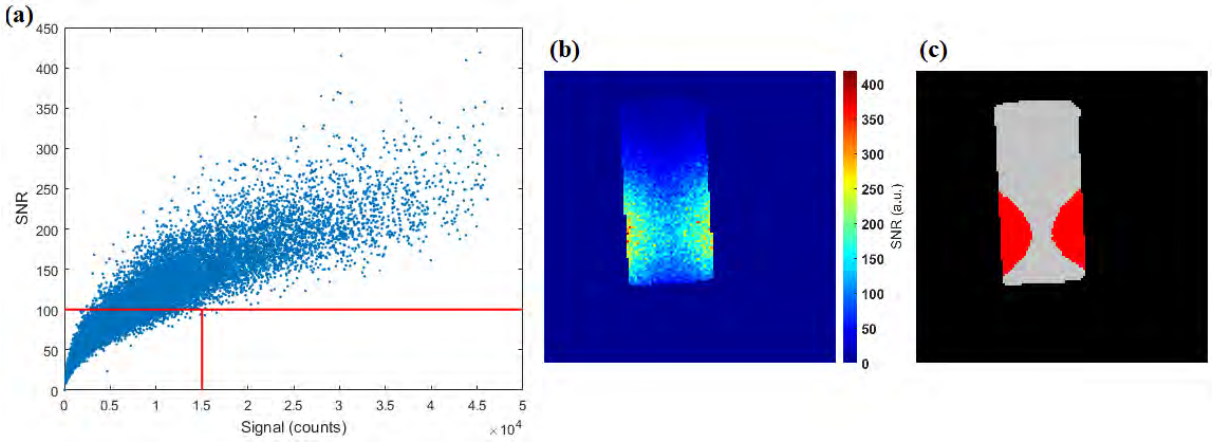

Figure 4.6: Results of SNR testing with raw CCD images of a cylindrical phantom before Gaussian kernel was applied with (a) SNR variation with signal strength across all pixels and source positions, and red lines showing the thresholds defined for signal from 100 SNR threshold. (b) Example map of SNR calculated from 20 measurements at a single source position and (c) corresponding pixels above defined threshold (in red).

The SNR characteristics of the data followed a square root relationship with signal, as would be expected from a shot noise dominated acquisition when using the auto-exposure routine, as shown in Figure 4.6 (a). Based on the 100 SNR threshold illustrated as the horizontal red line, this corresponded to a threshold of approximately 15,000 counts, below which 45.4% of pixels would have been disregarded across all source positions, including many source-detector pairs with lower signal measurements sampling volumes of interest through the centre of the phantom or joint as a consequence of their increased pathlength, as illustrated in Figure 4.6(c). To improve the SNR characteristics, 5 × 5 pixel Gaussian kernel was applied to the raw image data in post-processing with a standard deviation set to 0.793 pixels, both of which were chosen based on the estimated equivalent NA of a 1mm

diameter optical fibre in contact with the boundary, as this is a commonly implemented experimental set-up used in DOT.

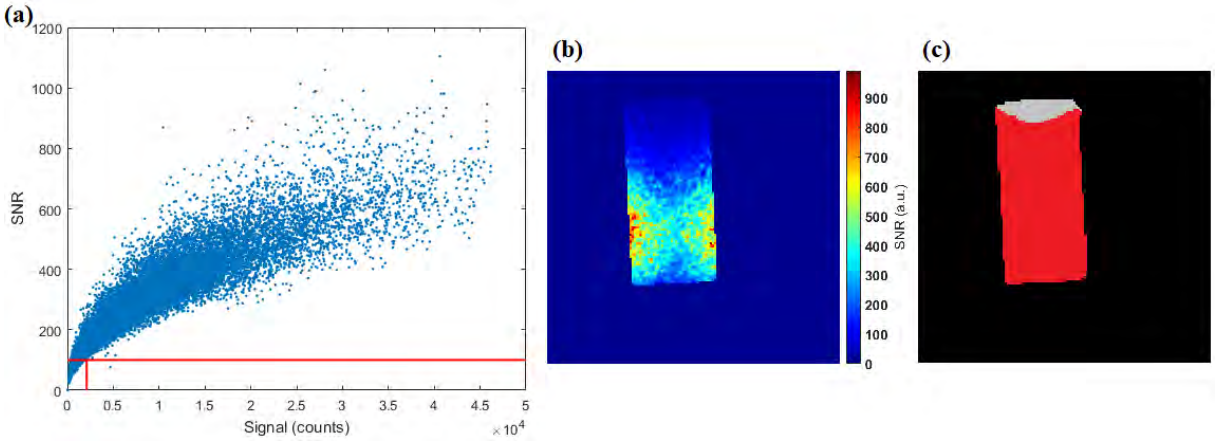

Figure 4.7: Results of SNR testing with processed CCD images of a cylindrical phantom after Gaussian kernel was applied with (a) SNR variation with signal strength across all pixels and source positions, and red lines showing the thresholds defined for signal from 100 SNR threshold. (b) Example map of SNR calculated from 20 measurements at a single source position and (c) corresponding pixels above defined threshold (in red).

After applying the Gaussian kernel less speckle noise in the SNR map was visually evident in Figure 4.7(b). As much higher SNR values were reached for the equivalent total signal in Figure 4.7(a), a SNR of 100 could now be achieved at a total signal threshold of ≈2500 counts, resulting in a much larger number of useful pixels, with 82.1% now acceptable for the cylinder at all source positions as illustrated in Figure 4.7(c).

4.2.2 Homogeneous Phantom Boundary Data

The homogeneous versions of each respective phantom were imaged. This data proved useful in three ways; (1) measurements of the homogeneous phantoms were required for calibrating the model/data mismatch and any source coupling variation, as discussed in Section 3.6, (2) spatial and spectral variation in measured boundary data could be compared with simulated forward model data, providing a metric of the systems accuracy for acquiring optical data and (3) to provide an initial guess for the inverse problem during iterative DOT image reconstruction.

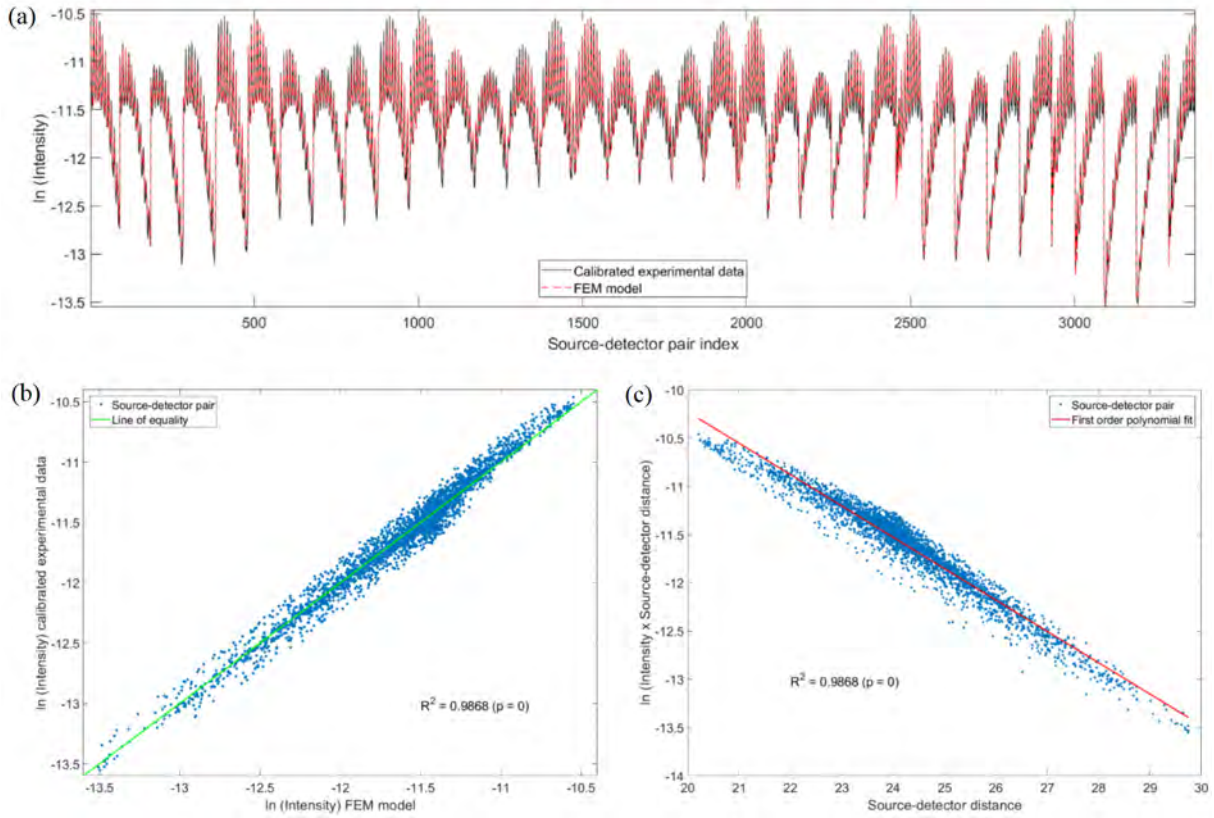

Figure 4.8: Comparison of boundary data for the homogeneous cylindrical phantom between calibrated experimentally measured data and that predicted by the FEM model with *a priori* optical properties assigned, displayed as either (a) ln(I) values of both datasets across all source-detector pairs or (b) a plot directly comparing the measured and predicted boundary data values. (c) Illustration of the linear decay in ln(Ir) of the experimentally measured boundary data with increasing source-detector separation distance.

Figures 4.8(b) and 4.9(b) illustrate the high correlation between data predicted by the homogeneous FEM model and experimental data acquired using the system, indicative of a high spatial alignment for both the source and detector positions when imaging either the cylinder or the cuboid, as shown in Figures 4.8(a) and 4.9(a) respectively. These results provide evidence that the mapping of optical data to the volumetric mesh using the registration process outlined in Section 3.6.1 achieved a high level of accuracy for both phantom geometries. The inferior correlation seen for the cylindrical phantom data was thought to be due to increased variation in both source and detector coupling from the cylinder's surface curvature, introducing systematic errors in boundary data not fully corrected through calibration. This difference is visible, for example, when comparing

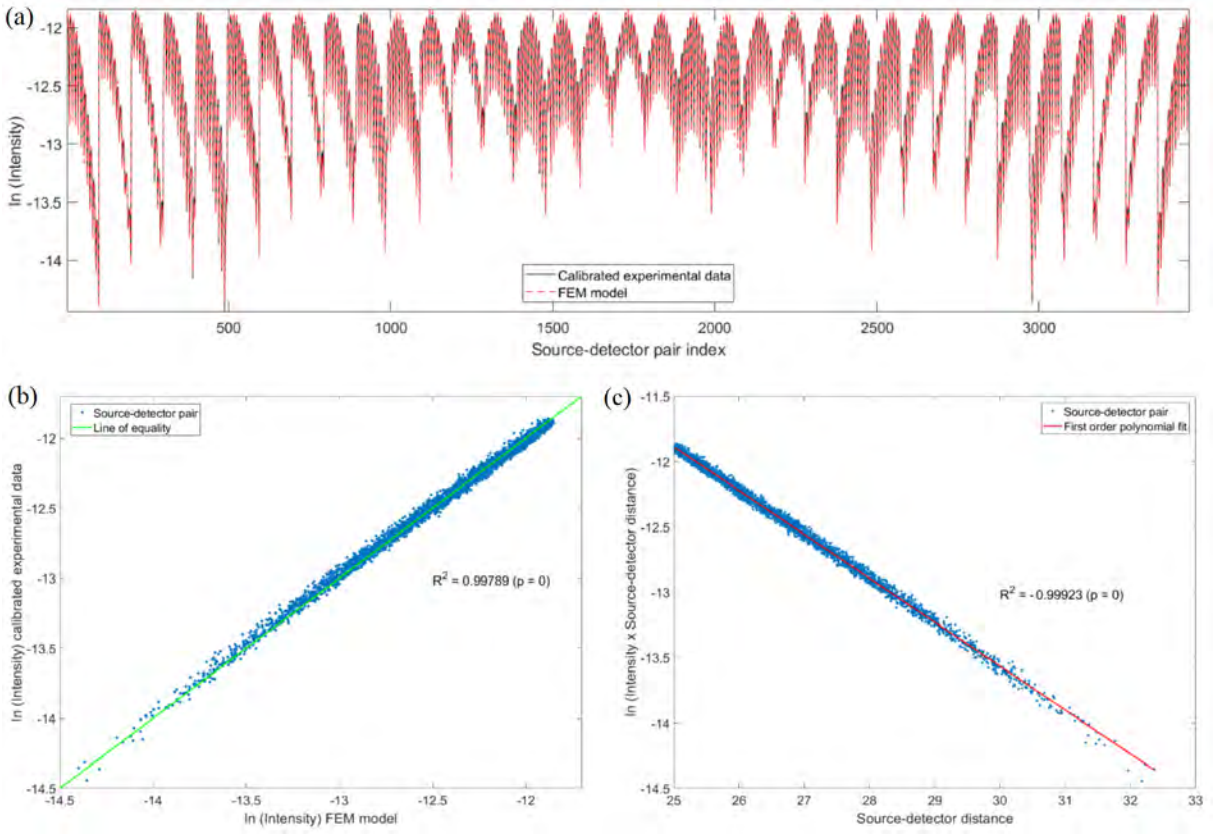

Figure 4.9: Comparison of boundary data for the homogeneous cuboid phantom between calibrated experimentally measured data and that predicted by the FEM model with *a priori* optical properties assigned, displayed as either (a) ln(I) values of both datasets across all source-detector pairs or (b) a plot directly comparing the measured and predicted boundary data values. (c) Illustration of the linear decay in ln(Ir) of the experimentally measured boundary data with increasing source-detector separation distance.

Figures 4.8(a) and 4.9(a), with the cuboid case displaying a much more consistent dynamic range across all 35 source position groupings.

4.2.3 Global Optical Properties

According to the Green's function for the DA, the relationship between source and detector separation, r, and ln(I * r) should be a linear decay for a homogeneous infinite medium [109], where I is the boundary intensity for the corresponding source-detector pair. This fundamental homogeneous DA relationship is clearly reflected in Figures 4.8(c) and 4.9(c), both displaying highly linear decays for the cylindrical ($R^2 = 0.9868$) and cuboid ($R^2 = 0.9979$) phantoms, again with superior linearity for the latter. Based on the gradient of the

first order polynomial fit of this linear decay in Figures 4.8(c) and 4.9(c), a global fit for μ_a at each wavelength was calculated using a previously presented method [195], in which an analytical solution for an infinite medium is first calculated as an initial guess, followed by a refined numerical fit using a FEM model. Due to the high degree of non-uniqueness in this global fit of μ_a and μ_s' when using CW measurements at a single wavelength, values for μ_s' were assumed *a priori*. From these experimentally measured μ_a values, corresponding dye concentrations were calculated for each using the Beer-Lambert law by regression into their *a priori* equivalents in the geometric case.

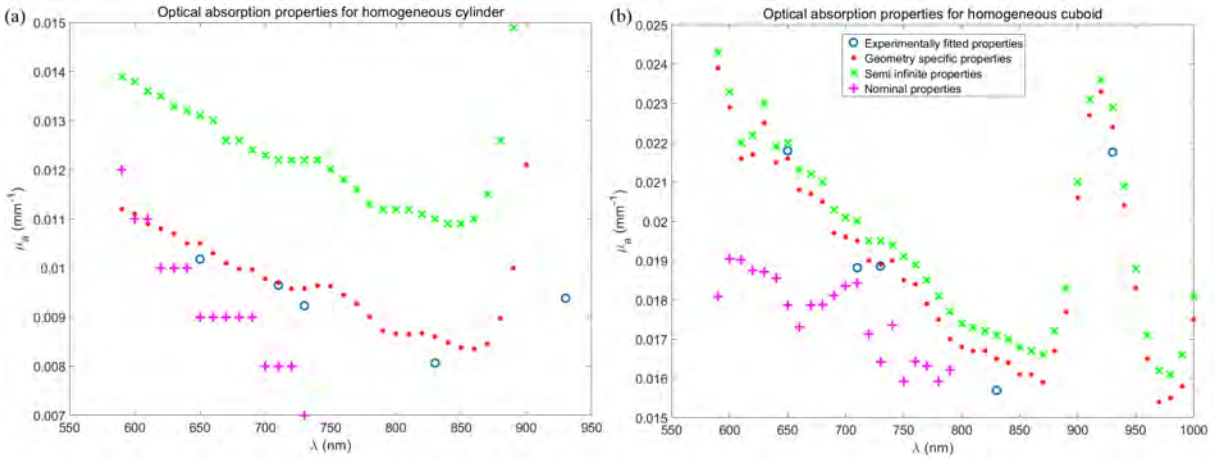

Figure 4.10: μ_a values comparing geometric, semi-infinite previously measured during time resolved experiments [194] and nominal provided by the manufacturer for either (a) the homogeneous cylinder or (b) the homogeneous cuboid.

The spectral response of experimentally measured global values for μ_a with wavelength closely matched the geometry specific absorption coefficients measured during previous time resolved experiments [194] for both phantoms. This capability to accurately recover global absorption coefficients across the measured wavelength range provided evidence of a high degree of accuracy achieved for the spectral calibration of the R_F, as detailed in Section 3.2.2. The global dye concentrations were quantitatively comparable to the ground truth as displayed in Table 4.2, but underestimated in both cases with percentage differences from the target concentrations of 5.1% and 1.9% for the cylindrical and cuboid phantoms respectively. A significant difference was seen with the manufacturer-provided nominal values and the three compared datasets, a distinction that was also reported in

experiments using the 1st generation imaging system with an 18% error in Dye-Conc-Cub compared to nominal values for the cuboid phantom [95], highlighting the challenges that can be faced when attempting to select reliable ground truth values for the optical properties of a phantom.

Phantom dye	Ground truth concentration	Experimental global concentration
Cylinder	1	0.949
Cuboid	1	0.981

Table 4.2: Global concentrations from numerical fits of μ_a in Figure 4.10 for both phantom geometries, in their respective Dye-Conc.

4.3 Phantom DOT Reconstruction

Heterogeneous versions of both phantoms containing anomaly regions were imaged in several experiments, with the purpose of assessing the entire work-flow of the presented system and its ability to reconstruct optical contrast using DOT.

4.3.1 Quantitative Evaluation Metrics

To measure the quantitative accuracy of the recovered images, three metrics were used: recovered contrast (RC), the volume ratio (VR) and the mean squared error (MSE). RC is the recovered contrast between the ground truth of the anomaly region and the ground truth of the background region, defined as follows:

$$RC = \frac{\frac{1}{N_{ANOM}} \sum_{i=1}^{N_{ANOM}} (c_i)}{\frac{1}{N_{BACK}} \sum_{i=1}^{N_{BACK}} (\bar{c}_i)} \tag{4.1}$$

where N_{ANOM} is the number of nodes in the ground truth anomaly region, N_{BACK} is the number of background nodes outside the ground truth anomaly region, c_i^j is the chromophore concentration of the nodes inside the ground truth anomaly region, $\bar{c}_i^j$ is the chromophore concentration of the nodes in the ground truth background region, i is the

node index. An optimum value for RC is equal to the contrast ratio of the value of the ground truth anomaly region over value of the background region.

VR is the ratio of the volume of the recovered anomaly and the ground truth target volume, providing a measure of the accuracy of the recovered target size:

$$VR = \frac{|ROI|}{|tROI|} \tag{4.2}$$

where $ROI = \gamma * max(conc)$ is the volume of the recovered anomaly, $tROI$ ground truth anomaly region, and γ is a predefined threshold chosen to be 0.65, based on visual inspection of images which consistently separate the anomaly from the background. Lower VR values correspond to a better resolved anomaly.

Finally the mean squared error between the ground truth and recovered values was calculated as

$$MSE = \frac{1}{N} \sum_{j=1}^{N} \left(c_i^j - \tilde{c}_i^j \right)^2 \tag{4.3}$$

where N is the total number of nodes, c_i is the recovered concentration and $\tilde{c}_i$ is the ground truth concentration. A lower value MSE indicates less difference between the ground truth and the recovered image across the whole domain.

4.3.2 Heterogeneous Cylindrical Phantom Imaging

A heterogeneous cylinder was used by inserting 6mm diameter cylindrical rods into the bored holes at different heights, which were either background matching or provided 2:1 contrast for Dye-Conc-Cyl. As the scattering properties for both rods matched the cylinder background, S_A and S_P were both taken with as constant, homogeneous *a priori* values of 1.70 and 0.17 respectively for all cylindrical phantom experiments, calculated using Mie theory in Appendix A.1.1.

The 2:1 contrast rod provided an anomaly region and was placed sequentially in each vertical position of the cylindrical phantoms bored holes, whilst the other hole contained

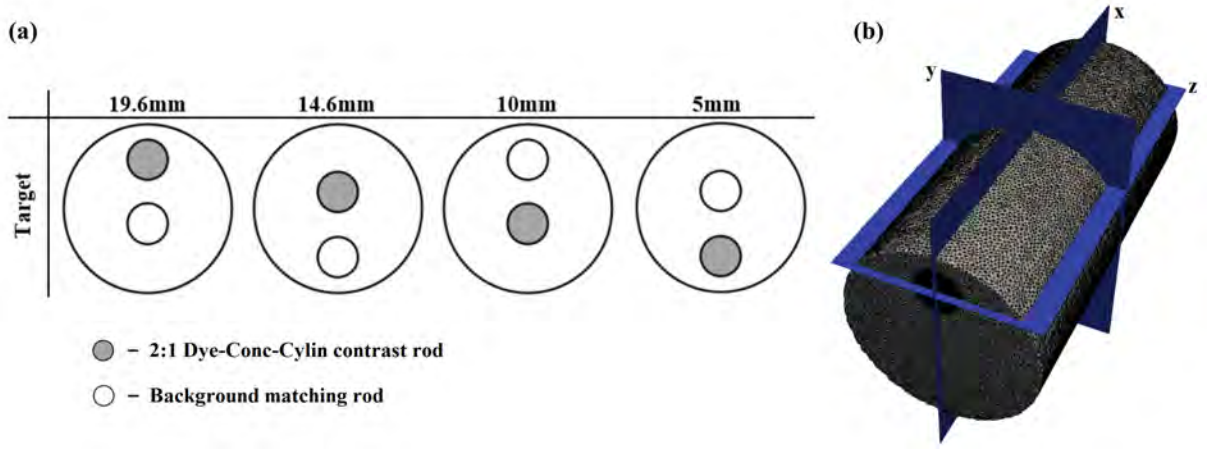

Figure 4.11: (a) Images illustrating the locations of the 2:1 absorption contrast and background matching rods at each height. (b) Orientation of x, y and z perpendicular 2D slices used for visualisation. Note the height of the z slice was altered such that it was equal to the height of the anomaly centroid.

the background matching rod. These two configurations were then repeated after rotating the cylindrical phantom by 180°, resulting in four distinct anomaly depths at 5mm, 10mm, 14.6mm and 19.6mm, as shown in Figure 4.11 (a), each of which were imaged using the same acquisition protocol. For visualisation, slices of the reconstructed contrast were taken at three perpendicular orientations, as shown in Figure 4.11(b). The homogeneous version of the cylindrical phantom was also imaged, enabling calibration of the model/data mismatch and any source/detector coupling variation.

A clear distinction in the boundary data could be seen between the homogeneous data and those experiments in which the contrast rod had been included, as illustrated in images of relative intensity in Figure 4.12(a). As would be expected, the homogeneous case provided the greatest overall boundary flux signal, with detectors at the edge of cylinder's surface curvature indexed 1, 9, 10, 18 etc. manifesting as signal peaks, due to their relatively shorter pathlength compared to other detectors, whilst the central detectors indexed 5, 14, 23 etc. produced signal troughs, shown in Figure 4.12(b). The spatial location of the anomaly in the horizontal direction can be most clearly identified at 19.6mm height, with the high density image array producing high resolution sensitivity to subsurface optical changes close to the imaged boundary. Across the measurements, this

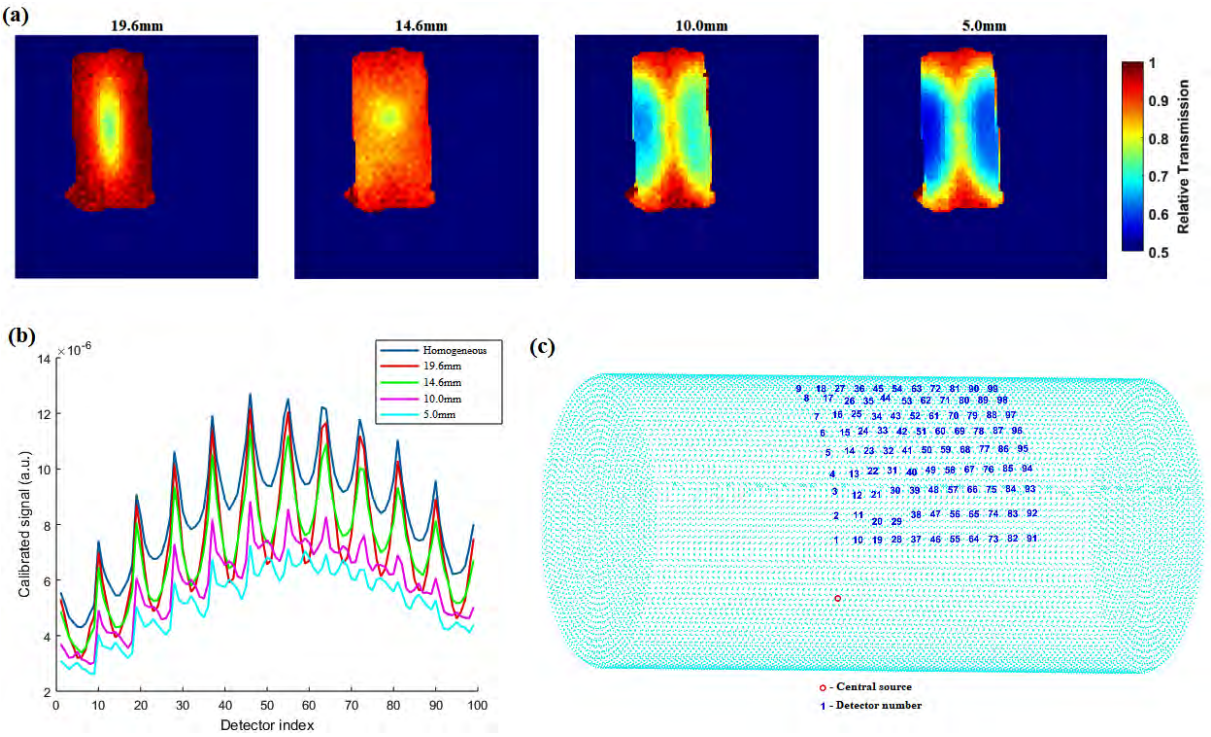

Figure 4.12: (a) Raw heterogeneous images normalised by their homogeneous equivalent at each height for a single central source position with 650nm data. (b) Calibrated optical boundary signal for both the homogeneous case and at each anomaly height for a single central source position. (c) Illustration of the corresponding source position and detector indices.

manifested as a similar flux to the homogeneous case for edge detectors, but significant drop in the calibrated signal for central detectors. As the anomaly height was lowered the overall relative transmission decreased, with more total flux being absorbed by the anomaly closer to this central source, but the ability to resolve the spatial location of the anomaly in the raw images decreased as the difference in calibrated signal between centrally placed and edge detectors diminished.

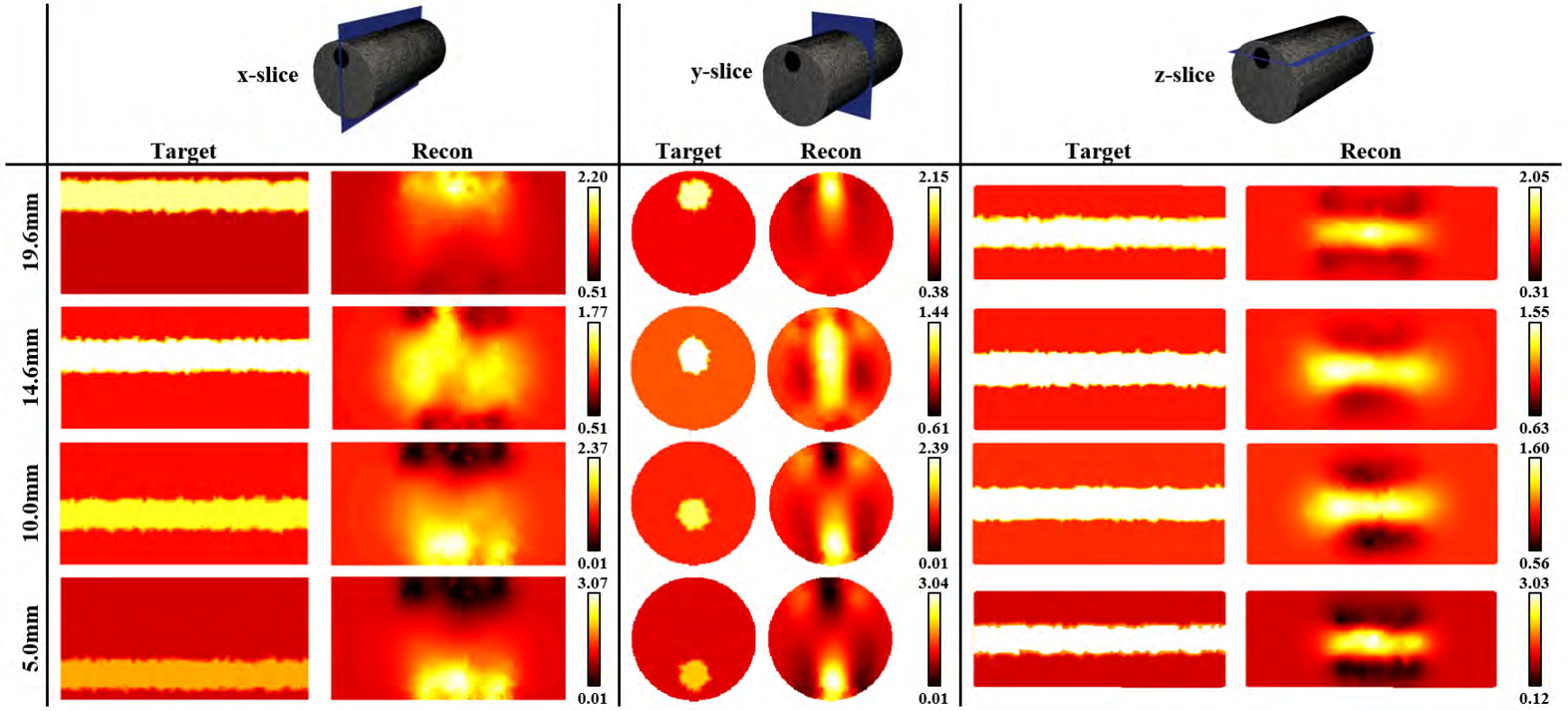

Figure 4.13: Reconstructed images of Dye-Conc-Cyl at compared at all four heights tested. Positions of x- and y-slices were positioned through the centroid of the entire cylinder, whilst the z-slice was positioned to pass through the anomaly rod centroid. The anomaly target in all cases provide 2:1 contrast in Dye-Conc-Cyl compared to background.

Reconstructed DOT image slices of Dye-Conc-Cyl revealed the anomaly's presence at all four anomaly positions within the region sampled by the sources-detector pairs, displayed in Figure 4.13. Resolution of the anomaly position was evidently superior in the lateral direction of the z-slices compared to the depth resolution in x-slices, an expected result of the transmission imaging source-detector set-up. The anomaly recovery at all heights was relatively uniform along the length of the cylinder in z-slices, important as contrast in human joints between the bone and synovial region was expected to occur in the same direction along the finger.

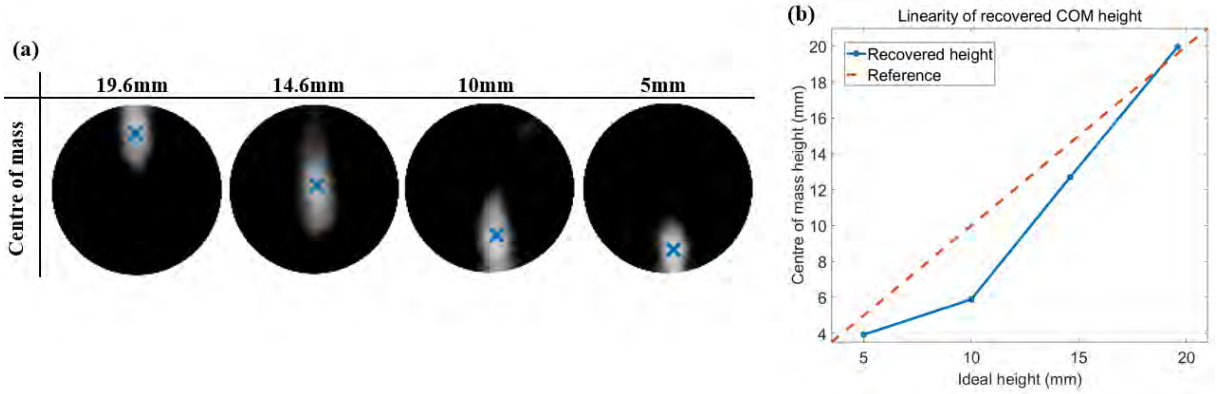

Figure 4.14: (a) Top row: Bottom row: Images of Cylin-Dye-Conc above a threshold of 60% of the maximum value summed along the length of the ROI, with the corresponding position of the centre of mass (blue cross). (b) Corresponding heights of the centre of mass against ideal height.

The correct height sequence is clearly identifiable in recovered images, supported quantitatively by the increasing height of the centre of mass in the y-plane as true anomaly height was increased in Figure 4.14. The anomaly height was most accurately located at 19.6mm, whilst a bias in the detector-source direction was evident at the remaining three heights, particularly at 10mm. The reconstructed anomaly appears most similar to the target at 19.6mm, with a well resolved anomaly and less background artefacts at this height, reflected in the lower MSE and VR values in Figure 4.15. At lower anomaly heights, background artefacts became more prevalent indicated by the increasing MSE, presenting as regions of abnormally lower or higher concentration in DOT images. The absolute values for Dye-Cylin-Conc were closest to the target value of 2 at 19.6mm, with concentration

underestimated in the centre of the cylinder at 14.6mm when resolution of the anomaly was significantly poorer with the correspondingly highest VR value. The Dye-Cylin-Conc was slightly overestimated at 10mm height and reached close to 3 at a height of 5mm, balanced by regions of lower concentration either side. RC values were reasonable consistent at all heights, except at 5mm when the RC was elevated, with a contrast of the anomaly against background visibly greater in the z-slice image at this height. As noise profiles were expected to be similar for all four different anomaly heights, the overall inferior performance at lower anomaly heights was thought to result from small inaccuracies in the calibration process, such as source positioning, introducing systematic errors that resulted in any changes close to the source locations being inflated by hypersensitivity at the boundary.

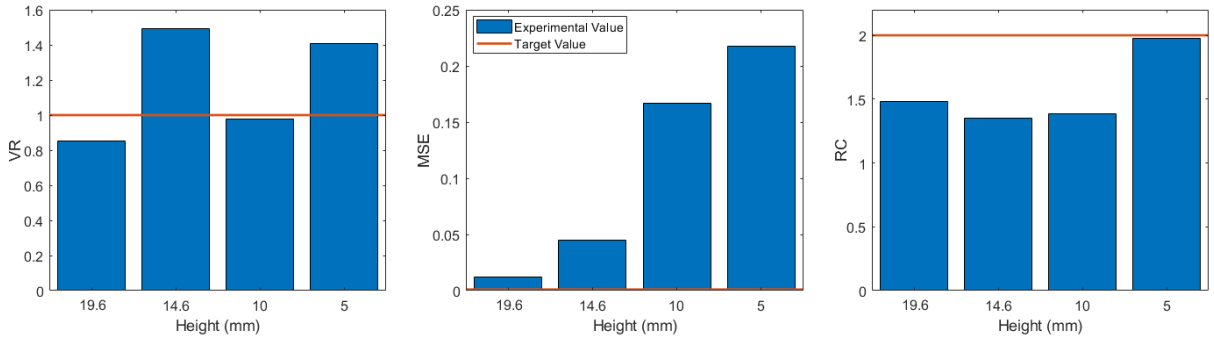

Figure 4.15: Bar charts of quantitative metrics, VR, MSE and RC, for all anomaly heights of the heterogeneous cylinder. The target value of the ground truth heterogeneous cylinder is displayed as reference (red).

Through implementation of an L1-based non-linear regularisation scheme, in collaboration with Wenqi Lu, it was demonstrated using the same boundary data for the heterogeneous cylindrical phantom that this alternative regularisation can supress background artefacts to improve contrast and spatial resolution [124], as displayed in Figure 4.16. As L1-based methods are only appropriate for sparse solutions, such as this single anomaly case, attempts to apply L1 regularisation methods to improve joint DOT images were unsuccessful, however this result highlights the contribution to reconstruction error from the smoothing effects of using L2 regularisation and further investigation into alternative regularisation techniques such as total variation models [196] for application to

joint imaging may prove promising in future studies.

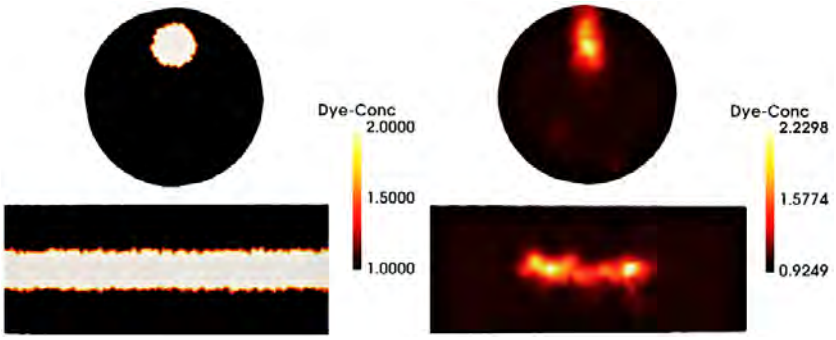

Figure 4.16: Reconstruction achieved at 19.6mm height anomaly with L1-based regularisation scheme, with the top row as y-slices and bottom row as z slices, demonstrating drastically supressed background artefacts, improved contrast and greater spatial resolution compared to reconstructions when using L2-based regularisation when using same data in Figure 4.13. Reproduced with permission from [124]

4.3.3 Heterogeneous Cuboid Imaging

The anatomy of the joint is heterogeneous in both absorption and scattering values, as outlined in Section 2.5. Although separation of scattering and absorption parameters with CW measurements is challenging due to the non-uniqueness of the DA, it has been demonstrated in the literature that it is possible to distinguish these parameters by solving a regularised inverse problem using multispectral data at a set of optimised wavelengths which both maximise the uniqueness and at the same time minimise the residuals, as implemented in Section 3.2.1. Experiments in the previous section using the heterogeneous cylindrical phantom provided contrast in Dye-Conc-Cyl using an anomaly rod with background matching scatter parameters, however in order to assess the capability of the system in recovering scattering parameters, a heterogeneous version of the cuboid phantom with anomalies in either S_A or Dye-Conc-Cub was imaged. This was constructed by inserting each rod version from the cylindrical phantom into two bored cylindrical 6mm diameter tunnels at distinct heights of 21mm for the cylinder background rod and 11mm for the cylinder anomaly rod, as illustrated in Figure 4.17. Respective values in Dye-Conc-Cub and S_A were calculated for each rod using the relative absorption coefficients at each

wavelength from Appendix A.1.1, with corresponding optical properties summarised in Table 4.3. Values for S_P were not recovered and assigned to be homogeneous, equal to that of the cuboid background of 0.20.

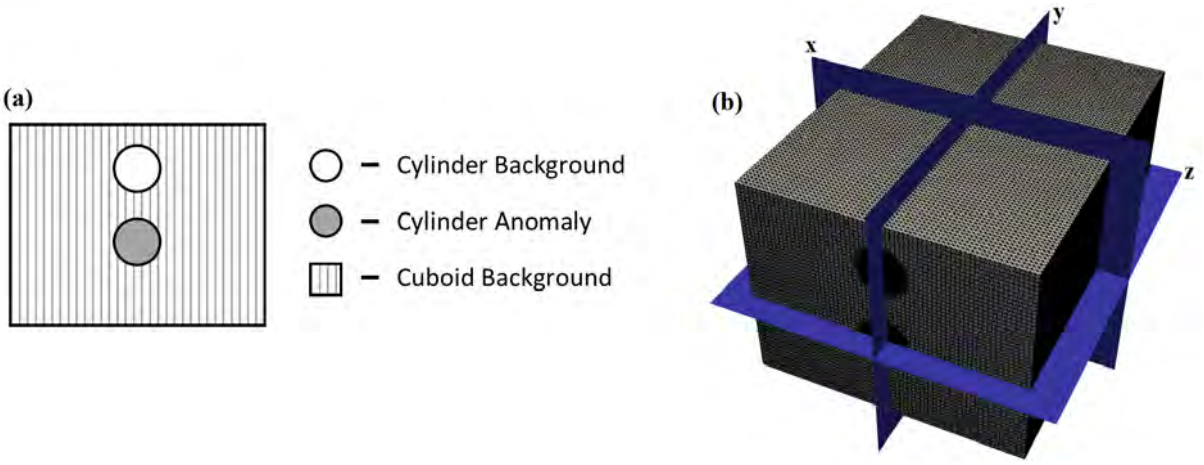

Figure 4.17: (a) Image illustrating the locations of the anomaly rods from the cylindrical phantom inserted into the bored holes to create a heterogenous cuboid phantom. (b) 3D rendering of cuboid phantom with illustrative x, y and z slice orientations.

Material	Target Dye-Conc-Cub	Recov. Dye-Conc-Cub	Target S_A	Recov. S_A
Cylin Back	0.51	1.09	1.70	1.35
Cylin Anom	1.01	1.36	1.70	1.47
Cuboid Back	1.00	-	1.70	-

Table 4.3: Optical properties for each region in the heterogeneous cuboid phantom, either *A priori* target calculated from respective mu_a and mu_s values in Appendix A.1.1 or recovered mean values using DOT in the ROI.

Encouragingly, all recovered images for the x and z slices in Figure 4.18 were highly uniform in the direction of the cuboid length, along which contrast within the joint was predominantly expected to occur. Images of S_A were more consistent with the target than Dye-Cylin-Conc, revealing an increase in scattering properties at both anomaly positions. This is reflected quantitatively in the elevated mean values within the target ROI in Table 4.3 and the maximum recovered S_A value reached 1.74, very close to the target value of 1.70. A narrower upper anomaly can be seen in z-slice1 compared to the lower anomaly z-slice2 again indicative of the increased resolution at the detector boundary, with some evidence of background artefacts of lower concentration laterally either side.

Dye-Cub-Conc images demonstrated changes between the respective two anomaly regions that were consistent with the changes in target, with greater concentrations observed in the upper anomaly region in z-slice1 compared to the lower anomaly in z-slice2, however quantitatively the absolute values were overestimated for both rods compared to their respective target values, with their mean recovered Dye-Cub-Conc 0.58 or 0.35 higher than the target value in the upper and lower anomalies respectively in Table 4.3. Although these discrepancies show evidence of some cross-talk between scattering and absorption parameters, this experiment has presented evidence that the multispectral system had a degree of sensitivity to changes in either of these optical properties.

4.4 Reliability and Reproducibility

The reliability and the reproducibility of results is an important aspect of a Biophotonic device to ensure that diagnostic accuracies are consistent, particularly when monitoring patients. During the human studies to be presented in Chapters 5 and 6, data was acquired from many participants over an extended time period, making it important to first ensure that the system could acquire data in a repeatable fashion and that reconstructed parameters were consistent. Sources of drift that could potentially impact the system performance over time included thermal expansion of components altering the optical alignment calibration, changes in the electrical read or dark noise profiles due to changes in ambient temperature or variation in the light source optical power. Solid, plastic phantoms are useful tools for assessment in this regard, due to their high stability of optical properties and durability over long time periods.

4.4.1 Short Term Stability

A typical joint imaging session lasted ≈15mins in total for all 8 PIP joints according to Section 3.4.2, making it important to characterise the stability of the system over time and ensure the optical transillumination measurement had reached a steady state. The halogen

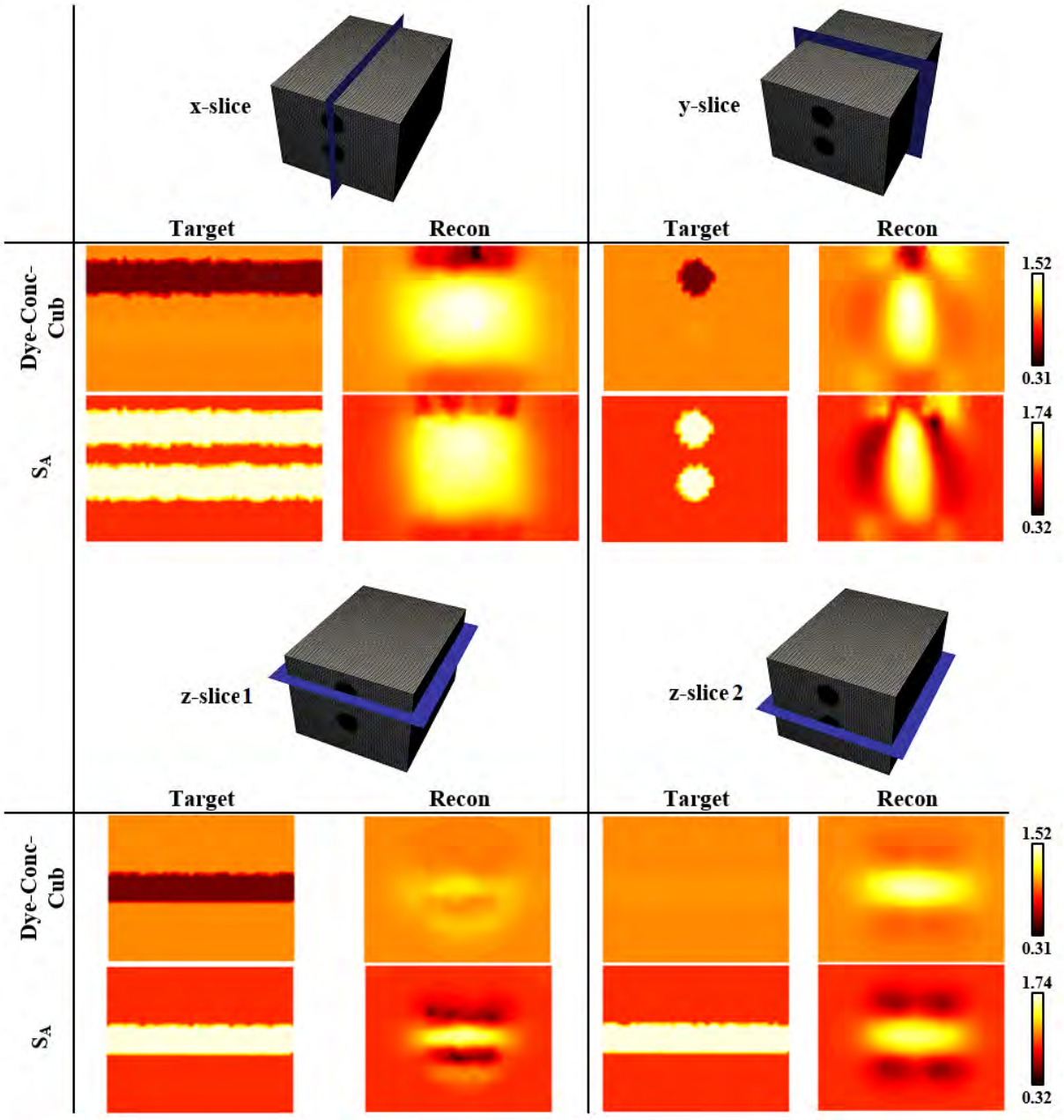

Figure 4.18: Reconstructed images of both Dye-Conc-Cyl and S_A for the heterogeneous cuboid. Positions of x- and y-slices were positioned through the centroid of the entire cuboid, whilst the z-slice1 and z-slice2 were positioned at heights of 19.6mm and 10mm respectively to pass through the anomaly rod centroids.

bulb in the light source and the CCD camera are two components susceptible to drift, both with temperature dependant performance. The nominal values for the stability of the tungsten-halogen lamp was stated as 0.5% with 0.1% drift per hour following a stabilising period of 5 minutes to allow the bulb to warm, whilst the CCD camera specifications

had no mention of stability but had a recommended operating temperature. A static experimental scene was used to assess the stability of optical data acquisition, in which repeat transillumination images of the homogeneous cylindrical phantom were acquired for a single, most central source position over 30mins immediately after switching on both the CCD camera and the light source. The exposure time was fixed such that the maximum initial signal in the optical cylinder image reached ≈50000 counts and the rate of change of boundary data calculated.

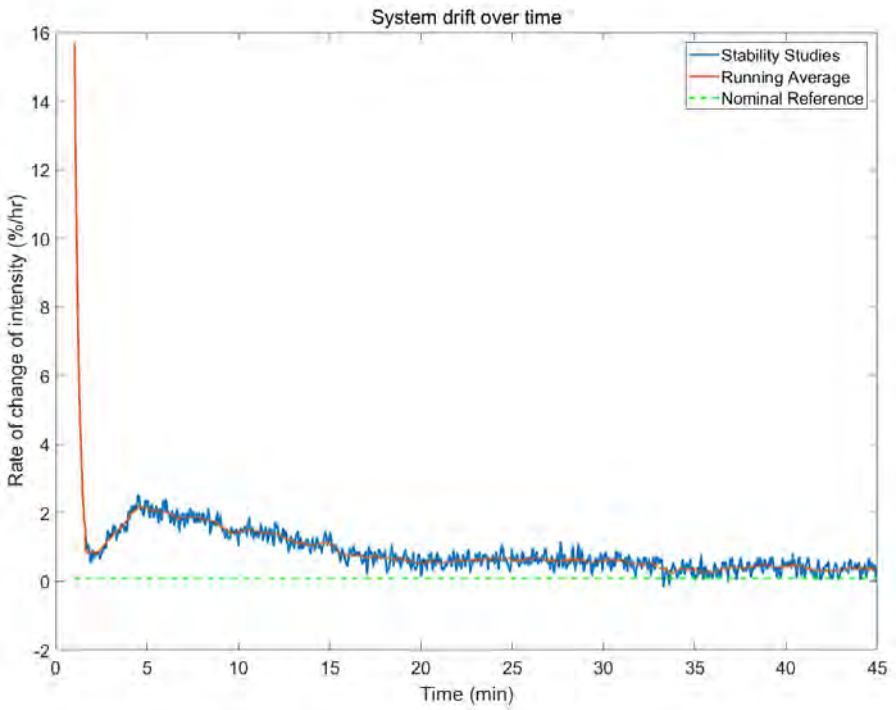

Figure 4.19: Rate of change of mean intensity in a 20 × 20 pixel central region for transillumination images at 730nm of the homogeneous cylindrical phantom, calculated difference in intensity between the start and end of a one minute sliding window multiplied by 60. The running average for a 65.2s window is also shown (red).

A clear period of stabilisation is evident for the first 20mins in Figure 4.19, as a result of a combination of the CCD camera cooling and the bulb warming in the light source. After this initial stabilisation period, the average drift in this the rate of change of intensity was calculated to be 0.488 ± 0.205% per hour, above the nominally stated reference value of 0.1% by the manufacturer displayed, but still reasonable considering imaging sessions typically lasted ≈15mins. After subtracting the running mean to account for this long

term drift, the stability was calculated by the standard deviation in signal to be 0.026%, well below the nominally stated value of 0.5%.

4.4.2 Longitudinal Reproducibility

Measurements acquired using the system were demonstrated to be stable over a short-time period of an imaging session using the static homogeneous cylindrical phantom following a 20min initialisation period, as summarised in Section 4.4.1. To assess the reproducibility of results over an extended time period, the heterogeneous cylindrical phantom was imaged using the same acquisition protocols every week over four weeks, with the anomaly rod included at a height of 19.6mm, chosen for its greatest accuracy in Section 4.3.2. To be consistent with the methods used in human joint imaging studies, calibration using the homogeneous cylinder of the source coupling and model-data mismatch was carried out at week one and not repeated at subsequent weeks.

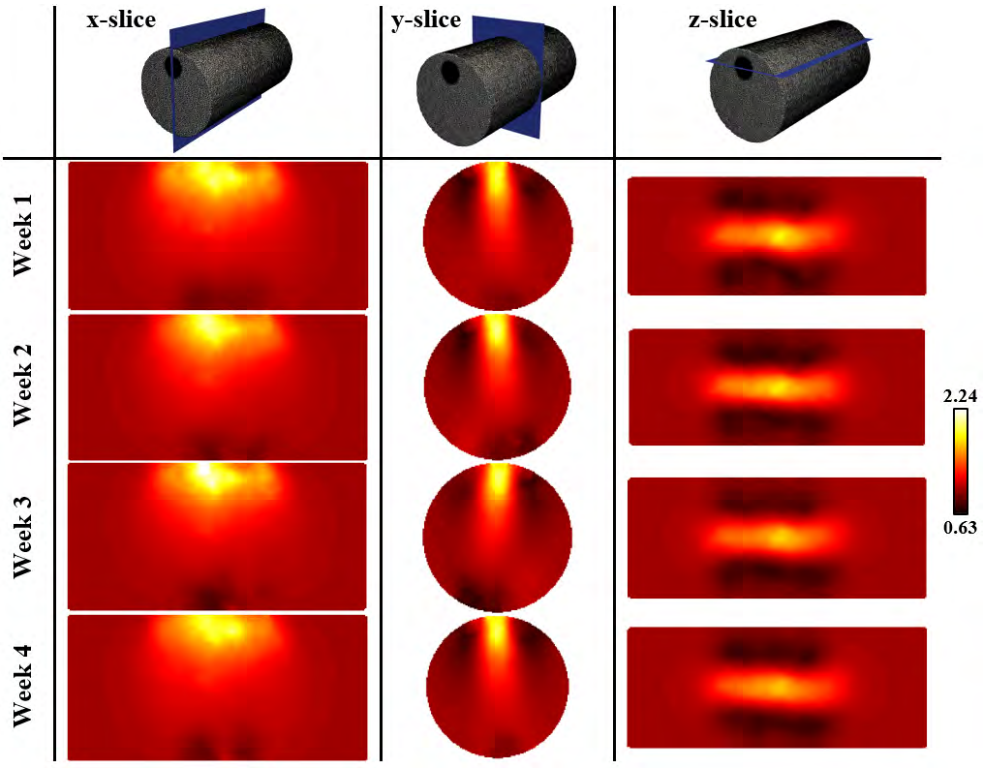

Figure 4.20: Repeat measurements of the cylindrical heterogeneous phantom with the 2:1 contrast anomaly included at 19.6mm height.

Repeat Number	Week 1	Week 2	Week 3	Week 4
RC	1.46	1.44	1.45	1.44
MSE	0.0129	0.0160	0.0167	0.0144
VR	0.843	0.837	0.863	0.757

Table 4.4: Values for quantitative metrics VR, MSE and RC, at all anomaly heights of the heterogeneous cylinder. The maximum value at week 1 was used to calculate VR at all weeks for a consistent comparison. The target value of the ground truth heterogeneous cylinder is displayed as reference (red).

The anomaly is clearly recovered at all four weeks of measurement in reconstructed DOT images in Figure 4.20, with quantitative metrics in Table 4.4 revealing a highly consistent RC for the anomaly ranging between 1.44 and 1.46. Subtle changes can be seen in the degree and location of background artefacts resulting in the MSE varying between 0.0129 and 0.0167, thought to result from a consequence of measurement noise and slight differences in the phantom positioning at each week. The shape of anomaly was also very consistent, with a slight decrease at week 4 in the VR.

4.5 Conclusion

Phantom experiments play a crucial role in assessing the performance of a system against a known ground truth. In this chapter, solid, biologically mimicking optical phantoms were used to validate the systems performance in terms of both data acquisition and capability to carry out DOT to spatially recover optical anomalies. The system capability to recover the surface profile with sufficient accuracy for this application was demonstrated for a number of objects, required for accurately measuring the human joint boundary.

Analysis of homogeneous phantom boundary data provided useful insights into the accuracy of the experimentally acquired optical data processing and registration, in comparison with theoretically predicted values using the FEM model and *a priori* optical properties. DOT imaging of heterogeneous phantoms has revealed consistent recoveries of anomaly regions, with relatively uniform recoveries seen along the expected direction of

contrast in the joint in all cases, some depth resolution achieved in cylindrical phantom despite the transmission imaging set-up and a degree sensitivity to both scattering and absorption changes illustrated in the cuboid phantom. The high level of reproducibility demonstrated for the heterogeneous cylindrical phantom over four weeks was important for ensuring that (1) a single time calibration approach was sufficient for this application, with recalibration of the system for every participant imaging session highly impractical in the clinic, (2) comparison of patient results acquired the over the study time period was valid and (3) longitudinal monitoring changes in optical properties within human subjects in Sections 5.2.6 and 6.4 was appropriate.

The complexity of non-contact DOT meant that the accuracy of reconstructed image maps was dependant on many measurement parameters, which together will have combined measurement errors in a non-trivial way. A rigorous data filtering operation based on absolute intensity and Gaussian smoothing was chosen utilising phantom studies, to ensure that the random noise in DOI data was kept to a minimum and the SNR was greater than 100 in all measurements. As with many optical-based devices, instrument calibration played a crucial role in accounting for a number offsets or system characteristics, including the intrinsic and extrinsic parameters for both CMOS and CCD cameras for SI, the spectral instrument response function for DOI data, light source coupling variation, the data-model offset and 3D source positions, all of which were relevant for tomographic reconstruction. These calibrations were all implemented on a "apply one-time basis" and fixed in all cases, an approach that was validated during repeat studies. This provided benefits by removing the need for regular, lengthy recalibration and additionally eliminated the introduction of random variation between datasets resulting from noise in recalibration data that would have an multiplicative impact on boundary fluence. Nevertheless, there will inevitably still be some systematic error in these calibrations, for example a degree of discrepancy between the calibrated and true source positions in 3D, which should be further minimised in future studies. The exponential relationship between boundary flux and pathlength, as described by the Lambert-Bouger law in Equation 2.6, highlights the importance of

accurate of SI to produce a FEM boundary truly reflective of the pathlength taken as any error in pathlength will also have a similar impact on boundary flux. Finally, a number of assumptions required for light propagation modelling, for example the conditions placed on the interaction of light at boundary or the use of the DA, will lead to systematic errors. Attempts have been made during system design and characterisation in this work to quantify and minimise these potential sources of measurement error, and importantly, an emphasis has been placed on ensuring consistency in acquisition and processing settings between subjects. This has allowed participant data in human studies to be quantitatively comparable in all instances and that results of classification are only indicative of any true differences between the pathophysiological states of inflamed and non-inflamed joints.

Although values for the phantom's optical properties used in these studies were biologically relevant, it would be highly in beneficial in future studies to develop a more complex phantom that more accurately mimics the joint physiologically and structure, for example based on either 3D printed tissue-equivalent phantoms [197], dynamic phantoms with tuneable optical properties [198], blood-based phantoms [199] or similar constructs to a previously proposed solid cylindrical phantom embedded with chicken bones [83]. In the next chapter, the *in vivo* performance of the system will be characterised through preliminary investigations imaging healthy participants, prior to clinical trials.

CHAPTER 5

HEALTHY SUBJECT STUDIES

In order to detect pathophysiological changes in inflamed RA joints, a good understanding of baseline values for healthy subjects was first required. In a healthy, non-inflamed joint, the anatomy of which is illustrated in Figure 1.2 (a), a contrast in optical properties is expected along the sagittal direction between the joint cavity and cartilage/bone either side, with the former reported to exhibit significantly lower absorption and scattering values during previous optical imaging studies [149, 3]. In this chapter, experiments in which joints from healthy participants were imaged using the presented multispectral-CW DOT system are presented and the recovered 3D maps of StO_2, tHb, S_A and H_2O assessed. These preliminary investigations provided distinct insights not attainable from static phantom studies, enabling the *in vivo* performance of the system to be assessed prior to clinical studies. These experiments included (1) assessing the degree of motion during subject imaging, (2) evaluating the typical transmitted signal and optical properties recovered in non-inflamed joints, (3) establishing levels of variability and repeatability of recovered parameters within a healthy subject cohort and finally (4) investigating the sensitivity of the systems response to physiological changes, either induced under cuff occlusion or resulting from recent traumatic injury. Ethical approval for these healthy subject studies was obtained from the University of Birmingham ($ERN\_16-1490$) with all volunteers contacted via word of mouth and required to sign informed consent forms prior to participating.

5.1 System Performance with Human Subjects

5.1.1 Joint Labelling Convention

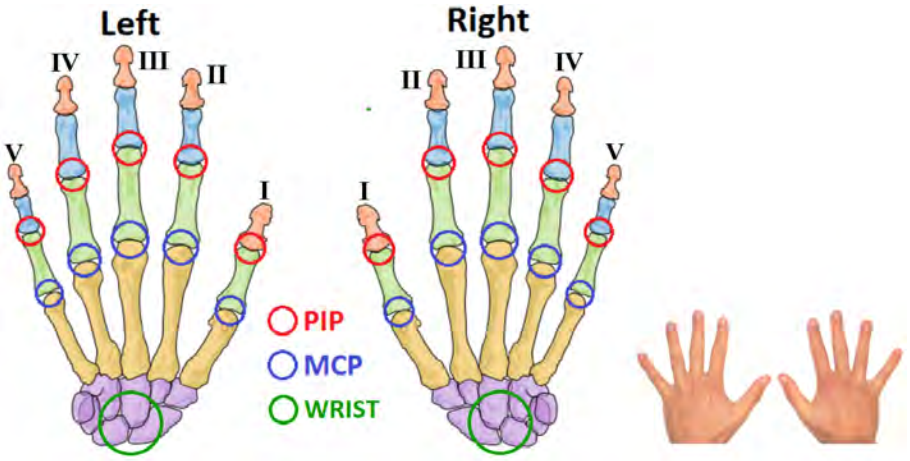

Figure 5.1: Skeletal images of the joint structure, with finger numbering convention in Roman numerals and location of the commonly afflicted joints in RA, including the PIP and MCP joints.

The labelling convention for human hand joints commonly afflicted in RA is outlined in Figure 5.1. A selection from the subset of II-V PIP joints from both hands were included in imaging studies throughout this work, chosen for two reasons: (1) the minimal geometrical variation along the sagittal direction of the PIP joint makes these joints more straightforward to image and (2) to allow direct comparison with performance in previous optical imaging studies in RA, the majority of which have involved PIP joint imaging. As the MCP joints are also commonly afflicted by RA, as detailed in Appendix A.4, this makes incorporation of these joints of interest in future studies. For reference, the anatomical terms used to describe the directions from the human hand are labelled in Figure 5.2

5.1.2 Motion During Data Acquisition

Participant motion during data acquisition is a commonly encountered challenge within medical imaging, particularly when multiple images are acquired over time and combined to generate 3D volumetric images. Reported examples in other imaging modalities include

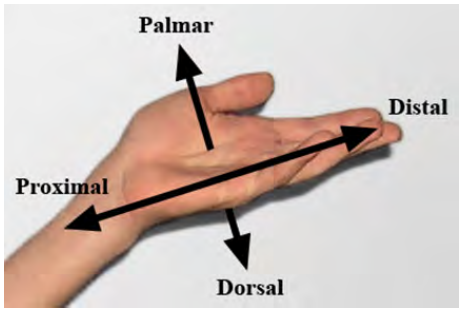

Figure 5.2: Anatomical terms used to describe the directions from the human hand.

the introduction of shading or streaking misregistration artefacts in CT scans [200], the reduction of grey matter volume and cortical thickness estimates in cerebral MRI [201] and high-frequency noise in fNIRS signals of HbO and Hb due to rapidly altered optical coupling [202]. In DOT, the expected impacts of participant motion during acquisition on absolute chromophore maps include reduced spatial resolution, poorer quantitative accuracy or the introduction of image artefacts.

To investigate the degree of motion during optical data acquisition, brightfield images of the left PIP II joint of two healthy subjects were acquired every 2 seconds over 10 minutes whilst neutral density filter was selected and binning was set to 1×1 for maximum spatial resolution, with a pixel in this case corresponding to 0.315×0.315mm. In order not to introduce bias, participants were not made aware that subject motion was being assessed, but instead told they were having a DOT scan. For each participant a threshold was manually selected to create a mask separating the finger boundary from the background within a region of interest, as shown in Figure 5.3 (a), with this threshold value remaining fixed for all subsequent images. The least squared difference in pixel number between the initial and each subsequent mask was then calculated at each time point to quantify any motion.

For participant A, an overall displacement of the joint position marginally right of its original position can be seen after 10 minutes, displayed in Figure 5.3 (b). Figure 5.3 (c) demonstrates the overall drift in the joint position over time for both participants, as the discrepancy between the initial and final threshold images gradually increased. The nature of this drift was variable between participants, with participant B showing more

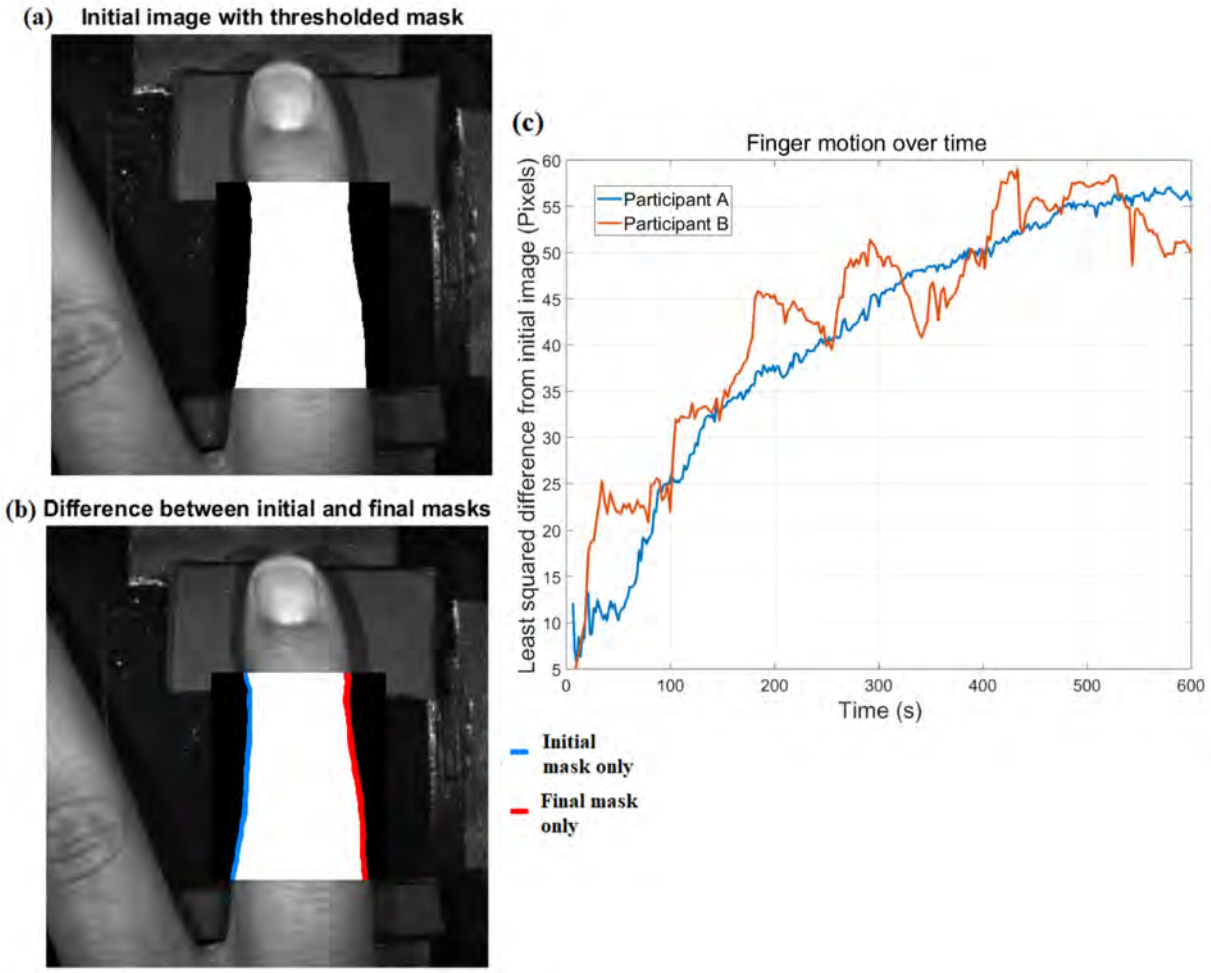

Figure 5.3: Example brightfield images for participant A overlaid with either (a) an image mask outlining the initial joint position (white) or (b) regions including both the initial and final masks (white), whilst coloured regions indicate a change in the mask location after 10 minutes, with blue pixels indicating initial mask only and red pixels indication final mask only. (c) Least squared difference in number of pixels between initial mask after 10 minutes for two participants.

fluctuating changes than participant A, as the joint moved back and forth over 10 minutes. These observations underline the importance of short total acquisition time, justifying the choice of a non-contact, galvanometer based scanning unit. Explored attempts to circumvent motion errors were challenging, including the use of a support structure to minimise motion, which was found to hinder optimal joint positioning, or the development of an algorithm to track finger motion, which proved difficult due to the varying source position over time. An alternative approach was therefore utilised to monitor whether any

significant motion had occurred during acquisition and if necessary retake the scan, such as is commonly implemented in MRI [203]. To achieve this, initial and final brightfield masks of the hand were compared in the same manner as outlined in Figure 5.3 and scans were retaken if the least squared difference was above 30 pixels, with examples of imaging acquisitions either below or above this threshold shown in Figure 5.4, preventing the processing of imaging sessions during which significant motion had occurred. Potential improvements for future work could include the use of fiducial markers to accurately track any subtle motions using the CMOS camera or further reduction in the total acquisition time to minimise the likelihood of motion occurring.

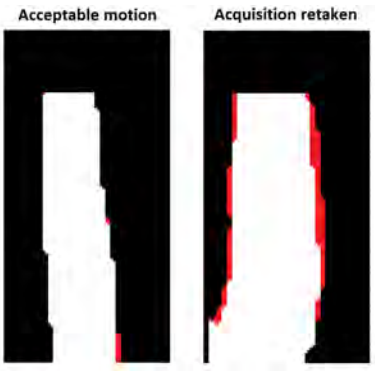

Figure 5.4: Example of finger with an acceptable amount of motion, with a 7 pixel change, and one which had moved significantly enough, with a with 93 pixel difference, that the data set was rejected and acquisition was repeated.

5.1.3 Typical *In Vivo* Healthy DOT Images

A typical set of image slices from a healthy PIP joint for the coronal, transverse and sagittal planes are displayed in Figure 5.5 with the corresponding orientations of these slices also shown by overlaying example slices of S_A on the hand surface profile, with reconstructed image maps of each of the clinically relevant parameters StO_2, tHb, S_A and H_2O shown.

The recovered contrast is most qualitatively apparent for S_A, with very low values of down to 0.05mm^{-1}, recovered in the centre of the transverse and sagittal images, consistent

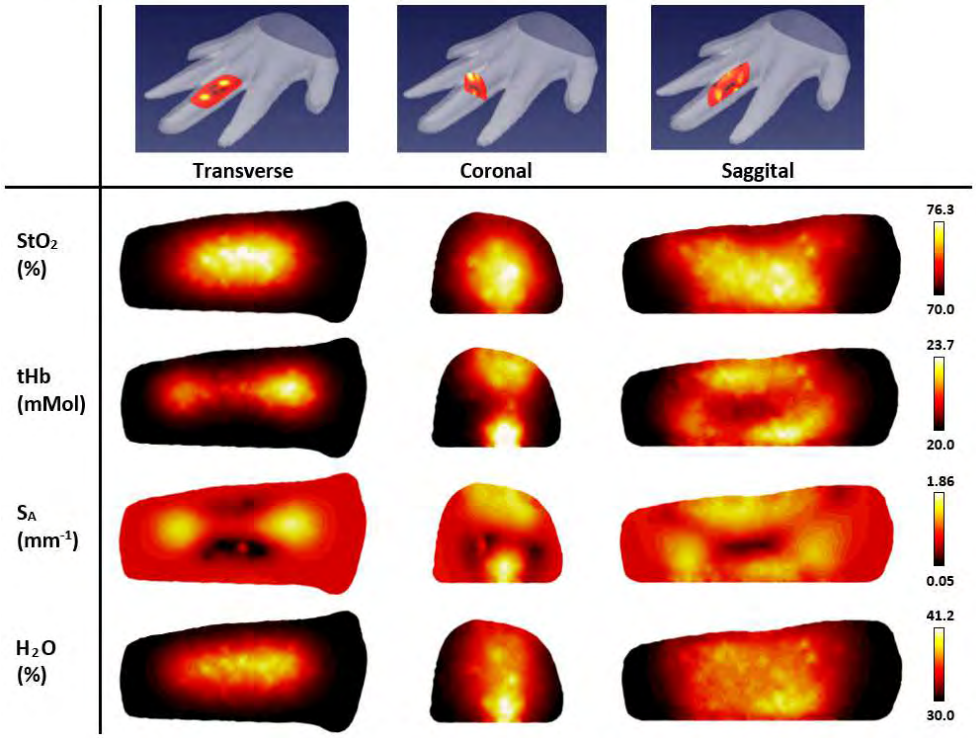

Figure 5.5: Example reconstructed images for a single healthy participant. The top row shows the captured surface profile of the hand overlaid with three perpendicular slices considered for visualisation. Corresponding image slices are displayed below of recovered parameters StO_2, tHb, S_A ,and H_2O. Reproduced with permission from [85]

with findings in previous literature [149, 153]. This region is expected to correspond to the joint cavity, where a key contributing factor to this contrast is attributed to the presence of synovial fluid, which is highly transparent and has low scattering properties. Regions either side of this with high S_A up to 1.865mm^{-1} are expected to be due to the bones on either side of the joint cavity, as bone is known to be highly scattering [189]. Lower concentrations of tHb are also observed in the central regions of the transverse and sagittal images, although the contrast between the joint cavity and bone regions is much less significant, with values for the example in Figure 5.5 ranging between 20.0 and 23.7 mMol. The linear relationship between chromophore concentration and absorption coefficient means this region of lower tHb would imply lower absorption coefficients in the centre relative to the surrounding bones, also consistent with findings in previous literature [149, 153]. The epiphysial-metaphyseal (end regions) of the bone and the synovium are highly vascularised, whilst the synovial fluid has an absence of direct blood supply and the

articular cartilage should be avascular to retain its mechanical performance [204], which may explain this observed contrast along the joint. Neither H_2O nor StO_2 images reveal any discernible information regarding the joint structure, with the distribution of these parameters much more homogeneous compared to S_A and tHb.

5.1.4 Finger Translation Experiment

To provide insight into the contributions from the underlying anatomy towards the typical recovered contrast outlined in Section 5.1.3, an experiment was carried out in which the PIP II joint from a single healthy participant (M,28) was translated along the distal-proximal direction. The same joint was imaged at five positions (A-E), as illustrated in Figure 5.6, with the hypothesis that as different sections of the joint were transilluminated, contrast in recovered images would shift accordingly. The translated distances were 3.8, 6.3, 9.5 and 12.0mm for finger positions B,C,D and E respectively relative to position A, measured from the GS images in Figure 5.6.

CCD images of the transilluminated joint displayed in Figure 5.6 clearly reveal a peak in intensity at the joint, the location of which is indicated by the wrinkles in the corresponding GS images. This is in good agreement with previous studies of non-inflamed joints from healthy participants [137, 86], in which this increased transmittance was attributed to aforementioned localised decreases in absorption and scattering properties from the presence of synovial fluid. As the finger position was translated in the distal-proximal direction, this region of high transmission in optical images also shifted correspondingly. For example, at position A when the joint was closer to higher numbered sources, the brightest peak was located at source 11, whilst when the finger had been moved towards the lower numbered sources at position E, source 6 now revealed the brightest peak. Line profiles in Figure 5.7 of summed intensity in the transverse direction demonstrate these relative changes of each source positions and this shift in peak position along the distal-proximal direction as the finger was translated.

Transverse and sagittal images of S_A and tHb reconstructed using DOT at each finger

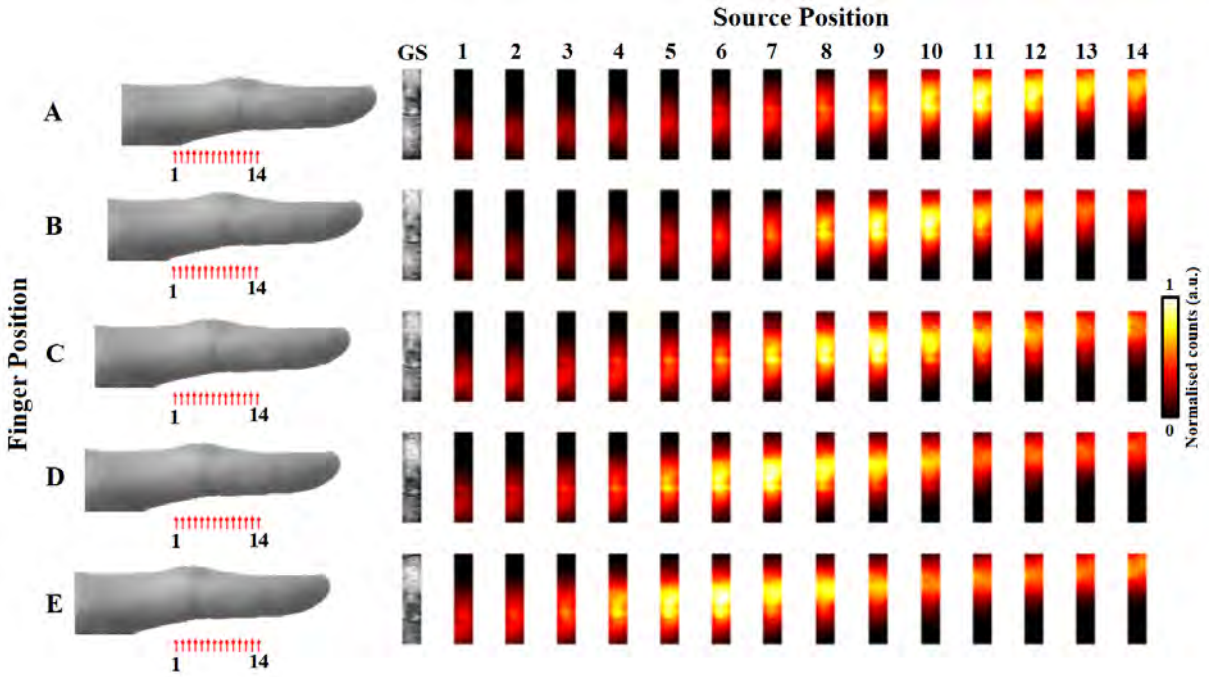

Figure 5.6: Left column contains schematic illustrating the distinct positions of the PIP joint relative to the sources for each measurement. The grid to the right contains transverse, transmission CCD images of the top of the joint, manually cropped to a region of interest above the sources for the central section of the finger. The GS column is greyscale, brightfield images to indicate the joint position, whilst the remaining columns display the optical transillumination images at 930nm for each source position.

position are displayed in Figure 5.8, as these parameters typically displayed more structural information than H_2O or StO_2. A progressive change in the contrast between regions of relatively low tHb and S_A in the joint region and surrounding regions of higher values can be seen as the finger position is moved. At position A, the contrast was greatest on the proximal side, when the proximal bone was being most prominently sampled, whilst the converse was true at position E, with contrast more evident for the distal bone. At the central finger position C, when the sources evenly sampled both ends of the joint, the recovered contrast between joint space and cartilage/bone was the most symmetrical.

These results provide evidence that the observed optical contrast in both raw CCD images and reconstructed DOT maps resulted from the underlying anatomical structure rather than for example artefacts of a systematic error in the instrument such as the angle of incidence of the light source. These findings additionally highlight the importance of a robust protocol for consistent joint positioning before imaging, such as presented in

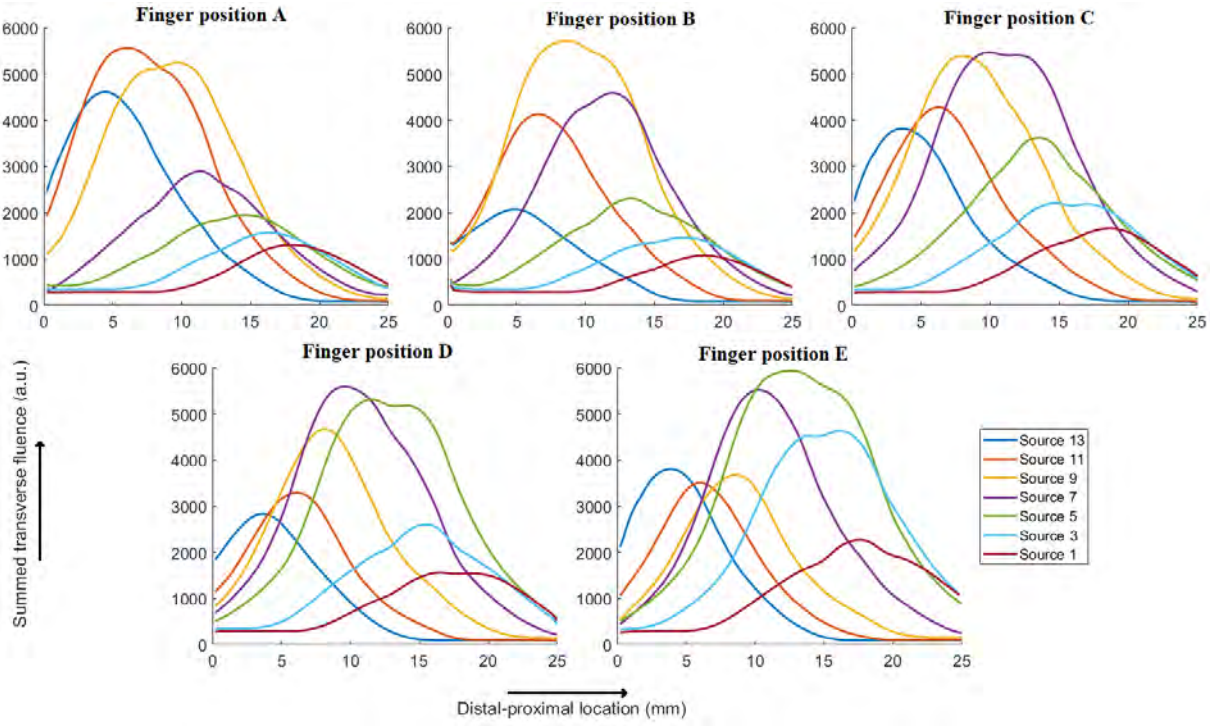

Figure 5.7: Line profiles of summed intensity for the corresponding transillumination images at each source position and finger position in Figure 5.6.

Section 3.4, as unsurprisingly any variation in joint positioning had an impact on the spatial distribution and quantitative values of recovered images.

5.2 Healthy Subject Variability Study

Achieving high sensitivities and specificities when classifying between diseased and healthy joints will rely on a combination of a low variation within each class and a large discrepancy between the two classes. In order to detect pathophysiological changes in inflamed RA joints, a good understanding of baseline values for healthy subjects was first required, to help establish the consistency of recovered parameters and identify those that may prove potentially useful for classification in studies that include patients with arthritis.

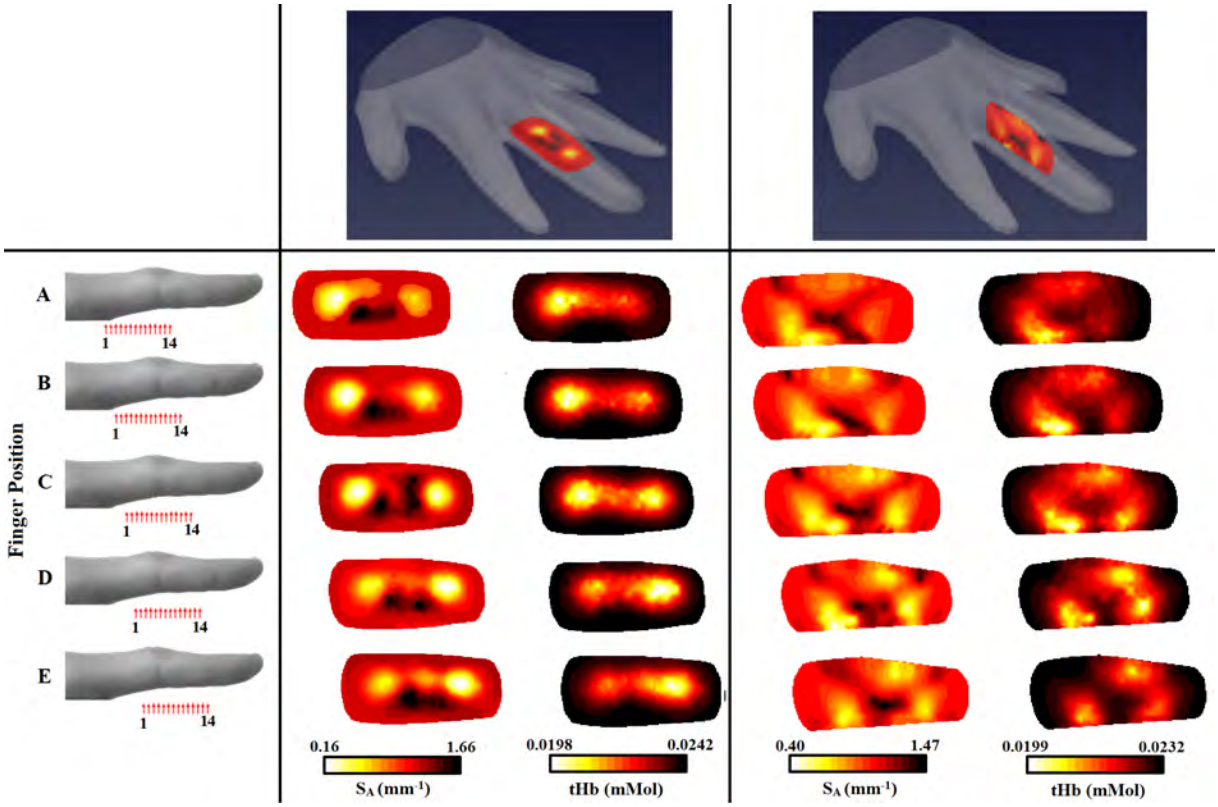

Figure 5.8: Transverse and sagittal slices through of reconstructed S_A and tHb at all 5 finger positions. The positioning of these images has been adjusted such that they would alight to create a single joint, meaning each finger position can be equivalently thought of as a set of 14 sources that are sampling regions translated along the joint.

5.2.1 Study Design

Ten healthy volunteers (4M / 6F; mean age 27.4 ± 5.6; age range 23 - 39) were enrolled over a one month period. Six finger joints for each participant were imaged, which included PIP joints II-IV from each hand, giving sixty joints in total and the variability in recovered haemoglobin, oxygenation, water and NIR scattering were systematically studied. For comparison, an additional participant (M; age 29) was recruited and imaged consecutively three times to assess repeatability of healthy finger data acquired using the system. All healthy volunteers reported no previous history of joint disease and no current joint pain.

5.2.2 Spectral Variation

To illustrate the non-uniformity in spectral response of the raw images across the joint, image data for five of the source positions were assessed with 9mm spacing across a single joint. The spectral response of the mean transmitted intensity within a region of interest of 4 × 4 pixels (2.5 × 2.5mm on the finger surface) in the images, which lies directly above the corresponding source position, is shown in Figure 5.9.

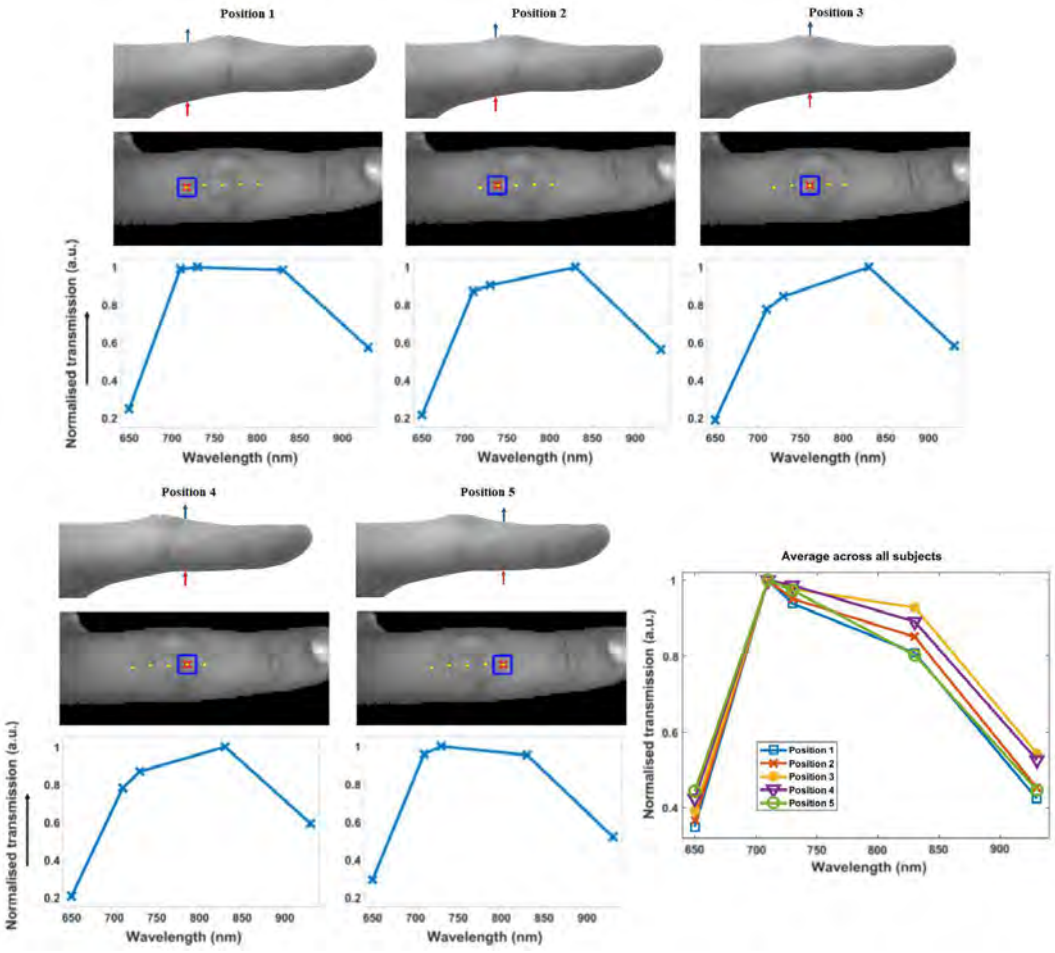

Figure 5.9: Top row shows the transmission detection (blue) and source (red) setup. Middle row shows finger image for the transmission imaging setup, with all source positions shown as yellow dots, and the current source position underneath the finger (red cross) and detector region directly above the finger (blue square). The corresponding normalised spectral response for that source detector pair is shown on the bottom row. Bottom right graph shows normalised spectral response averaged over all fingers in all ten subjects, for each position.

The example spectral response curves shown for one finger in Figure 5.9 demonstrates

evidence of a distinction between position 3, predominantly expected to sample the joint cavity, compared to positions 1 and 5, where the transmitted volume will mainly contain bone and soft tissues. Compared to positions 1 and 5, the spectra at position 3 shows comparatively greater relative transmission at higher wavelengths 830nm and 930nm compared to the lower wavelengths 650nm, 710nm and 730nm. This pattern is again evident when comparing similar regions averaged over all fingers in all subjects, with greater relative transmission at the higher wavelengths for positions 3 and 4, as shown in Figure 5.9. This illustrates the additional information obtained from collection of data at multiple wavelengths, which can be used to distinguish the pathophysiological differences between the joint cavity and the surrounding bones.

5.2.3 Feature Extraction

For quantitative assessment of the metabolic images, the basic statistical features (mean, variance, maximum and minimum) were calculated for nodes within a volume of interest (VOI), as shown in Figure 5.10. The VOI was defined to only include nodes lying directly below the detector grid, as low sensitivity outside this volume means optical properties were not updated. Additionally, the VOI ignored 50% of nodes closest to the boundary, as it is known that hypersensitivity close to the sources and detectors, as illustrated in Section 2.4, can amplify errors in this region [128].

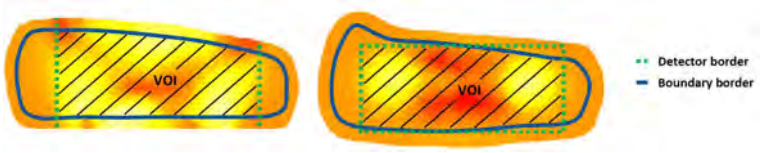

Figure 5.10: VOI only included nodes lying directly below the detector grid and ignoring 50% of nodes closest to the boundary. Examples of the cut off border lines shown for both a sagittal slice (left) and a transverse slice (right) on an S_A image.

5.2.4 Statistical Analysis

The Kruskal-Wallis (KW) test was used to determine if any statistically significant differences were seen between groups, with a null hypothesis that the medians of all groups were equal. The KW test is non-parametric and establishes confidence levels based on analysis of data rank, instead of the actual data values such as used in analysis of variance (ANOVA) tests, meaning it does not rely on any assumptions about the underlying distribution of the data. Groups chosen for comparison were: "different subjects" with each group containing all fingers for each of the individual participants A-J, "different fingers" with each group containing all participants A-J for a particular finger index, and finally "different repeats" with each group containing all fingers for every repeat data set for participant K. The steps for the KW test, given for example in the context of tHb for "different subjects", were as follows [205]:

1. Rank the data such that all data values for tHb are ordered from smallest to largest, irrelevant of the group, such that the smallest data point will have a rank 1 and the largest data point will have a rank N.

2. Calculate the test statistic, H, using

$$H = \frac{12}{N(N+1)} \sum_{i=1}^{T} \frac{(\bar{M}_i)^2}{n_i} - 3(N+1), \tag{5.1}$$

where N is the total number of measurements, T is the total number of groups eg. the number of subjects being compared, $\bar{M}_i$ is the sum of the ranks of all measurements in a group i, eg. from all 6 joints of interest from a single subject, and n_i is the total number of entries in each group, in this case 6.

3. The p-value can be found from the corresponding value equal to H in a χ^2 distribution look-up table with T - 1 degrees of freedom, from which the look-up entry is determined by both T and the respective n_i of each group.

4. If H is greater than the critical χ^2 value then the null hypothesis is rejected. In all comparisons, differences between groups were taken as significant if p was less than 0.05.

5.2.5 Healthy Subject Variability

For visualisation of all imaged joints in Figures 5.11 to 5.14, slices were taken along the central transverse plane of the joint, as illustrated in Figure 5.5. A delineation of the joint cavity from the surrounding bone is consistently visible for all fingers, with a central region of lower S_A and tHb compared to either side. This contrast is consistently most pronounced in S_A images, with an S_A of around $2mm^{-1}$ in the region expected to reflect bone, whilst some very low scattering is measured in the joint cavity, approaching $0.01mm^{-1}$. All reconstructed images of StO_2 and H_2O shown in Figures 5.11 and 5.14 do not demonstrate the same evidence of joint structure as in tHb and S_A. Some fingers are showing a recovered oxygenation lower than the initial estimate, as low as 62%, whilst other fingers give a recovered oxygen saturation of up to 82%. This variation may be the result of a natural variability in the oxygenation between participants or it may be a result of amplification of measurement error due to StO_2 being computed from the division of HbO by tHb. Qualitatively, PIP joint images for participants A-J in Figures 5.11 to 5.14 appear more similar between fingers from the same participant compared to images from different participants. For example, contrast in all reconstructed parameters appears consistently lower for participants F and I compared to the other participants.

The three repeat measurements of participant K are also shown in Figures 5.11 to 5.14. These appear qualitatively more similar than when compared to other participant finger sets, however some variation between repeats is evident, particularly for StO_2 images of 2nd and 4th PIP joints of the left hand, ranging between around 65% to 75%, again indicating that this parameter is particularly sensitive to measurement errors. To illustrate the variance in these image features for healthy subject data, box plots overlaid with beeswarm plots of tHb are displayed in Figure 5.15.

The variance in image feature values across fingers within individual participants A-J, shown in Figure 5.15(a), is generally smaller than the variance across participants for a given finger index, shown in Figure 5.15(b), indicated by the narrower interquartile ranges and total ranges seen. Additionally, the median values of each finger index for the ten

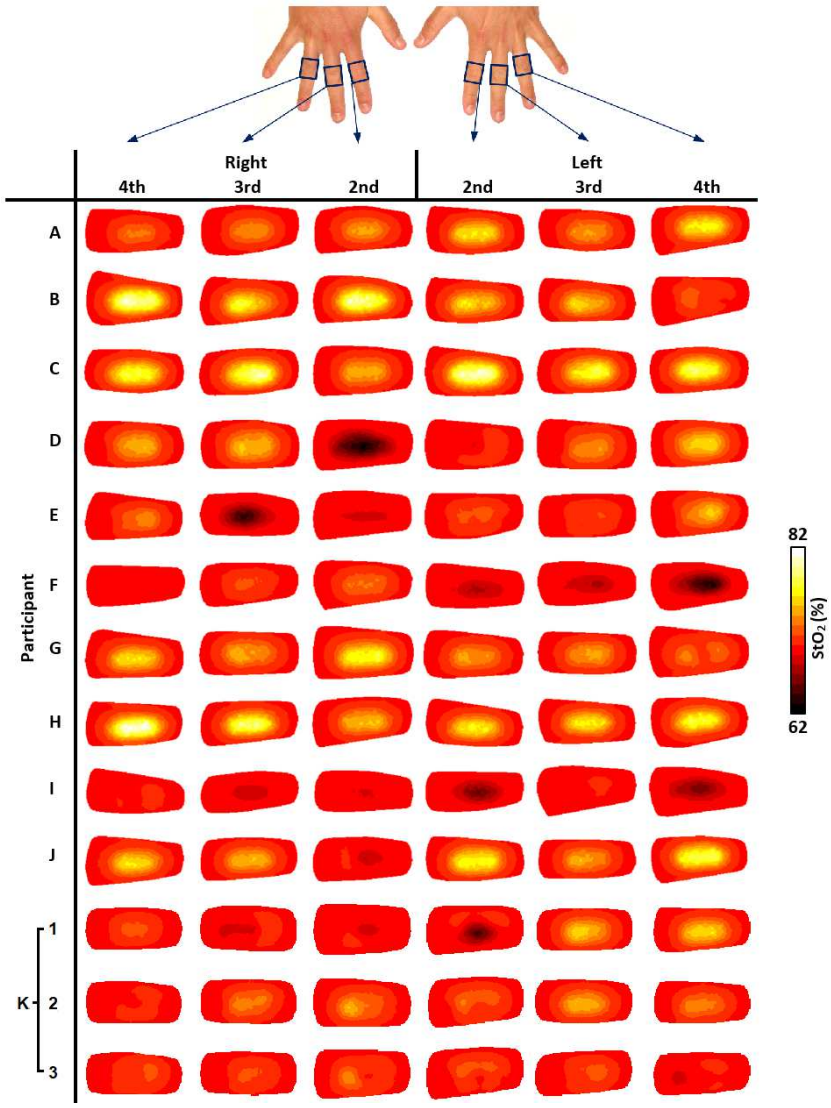

Figure 5.11: Transverse slices half way through the finger of StO_2 (%), for all imaged joints.

participants in Figure 5.15(b) are more similar than the median values of each participant for all six fingers in Figure 5.15.(a). Boxplots of the three repeats for participant K show similar median values and variance to one another, for all image features. Due to space considerations, boxplots for S_A, H_2O and StO_2 have not been shown, however these also display similar trends in distributions to those discussed for tHb.

The resulting p-values for all KW tests are displayed in Table 5.1. The null hypothesis that the median values between different subjects were equal was rejected for all features except minimum S_A, with the majority of p-values much less than 0.05, meaning a

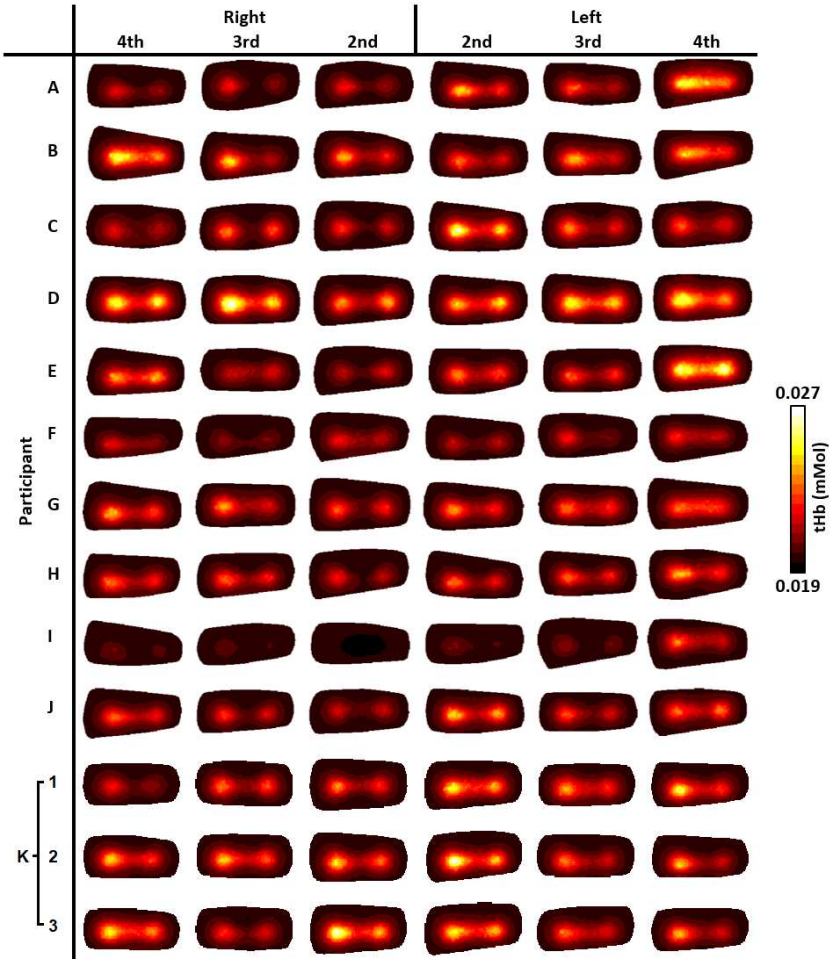

Figure 5.12: Transverse slices half way through the finger of tHb (mMol), for all imaged healthy joints.

	Different subjects				**Different fingers**				**Different repeats**			
	Mean	Var	Max	Min	Mean	Var	Max	Min	Mean	Var	Max	Min
StO_2	0.000014*	0.00049*	0.000011*	0.000030*	0.87	0.73	0.80	0.79	0.23	0.49	0.57	0.46
tHb	0.000073*	0.000094*	0.000080*	0.0011*	0.062	0.11	0.17	0.01*	0.71	0.64	0.65	0.65
S_A	0.000028*	0.00017*	0.00014*	0.063	0.17	0.43	0.32	0.94	0.53	0.65	0.52	0.33
H_2O	0.000063*	0.000061*	0.000023*	0.0000057*	0.20	0.16	0.31	0.92	0.88	0.99	0.93	0.98

Table 5.1: p-values for the KW test assessing variance between different subjects, different fingers and different repeats, displayed for all four image features; mean, variance, maximum and minimum, and all four metabolic parameters. Significant values are marked *. The test indicated a significant difference in the median value when comparing different subjects in a majority of cases, whilst in the case of comparing the joint indices of different fingers or comparing different repeats of the same joint index, there was no significant difference in the median value for a majority of the features.

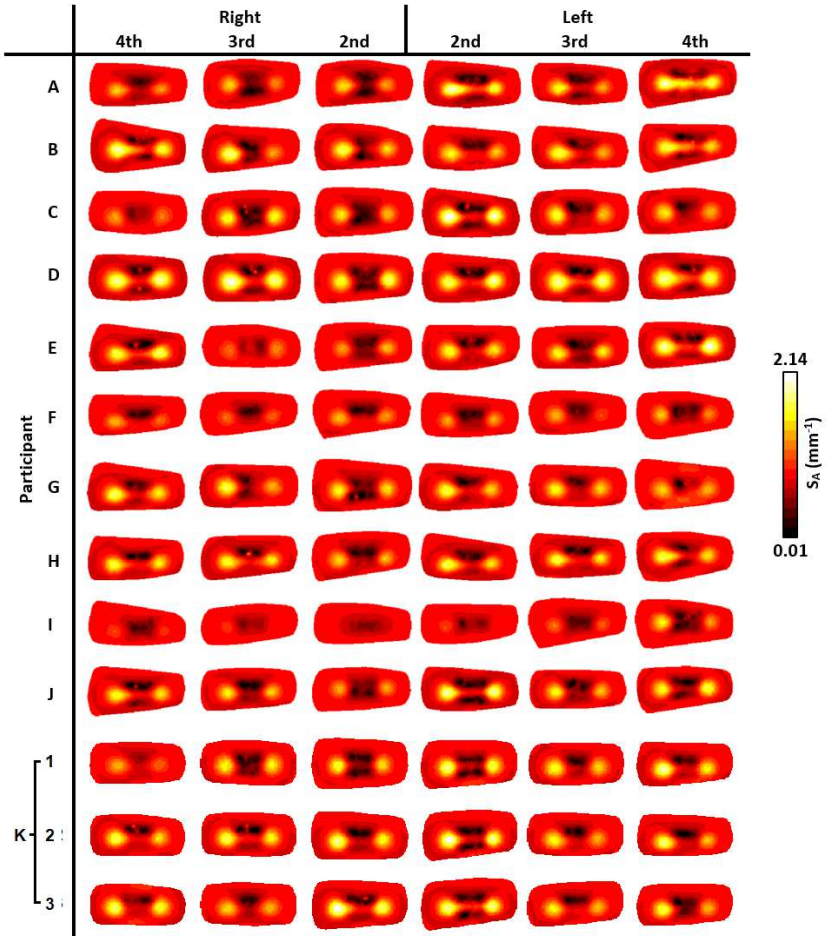

Figure 5.13: Transverse slices half way through the finger of S_A (mm^{-1}), for all imaged healthy joints.

statistical difference was seen between different participants in recovered pathophysiological parameters in these cases. In contrast, the null hypothesis that the median values were between different subjects was accepted for all features for variability between fingers, with the exception of minimum tHb. These two results will be due to a combination of: low variation between joints of the same participant, and high variation between joints of different participants. The null hypothesis is also accepted for all features when comparing the three repeat measurements of participant K, demonstrating that the system is capable of recovering similar pathophysiological values from a subject over multiple imaging sessions. The current methodology appears to be able to discriminate between healthy participants, with variation between subjects more significant than variation between fingers or between repeat measurements, hence demonstrating that the system is

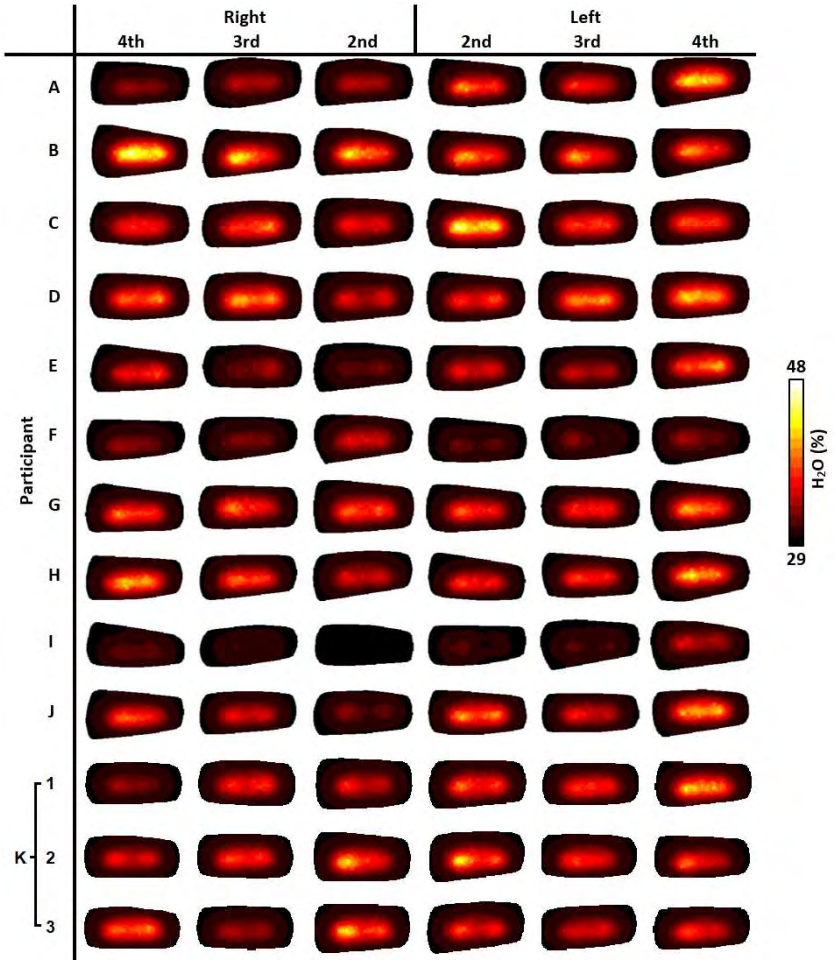

Figure 5.14: Transverse slices half way through the finger of H_2O (%), for all imaged healthy joints.

capable of consistently recovering similar values within joints of the same participant.

In healthy subjects, variation between different finger indices was statistically less variable than the variation between participants. This indicates that the outlined system and data recovery algorithm is more consistently capable of recovering useful parameters from different joints of the same participant than across joints from different participants. This is perhaps not surprising if metabolic parameters are expected to be more consistent within the hands of one person experiencing the same physiological conditions. It also must be acknowledged that absolute values recovered in optical imaging are often influenced by other factors, for example the structure of the finger joint may introduce quantitative discrepancies, an effect which would be less significant between fingers from the same person with similar sizes and underlying anatomy. High levels of inter-subject variation

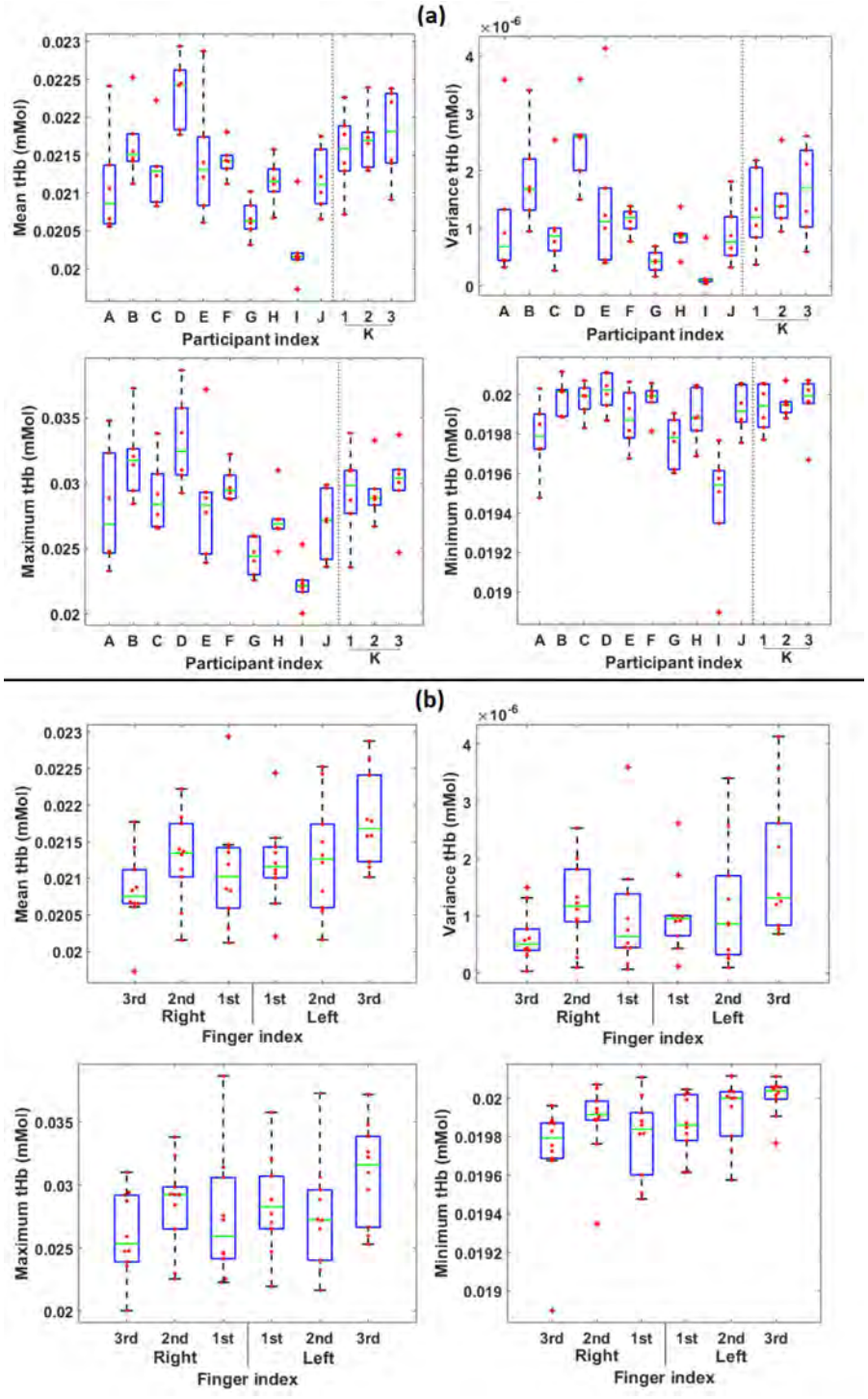

Figure 5.15: Box plots of tHb with (a) each group containing values for all six fingers from the same participant, for participants A - J and three repeats of participant K and (b) each group containing values from participants A - J for the same finger index. All four image features are plotted, displaying the median (green line), interquartile range (blue box), range (black) and outliers (red cross), overlaid with a beeswarm plot of all data points (red dot).

are widely acknowledged in recovery of absolute parameters using optical imaging. For example, this was reported for tHb when recovering absolute values with DOT studies of the breast [206, 207]. As the severity of inflammation is typically not uniform across all joints in the hands of an RA patient, with certain joints more severely afflicted than others [34] (although a degree of symmetry is commonly seen), the level of variability across fingers of the same subject should increase in patients with joint inflammation compared to healthy subjects.

5.2.6 Longitudinal Variation in Healthy Joints

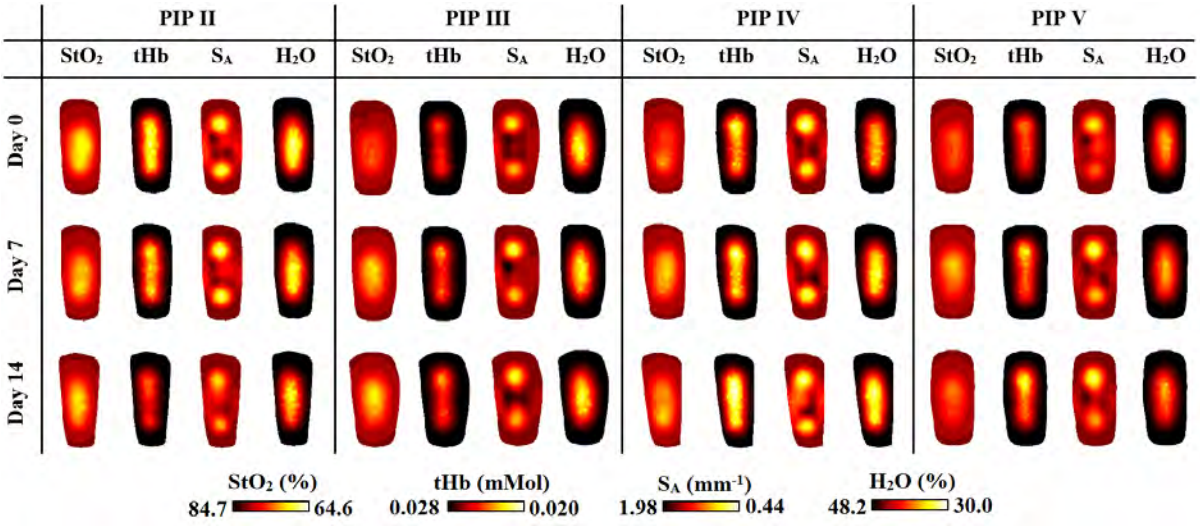

Figure 5.16: Transverse slices half way through the finger of PIP joints II - V for the same healthy volunteer at three time points, for all four clinical parameters.

The system was shown to be reproducible and stable over one month in Section 4.4.2 during phantom studies. Prior to longitudinal monitoring of patients, it was useful to ascertain the degree of typical variation occurring in healthy, non-inflamed joints over time. A single healthy volunteer (M, 31) was recruited for weekly imaging of the right PIP joints II-V over 3 weeks, with no joint pain or swelling reported over this time period by the subject.

Transverse slices of DOT images in Figure 5.16 indicate relatively consistent structures in each parameter at all time points, with the exception of tHb and S_A for PIP II at

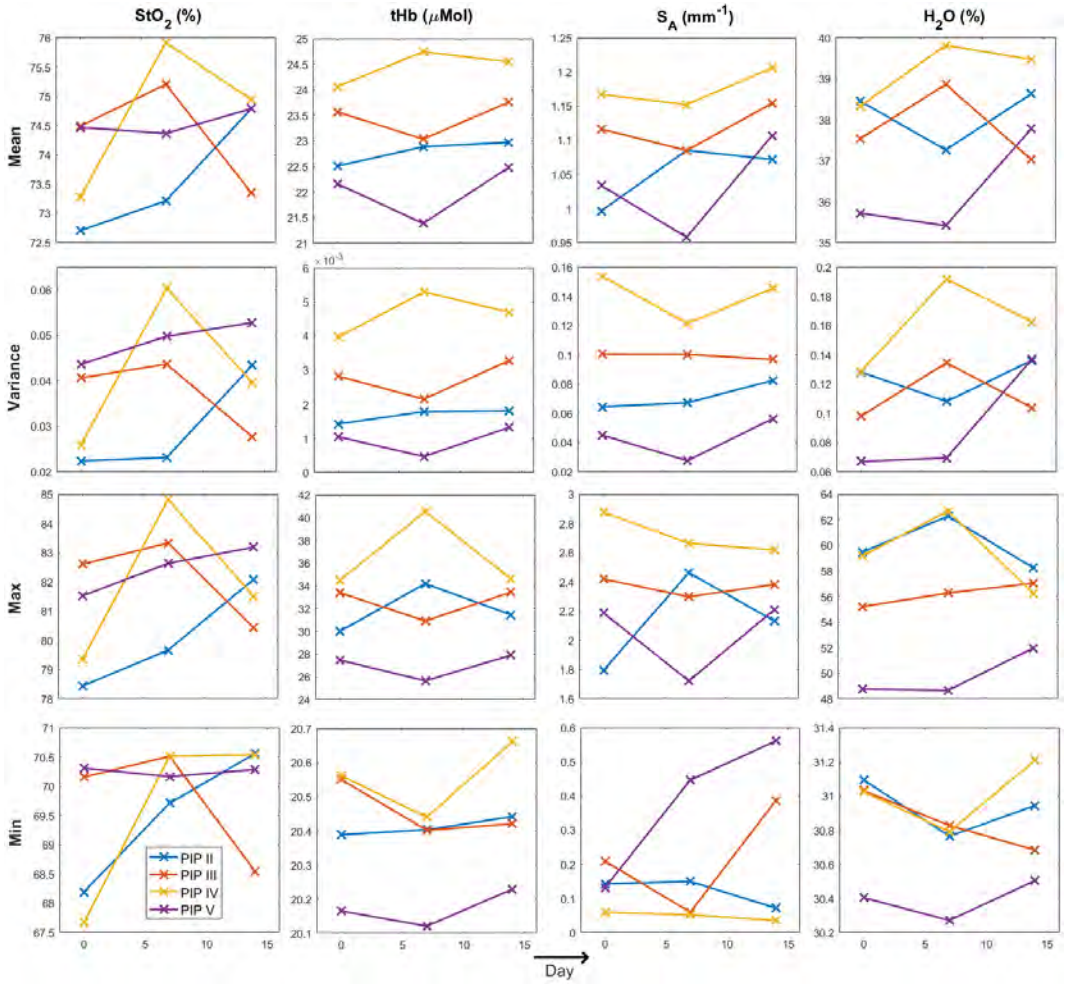

Figure 5.17: Recovered statistical parameters in each PIP joint II - V for the same healthy subject, demonstrating changes between Days 0, 7 and 14 in all four clinical parameters.

Day 14, which appear to have both decreased in these slices, and increases in recovered StO_2 for both PIPs II and IV after Day 0. The mean and variance of both tHb and S_A were the statistical parameters from the VOI in Figure 5.17 that were most quantitatively stable across joints, with StO_2 and H_2O suffering from greater overlap and the changes in maximum or minimum values potentially impacted by outliers in recovered images. Although it was not possible to deduce whether these changes observed were due to natural variability in the physiology over time or a consequence of other subtle systematic fluctuations, such as ambient temperature or joint positioning, these studies indicate that, relatively speaking, the recovered *in vivo* parameters were reasonably consistent in absolute terms over time for this single volunteer. Further investigations monitoring a larger sample

of healthy volunteers are required, to allow tolerances for atypical variance in parameters can be established to identify potential inflammatory-led changes in the joint.

5.3 Dynamic Cuff Studies

Previous studies have demonstrated the benefit of inducing a haemodynamic response in the joint by using a Sphygmomanometer to restrict blood flow on optical data recovered from finger joints, as discussed in Section 2.5.5. This dynamic method elicits new information directly related to the vascularity in RA [158], whereas static data, such as that presented so far, is more indicative of pathological changes. To assess the changes in 3D pathophysiological images of healthy finger joints measured using multispectral DOT when a haemodynamic response of this nature is induced, two volunteers (1M / 1F), ages 23 & 30, with no known history of joint disease were enrolled, each completing written informed consent. For each participant, the right and left III PIP joint was imaged and a haemodynamic change was induced using a DS400 Aneroid Sphygmomanometer (Hokanson, Washington, USA) connected to a 13 $\times$ 85 cm SC12 cuff attached to the upper arm. The experimental procedure used for collection of data for each finger joint is outlined as follows; initially the surface profile of the hand was captured using two surface imaging units, next a three-stage protocol was carried out, throughout which full multispectral data sets were repeatedly acquired consisting of: 63s rest, 84s venous occlusion at a pressure PV = (Psystolic+Pdiastolic)/2 = 100mmHg, and finally cuff release followed by 168s recovery, giving a total imaging time of $\approx$5mins per joint. This resulted in full multispectral optical datasets of the joint at 15 separate time points corresponding to a single SI dataset.

To minimize acquisition time, the transmission imaging arrangement for these experiments consisted of 5 source positions under the finger and 43 virtual detectors on the top side, with the galvanometer based illumination setup allowing rapid sequential switching between these source positions, thus enabling a full tomographic image to be acquired every 21 seconds.

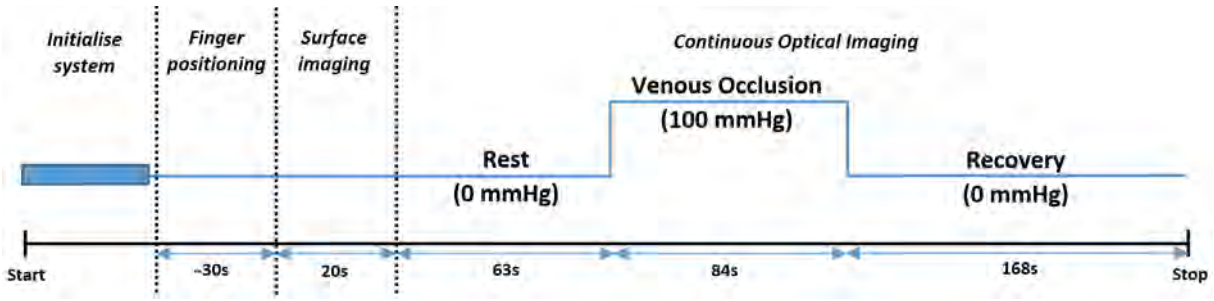

Figure 5.18: Transverse slices half way through the finger of StO_2 (%), for all imaged joints.

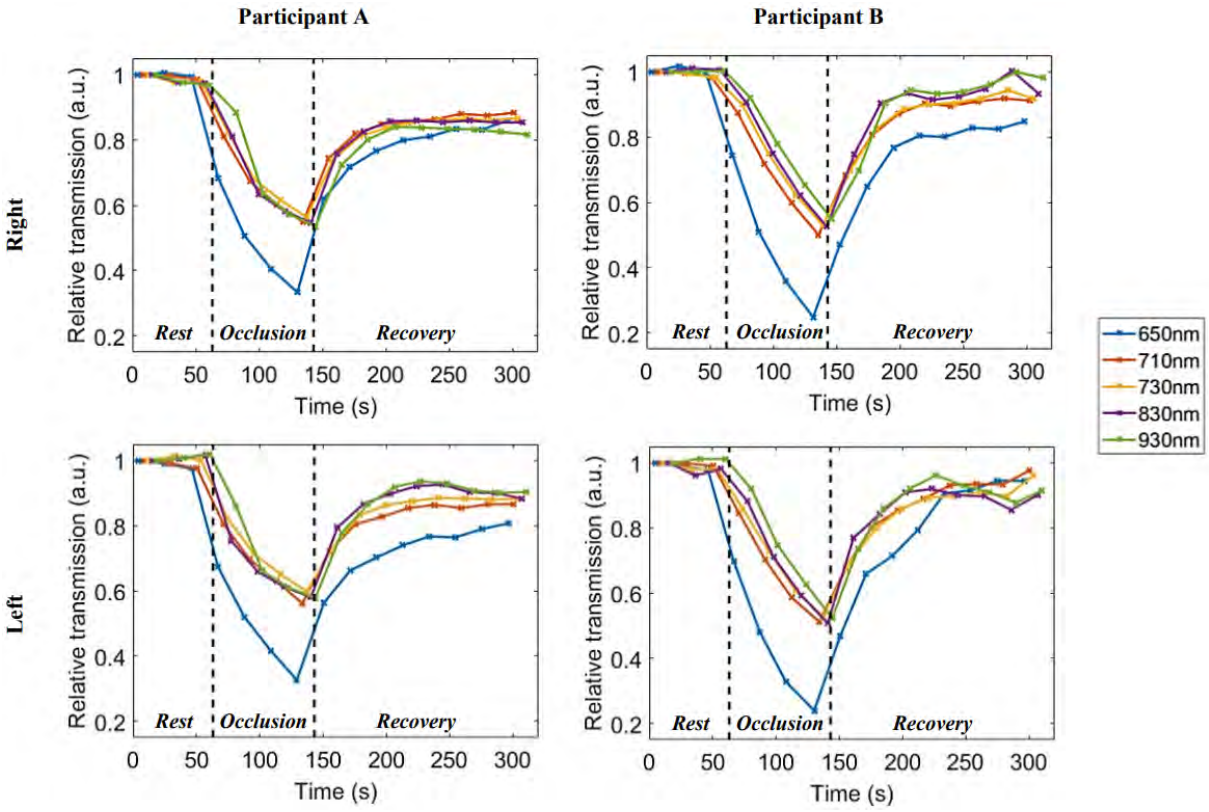

Figure 5.19: Temporal changes in joint transmission for the central source and all detectors, normalized by the first measurement.

For all imaged finger joints at all wavelengths, a rapid drop in total transmission for the central source and all detectors was observed upon inflation of the cuff, displayed in Figure 5.19. Following the release of the cuff pressure, the total optical transmission increases, typically returning to a slightly lower value during recovery than initial baseline at rest. This may be a result of the large level of blood pooling occurring during venous occlusion and would be expected to return to baseline values given a longer total monitoring time. These temporal changes were not uniform across wavelengths, with 650nm transmission

consistently dropping more significantly during occlusion than other measured wavelengths.

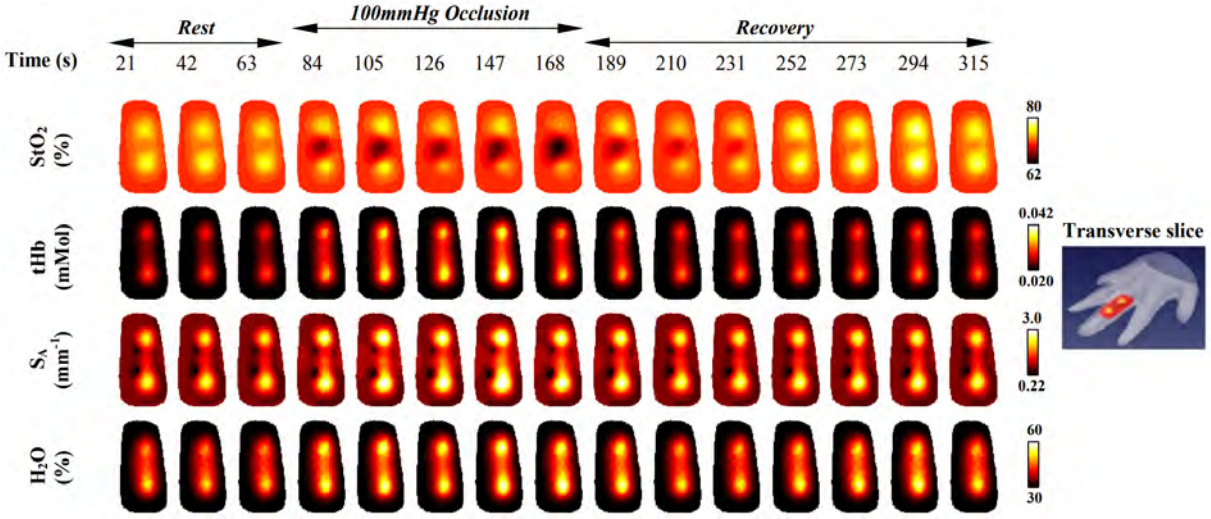

Figure 5.20: Schematic of experimental stages during dynamic cuff occlusion studies.

Example transverse slices of reconstructed 3D joint images for one participant are shown in Figure 5.20 for all time points and all four metabolic parameters. Inflation of the cuff leads to an increase in both tHb and S_A. This reflects pooling of blood, which typically consists of ≈45% haemoglobin [208], as a result of the restriction of venous return, and the associated increase in density of scatter particles, which according to Mie theory will increase S_A. For example, a 17% increase in reduced scattering coefficients at 790nm and 850nm was reported for brain measurements when undergoing a Valsalva manoeuvre, during which blood pooling also occurs [209]. StO_2 sees a marked decrease, particularly at the image centre corresponding to the joint cavity, a change which would be expected from prolonged cuff pressure as the ratio of arterial to venous blood decreases.

To quantitatively assess the observed changes, mean values of all recovered parameters lying within a VOI defined in Section 5.2.3 were calculated for each time point and all metabolic parameters, shown in Figure 5.21. The greatest changes during occlusion were seen in S_A and tHb, with percentage increases of 25% and 13% respectively from time point 1 (initial rest) to 7 (final occlusion) averaged over all fingers, whilst StO_2 consistently decreases for all fingers with an average percentage drop of 4% between these time points. Changes in H_2O were not as consistent as other parameters.

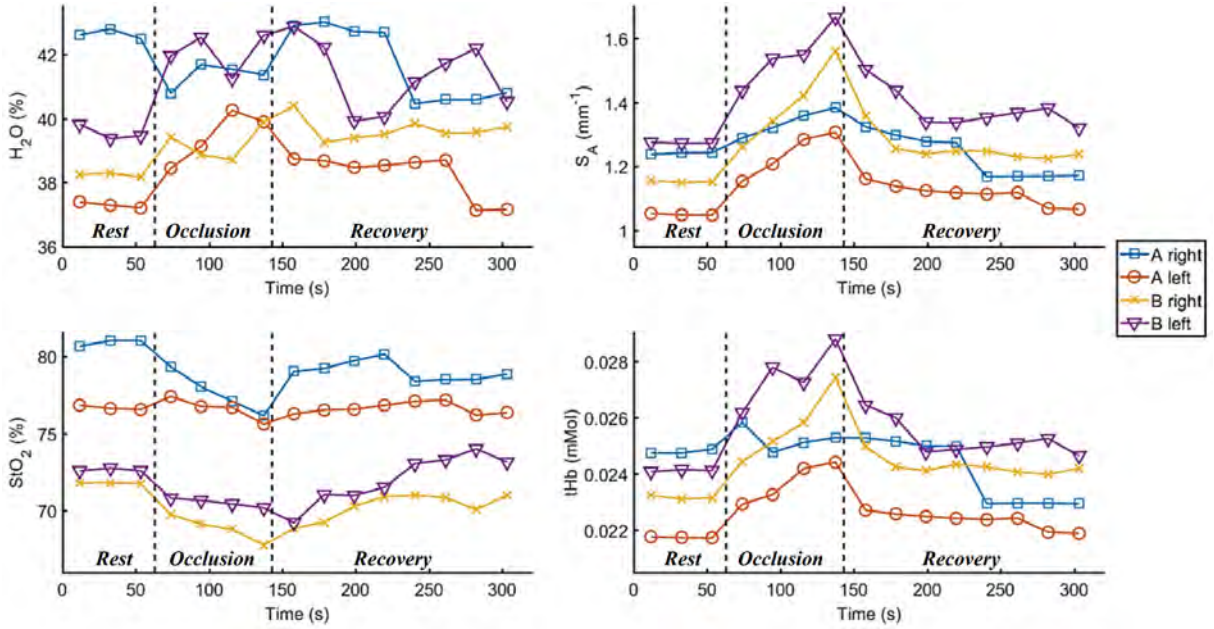

Figure 5.21: Changes in mean tHb, StO_2, S_A and H_2O within a defined volume of interest of the right and left III PIP joints for both participants A and B.

5.4 Traumatic Injury To Healthy Joint

The inflammatory cascades occurring in the joints of patients with rheumatic conditions, as described in Section 1.1.2, are extremely similar to localised inflammation and swelling due to traumatic mechanical injury of the joint. For example, patients who have underlying systemic conditions that present with musculoskeletal complaints can have symptoms that initially mimic those of sporting injuries [210]. As a preliminary study prior to transferring the system to the hospital, the opportunity arose to recruit a single healthy participant who had recently experienced a cricket-related finger injury to investigate the systems ability detect any contrast in the recovered pathophysiological parameters resulting from the underlying inflammation in this injured joint. At the initial imaging session (day 0), the subject reported pain and swelling in the right PIP IV as a result of the injury, whilst all remaining joints were uninjured and asymptomatic. The subject underwent the same imaging protocol following 9 weeks of recovery (day 63), at which point the subject reported that any symptoms in the right PIP IV had subsided and were no longer present. All recovered joint images were assessed using the feature extraction methodology and

basic statistical parameters outlined in Section 5.2.3.

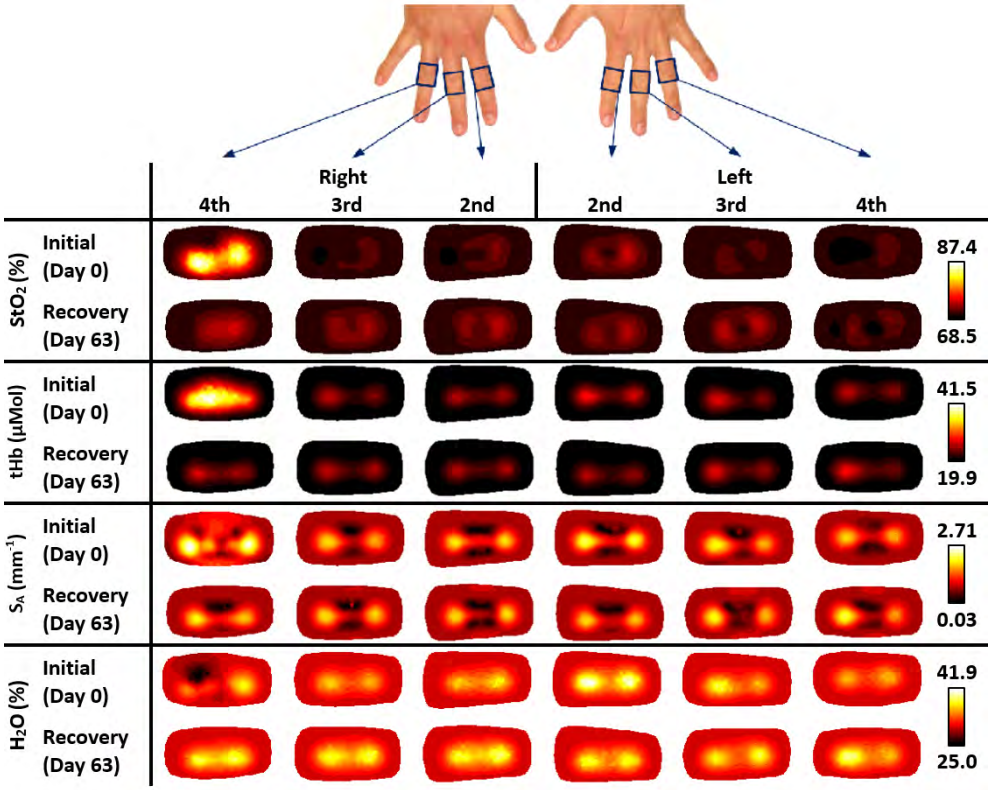

Figure 5.22: Images for a single healthy participant with a sports injury to right 4th PIP. Transverse slices half way through the finger for all four recovered parameters, at both at day 0 and the same joints after 63 days recovery.

For all four metabolic parameters, a clear qualitative distinction is visible in Figure 5.22 between the injured right IV PIP and all remaining non-injured joints at Day 0, which appear similar. Following 63 days recovery, this injured joint were restored to the subsequent changes following recovery.

The greatest quantitative changes in mean values from the VOI were elevated S_A and tHb displayed as boxplots in Figure 5.23, expected to result from an increased localised blood volume and leukocyte concentration in the injured joint as a result of vasodilation associated with inflammation. Localised changes in mean StO_2 and H_2O were smaller and more data would be desirable to confirm these distinctions. There was also a significantly greater variance in all four parameters as a result of the greater distinction between localised changes in the joint and background values not updated during reconstruction. Encouragingly in the uninjured joints, mean and variance values of all four recovered

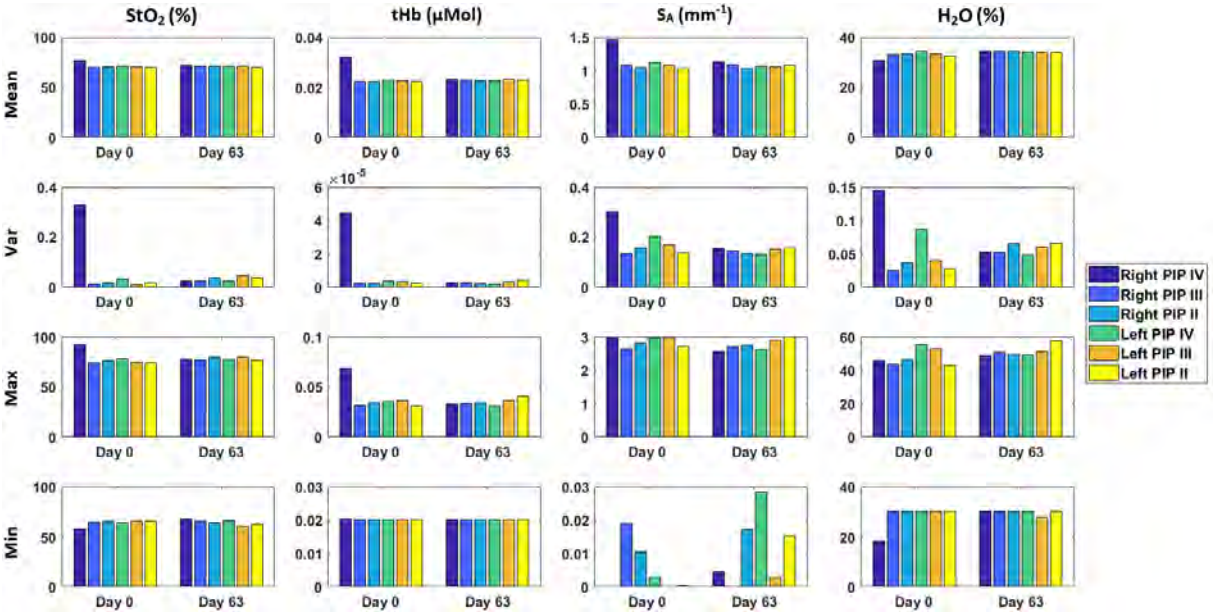

Figure 5.23: Boxplots for all four basic statistical parameters within the VOI for either tHb, S_A, StO_2 or H_2O, comparing values for all six joints (labelled by colour) of a single healthy participant. At day 0, at which point a traumatic injury had been sustained to the right PIP IV with the remaining joints unaffected, a significant distinction in values is seen between this injured joint and the other five joints in a number of features, such as for example drastically elevated variance in both StO_2 and tHb. The same joints following 63 days of recovery are displayed, with values for the right PIP IV reverting to be similar to the remaining joints for a number of parameters.

parameters were reasonably consistent, both between each other at each time point or when comparing the same joint at two time points. Following 63 days recovery, at which point the injured joint was now asymptomatic, all measures in the right IV PIP were quantitatively restored to be similar to the remaining non-injured joints. The maximum and minimum values were more variable and not as useful at discriminating the injured joint, in a number of cases reaching their upper or lower limits, for example 3mm^{-1} for S_A or 0.02 for tHb.

Although this preliminary study provided evidence that the system was sensitive to underlying pathophysiological changes as a result of inflammation, the ground truth for this data was limited to self-reported symptoms by the participant, making it not possible to compare the severity of inflammation during this acute traumatic injury and those typically experienced in inflamed joints of RA patients.

5.5 Conclusion

In this chapter, a series of investigations in which human hand joints of healthy participants were imaged have been presented, with the aim of assessing the *in vivo* performance of the multispectral CW DOT system and to establish an understanding of baseline values in healthy subjects prior clinical studies. Results from a healthy cohort demonstrated the capability to recover pathophysiological parameters which consistently delineate the joint cavity from surrounding bone for 66 PIP joints, including 3 repetitions of 6 joints. Recovered images demonstrated a consistent distribution, with central regions of lower S_A and tHb. This contrast is qualitatively in good agreement with optical measurements reported previously in the literature, with regions of lower values expected to reflect the joint cavity compared to relatively greater values either side, anticipated to correspond to bone. This was supported by images during translation of the finger in the distal-proximal direction. Images of parameters StO_2 and H_2O were not able to distinguish the joint structure with the same clarity, however quantitatively these parameters are both consistent at around 72% and 33% and may still prove useful for classification if a large difference is seen in images of arthritis patients, such as significant hypoxic conditions [23] or bone marrow oedema [60]. Reconstructed values across the cohort demonstrated good consistency between finger joints from the same participant, with greater variation seen between subjects. Furthermore, statistical analysis indicates that the system is more consistent between different finger joints within the same subject, than for the same finger joints from different subjects. Evaluation of the significance of the variability observed in this healthy subject study for diagnosing RA, either between different subjects, different fingers or repeats, requires a knowledge of the typical ranges of values for patients with RA. Several potential sources could contribute to intersubject variability when imaging of human joints included: (1) during the data-model mismatch calibration it was assumed that the boundary conditions and therefore the source coupling was the equivalent for the phantom and the finger surface, however factors such as skin colour have been shown to significantly impact on SNR [211] (2) in optical transmission images, wrinkles on the surface

of the finger appeared as low frequency spatial noise, the degree of which typically varied depending on the subjects age and (3) variability in joint physiology between subjects will have existed that inherently would have changed their baseline optical properties. In future work, extending these healthy studies to a larger cohort, in which volunteer enrolment is controlled for age and sex matching with arthritis patient demographics, would be beneficial in order to minimise any volunteer bias and provide a control group dataset more comparable with patient studies.

Studies of haemodynamic changes during cuff occlusion supported evidence that the parameters recovered using the system were sensitive to underlying pathophysiological changes, with increases in tHb and S_A, and decreases in StO_2 observed during venous occlusion, consistent with the expected blood pooling. The observed distinctions in one healthy subject between a joint which had experienced traumatic injury and their remaining uninjured joints provided strong motivation to proceed to clinical trials involving patients with inflammatory arthritis for further assessment of the systems performance, which will be presented in the proceeding chapter.

CHAPTER 6

ARTHRITIS PATIENT STUDIES

Controlled clinical trials are a crucial requirement for successful translation of a medical device from bench-top to clinic, involving either *in vitro* biological samples or *in vivo* volunteers from a cohort of patients with known disease. These studies also facilitate the assessment of the performance of a biophotonic device within the context of its specific design purpose, in this case detection of joint inflammation in patients with RA. In the preceding chapters, a multi-spectral, non-contact DOI system was presented and its performance systematically characterised, through both phantom and *in vivo* healthy subject studies. The focus of this chapter is on presenting results of a five month clinical trial, in which symptomatic patients presenting at a Rheumatology outpatient clinic were imaged using the system. Details covered are the study design, analysis of both reconstructed tomographic images using DOT and raw optical transmission images, and monitoring longitudinal changes in a subset of patients. This clinical study served a number of purposes including (1) to identify any image features capable of discriminating between inflamed and non-inflamed joints, (2) to establish if these pathophysiological differences could be used to identify patients with underlying disease and (3) to carry out comparative analysis of detection rates with similar, previously reported optical technologies. Ethical approval for this clinical study was granted by the West Midlands Black Country Research Ethics Committee as part of the Birmingham early arthritis cohort (BEACON) observational cohort study (REC reference 12/WM/0258), with all

subjects providing written informed consent prior to participating.

6.1 Study Design

Between March and August 2018, a controlled pilot study was carried out, in which twenty-one adult patients (age > 18) were recruited through the NIHR CRF Early Arthritis Clinic in University Hospitals Birmingham NHS Foundation, Birmingham. Inclusion criteria for the study were treatment-naïve new onset of (1) at least one inflammatory joint symptom, from either joint pain, swelling or morning stiffness and/or (2) at least one joint displaying evidence of clinically apparent synovitis. For this study, patients within this cohort were classified into one of two groups according to their baseline diagnosis as shown in Table 6.1, which were either diag-RA, which included patients diagnosed with RA according to the ACR/EULAR 2010 criteria, or non-RA, which included all remaining diagnoses which did not currently fulfil these criteria. Baseline diagnosis within the non-RA group consisted of a range of inflammatory conditions including; unclassified arthritis (UA), inflammatory arthralgia (IA), parvovirus arthritis (PV) or palindromic arthritis (PA). Although patients within the non-RA group did not fulfil the diagnostic criteria for RA upon presentation, the disease in some of these patients may progress into established RA at a later stage and in some cases was associated with the presence of autoantibodies. Patients were imaged with the multispectral, non-contact DOI system using the same protocols as outlined in Chapter 3, which was highly tolerated with no adverse effects reported. Imaged joints included the II, III, IV and for some later participants the V PIP joints, on each hand. The left hand of two participants could not be imaged, due to the presence of Dupuytren's contracture, where nodules in the ligaments on the palmar side can prevent flattening of the hand, or the inability to remove jewellery due to swelling which would interfere with optical signal, giving 144 finger joints in total.

Diagnostic Group	**diag-RA**	**non-RA**
Number, n	12	9
Baseline diagnosis, n (%)		
Rheumatoid arthritis	12 (100)	(0)
Unclassified arthritis	0 (0)	4 (44)
Inflammatory arthralgia	0 (0)	2 (22)
Palindromic arthritis	0 (0)	1 (11)
Parvovirus arthritis	0 (0)	2 (22)
Age, *mean* ± *S.D.*, years	52.6 ± 18.9	49.1 ± 18.3
Female, n (%)	8 (66)	6 (66)
RF positivity, n (%)	9 (75)	5 (56)
CCP positivity, n (%)	9 (75)	3 (33)
Global US score, *mean* ± *S.D.*		
SH	3.3 (4.8)	0.89 (1.4)
PD	1.9 (3.1)	0.78 (1.4)
Global CE score, *mean* ± *S.D.*		
CTE	1.7 (2.6)	0.89 (2.0)
CSW	1.3 (2.4)	0.11 (0.33)

Table 6.1: Patient demographics and global clinical scores summed across II-V PIP joints from both hands. Percentages in brackets are relevant to each group.

6.1.1 Ultrasonography and Clinical Examination

All patients underwent both US scans and CE. Ultrasonography was carried out using an US scanner (LOGIQ-E9; GE healthcare, Cardiff, UK) equipped with a 6-15MHz linear array transducer and musculoskeletal presets using high frequencies of >13MHz in order to provide the best axial resolution for superficial structures. The relevant PIP joints were scanned from the dorsal aspect. Three features of interest in US images relevant for the assessment of joint involvement in RA were considered: synovial hypertrophy (SH) which is visible thickening of the synovial membrane seen as hypoechoic tissue in greyscale images, effusion (EF) which is accumulation of fluid observed in greyscale images as a black anechoic region and finally hyperaemia (PD) is abnormal blood flow visible during power Doppler mode compared to background levels in synovial blood vessels, as summarised in Table 6.2. These clinical features were scored using a four-grade semi-quantitative scoring system on a scale of 0 (None), 1 (Mild), 2 (Moderate) and 3 (Severe). This was carried out by a single experienced examiner in accordance with the EULAR-OMERACT consensus

definition [212, 213]. Examples of these US features, either all graded at 0 or graded at 3 for each, are displayed in Figure 6.1.

Acronym	Feature	Image type	Definition
SH	Synovial Hypertrophy	Greyscale	Increased thickness of synovium
EF	Effusion	Greyscale	Build up of fluid in the joint space
PD	Hyperaemia	Power Doppler	Increased vascularity and associated blood flow

Table 6.2: Summary of clinical US features for scoring system.

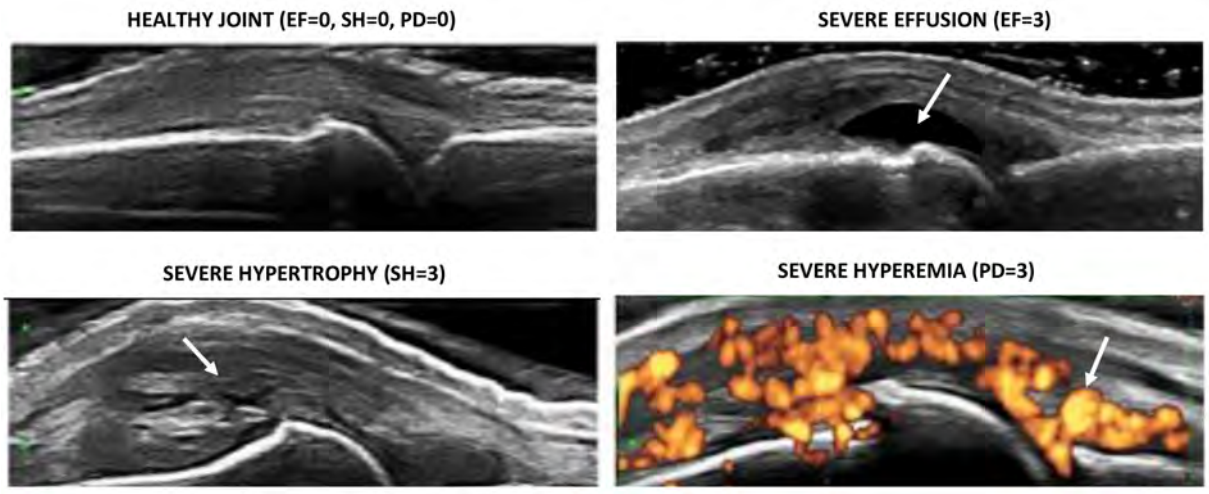

Figure 6.1: Example US images of PIP joints along the sagittal direction of the finger, with the top left showing a healthy joint with no effusion, hypertrophy or hyperaemia, and 3 examples of subjects with severe (grade 3) cases of each US feature.

CE was carried out by trained metrologists for all patients, which involved bi-manual palpation of 28 joints for binary scoring of the presence of clinical swelling (CSW) and / or clinical tenderness (CTE). Both US and CE examiners were blinded to optical image data. When displaying these scores the following convention will be used [SH EF PD] (CTE CSW). Laboratory tests were also carried out, including RF and cyclic citrullinated peptide (CCP), for aiding diagnosis.

6.1.2 Statistical Analysis

In medical diagnostics, S_E and S_P are determined solely on the number of accurate or inaccurate classifications and indicate a test or devices reliability in detecting the presence of disease. To calculate these parameters, ground truth labels were first required, based on the "Gold standard". Two sets of classes were generated, based on either US or CE scores, in which finger joints were labelled as either inflamed or non-inflamed. For US labels, PIP joints with a total score across all features of greater than 0 when summing all semiquantitative features were defined as inflamed, whilst for CE a score of 1 for either CTE or CSW were labelled as inflamed. Each feature extracted was then classified as true or false according to a discriminating threshold. True positives (T_P) or true negatives (T_N) reflect either the correct detection of inflammation or the correct detection of a healthy joint respectively. False positives (F_P) were cases when the test wrongly detects disease which is in fact not present, whilst false negatives (F_N) were cases when underlying disease had failed to be detected by the test. These values are represented in a "confusion table", as shown in Figure 6.2(b), from which S_E and S_P values were calculated as,

$$S_E = \frac{T_P}{T_P + F_N}, \qquad (6.1) \qquad\qquad S_P = \frac{T_N}{T_N + F_P}. \qquad (6.2)$$

A discriminant threshold resulting in values of 1 for both S_E and S_P corresponded to a perfect predictive test, where both inflamed and non-inflamed joints were classified with 100% accuracy. As the discriminant threshold was altered to increase the test's S_E, this typically came at a cost of reduced S_P, and vice versa. In medical diagnostics, the importance of balancing S_E vs. S_P depends on the specific disease and their respective impacts on overall patient outcomes. For example, higher S_E may be desired if the disease is serious and treatable, such as for example RA, whilst a higher S_P is desired if the disease cannot be easily treated or false-positive results can lead to serious psychologic or economic trauma to the patient [214]. The Youden index (J) is a combined measure of both the S_E and S_P [215] and varies between -1 and +1. In this work the standard Youden index was used, defined as

$$J = S_E + S_P - 1, \tag{6.3}$$

with equal weightings on each parameter, however an approach for weighting the Youden index has been proposed [214] to add preference to certain parameters and should be further explored in future work. Finally disease prevalence (P_R) was defined as,

$$P_R = \frac{T_P + F_N}{T_P + T_N + F_P + F_N}. \tag{6.4}$$

To determine the significance of differences observed between groups, inflamed vs. non-inflamed joints or diag-RA vs. non-RA, the non-parametric, Mann-Whitney U (MWU) test was used as this does not require the assumption of a normal distribution for the data, with the null hypothesis defined to be the probability that a randomly selected member from the first sample exceeds a randomly selected member from the second sample is 50%. The steps for the MWU test were as follows [205]:

1. Rank the data such that all data values are ordered from smallest to largest, irrelevant of the group, such that the smallest data point will have a rank 1.

2. Calculate the paired difference number of test statistic, W, using

$$H = \frac{12}{N(N+1)} \sum_{i=1}^{T} n_i(\bar{M}_i - \bar{M})^2, \tag{6.5}$$

where is N is the total number of measurements, T is the total number of groups, the $\bar{M}_i$ average rank of all measurements in group i, $\bar{M}$ is the average rank across all measurements.

3. The p-value can be found from the corresponding value equal to H in a χ^2 distribution table, with T - 1 degrees of freedom.

Receiver operator characteristic (ROC) curve analysis was used to explore the range of potential S_E and S_P values achieved when using a certain features to distinguish between the two classes, in this case discriminating between inflamed and non-inflamed joints. To generate ROC curves, values were calculated and plotted as S_E against (1 - S_P) at a

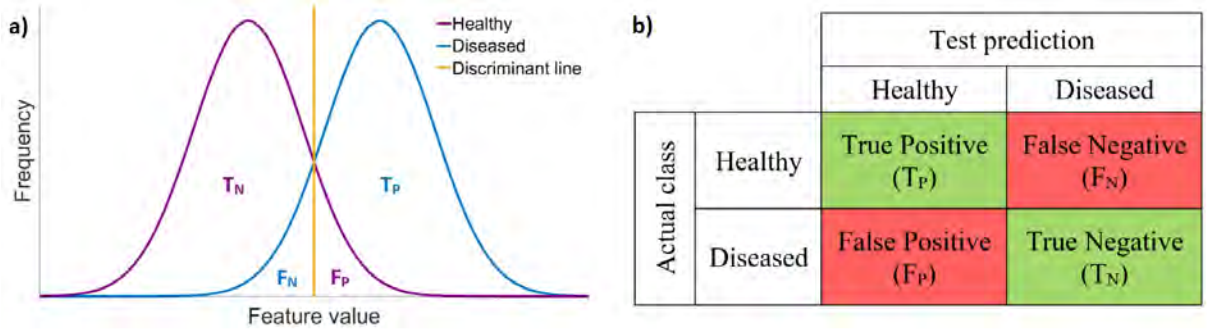

Figure 6.2: Diagrams illustrating detection accuracy measures a) resulting from a given discriminant line for a graph of normally distributed healthy and diseased example data sets and b) as a confusion matrix resulting from test predictions.

range of threshold values, an example of which can be seen in Figure 6.19(c). The 45° diagonal line for x = y on these plots corresponding to points with an average S_E and S_P of 0.5, indicating no ability to differentiate between classes, whilst points close to the upper left corner indicated high values for both S_E and S_P, representing the most superior classification. The area under the curve (AUC) was calculated as a metric of accuracy of detecting inflammation by numerical integration of this ROC curve using the trapezoid rule, with an AUC of 0.5 corresponding to random guessing with no diagnostic value, whilst a value 1 meant correct classifications in 100% of cases. Optimal S_E and S_P values were chosen based on selection of a threshold value that corresponded to the highest J.

Significance levels were shown at *, ** or *** defined as either $p<0.05$, $p<0.005$ or $p<0.0005$ with a two-tailed p value. Finally, the significance of Pearson correlation coefficients at a patient level were assessed using a two-tailed T-test, with the null hypothesis that the relationship between the two test variables is not linear. All data processing and statistical analysis was performed using MATLAB (The MathWorks, Natick, Massachusetts, USA).

6.2 Patient DOT Images

For qualitative comparison, transverse reconstructed images for PIP II-IV joints for all participants are displayed in Figures 6.3 to 6.6, with inflamed joints each labelled according

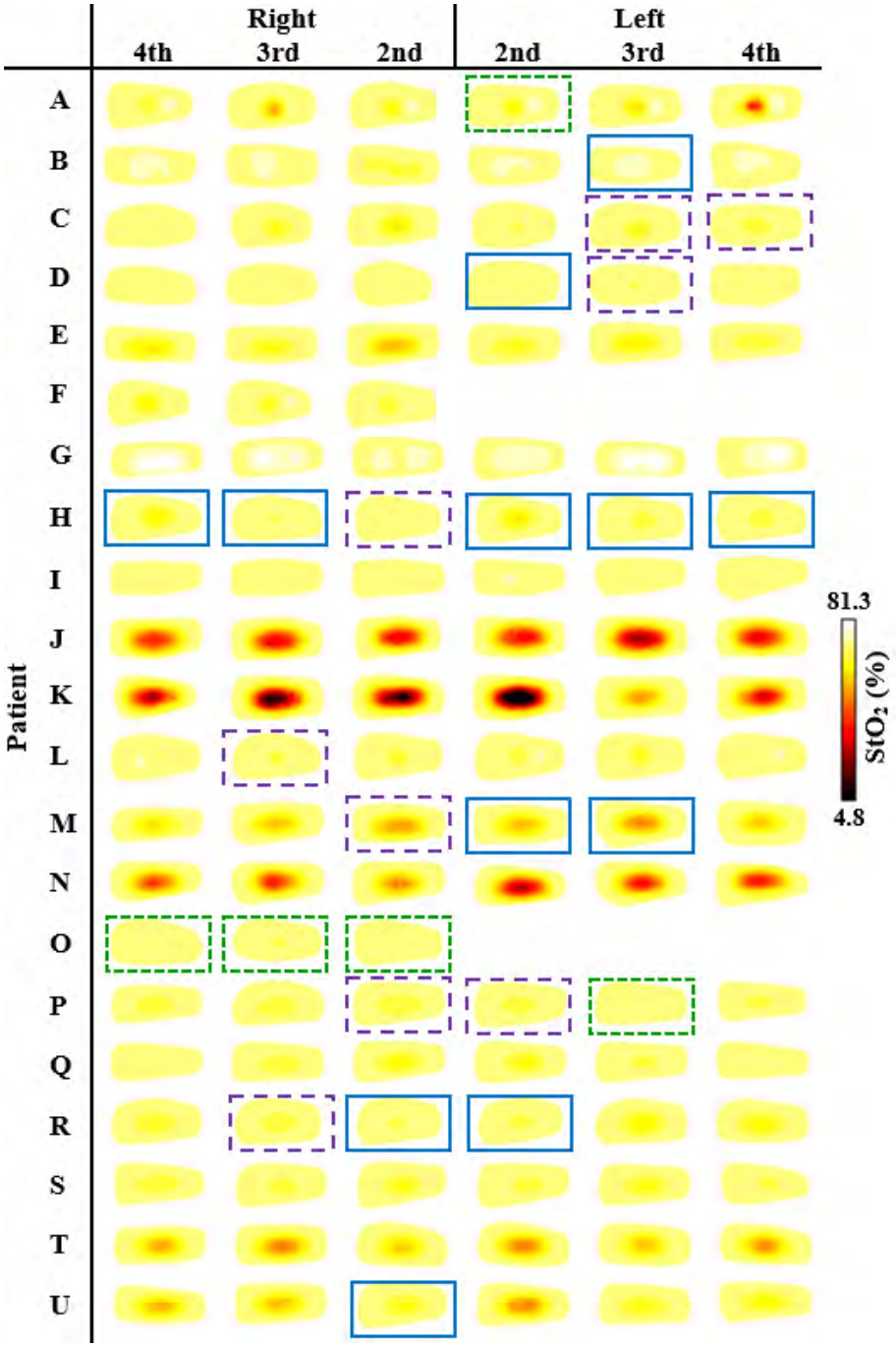

Figure 6.3: Transverse slices half way through the finger of StO_2 (%), for imaged patient PIP joints II-IV. Reference labels are displayed as inflamed in either both US and CE (solid blue), US only (long dashed purple) or CE only (narrow dashed green), with all remaining joints non-inflamed.

to reference data by encapsulating joints with colour coded boxes for either CE only, US only or both US and CE, for each clinical relevant parameters StO_2, tHb, S_A and H_2O.

The high levels of inter-subject variability demonstrated in Chapter 5 can again be

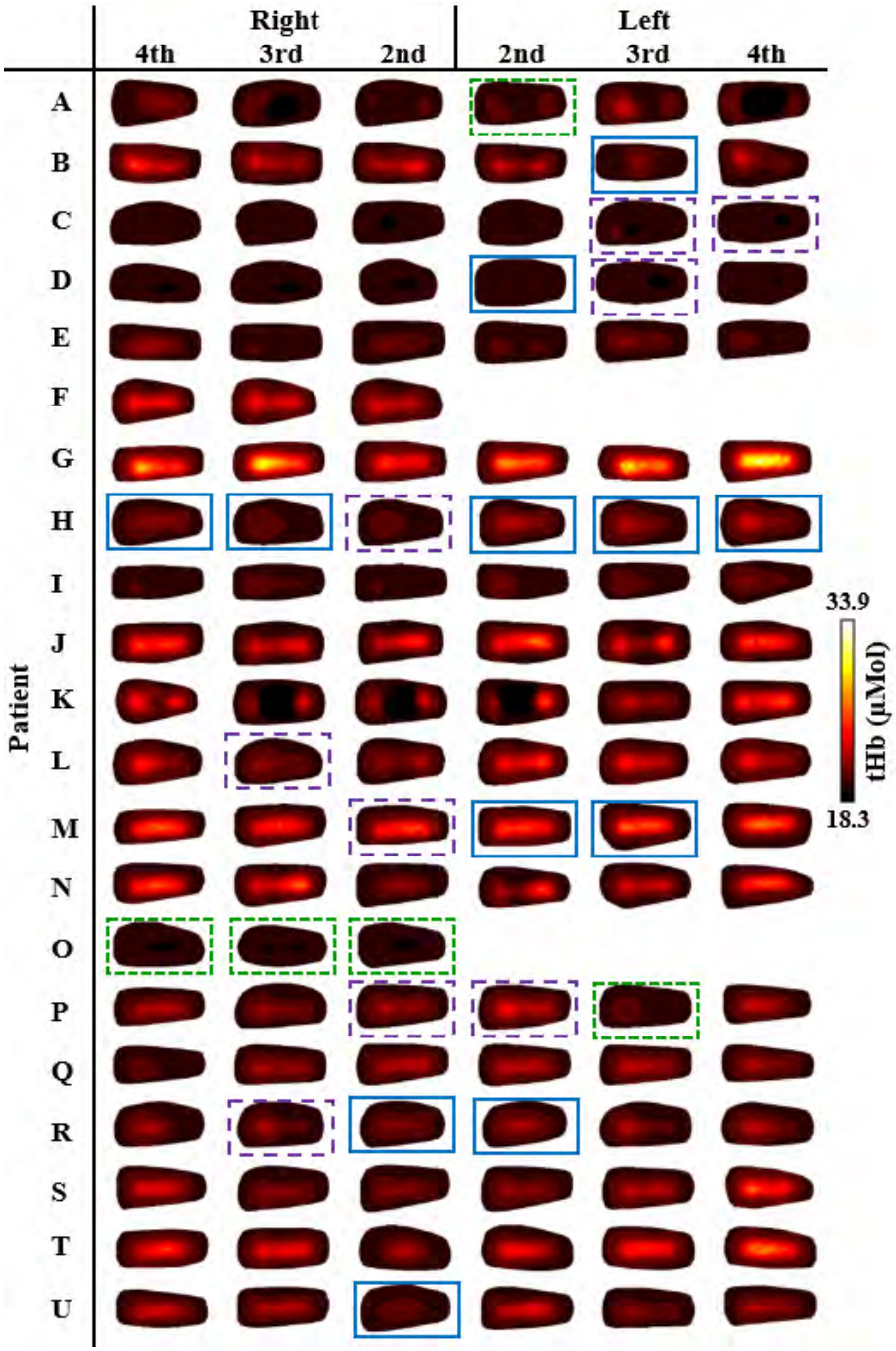

Figure 6.4: Transverse slices half way through the finger of tHb (mMol), for imaged patient PIP joints II-IV. Reference labels are displayed as inflamed in either both US and CE (solid blue), US only (long dashed purple) or CE only (narrow dashed green), with all remaining joints non-inflamed.

observed qualitatively when comparing groups of joints from different patients, compared to the variation between joints from the same subject. Evidence of the joint structure was again seen for a majority of S_A and tHb images, as lower central values corresponding to

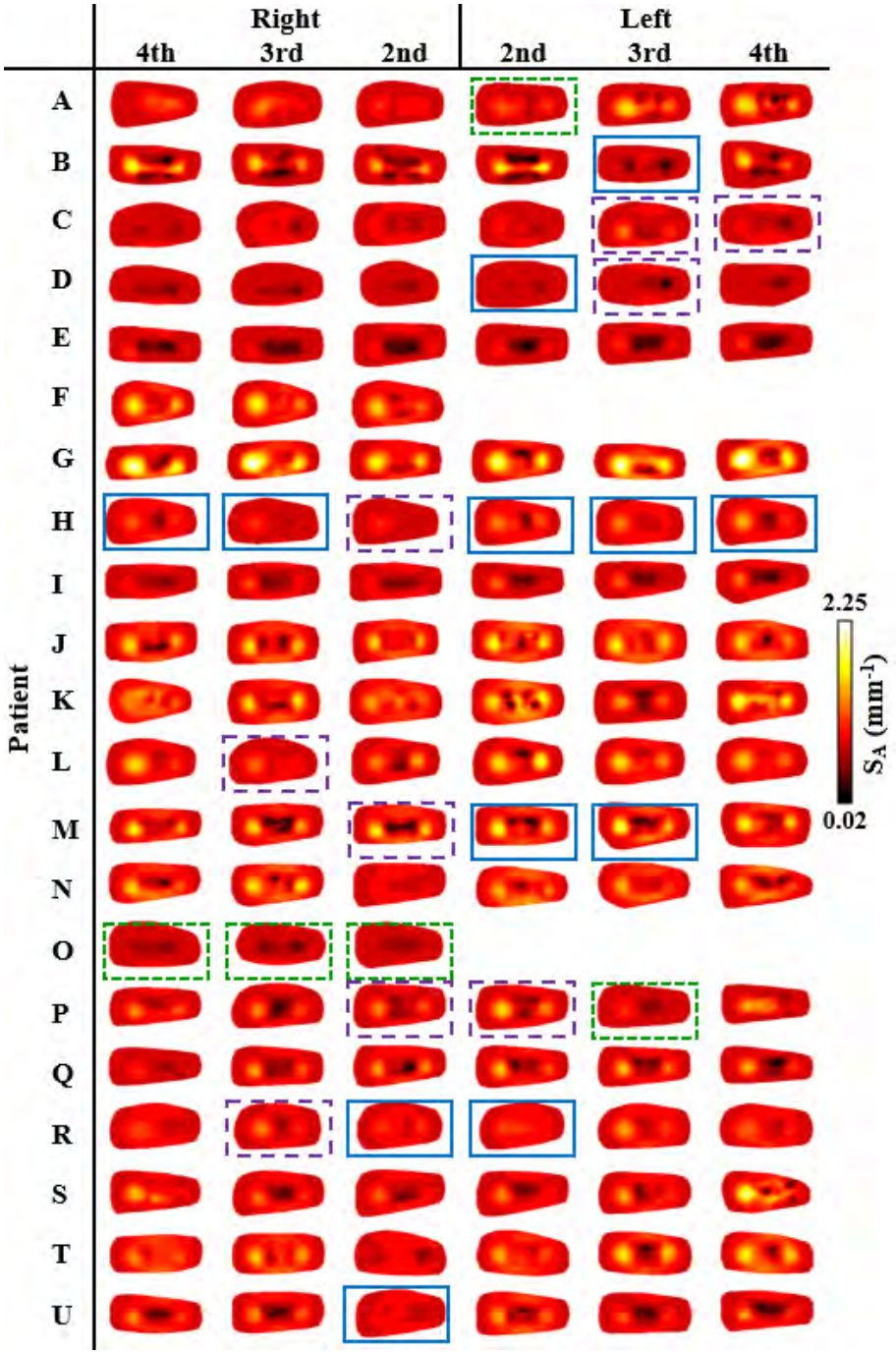

Figure 6.5: Transverse slices half way through the finger of S_A (mm^{-1}), for imaged patient PIP joints II-IV. Reference labels are displayed as inflamed in either both US and CE (solid blue), US only (long dashed purple) or CE only (narrow dashed green), with all remaining joints non-inflamed.

the joint space compared to elevated values either side as a result of bone. For a subset of patients, named C, D, H, I, O and R, this contrast was less evident in transverse images, all of whom had at least one joint labelled as inflamed in either US or CE. Furthermore, in

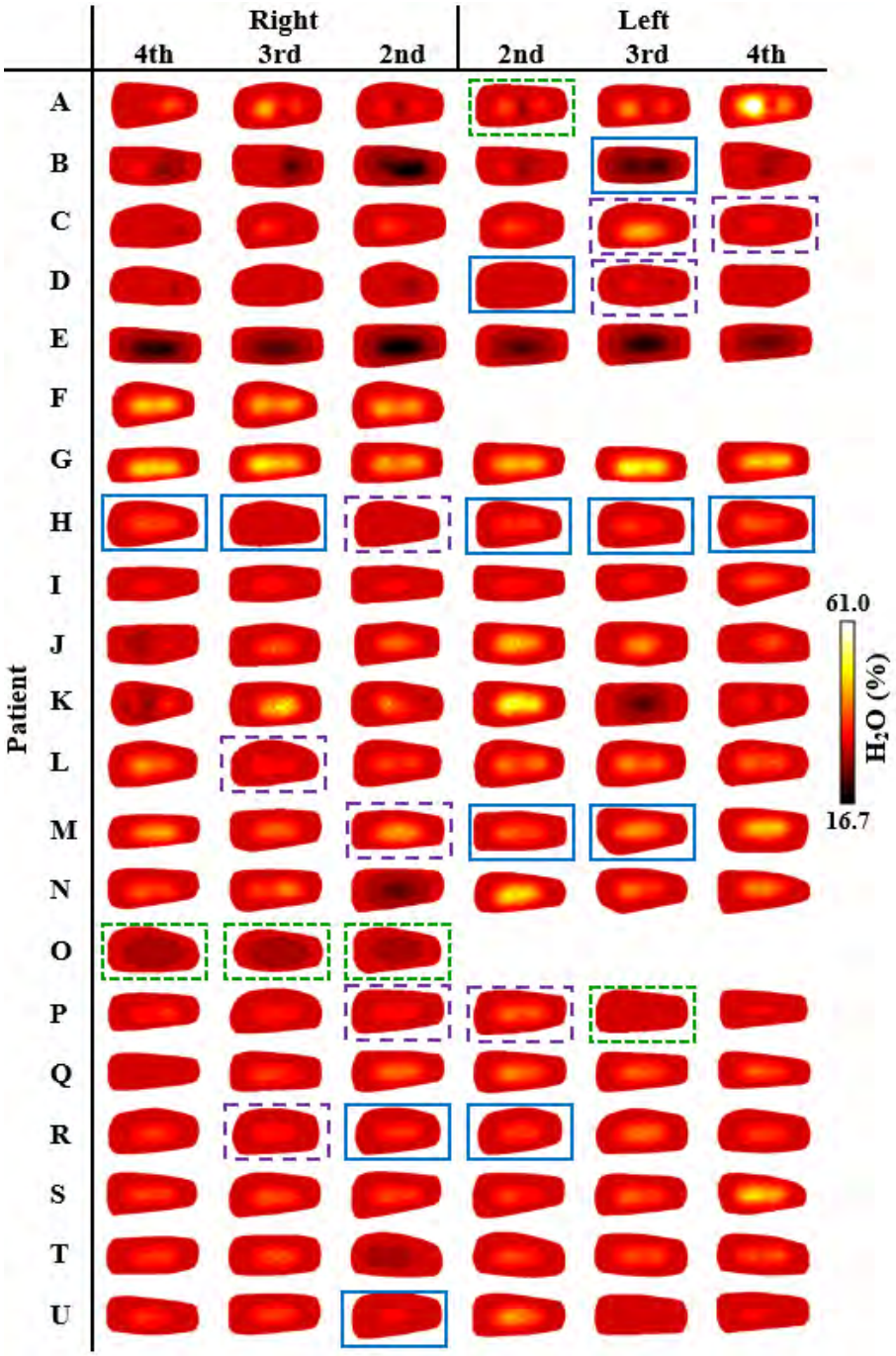

Figure 6.6: Transverse slices half way through the finger of H_2O (%), for imaged patient PIP joints II-IV. Reference labels are displayed as inflamed in either both US and CE (solid blue), US only (long dashed purple) or CE only (narrow dashed green), with all remaining joints non-inflamed.

patients B, L and U a distinction in this S_A and tHb contrast between images of certain joints labelled as inflamed showed a clear lack of contrast compared to remaining non-inflamed joints in the same subject, with the nature of these structural changes consistent

with observations in previous literature [149] as displayed in Figure 2.11. The loss of discernible structure in these images is attributed to a reduction in quantitative contrast between the inflamed joint cavity and surrounding bone, as both scattering increases, due to a greater number of inflammatory cells, and local blood volume fraction increases, resulting from synovial angiogenesis. This distinction does not appear to be completely specific, with additional examples of joints which display less contrast in transverse images of S_A and tHb that were not labelled as inflamed according to US or CE, for example in Patients C, H, O and U, and patient N displaying a clear lack of contrast in the right PIP II compared to remaining joints, but no evidence of inflammation according to reference scores. Additionally this pattern was not completely sensitive, for example Patient M did not display any differences in S_A and tHb contrast although several joints were labelled as in inflamed. Images of StO_2 and H_2O were more difficult to qualitatively interpret any patterns with no evidence of structure in all joints except H_2O for participant A. In two patients J and K, very low values for StO_2 below $\approx$30% were observed across all joints, with these outliers unlikely to be physiologically realistic, particularly considering all of these joints were non-inflamed. These erroneous results could have been a result of elevated cross-talk between chromophores during the inverse problem or systematic errors not accounted for during the data acquisition in these patients, highlighting the need for more stringent measures of data quality during preprocessing in future system generations.

6.2.1 Feature Extraction

Dimensionality reduction of recovered DOT images into quantitative features was necessary, as variation of mesh joint dimensions between subjects meant that values on the FEM node basis were not comparable. Four basic statistical features mean, variance, maximum and minimum were first extracted from the VOI by ignoring FEM nodes close to the boundary and outside the source and detector field of view as described in Section 5.2.3 and were denoted "Volumetric" features. When attempting to classify between inflamed and non-inflamed joints in clinical studies, extension of feature extraction to include more

advanced, complex features from the 3D images was more meaningful as "Gold Standard" references allowed for comparison between each feature's performance and identification of those most able to differentiate between diseased and healthy classes. To automate and simplify the feature extraction process, recovered DOT images were first interpolated from the tetrahedral based FEM mesh, which had acted as the basis for solving the forward model during reconstruction, onto a regular grid basis using the following steps:

1. Principal component analysis transformations to align a 3D grid of calibrated sources positions onto a 2D plane were also applied to all FEM meshes to orientate all joints in the same Cartesian coordinate system.

2. A regular pixel basis was defined to encapsulate these joint based on their dimensions, with cubic intervals of equal 0.3mm spacing.

3. Recovered values for each clinical parameter were interpolated from all nodes in the FEM mesh onto this pixel basis using the MATLAB function triscatteredinterp.

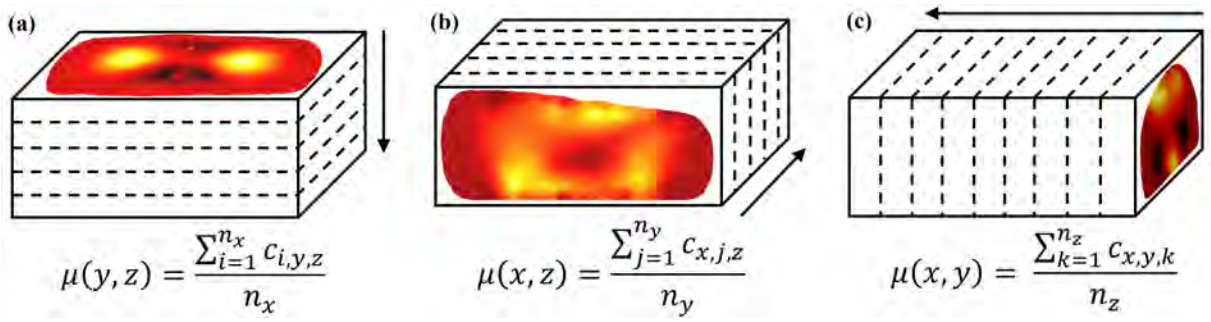

Figure 6.7: Illustration of the computation of orthogonal stack averages for either the (a) transverse, (b) sagittal or (c) coronal directions.

From this regular basis, twenty-four additional features were extracted, as summarised in Table 6.3, which included calculation of the four statistical parameters for the central 2D image slices displayed in Figure 5.5 or the 2D image resulting from calculating the mean of the pixel stack along that axis, as illustrated in Figure 6.7, both of which were implemented at each orthogonal transverse, sagittal or coronal direction in the pixel basis. A potential advantage to calculating features in these approaches is that they will be more

biased towards sensitivity of the spatial distribution of recovered parameters along the orientations of sampling through the joint. All 28 features were extracted per metabolic parameter, tHb, StO_2, H_2O and S_A, resulting in 112 separate features for comparison.

Feature	Mean	Variance	Maximum	Minimum
Volumetric	#1	#2	#3	#4
Transverse Slice	#5	#6	#7	#8
Sagittal Slice	#9	#10	#11	#12
Coronal Slice	#13	#14	#15	#16
Transverse Stack	#17	#18	#19	#20
Sagittal Stack	#21	#22	#23	#24
Coronal Stack	#25	#26	#27	#28

Table 6.3: Numbering convention for extracted features.

6.2.2 Diagnostic Accuracy of Features

The majority of extracted features were of little discriminatory value, particularly for H_2O and StO_2 images, neither of which had any P values for the Mann-Whitney U test less than 0.05 when US was used as a reference label and only three instances when CE was used, summarised in Table 6.4. The null hypothesis that the median values for inflamed and non-inflamed joints were the same could be rejected for a number of features when using S_A or tHb images, with statistically significant differences observed with $P < 0.05$, supporting quantitatively observations that these two pathophysiological parameters were sensitive to the state of inflammation. Features measuring the variance within images, including #2, #6, #14, #18, #22 and #26, provided more discriminatory value with many recording statistically significant ($P < 0.05$) differences, highlighting that the distribution of recovered parameters was a key indicator for inflammation.

Despite seeing significantly different medians for a number of features, ROC analysis was carried out to effectively evaluate the diagnostic accuracy of all 112 features and

Feat. No.	StO_2 (%)	tHb (μMol)	S_A (mm^{-1})	H_2O (%)
#1	0.503 *(0.226)*	0.248 ***(0.035*)***	0.283 *(0.057)*	0.858 *(0.148)*
#2	0.180 *(0.144)*	0.082 ***(0.011*)***	**0.013*** ***(0.001*)***	0.161 *(0.054)*
#3	0.378 *(0.244)*	0.190 ***(0.025*)***	0.238 *(0.067)*	0.640 *(0.067)*
#4	0.444 *(0.317)*	0.830 ***(0.025*)***	0.207 *(0.053)*	0.063 *(0.654)*
#5	0.389 *(0.191)*	0.140 ***(0.024*)***	0.406 *(0.115)*	0.938 *(0.115)*
#6	0.102 *(0.104)*	0.057 ***(0.004*)***	**0.002*** ***(0.001*)***	0.321 *(0.058)*
#7	0.318 *(0.244)*	**0.043*** ***(0.008*)***	**0.025*** ***(0.001*)***	0.426 *(0.051)*
#8	0.311 *(0.280)*	0.918 *(0.404)*	0.146 *(0.074)*	0.155 *(0.594)*
#9	0.484 *(0.239)*	0.272 ***(0.041*)***	0.276 ***(0.038*)***	0.854 *(0.199)*
#10	0.169 *(0.170)*	0.206 ***(0.031*)***	0.069 ***(0.028*)***	0.417 *(0.141)*
#11	0.200 *(0.158)*	0.299 *(0.075)*	0.549 *(0.130)*	0.846 *(0.169)*
#12	0.490 *(0.366)*	0.584 *(0.090)*	0.591 *(0.467)*	0.120 *(0.464)*
#13	0.316 *(0.248)*	0.211 ***(0.017*)***	0.362 ***(0.033*)***	0.994 ***(0.043*)***
#14	0.263 *(0.191)*	0.095 ***(0.002*)***	**0.002*** *(0.001)*	0.429 *(0.040)*
#15	0.902 *(0.525)*	0.186 ***(0.005*)***	0.079 ***(0.002*)***	0.733 ***(0.042*)***
#16	0.341 *(0.295)*	0.874 *(0.354)*	**0.015*** ***(0.040*)***	0.137 *(0.426)*
#17	0.481 *(0.191)*	0.21 ***(0.025*)***	0.326 ***(0.034*)***	0.994 *(0.129)*
#18	0.156 ***(0.064*)***	0.170 ***(0.007*)***	**0.023*** ***(0.012*)***	0.779 *(0.148)*
#19	0.397 *(0.246)*	0.230 ***(0.028*)***	0.450 ***(0.045*)***	0.926 *(0.116)*
#20	0.601 *(0.235)*	0.958 *(0.521)*	0.854 *(0.290)*	0.164 *(0.544)*
#21	0.406 *(0.191)*	0.185 ***(0.025*)***	0.349 ***(0.043*)***	0.970 *(0.124)*
#22	0.116 *(0.095)*	0.089 ***(0.006*)***	**0.008*** ***(0.004*)***	0.468 *(0.083)*
#23	0.221 *(0.207)*	0.130 ***(0.020*)***	0.151 ***(0.031*)***	0.707 *(0.104)*
#24	0.378 *(0.288)*	0.906 *(0.282)*	0.169 *(0.610)*	0.141 *(0.503)*
#25	0.432 *(0.193)*	0.185 ***(0.023*)***	0.228 ***(0.027*)***	0.970 *(0.137)*
#26	0.092 *(0.087)*	0.139 ***(0.012*)***	**0.041*** ***(0.033*)***	0.230 *(0.074)*
#27	0.213 *(0.193)*	0.386 *(0.076)*	0.722 *(0.288)*	0.622 *(0.152)*
#28	0.338 *(0.265)*	0.714 ***(0.023*)***	0.516 *(0.285)*	0.096 *(0.551)*

Table 6.4: P-values resulting from the Mann-Whitney U test comparing inflamed and non-inflamed joints across the cohort for each image feature, when either US (non-italic) or CE (italic in brackets) reference labels were used. Statistically significant values were highlighted in bold with an asterisk.

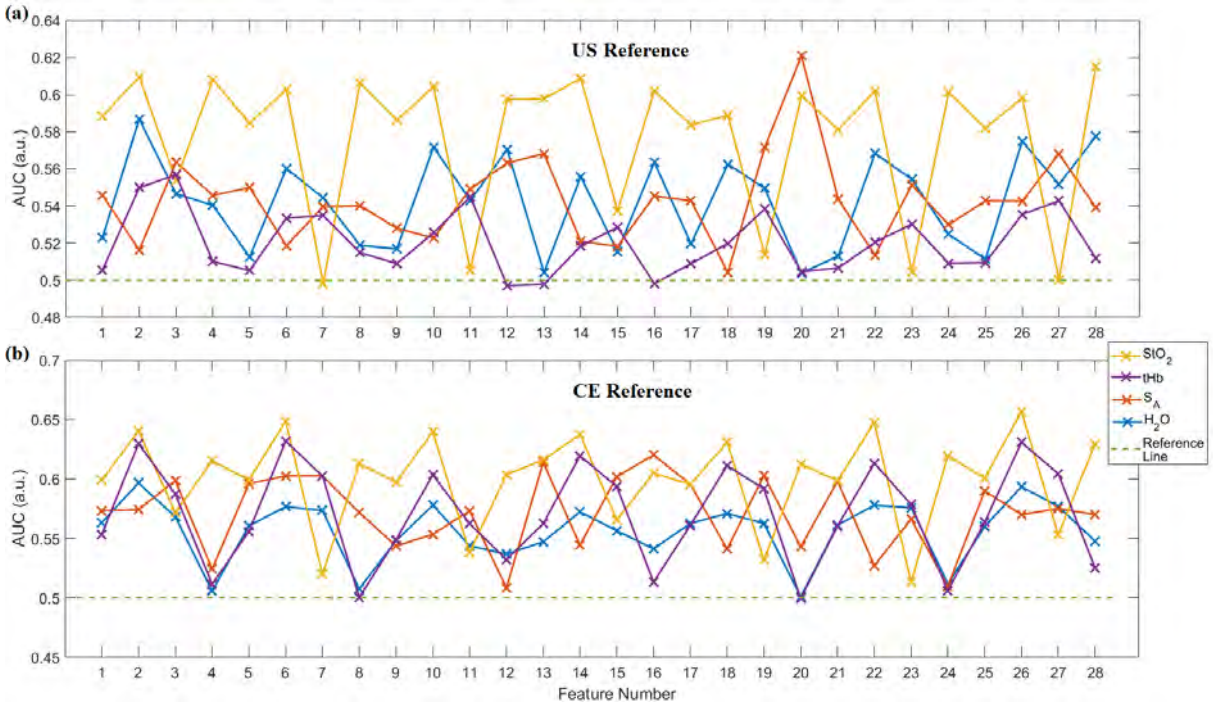

Figure 6.8: AUC values from ROC analysis plotted for all image features and each clinical parameter, when either (a) US or (b) CE were used as labels. The reference line of AUC = 0.5 corresponds to random assignment of classes.

compare their individual utility for detecting inflammation. The threshold was varied between 0 and the maximum feature score, in 10,000 equally sized intervals whilst plotting S_E against (1 - S_P). As features could by the presence of inflammation be either elevated, for example tHb following angiogenesis, or lowered, for example StO_2 under hypoxia, two decision strategies were employed. The first considered values below the threshold when assigning T_P or F_N results to joints labelled as inflamed according to US or CE reference, whilst the second considered values above this threshold for the same assignment and the maximum AUC or J values were then chosen from these two cases on a feature by feature basis.

Slightly better agreement was seen with CE labels compared to US, although diagnostic accuracies displayed in Figure 6.8 were generally reasonably low in the context of a medical imaging application, ranging between 0.498 and 0.657. Similar conclusions could be drawn from diagnostic accuracy scores in Figures 6.9 and 6.10, with all J indices ranging between -0.133 and 0.411. The optimum values for J and AUC when US was used for

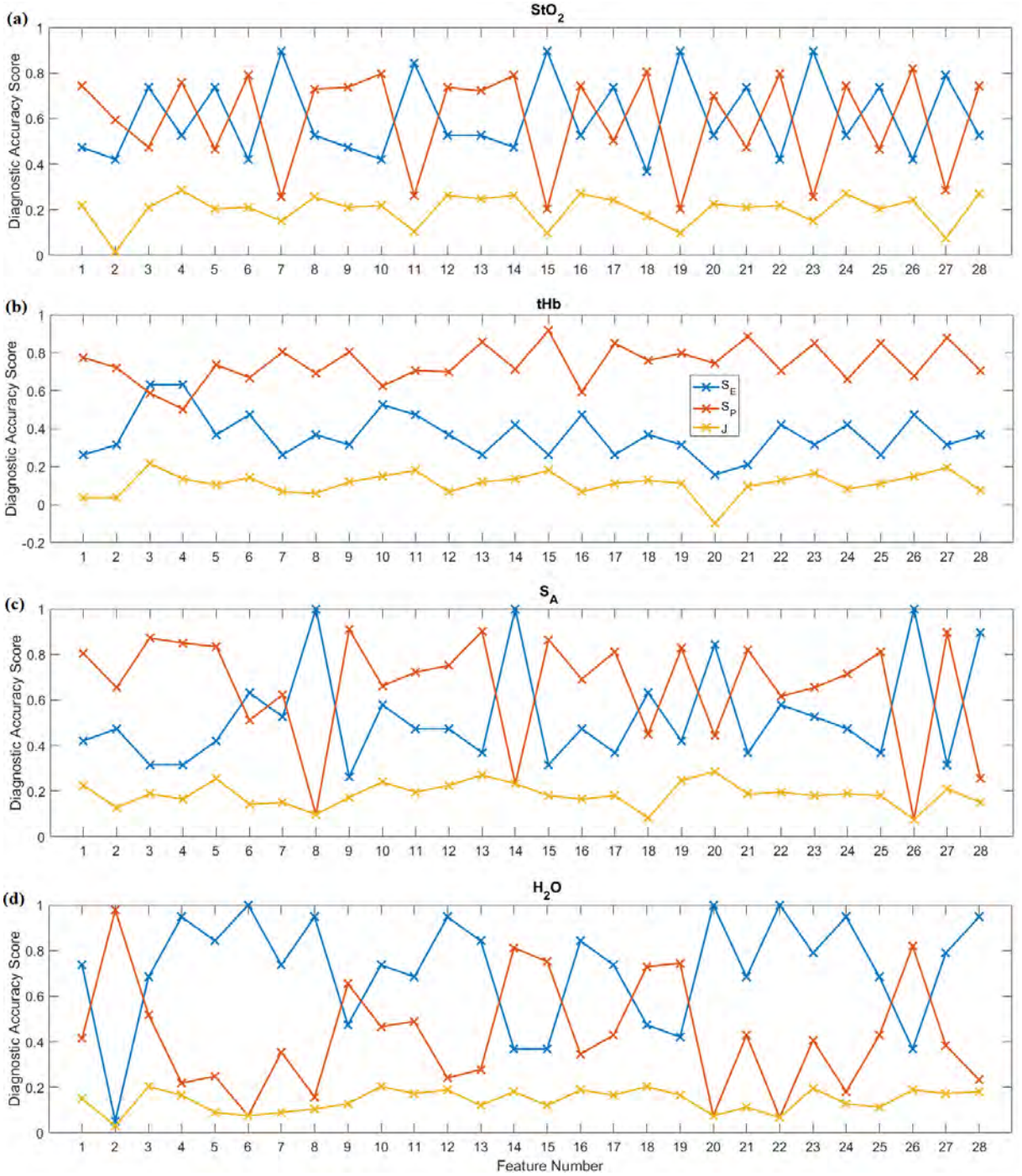

Figure 6.9: Maximum J indices for each image feature, with corresponding values for S_E and S_P, plotted for all image features and each clinical parameter, when US was used as labels.

reference were 0.286 and 0.621 respectively, both occurring for the minimum transverse stack of S_A evident as a peak in Figure 6.8(a) and with corresponding S_E and S_P values of 52.6% and 75.9% respectively. For CE reference labelled data, the optimum J and AUC

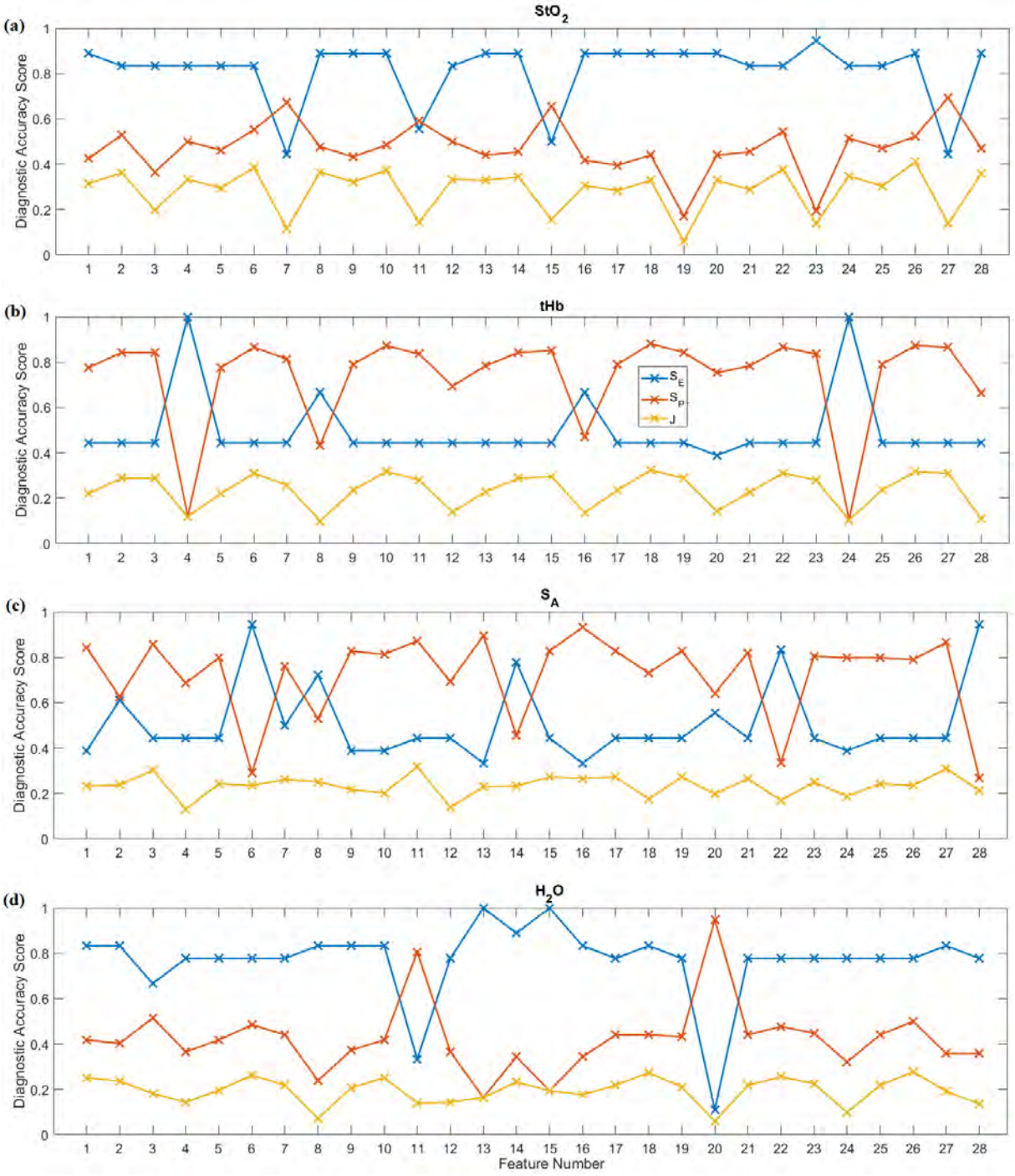

Figure 6.10: Maximum J indices for each image feature, with corresponding values for S_E and S_P, plotted for all image features and each clinical parameter, when CE was used as labels.

values were slightly superior at 0.411 and 0.657 respectively, occurring for the variance of coronal stack images of StO_2, with corresponding S_E and S_P values of 86.9% and 52.2% respectively. A clear pattern in performance of StO_2 was evident, with higher AUC values

overall with the exception of maximum image features that recorded values close to 0.5 equivalent to random assignment. The drastically lowered StO_2 anomaly values, all of which occurred in non-inflamed joints discussed previously, were expected to have influenced these classification accuracies. The extraction of additional, more complex spatial features (#5-#28) did not appear to provide drastically improved classification accuracies overall compared to the basic volumetric statistical features (#1-#4), although it is possible that other even more complex features such those as implemented in previous studies [149] may prove beneficial in future investigations. These comparatively low AUC and J values are indicative that any contrast identified by features between inflamed and non-inflamed joints in DOT images were not found generalise well for accurate detection across the cohort. Results from this dataset were comparable with previous reports demonstrating diagnostic accuracies of 64% S_E and 55% S_P with single wavelength CW-DOT images [4], inferring the use of multi-spectral information in this case did not provide noticeable benefits in terms of diagnostic accuracy. Factors expected to hinder performance were high levels of inter-subject variability in optical properties demonstrated in Chapter 5 and the challenges posed to reconstruction by the complex heterogeneity of the joint in terms of both scattering and absorption. The inclusion of phase measurement [4], which is orthogonal to amplitude in μ_a vs. μ_s' space [107], or spatial *a priori* information about the joint structure [153] are likely to improve the conditioning and uniqueness of the inverse problem.

6.3 Optical Transmission Image Analysis

In healthy subject studies in Chapter 5 a peak in intensity was observed at the joint region which moved correspondingly as the finger was translated, however during the clinical pilot study a central region of lower intensity was observed in some patients during acquisition, a typical example of which is illustrated in Figure 6.11 of the line profiles along the central sagittal sections of an inflamed and a non-inflamed joint. The nature of this contrast was

in agreement with previous studies, also reporting a decrease in intensity in transmission images of inflamed joints [216], with the quantitative differences between the joint cavity and the bone expected to reduce as a consequence of inflammation as both localised blood volume fraction increases, resulting from synovial angiogenesis, and localised scattering increases, due to a greater cell concentration. In previous studies, accurate classification using non-occlusion based CW transillumination images was limited to patient specific changes during follow-up examination as opposed to single time-point examination, which was attributed to high inter-subject variability, as discussed in Section 2.5.2.

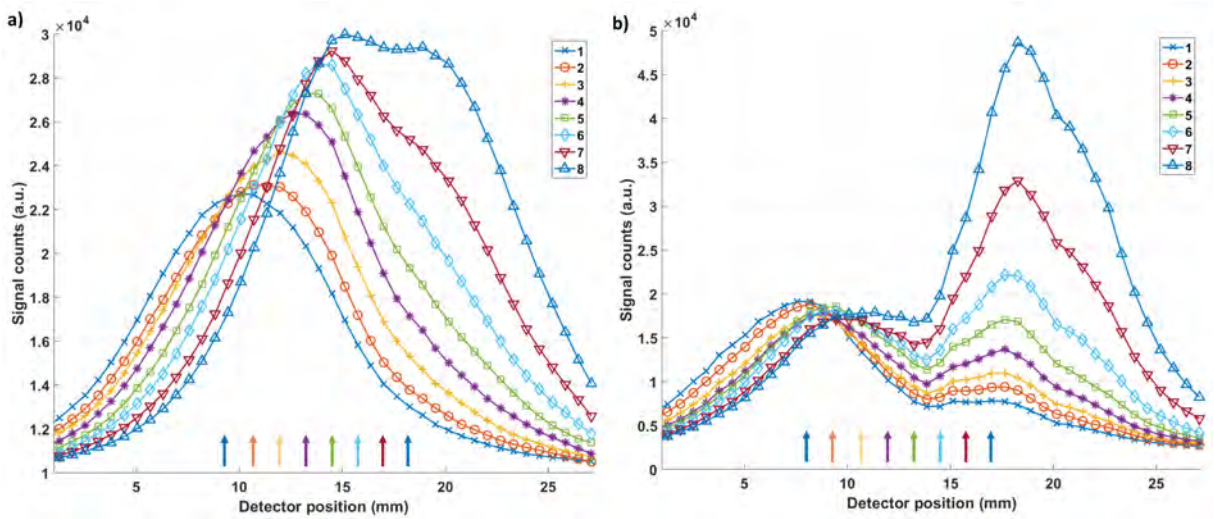

Figure 6.11: Central line profiles of 650nm images at a sparse set of 8 source positions along a) an example of a typical non-inflamed, healthy joint and b) an example inflamed joint of a typical inflamed joint from a patient with RA.

For all datasets, the optical transmission image which corresponded with when the light source was directly under the joint was manually selected for further analysis, based on the wrinkles in the PIP joint. The mean total flux for a central region of interest of 4 $\times$ 4 pixels (2.5 $\times$ 2.5mm on the finger surface) region, after processing that accounted for both $R_F(\lambda)$ and exposure time, was compared between labelled joint groups.

Despite this indication of a presence of decreased intensity in certain joints of patients, no statistically significant differences in mean intensity were observed between inflamed and non-inflamed joints when using US labels ($p = 0.39$). Evidence of a significantly lower intensity in inflamed joints was seen when joints were labelled using CE ($p = 0.00060$)

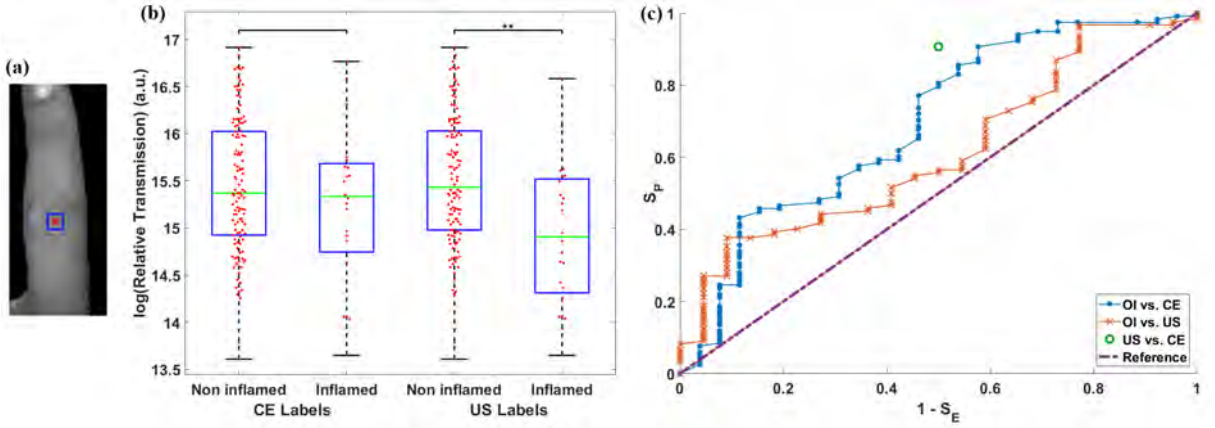

Figure 6.12: (a) Grayscale image indicating region of relative transmitted intensity measurement on the joint (blue box) for the corresponding central source position (red cross). (b) Boxplots overlaid with beeswarm plots for Relative Transmission at 650nm and (c) corresponding ROC analysis for all joints labelled using either US or CE.

between inflamed and non-inflamed. Yet ROC analysis in Figure 6.12 (c) indicated insufficient diagnostic accuracies, particularly for US which was close to the reference line that represented random assignment, with comparatively lower AUC values of 0.614 and 0.695 for US and CE respectively. The superior performance of CE may be a result of a greater sensitivity during examination of CSW and CTE scores to physical increases in the joint dimensions resulting from swelling. The large variation in total flux transmitted through the joints evident in Figure 6.12 due to differences in joint dimensions and underlying optical properties, was expected to be a key factor hindering the ability to detect inflammation using this measure.

6.3.1 DOI Image Feature Engineering

A series of image processing steps were applied, designed to extract heuristic features indicative of the spatial distribution of light transmitted along the sagittal direction of the finger joint, as illustrated in Figure 6.13, selected based on evidence from insights in the preceding section together with an understanding of the nature of pathophysiological changes expected to occur in the joint discussed in Section 1.1.2. Firstly, the threshold mask from the autoexposure routine, which distinguished the finger from the background,

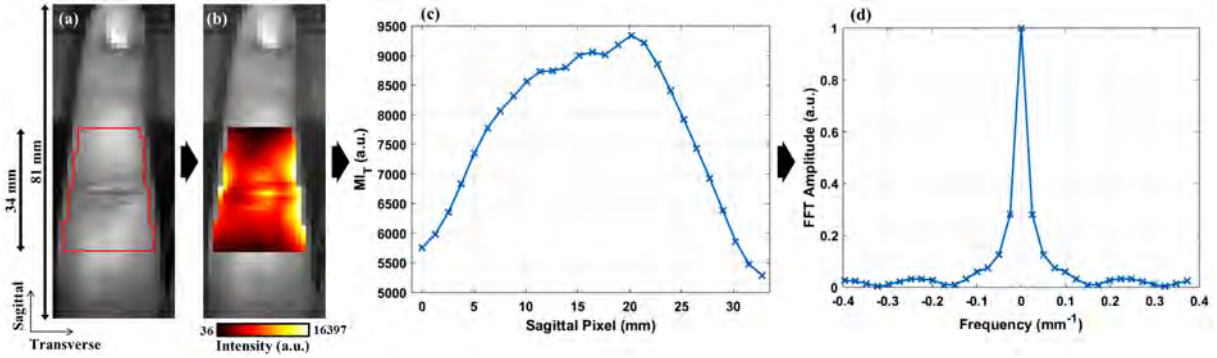

Figure 6.13: Data processing steps applied to an example PIP joint, for feature extraction, with (a) greyscale image of finger with red line showing boundary of ROI defined from image mask (b) greyscale image overlaid with transmitted DOI image from through the joint in colour, (c) mean intensity across transverse of DOI image plotted for each sagittal pixel, and (d) FFT amplitude spectrum of the normalised MI_T profile.

was eroded using a 2 pixel radius disk to discard boundary pixels and truncated to a section in the sagittal direction 27 pixels (≈34mm) in length, defining a region of interest (ROI) expected to contain the most useful information relevant to the pathological state of the joint. The mean intensity across the transverse direction (MI_T) of the DOI transmission image within this ROI image mask was computed, defined as,

$$MI_T(m) = \frac{\sum_{n=1}^{P} I(n,m)M(n,m)}{\sum_{n=1}^{P} M(n,m)} \tag{6.6}$$

where I is the image intensity in counts, n is the pixel index in the transverse direction, P is the transverse image width in pixels and M is the binary image mask, for each sagittal pixel (m). As wrinkles on the surface of the finger could introduce small fluctuations in the MI_T profile which appeared as high frequency noise, a 10 pixel window Gaussian smoothing filter was applied to this curve. A one-dimensional discrete FFT was applied, with zero padding first added to the next highest power of two (N = 32), to decompose the MI_T curve into its underlying frequency components by calculating the amplitude spectrum of the complex FFT coefficients. To minimise the impact of inter-subject variability in the absolute intensity resulting from variation in finger size or underlying optical properties, the MI_T of each profile was normalised such that the total sum of all points was equal to 1, which is equivalent to the value of the first (or DC) Fourier coefficient. The impact of

normalisation is that remaining FFT coefficient values represent the relative amplitude for their corresponding frequencies and only depend on the spatial distribution of the transmitted light. The number of coefficients used as heuristic features for assessment of inflammation was reduced to $(N/2 + 1) = 17$ unique values, as a consequence of the symmetrical properties of the FFT. A decision strategy was employed such that for joints labelled as inflamed according to US or CE reference, either a T_P or F_N was recorded if the FFT amplitude was either above or below this threshold respectively, whilst for joints labelled non-inflamed, either a F_P or T_N was recorded if the FFT amplitude was either above or below the threshold, respectively.

6.3.2 Impact of Asymmetrical Inflammation

In non-contact, camera-based transmission DOI systems, the pixel-based measurements provide a high density array of detectors, whilst the joint is illuminated at a single source position for a given wavelength on the opposing boundary. Previous point-source based joint imaging systems have all implemented an orientation in which images were acquired from the palmar side of the finger joint with light focused on the dorsal side [91, 141, 136, 217, 218], however in the coronal direction, the anatomy of the finger joint is not symmetrical, with the synovium larger in volume on the dorsal than the palmar side to facilitate flexion of the joint when gripping. Consensus among rheumatologists is that the distribution of clinically significant synovitis is asymmetric, as illustrated in Figure 1.4 (b), with attempts to establish a consensus-based, RA synovitis scoring system reporting 100% agreement that the dorsal approach is more sensitive using PD-US than the palmar between seventeen expert musculoskeletal sonographers [213]. This was reflected by higher kappa values for intraobserver and interobserver reliability of scoring of 0.51 for dorsal imaging compared to 0.30 for palmar. Furthermore, a randomized, placebo-controlled, two-centre study reported high parallel scan, inter-reader reliability for dorsal PD-US scores (ICC > 0.61), demonstrating it to be a sensitive and reliable endpoint for drug therapies in RA [219]. A study involving a cohort of 70 patients diagnosed with RA directly compared

the dorsal and palmar approaches using PD-US, reporting greater prevalence of 22.1% versus 8.9% and greater double-positive rates, in which both greyscale US and PD-US are simultaneously observed, of 57.5% versus 17.4% for dorsal compared to palmar imaging of PIP joints [220]. Fluorescence tomographic imaging of injected contrast agent indocyanine green in inflamed fingers also concurs, revealing a greater degree of vascularisation on the dorsal aspect [172]. This asymmetrical distribution of inflammation makes imaging orientation of joints using non-contact DOI systems of importance, the impact of which has not previously been investigated.

Two orientations are feasible using the presented system when acquiring transillumination images of a PIP joint, either with the joint illuminated on the dorsal side and optical detection on the palmar, or the reverse set-up with palmar illumination and dorsal detection. To assess the impact of depth of inflammation on contrast using the proposed normalised FFT feature, a simple 20 $\times$ 30mm 2D model representing the anatomy of the PIP joint was constructed, as shown in Figure 6.14, with the skin and bone thickness assigned as 1mm and 10mm respectively, dimensions approximately estimated from an available MRI image of a PIP joint. Physiological values assigned to each of these regions are shown in Table 6.5, with tHb and H_2O chosen according to previous literature [189], all tissue oxygenation values assumed to be 70% and values for the synovia region based on previous joint imaging studies [153], whilst S_A and S_P were both assumed to be homogeneous with values of 0.77mm^{-1} and 2.145 respectively. A single source and 27 virtual detectors separated by 1mm along the opposing boundary were assigned to this model, to reflect the point source illumination and a pixel array from camera-based detection used in this study.

A circular anomaly with a 3mm radius was assigned as a basic representation of inflammation in an RA patient, the centre depth of which was varied at five depths, 3, 6.5, 10, 13.5 and 17mm, as shown in Figure 6.15. Values for this anomaly are shown in Table 6.5, with increased tHb and decreased StO_2 to reflect the associated angiogenesis and hypoxia typically observed in an inflamed joint. At each height, boundary fluence

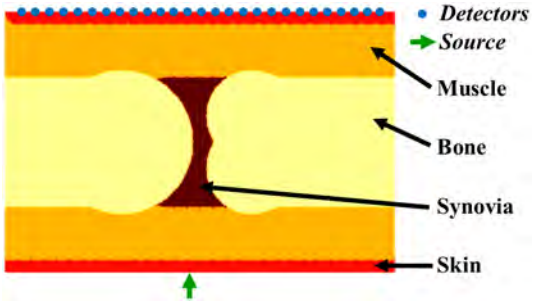

Figure 6.14: Simplified 2D model of the joint and imaging setup with a single source and 27 virtual detector positions.

Tissue	tHb (μMol)	StO_2 (%)	Water (%)
Muscle	0.07	70	0.5
Skin	0.06	70	0.5
Bone	0.049	70	0.15
Synovia	0.02	70	0.5
Inflammation	0.14	35	0.5

Table 6.5: Physiological values assigned to each tissue in the joint model.

data for all detectors was generated at 650nm, either with or without the inflammation anomaly, implemented using open-source, light modelling finite element method package NIRFAST [72].

At a 3mm height, intensity plots in Figure 6.15 show a decrease in the absolute transmitted flux when the inflammation anomaly was close to the source, compared to the non-inflamed case, however a negligible change in the normalised FFT amplitude spectra is observed, indicating that the spatial distributions in intensity are similar. As the height of the inflammation anomaly is increased closer to the detection boundary, the spatial distribution of intensity in the inflamed case becomes more distinct from the non-inflamed case, with the presence of a visible dip in the profile, reflected in the increasing difference between their normalised FFT amplitude spectra. For example, the normalised amplitude for the 3rd FFT coefficient was 0.0072 in the non-inflamed simulation, whilst when the inflamed anomaly was added at heights of either 3, 6.5, 10, 13.5 or 17mm, the corresponding score was increased to either 0.016, 0.049, 0.090, 0.144 or 0.189 respectively, indicating a

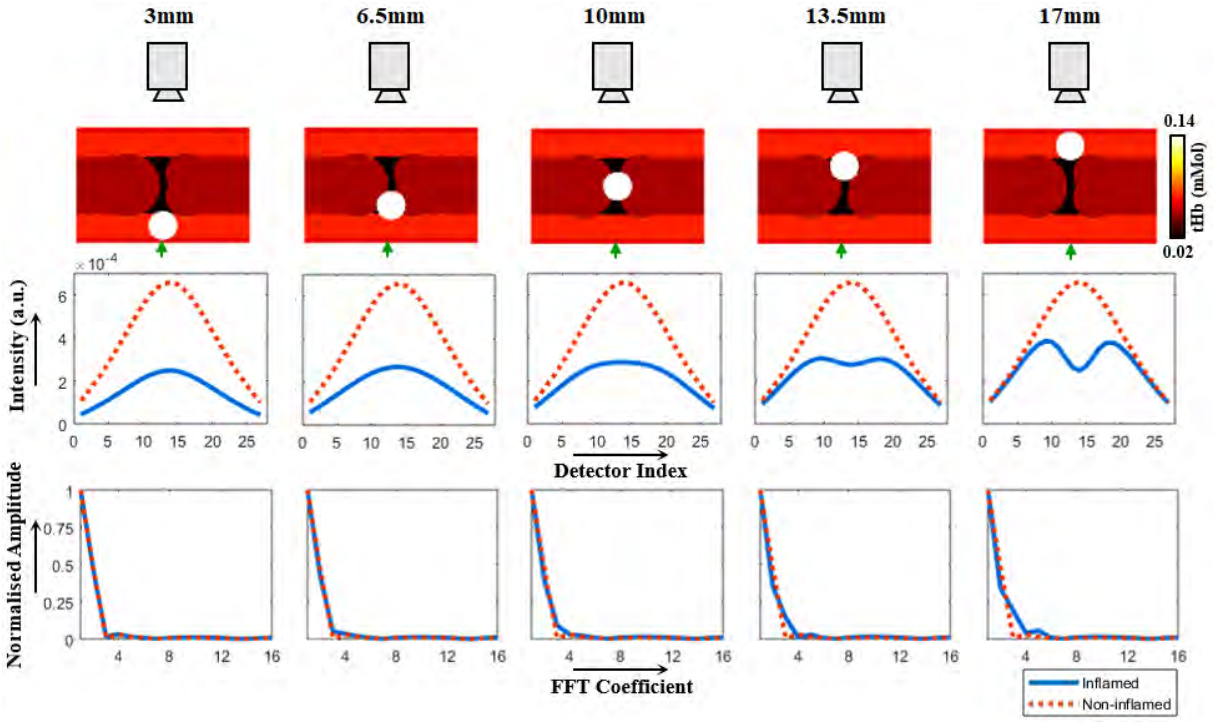

Figure 6.15: Simulation demonstrating the impact of depth of inflammation in finger from detection boundary on observed contrast in spatial profile of boundary data.

greater sensitivity of this feature score as the height was increased. These observations are an intrinsic result of the diffuse nature of light in biological tissue, with greater spatial resolution for a single source and camera set-up typically closer to the detection boundary, making the source and detector orientation of importance when using features sensitive to the spatial distribution of flux. This principle is illustrated in Figure 6.16, in which vein structures present on the upper dorsal side of the joint were clearly resolved in images computed by taking the ratio of DOI images from different sides of the isosbestic point at 630 × 710 nm over 730 × 830 × 930nm, whilst any deeper structures remain unresolved.

Increased resolution closer to the detector side for single source - multiple detector transmission geometry is an inherent result of the physics of diffuse light, which can be understood by considering the narrower shape of the Jacobian sensitivity matrix close to the boundary and was also observed during cylindrical phantom studies in Section 4.3.3 when the anomaly's transverse location was most evident at its highest position of 19.3mm. Evidence from the literature of a higher prevalence of clinically significant synovitis on the dorsal side therefore implies that dorsal imaging should improve sensitivity compared to

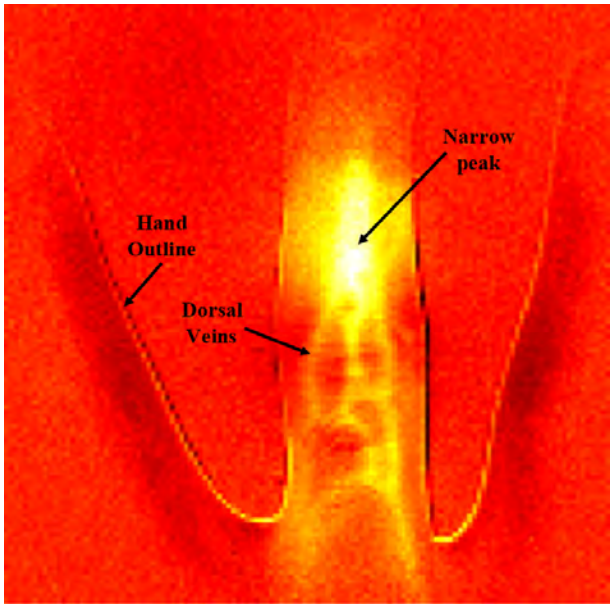

Figure 6.16: Left PIP III joint illuminated on the palmar side, with the image shown resulting from multiplying the DOI transmission images acquired at 830 and 930nm above the isobestic point, then divided by corresponding images at 630, 730 and 810nm, which are below the isobestic point, with the aim of providing a degree of contrast to deoxygenation. The resulting image illustrates the sensitivity to surface contrast, with the veins on the dorsal side of the joint clearly resolved. The peak in intensity seen above the joint is a result of the reduced pathlength when the joint is narrower.

palmar imaging for non-contact, camera-based set-ups.

6.3.3 Typical DOI Contrast

Dorsal optical transmission images of two fingers from the same participant displayed in Figure 6.17 illustrate the typical optical contrast observed between inflamed and non-inflamed joints. The right PIP II, which according to US had no sign of inflammation, showed a peak in intensity at the joint region, similar to that seen reported in transmission images of healthy fingers [85]. Conversely, the left PIP III exhibits an area of lower intensity at the joint region compared to the immediately surrounding finger surface and was clinically inflamed according to US measurements scoring severe synovial hypertrophy, mild effusion and moderate hyperaemia. This manifested as a significant dip in transverse mean intensity profile at the joint region and a correspondingly increased value for the FFT amplitude, compared to that seen in the right PIP II. Both joints were classified

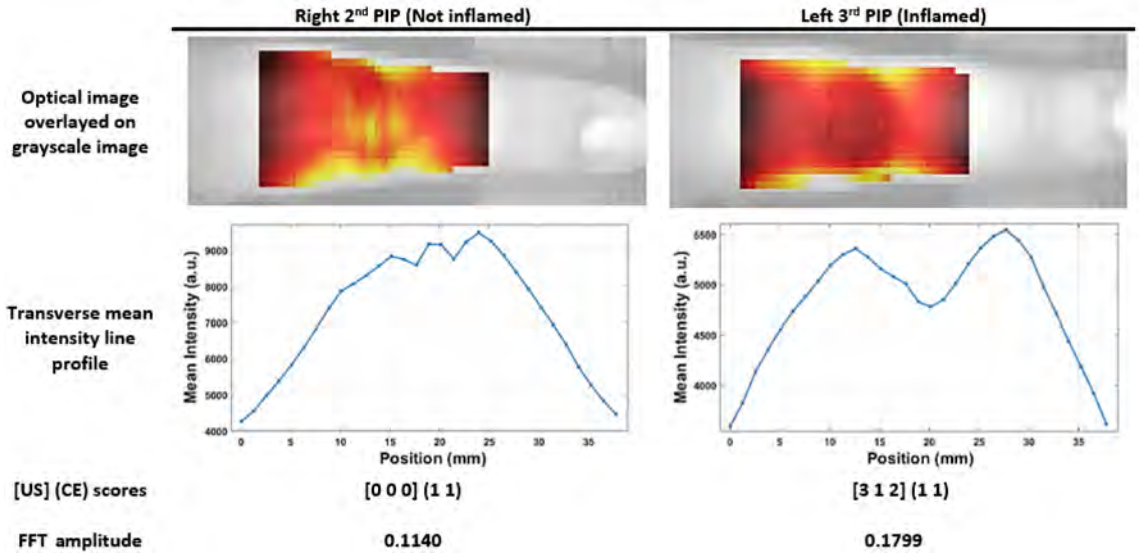

Figure 6.17: Two example PIP joints from the same participant with; top row: optical dorsal transmission images at 650nm when the point source is directly under the joint, overlaid on a brightfield image of the finger, second row: corresponding line profiles of the mean intensity in the transverse direction, third row: reference scores [SH EF PD] (CTE CSW) for each joint and bottom row: normalised FFT amplitude score at 0.050mm^{-1} frequency.

as swollen and tender in clinical examination, highlighting the subjective nature of CE. To investigate whether this optical contrast was observable with illumination from the dorsal side and detection from the palmar side, a single patient (F / 29) with evidence of clinical synovitis in the right and left PIP IV joints, with moderate hypertrophy, clinical tenderness and swelling in both joints and one joint with mild hyperaemia, was asked to place their hands on the imaging platform in both orientations, such that these joints were imaged in the dorsal approach as shown in Figure 3.1, and then rotated 180° such that the palmar side faced the camera and the dorsal side was illuminated.

A region of lower intensity was observed in both joints when imaging from the dorsal approach, shown in Figure 6.18, consistent with that seen in a number of inflamed joints throughout the study, whilst when imaging orientation was reversed such that transmission images were acquired from the palmar side, this optical contrast was no longer visible, with a peak intensity still seen at the joint region. This distinction between dorsal and palmar approaches are similar to differences observed during simulations in Section 6.3.2, when inflammation was either close to the detection side, corresponding to dorsal imaging,

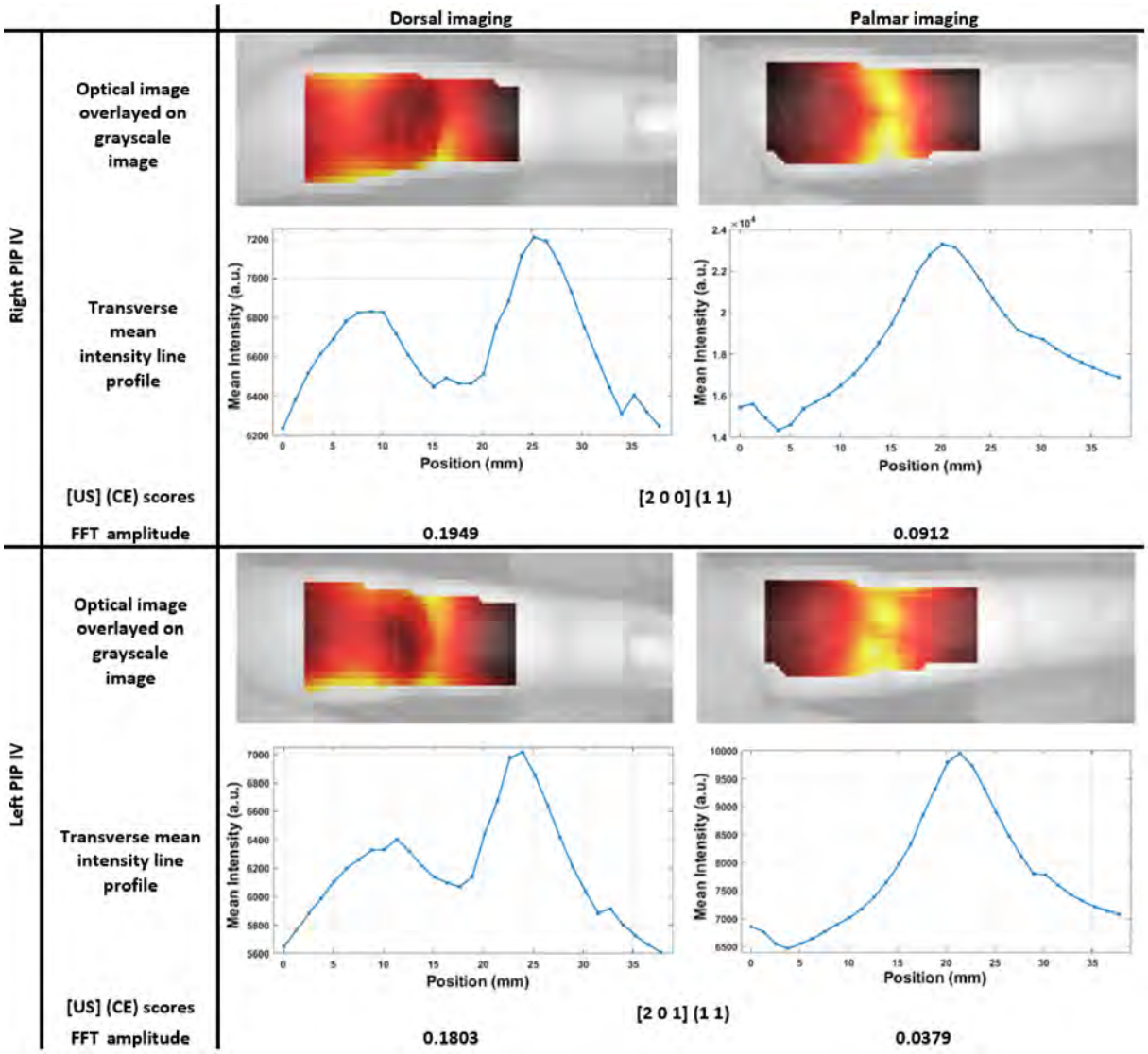

Figure 6.18: Two PIP joints from the same participant each with examples of both the dorsal and palmar imaged from approaches for the same joint. For each joint, top row: optical dorsal transmission images at 650nm when the point source is directly under the joint, overlaid on a brightfield image of the finger, second row: corresponding line profiles of the mean intensity in the transverse direction, third row: reference scores [SH EF PD] (CTE CSW) for each joint and bottom row: normalised FFT amplitude score at 0.050mm^{-1} frequency.

or close to the illumination side, corresponding to palmar imaging, indicating the potential advantage of a clear, identifiable contrast when imaging from the dorsal side.

6.3.4 Inflammation Detection Accuracy

To assess the diagnostic accuracy of DOI, ROC analysis was carried out by varying the threshold value for the FFT amplitude between 0 and 1 in 0.0001 increments and plotting S_E against (1 - S_P). A decision strategy was employed such that for joints labelled as inflamed according to US or CE reference, either a T_P or F_N was recorded if the FFT amplitude was either above or below this threshold respectively, whilst for joints labelled non-inflamed, either a F_P or T_N was recorded if the FFT amplitude was either above or below the threshold respectively.

Results from the pilot study involving all 21 patients are displayed as boxplots of the normalised FFT amplitude at a frequency of 0.050mm^{-1} with 650nm data in Figure 6.19 (a), demonstrating a significantly higher median amplitude for inflamed joints compared to non-inflamed joints, when either US or CE labels are used. The resulting ROC curves shown in Figure 6.19 (c) produce AUC values of 0.801 or 0.888, for US or CE labelling respectively. For example, optimal values for S_E and S_P from for this dataset in Figure 6.19 were 57.6% and 92.3% with CE labels at a threshold value of 0.0861 and 77.9% and 90.9% with US labels at a threshold of 0.1143. Comparison between joints of patients diagnosed with RA compared to joints from non-RA patients with other classified diagnoses in Figure 6.19 (b) demonstrated a significantly increased median amplitude in the diag-RA group, indicative of a comparatively higher prevalence of inflamed joints in this group. This is in good agreement with US and CE labels, with ratios calculated of 2.88 or 2.06 respectively for the prevalence of inflamed joints in diag-RA compared to non-RA and correspondingly greater global scores displayed for the diag-RA group in Table 6.1.

Median FFT amplitude values were statistically higher in inflamed joints compared to non-inflamed at all wavelengths, for both US or CE labelled data, as displayed in Table 6.6 with corresponding p-values calculated using the MWU test. The greatest AUC scores and lowest p-values were seen with 650nm data, whilst the contrary lowest AUC scores and highest p-values occurred with 930nm data. This corresponds with a decrease in the median FFT amplitude as wavelength is increased for both the inflamed and non-inflamed

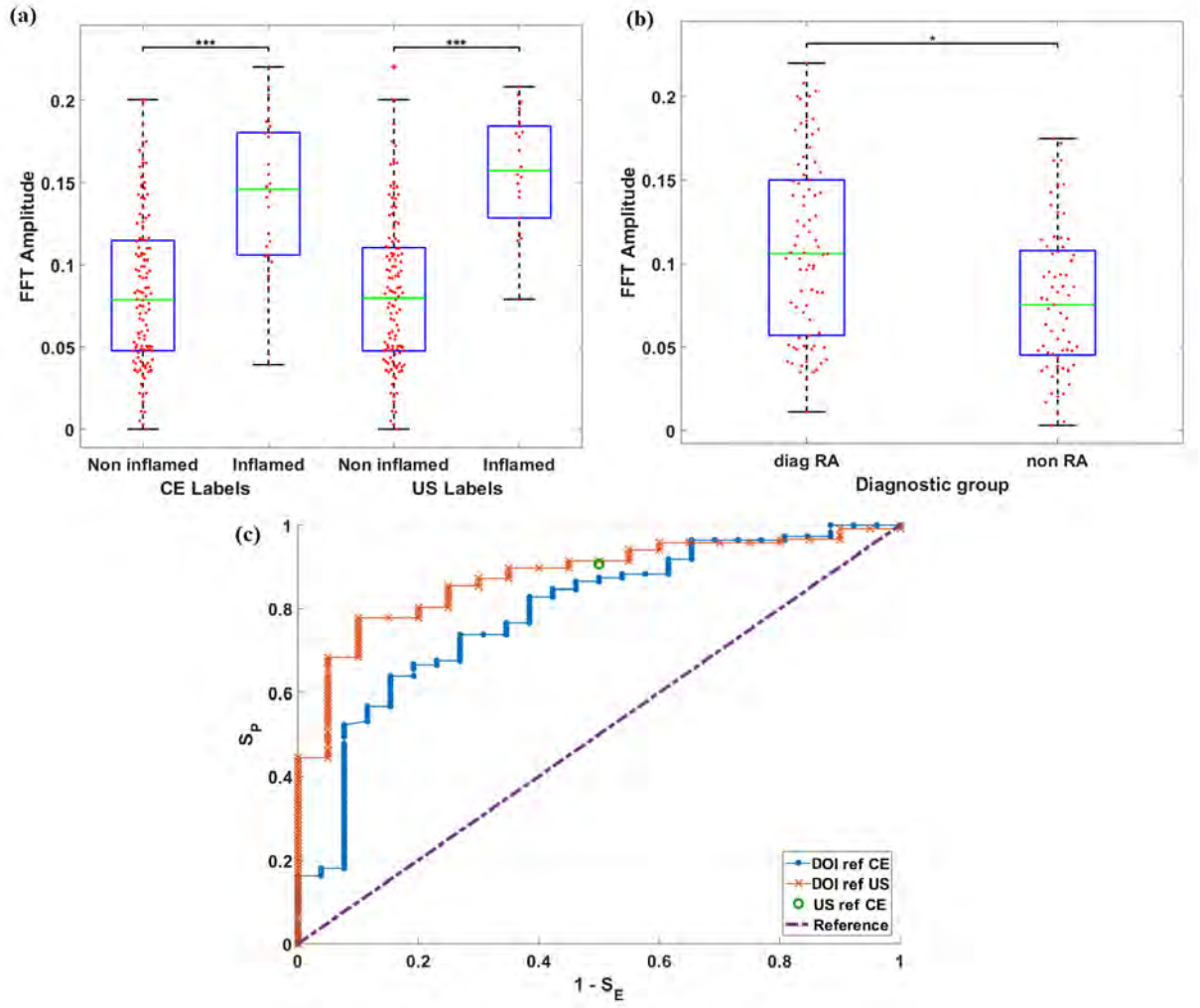

Figure 6.19: Example boxplots for the FFT amplitude at a frequency of 0.050mm-1, (a) comparing non-inflamed against inflamed joints, labelled either using CE or US, or (b) comparing joints from the diag-RA patient group with those from the non-RA group. (c) ROC plots for DOI with either CE or US as reference labels, corresponding plot of S_E and S_P for US when CE is used as a reference label and the reference line corresponding to no ability to differentiate between inflamed and non-inflamed joint. A marker of the sensitivity using US with CE For each graph DOI data was collected at either 650nm.

groups, indicating a decrease in optical contrast from inflammation at higher wavelengths. Consistently, AUC scores were lower and p-values higher for CE rather than US labelled data, indicating better agreement between DOI and US than CE.

The accuracy of detecting inflammation using the normalised FFT amplitude was analysed at all frequencies, with AUC values generally highest at frequencies of either 0.05 or 0.1 mm^{-1}, as shown in Figure 6.20. The corresponding length scales of 20mm or 10mm are approximately similar in scale to the width of the dip typically observed

	λ (nm)	Median FFT Amplitude		p-value	AUC
		Non-inflamed	Inflamed		
US	650	0.0797	0.157	0.00000000757	0.888
	710	0.0785	0.152	0.0000000201	0.877
	730	0.0785	0.151	0.0000000141	0.880
	830	0.0712	0.150	0.0000000201	0.877
	930	0.0582	0.137	0.0000000906	0.859
CE	650	0.0789	0.146	0.00000166	0.801
	710	0.0785	0.132	0.00000844	0.780
	730	0.0785	0.133	0.00000493	0.787
	830	0.0717	0.124	0.0000189	0.767
	930	0.0595	0.111	0.0000181	0.769

Table 6.6: Median FFT Amplitude values for either non-inflamed or inflamed joints as labelled with US scores and corresponding p-values and AUC values from ROC analysis, for all wavelengths when either CE or US were used as class labels.

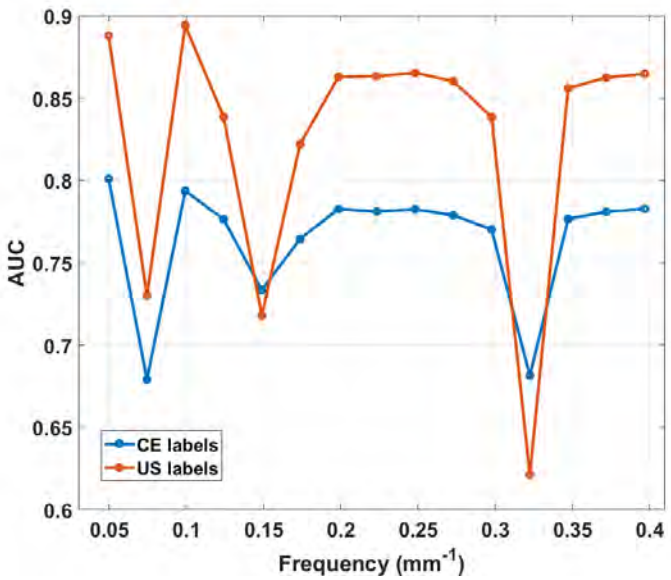

Figure 6.20: Variation of AUC in ROC analysis at all FFT frequencies for 650nm DOI data when either US or CE were used as labels.

in the intensity profiles. This pattern was consistent for all wavelengths, and therefore for conciseness results using amplitude scores at a frequency of 0.05 mm^{-1} have been displayed in this work.

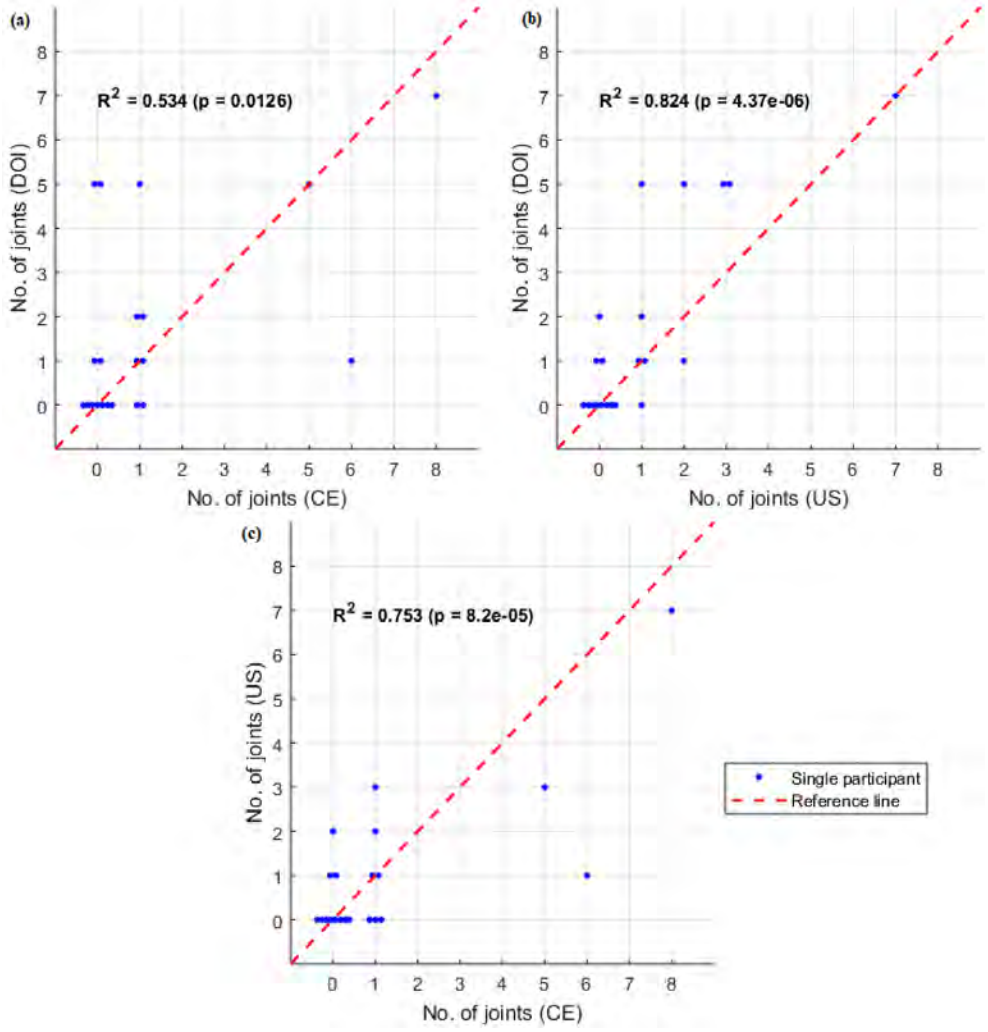

Figure 6.21: Plots comparing the number of inflamed joints on a patient level between either (a) DOI vs. CE, (b) DOI vs. US or (c) US vs. CE, with each marker representing a single participant. Joints were classified as inflamed for DOI using 650nm data, with a threshold corresponding to the optimum Youden index (J = S_E +S_P -1) established from ROC analysis.

All three plots comparing the total number of inflamed joints on a patient level showed statistically significant correlations between each imaging modality ($p<<0.05$). A better agreement was seen between DOI and US than for DOI with CE, with greater R^2 values as shown in Figure 6.21. Plots of CE versus US are also shown for comparison, again with a reasonably strong correlation, but still some disagreement between these two ground truth references.

Regression analysis comparing the relationship between the four-grade, semi-quantitative US scoring system and the normalised FFT amplitude values demonstrated weak but

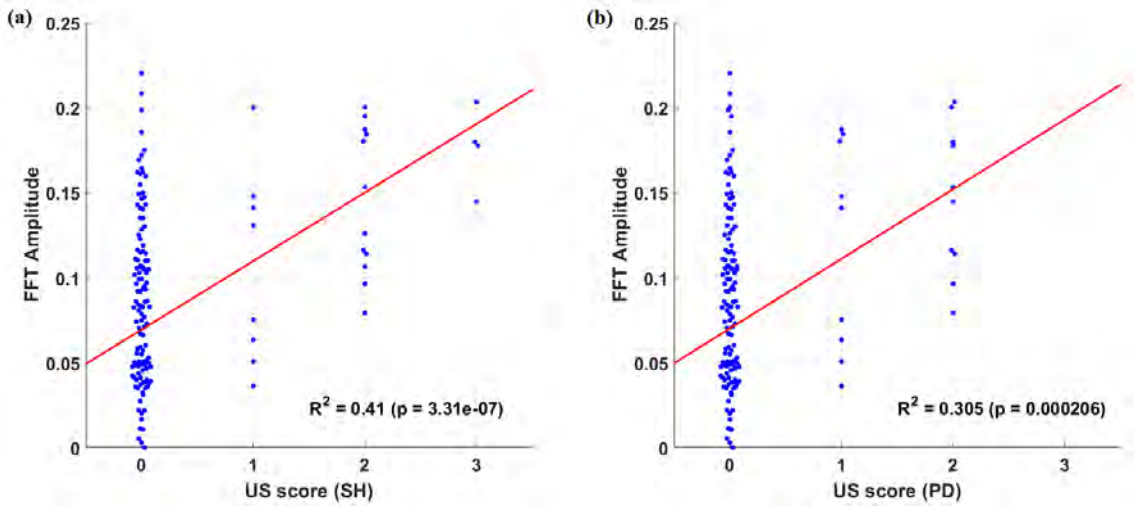

Figure 6.22: Beeswarm plots with each marker representing an individual joint, comparing the relationship for US scores for (a) synovial hypertrophy or (b) hyperaemia (power doppler) with normalised FFT amplitude values at 0.050mm^{-1} frequency using 650nm data. The red line shows the first order polynomial fit.

statistically significant positive correlations in both cases, as displayed in Figure 6.22, providing further evidence that the normalised FFT amplitude is sensitive to altered optical properties that result from localised inflammatory changes within the joint. Agreement with PD ($R^2 = 0.305$) was slightly inferior to SH ($R^2 = 0.41$), however this is most likely a result of the lack of grade 3 scores in the former. This highlights the potential for DOI as a tool for quantitative assessment of severity of inflammation, although a cohort with higher prevelance at scores of 1, 2 and 3, in addition to further comparison with scoring systems utilised in other modalities such as MRI [221], would be required to validate this hypothesis more robustly.

Significantly higher median FFT amplitudes were consistently seen in inflamed joints at all measurement wavelengths, with greatest AUC values at 650nm which generally decreased with increasing wavelength. This corresponds well with the previous literature, with studies of inflammatory mice models using hyper-spectral diffuse reflectance measurements also reporting reduced transmitted intensity at all measured wavelengths, but greater changes recorded for the visible red region (600-700nm) compared to in the NIR window (700-900nm) [2]. Early studies of extruded synovium and synovial fluid samples from human subjects also reported an increase in absorption in diseased tissue for all wavelengths (600

-1100nm) for synovial fluid and for a majority of measured wavelengths for the synovium (600-900nm and 1000-1100nm) [140], with greatest discrepancy in optical properties seen at 650nm, motivating this choice of wavelength for single wavelength studies [91]. Better agreement was seen between DOI and US than DOI and CE, both in ROC analysis and in number of inflamed joints on a patient level, which is encouraging as US has been shown to be more sensitive and reliable than CE [52, 53, 54].

To assess generalisation using this methodology, the data set was partitioned using a patient level leave one out cross-validation (PL-LOOCV) methodology, in which all joints from a single participant were used for testing whilst joints from all remaining participants were used for training, due to the intra-relationship between joints from the same participant. Decision boundaries were established using multivariate fisher's linear discriminant analysis (LDA), with class frequencies used as prior probabilities. When using multivariate LDA, the methodology was shown to generalise well in the PL-LOOCV partitioning scheme, with data from all 5 wavelengths and FFT amplitudes at all frequencies included enabled S_E and S_P of 53.9% and 89.0% respectively to be achieved. Although 144 joints were imaged in this study, due to the expected dependence within joints from the same subject, there are effectively only 21 independent sets of samples in this dataset, meaning a larger cohort would be beneficial for testing this generalisation more robustly.

6.4 Monitoring of Response to Therapy

In addition to diagnosis, medical imaging modalities also play a key role in longitudinal monitoring of disease, particularly for conditions that are highly amenable to a range of treatments and which have varying efficacy, such as for RA as outlined in Section 1.2.3. The utility of multispectral DOI for monitoring response to therapy has been reported for several other conditions, for example to accurately classify between responders and non-responders within the first few weeks of treatment in patients with breast cancer

undergoing neoadjuvant chemotherapy [222, 223, 224], with some evidence of a correlation between recovered oxyhaemoglobin and response rate after a single day of treatment [225]. These studies highlight the sensitivity and improved statistical power of optical techniques for monitoring changes within individuals, particularly in cases of high inter-subject variability.

Two patients within the cohort, denoted patient A (24 / F) and patient B (29 / F) fulfilled the inclusion criteria for regular monitoring as part of an existing study *"is the window of therapeutic opportunity real?"* (TETRA) and agreed to also concurrently participate in follow-up scans after approximately two months using the DOI system. Both patients were treatment-naïve upon initial presentation and diagnosed with RA following assessment in the clinic. DOI data was collected at baseline (Day 0), following which patients began treatment plans using the DMARD Methotrexate at a weekly dose of 15mg, in addition to weekly 5mg supplements of Folic Acid. Due to the severity of inflammation in patient B, a course of the steroid Prednisolone at 15mg daily was also taken following baseline, with this dosage decreasing to 2.5mg over a 5 week period. Both Patients A and Patient B were re-assessed at follow up (Day 42 or 28 respectively) using CE, US and DOI to assess changes in the inflammatory status' of their joints. This longitudinal sub-study provided additional comparison of optical features and US or CE scores in the context of intra-subject temporal changes. Importantly data acquired using the system was demonstrated to be longitudinally reproducible during phantom measurements in Section 4.4.2 and DOT images of joints were shown not to significantly vary over time in a healthy subject in Section 5.2.6.

For patient A only mild inflammation in the left PIP III was observed in US at baseline, with scores of 1 for all three US features and CE indicated both CTE and CSW in the same joint, whilst all remaining joints had scores of 0 for both US and CE features. DOT images of both S_A and tHb in Figure 6.23 revealed a clear distinction in the inflamed joint at baseline, displaying increased scattering and absorption in the central region and a corresponding decreases either side, compared to the remaining non-inflamed joints.

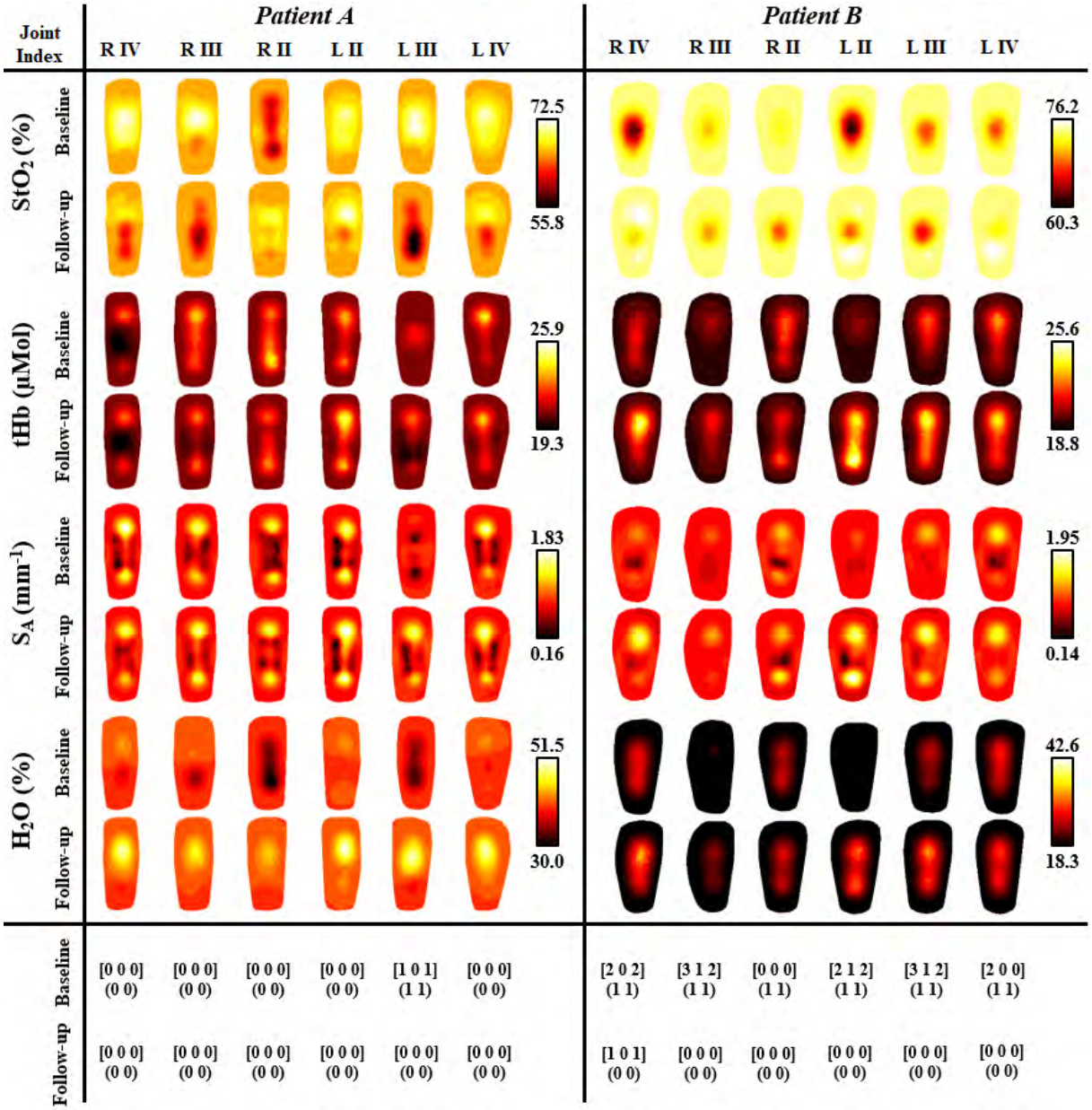

Figure 6.23: Transverse slices of DOT images half way through the joint for all four pathological parameters, both at baseline and follow up scans. Corresponding CE and US reference scores are shown as [SH, EF PD] (CTE CSW) at both time points.

Following 5 weeks of therapy, all joints in patient A were scored 0 on US and CE features and images of S_A and tHb for the left PIP III reverted to a similar structure to the remaining joints, which were reasonably consistent across both time points. Patient B presented with significantly more active disease, with moderate or severe inflammation in US for the left PIPs II-IV and right PIPs III-IV from SH or PD scores, and all joints were tender and swollen in CE, but no inflammation for US for the right PIP II at baseline.

Following 28 days of treatment and the intra-articular steroid injection, US and CE scores had all dropped to 0, with the exception of the SH and PD in the right PIP IV. Although obvious evidence of inflammation from DOT images in Figure 6.23 was less discernible for Patient B than Patient A, there appears to be a consistent change in inflamed joints between the two time points, with greater contrast between the central joint region and the bone either side at follow up scans than baseline in S_A and tHb images, whilst the non-inflamed right PIP II did not qualitatively change as significantly. Images of StO_2 and H_20 were mixed for both patients, with no obvious pattern corresponding to inflammation.

Statistical features displayed in Figure 6.24 revealed a significantly lower mean, max and variance values for S_A in the inflamed joint of Patient A compared to the other joints, indicative of its loss in contrast between the bone and the joint region. In Patient B all joints observed a consistent increase in the mean, max and variance values for both S_A and tHb. Although the absolute global changes are contrary to the expected physiological responses to reduction in inflammation outlined in Section 1.1.2, localised values for the central joint region appear elevated in inflamed compared to non-inflamed joints. The increase in variance as inflammation subsided following treatment indicative of an increase in structure and contrast between bone and joint space in reconstructed images is in agreement with previous optical RA studies [149, 153]. The global increase in H_2O from baseline to follow-up in both patients did not particularly correspond to reference score changes in patient A. As the medication administered had a systemic impact, it's possible that the physiological parameters of all joints may have been altered independent of their inflammatory status, although it would require administering this medication to healthy volunteers with non-inflamed joints to verify this hypothesis.

Longitudinal changes in DOI transmission images were also assessed, shown in Figure 6.25. In patient A, a drastic intensity drop in the centre of the transverse mean intensity profile was seen in the inflamed left PIP III at Day 0 compared to the remaining non-inflamed joints, which diminished as inflammation subsided in this joint to produce a clear peak after 42 days of treatment. This is reflected in the FFT amplitude scores with 0.206

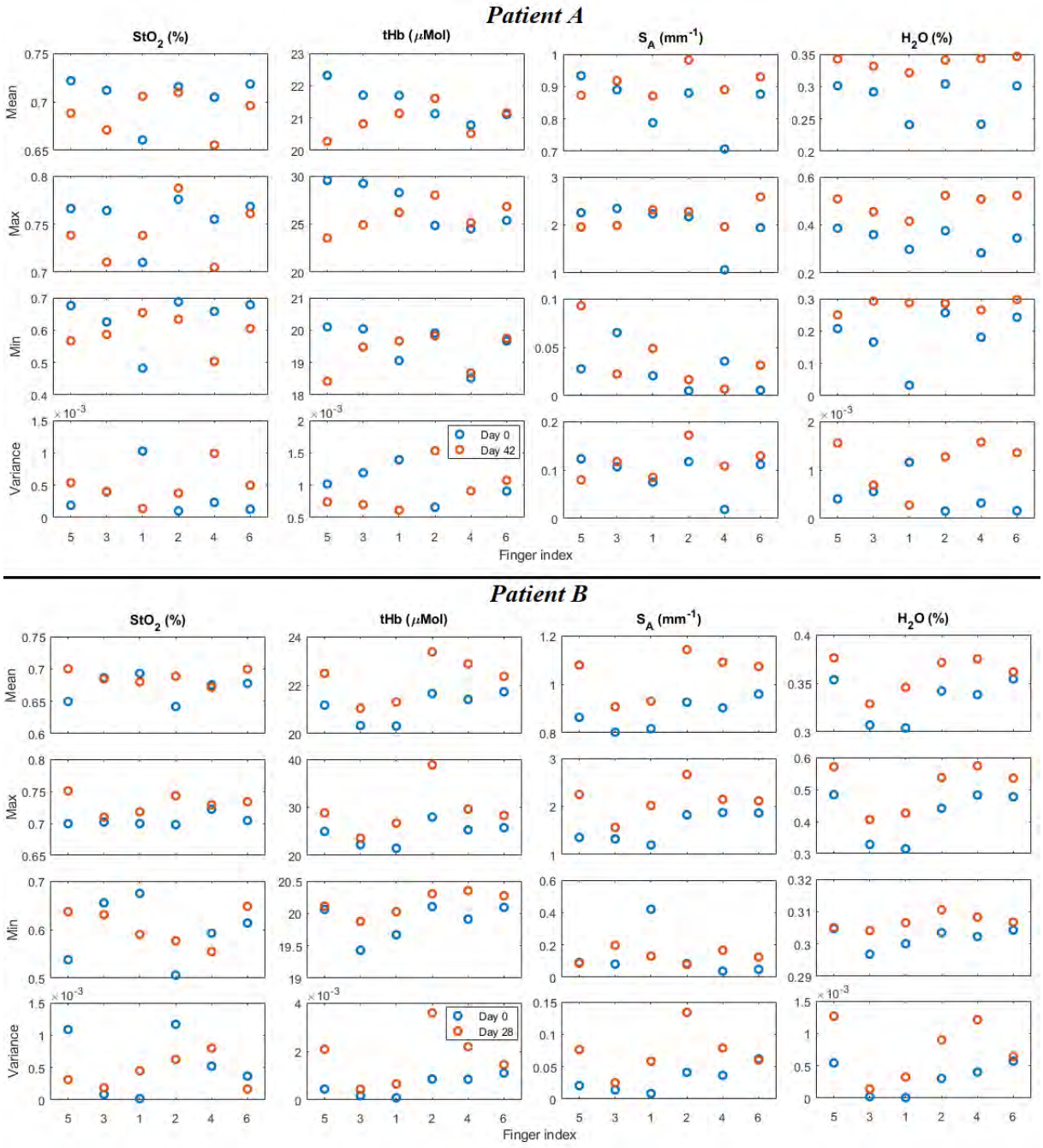

Figure 6.24: All four basic statistical parameters plotted for each joint and each patho-physiological parameter. Values are displayed at both baseline (blue) and follow-up (red) for both longitudinally monitored patients.

in the inflamed joint compared to non-inflamed values (0.071-0.148). Furthermore, the changes in transverse mean intensity profiles between Day 0 and Day 42 were relatively small in non-inflamed joints compared to the left PIP III. Transverse mean intensity profile drops were again evident in the right PIP III and IV and left II-IV inflamed joints at

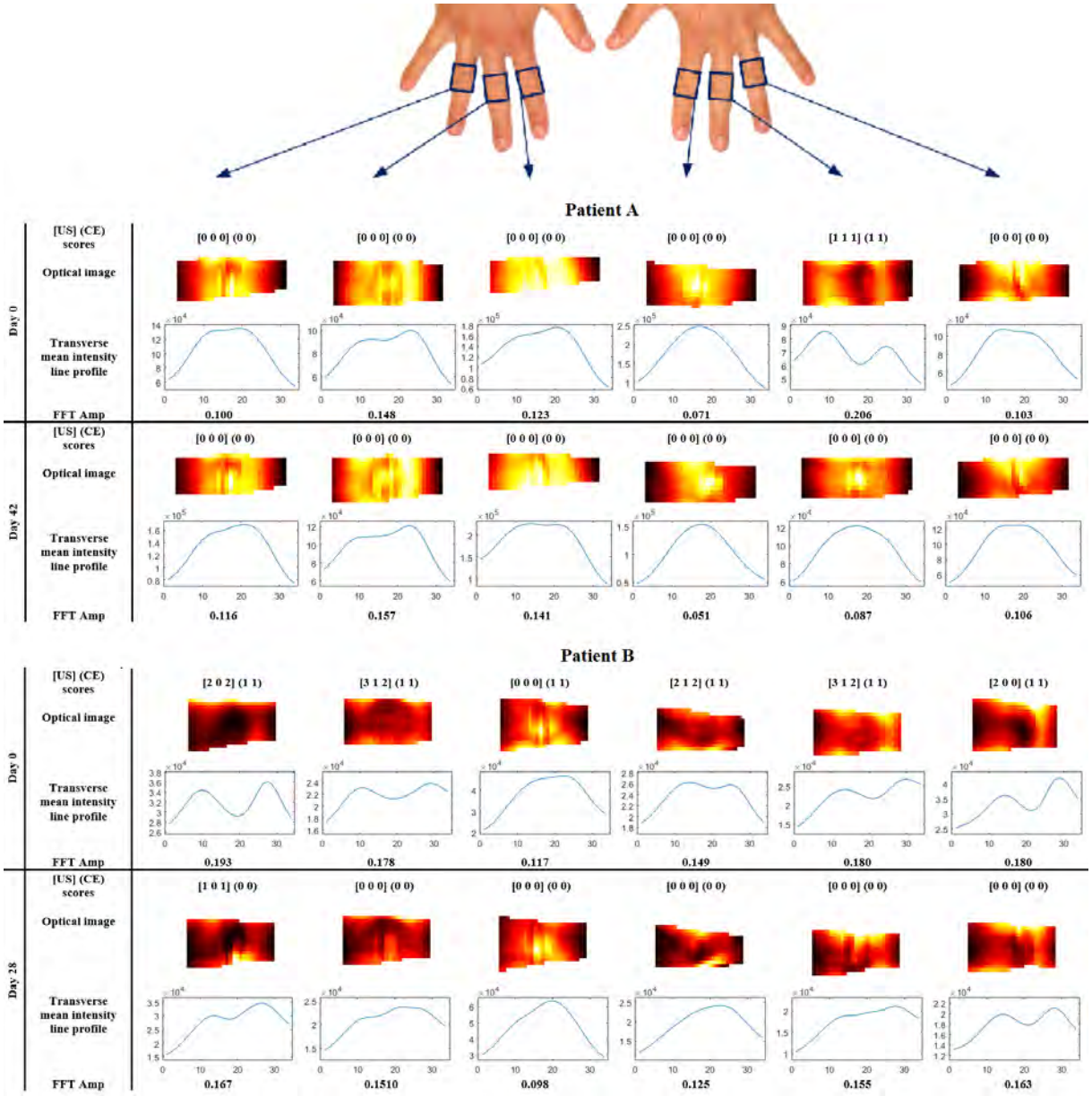

Figure 6.25: DOI images both at baseline and follow up for 650nm, with respective transverse mean intensity profiles and FFT amplitude scores. Corresponding CE and US reference scores are shown as [SH, EF PD] (CTE CSW) at both time points.

baseline. At Day 28, a visible increase in signal could be directly observed in the central region of DOI images, with all joints recording a corresponding decrease in the FFT amplitude from baseline. Quantitatively, these changes in FFT amplitude from baseline to follow-up were in good agreement with the total sum of all US and CE reference scores for both patients, as shown in Figure 6.26. Transverse mean intensity profile drops and elevated FFT amplitudes were still seen at follow-up in both the right PIP IV and left PIP

IV, which were recorded to have either mild inflammation or no inflammation respectively according to US, the latter of which may be a false positive, as a result of erroneous image analysis or wrinkles in the finger, or it may be reflective of true underlying inflammation undetected in US and CE.

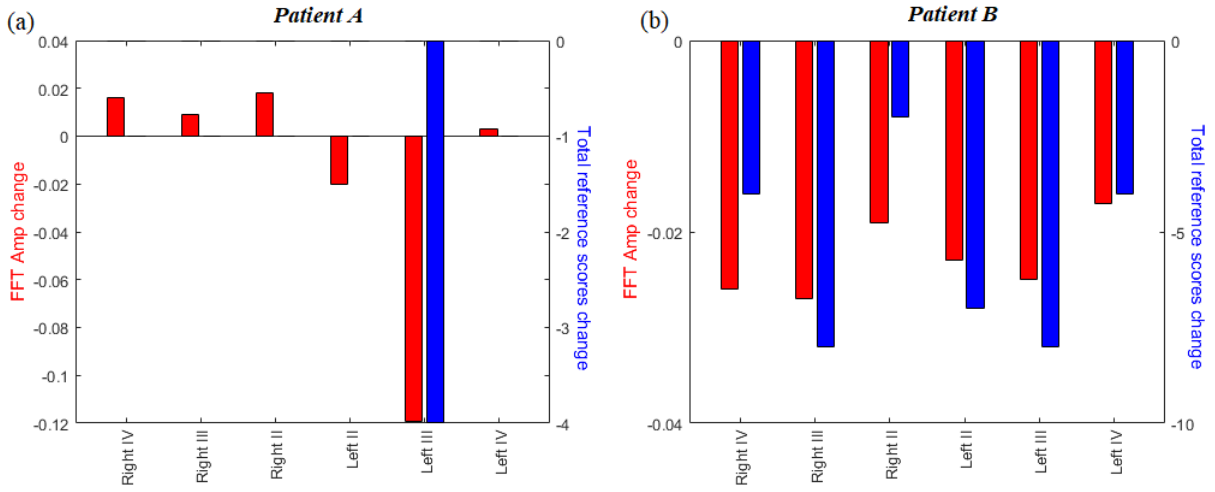

Figure 6.26: Comparison of change from baseline to follow-up scans for FFT amplitude from DOI and total reference scores, calculated as the sum of SH, EF, PD, CTE and CSW, for both patients and each joint.

During this small longitudinal study monitoring patients undergoing treatment, certain optical biomarkers appeared sensitive to inflammatory changes in the joint, including S_A, tHb and FFT amplitude, which to the authors knowledge, is the first evidence of detection of response to therapy in RA patients using optical techniques. A greater sample size, which includes both non-inflamed joints and inflamed joints undergoing a range of changes in inflammatory status will be required to determine the capabilities of DOI for distinguishing between responders and non-responders and produce statistically significant conclusions.

6.5 Patient Feedback

A key advantage of the proposed device is its non-invasive, safe and easy to use nature, however as a relatively unknown imaging modality amongst the general public, it will be

important to ascertain patients views and experiences to allow successful implementation in Rheumatology clinics. Following a presentation and demonstration of the system during the annual Rheumatology Patient Group Meeting, imaged patients were asked to provide feedback on their experiences as either excellent, OK, poor or not sure, from which 7/7 (100%) answered excellent, indicating that a desire for novel, diagnostic imaging modalities for inflammatory arthritis such as these also exist from a patient perspective. As a prototype clinical device, it was useful to document the design challenges faced and verbal feedback on areas for improvement to make future systems more reliable, safe and comfortable data acquisition protocols. Patient feedback during the study was that further improvements in the ergonomic design of hand supporting platform and seating were highly desirable, particularly as RA patients are commonly elderly or experiencing a degree of disability. For example, positioning the platform adjacent to the body would provide a more natural position, such that any strain on commonly afflicted joints such as the elbow, wrist, shoulder or back is minimised, incorporating more support to help patients remain still during imaging or finally a design that allowed a patient to sit at a lower height or in a wheelchair. Patients also commented that being able to see the live feed of optical images being acquired helped to make them feel more comfortable during the scan.

It is hypothesised that like in breast imaging, optical techniques are highly sensitive to changes in underlying inflammation and should show strong predictive power when monitoring the same individual for response to therapy. Wider and more in depth longitudinal studies are needed to test this hypothesis.

6.6 Conclusion

The focus of this chapter was on presenting results from a pilot clinical study involving 144 joints from 21 patients with inflammatory arthritis, with the aim of detecting joint inflammation for diagnosis and monitoring of RA. Analysis of reconstructed DOT images indicated some sensitivity to the inflammatory state of tissue during longitudinal studies

of changes in clinical parameters in response to therapy. Achieving high classification accuracies from single-time point examination across the cohort proved challenging using DOT images, despite the extraction of additional, more complex features, with AUC values of up to 0.621 or 0.657 reached when US or CE measurements were used as reference labels, respectively.

A normalised FFT based algorithm, was presented for the detection of inflamed joints, engineered to extract features which assesses the spatial distribution of transmitted light flux through the joint that were less dependent on total intensity. The aim of this approach was to minimise the impact of inter-subject variability in absolute boundary flux without the need for complex modelling in solving an under determined and ill-posed tomographic inverse problem. Similar statistical processing approaches have proved beneficial in DOI, for example in breast cancer diagnosis using Z-score normalisation, in which the number of standard deviations of a measurement from the sample mean was calculated to transform all scores to a similar magnitude, thus reducing the impact of inter-subject optical variability [224]. The impact of joint orientation on DOI was demonstrated through simulation studies, in which the normalised FFT amplitude showed greater sensitivity to inflammatory changes occurring closer to the detection boundary for a non-contact, camera-based set-up, supported by results from a single patient able to rotate their hands. Evidence from the literature of a higher prevalence of clinically significant synovitis on the dorsal side consequently makes imaging orientation of importance in transmission DOI. These preliminary results have highlighted, for the first time to the authors knowledge, the importance of considering orientation in DOI of joints, although more comparative studies between dorsal and palmar approaches are needed in future. Using the proposed normalised FFT methodology applied to dorsal optical CW transmission images demonstrated accurate detection of inflamed joints from single time-point examination, with AUC of up to 0.888 and diagnostic accuracies of up to 77.9% and 90.9% for S_E and S_P respectively achieved when optimal thresholds were selected based on a maximum value for the Youden index, drastically superior to values reached when using absolute transmitted intensity only.

A large number of extracted features were considered in this chapter, from either 3D images of the joint pathophysiology using multispectral DOT or raw DOI transmission images at individual wavelengths. AUC values from ROC analysis provided useful insight into the variation of these distinct features and their individual capabilities for classifying inflamed and non-inflamed joints. For example, this analysis highlighted the potential benefit of considering spatial analysis of DOI transmission images as opposed to absolute transmitted signal. The natural extension of this work, when a larger cohort of patients is available, is the implementation of a more complex ML scheme, in which data is partitioned into appropriate training, testing and validation sets in order to fully assess the potential diagnostic accuracy of these features. In this way, optimal weightings and thresholds can be selected using the training data based on their performance when classifying unseen test data, with generalisation of this performance then verified on a separate validation set [226]. In such a scheme, the benefits of combining multiple features that provide distinct discriminatory value can be properly assessed without the risk of over-fitting. FFT features based on DOI measurements were subject to a very distinct processing pipeline compared to the additional SI data and more complex reconstruction algorithms required to recover pathophysiological parameters using DOT. These two techniques may therefore contain orthogonal information that when combined could improve diagnostic accuracies. One drawback of this approach is that the benefits of simplicity for data acquisition, speed and low cost of DOI transmission imaging on its own would no longer be relevant when tomographic data is additionally incorporated, so a significant increase in diagnostic accuracy would have to be demonstrated to make this approach worthwhile.

CHAPTER 7

CONCLUSIONS AND FUTURE WORK

7.1 Conclusions

Current paradigms in the treatment of rheumatoid arthritis, such as the importance of early diagnosis and a variation in efficacy of treatments, create a burden on healthcare systems across the world and create a requirement for novel, low-cost and effective imaging tools able to support clinical decision making. Successful translation of optical imaging devices from bench-top investigations to application in rheumatology clinics will require certain characteristics to justify their usefulness over existing imaging modalities, such as low cost, ease of implementation by non-clinical staff and non-invasiveness. Despite promising results reported within the academic community, the routine implementation of optical devices by clinicians for the diagnosis and monitoring of arthritis patients has not yet been realised. In previous studies involving transillumination diffuse optical imaging for detecting joint inflammation [159, 91, 141, 136, 217, 218], all devices had specific limitations in the context of clinical translation, relying on either; follow up assessment for comparison to baseline, cuff occlusion to induce haemodynamic changes, or expensive, tomographic, frequency domain measurements, for accurate detection of inflammation.

In this work, a hand imaging system combining surface imaging techniques and optical transmission imaging in a single data acquisition work-flow was presented in Chapter 3 for detecting inflamed joints in patients with rheumatoid arthritis using multi-spectral,

continuous wave diffuse optical imaging. A fully non-contact novel methodology was developed through a combination of complementary metal-oxide-semiconductor-based projector-camera surface imaging technology and galvanometer-based optical diffuse optical imaging data, which together allowed for rapid acquisition of tomographic datasets in ≈2mins per joint, important for minimising the possibility of motion errors and time pressure on arthritis clinics. From these measurements patient specific finite element method meshes were created and used to model light propagation through the joint, with multispectral transmission data at a set of optimised wavelengths allowing three dimensional maps of pathophysiological parameters oxygen saturation, total haemoglobin, water and scattering amplitude to be recovered. The resulting device provided safe, low build cost (≈ £30,000), operator independent and quantitative measurements of the human hand joint.

The proposed clinical-prototype system was systematically studied during phantom experiments outlined in Chapter 4, demonstrating its ability to; accurately recover the surface profile the hand, spatially and quantitatively reconstruct optical contrast in three dimensions, and provide stable measurements over a period of several weeks. Subsequent results from healthy subject studies in Chapter 5 demonstrated consistent evidence of the synovial region between the proximal and intermediate phalangeal bones in recovered images, a responsivity to dynamic changes during cuff occlusion and a greater variability in continuous wave diffuse optical tomography images between different patients than when comparing fingers from the same patient. The observation of high intersubject variability in absolute diffuse optical imaging is not unique to this work, with similar observations for total haemoglobin in absolute breast imaging [206, 207] and cerebral near infrared spectroscopy, which has proven useful for monitoring intra-subject changes in cerebral oxygenation during cardiac surgery [227], but high intersubject variability has made single time-point measurements of tissue oxygen index insufficient for the detection of hypoxia during traumatic brain injury when baseline measurements will never be available [173, 228]. The same conclusions were also reached in the context of previous joint imaging

studies, with one study stating that "laser images showed high inter-individual variations in optical joint characteristics, resulting from individual differences in joint anatomy" [87].

In the final Chapter 6, results from a pilot study involving 144 joints from 21 rheumatology patients were presented. Despite evidence during longitudinal monitoring studies of two patients demonstrating that biomarkers such as scattering amplitude and total haemaglobin image features may be sensitive to inflammatory joint changes, identification of diffuse optical tomography image features capable of consistently discriminating between inflamed and non-inflamed joints from single time-point examinations across the whole cohort was challenging. A normalised fast Fourier transform algorithm applied to optical continuous wave transmission images was presented and, in distinction from previous work, optical images were acquired from the dorsal side with illumination on the palmar side and with areas under the reciever operator curve of up to 0.888 and diagnostic accuracies of up to 77.9% and 90.9% for sensitivity and specificity respectively achieved when using the proposed normalised fast Fourier transform methodology. These studies have demonstrated a clear indication of the presence of an information content particularly related to the spatial signature of transmitted flux that was indicative of the inflamed state of a joint. Spatial analysis of dorsal optical transmission images using the presented work-flow may enable future development of a clinically viable, low cost device for assessing inflammation in arthritis patients, without invasive contrast agents, cuff occlusion or comparison to baseline. This type of device would prove particularly beneficial as pre-clinical screening tool, for example in the general practitioner surgery, to assist primary care practitioners in overcoming the challenges highlighted in Section 1.2, such as the poor specificity to rheumatoid arthritis of commonly reported joint symptoms and the consequently longer delays in referral of patients to specialist clinics. Further analysis of diffuse optical tomography images using ML approaches such as deep neural networks together with sufficiently large clinical datasets are likely to prove powerful for achieving superior diagnostic accuracies from diffuse optical imaging transmission images, predominantly due to their automated approach for extracting optimal features, and

preliminary investigations using simulated arthritic diffuse optical tomography data have demonstrated a degree of improvement [229, 230].

The major achievements resulting from this work include the design of a fast, safe, operator independent and accurate system for imaging through rigorous testing and characterisation, the demonstration that a galvanometer-based illumination set-up can provide a flexible and robust approach for controlling source positions when imaging human joints and the reaffirmation that diffuse optical imaging measurements are subject to high levels of inter-subject variability for human joints. Finally, the development of a novel normalised fast Fourier transform algorithm, engineered to extract spatial signature reflective on inflammation has been proposed and demonstrated, for the first time within the academic community, the importance of considering the asymmetrical distribution of inflammation on optical contrast, with a preference towards dorsal imaging for this presented algorithm.

7.2 Future Work

Wavelength optimisation carried out in Section 2.4.1 was a theoretical process based on maximising the uniqueness and minimising the residual of the inverse problem for the given number of wavelengths and chromophores of interest. A data driven approach, such as outlined previously [231], in which hyperspectral clinical data of patients could be collected using a tuneable liquid crystal device [232] or a pushbroom camera [233] would allow a specific set of wavelengths to be chosen based on those with greatest differentiation between inflamed and non-inflamed joints in a ML construct. The small dimensions of finger joints make it feasible that data below 650nm could even be acquired with a sufficient signal to noise ratio in relatively short integration times, which may add value. Free space modelling of light propagation between the finite element model mesh boundary and corresponding camera pixels has been shown to improve accuracy of flux mapping in bioluminescence tomography [185], to account for the impact on detector coupling from either varying

pathlength or the Lambertian reflectance, in which the normal to the surface is the angle of maximum photons exiting the tissue. Although this variance was minimised by only assigning detectors to a central region across the uppermost surface of the joint, further investigation is required to assess the quantitative impact of incorporating free space modelling on reconstructed diffuse optical tomography images in the proposed non-contact work-flow. The presence of low scattering fluid together with the small dimensions means that implementation of higher order solutions to the radiative transport equation such as spherical harmonics for the forward problem, as outlined in Section 2.5.6, would be of great interest in future as these are likely to improve the accuracy of predicted boundary data and therefore boost the achieved diagnositics accuracies, such as has been reported in previous comparable studies [162, 161]

In order to fully assess the capabilities of diffuse optical imaging for diagnosis and monitoring of rheumatoid arthritis patients, extensive patient studies will be required to assess the clinical relevance of the recovered parameters in future. One limitation with the presented pilot-study is that the ultrasound and clinical examination reference measurements may not be representative of the ground truth inflammatory status, particularly as some disagreement was seen between these two variables. Furthermore, optical imaging is known to be a highly sensitive to pathophysiological changes, so further investigation will be required to ascertain whether false positives are a result of noise, for example excessive wrinkles in the finger, or truly reflect underlying inflammation which remains undetected by ultrasound or clinical examination. The additional inclusion of magnetic resonance imaging measurements would be useful further validation in this regard. Additionally, the small number of patients together with a low prevalence of inflammation (13.9% and 16.7% for ultrasound and clinical examination respectively) mean it will be important to assess the generalisation of these accuracies in future work, using a larger patient cohort and testing different ML classification schemes such as those presented previously [88, 87], including linear discriminant analysis, quadratic discriminant analysis, k-nearest neighbours, self-organizing maps and support vector machines. Finally extension

of classification to multivariate analysis, in which many features are combined to improve predictive capabilities, should provide improved diagnostic accuracies, for example through combining total haemaglobin and scattering amplitude or many fast Fourier transform amplitudes at multiple wavelengths. The distinction in transmitted optical signal between acquisitions from either the palmar or distal approaches during simulation and in two joints from a single patient, and its significance due asymmetrical prevalence of joint inflammation in rheumatoid arthritis patients, means that further investigations that directly compare these modes of acquisition should be carried out. For example, a mirror based system capable of switching between dorsal and palmar transmission imaging modes during the same imaging session could be designed to facilitate this study. Although proximal interphalangeal joints have been the focus of this work, inflammation is more prevalent in rheumatoid arthritis patients in the metacarpophalangeal joints as outlined in Appendix A.4 and therefore should be included in future studies. Finally, longitudinal studies similar to those carried out for ultrasonography [58], in which scores during early rheumatoid arthritis patient assessments are compared with long-term outcomes and responses to therapy, are highly desirable to assess the predictive significance of these optical biomarkers and ascertain their usefulness for guiding clinical decision making.

A number of uncontrolled latent variables can potentially impact the pathophysiological state of arthritic joints, some examples of which include; age, gender, smoking, Raynaud's syndrome, body temperature, vasoactive medication and even time of day, with the circadian clock known to impact severity of symptoms in rheumatoid arthritis [234]. The sensitivity of optical signals on the physiological state of tissue means is would be of interest to explore the effects of these variables on optical scores. Finally, inflammation in the joint is associated with other musculoskeletal diseases, including gout, osteoarthritis, psoriatic arthritis etc. and further investigation to assess whether optical features can distinguish between these conditions could be extremely beneficial to clinicians.

APPENDIX A

APPENDIX

A.1 Materials for System Calibrations

A.1.1 Biological Tissue Mimicking Phantoms

Two plastic phantoms (INO, Quebec, Canada) were used for experimental testing of the system against a known ground truth, a cylindrical version and a cuboid version as shown in Figure A.1. These were both constructed from a polyurethane base, with carbon black dye added as an absorbing chromophore.

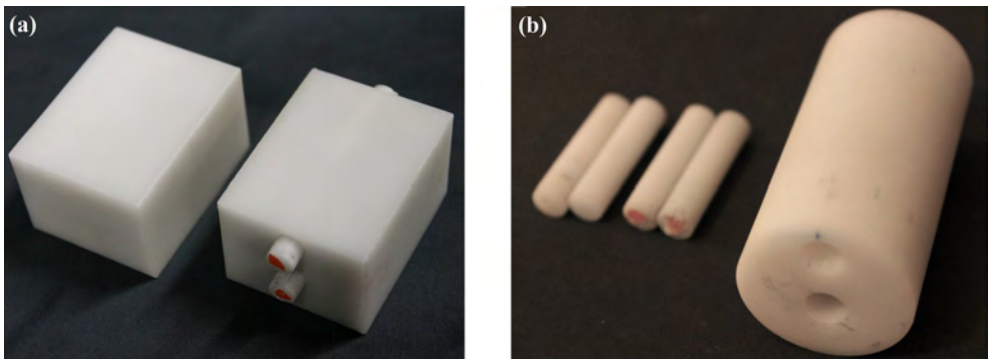

Figure A.1: Photographs of (a) the heterogeneous cuboid phantom with cylindrical anomaly rods included and (b) the cylindrical phantom next to its background matching or anomaly rods.

The spectrally varying optical properties of these phantoms were measured previously in time resolved experiments [194], plotted in Figure A.2. The three sets of data from these studies were; nominal values provided by the manufacturer, values resulting from

time resolved measurements when a semi infinite slab is assumed, and finally values when the specific geometry of the object is included in the forward model for the same time resolved measurements. For the purposes of this work, the geometry specific values from these studies were expected to be most accurate and used as *a priori* ground truth values. During these time resolved experiment the optical properties for the cuboid were measured between 600-1000nm, whilst the cylinder measurements were limited to 600-900nm. As data was collected using the system at 930nm, the optical properties of the cylinder at this wavelength were estimated, by assuming the spectral profile of μ_a was the same for both phantoms as they were constructed from the same material and regressing the spectral response of the cuboid phantom to the cylinders, to extrapolate a value for μ_a at 930nm as summarised in Table A.1.

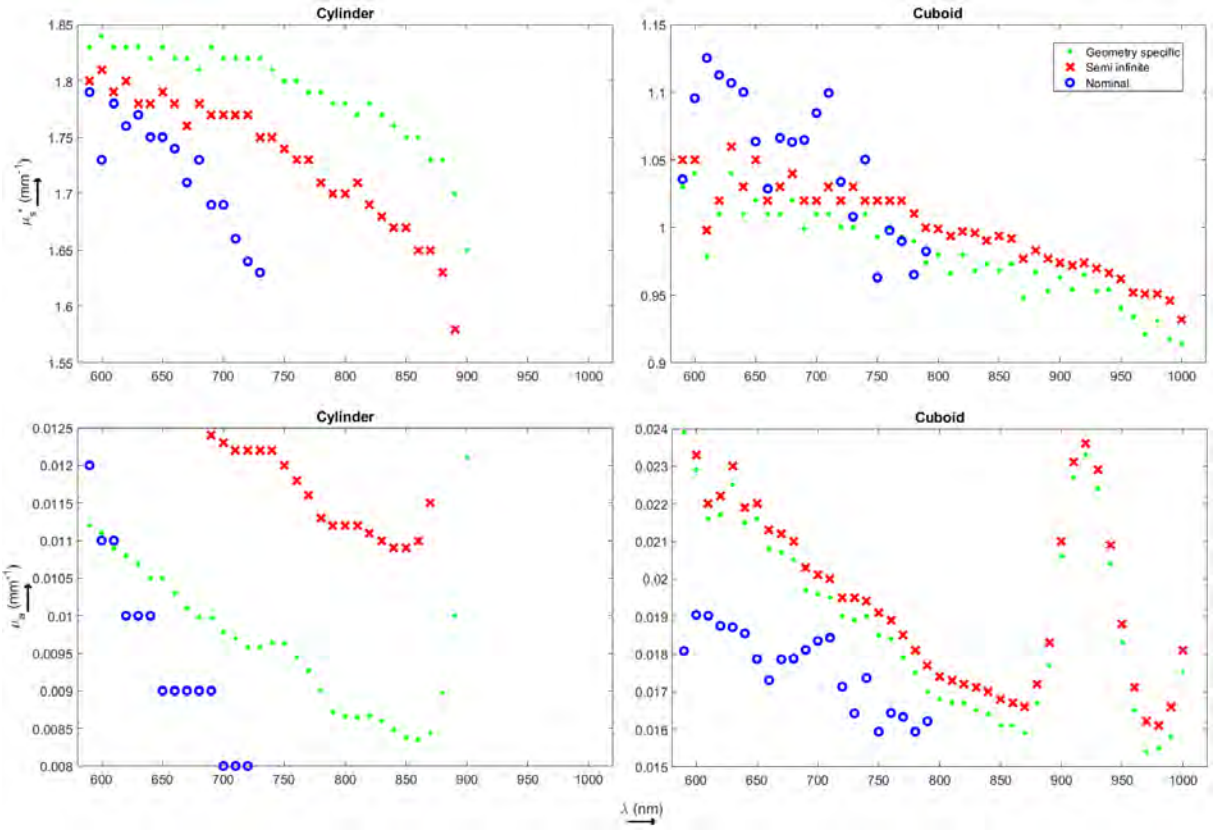

Figure A.2: Spectrally varying absorption and reduced scattering coefficients for either the cylindrical or cuboid phantoms, including nominal values provided by the manufacture or analytical semi-infinite and geometry specific solutions for time-resolved data provided by Jamie Guggenheim [194].

The final geometric specific background values for μ_a at each wavelength of interest

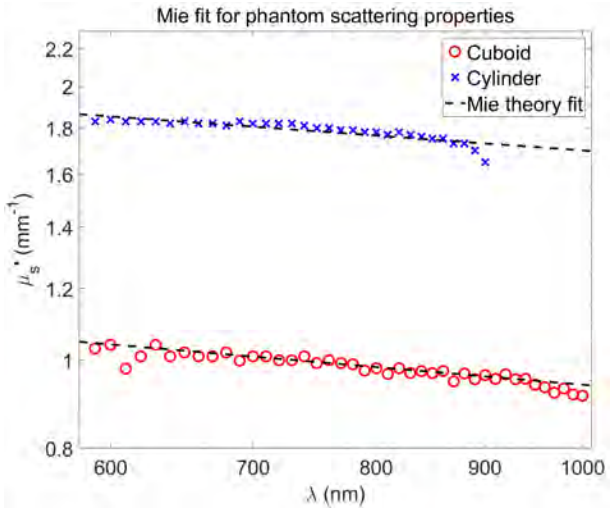

Figure A.3: Reduced scattering coefficients for the Cuboid and Cylinder against wavelength, plotted with a log-scale y-axis, with corresponding first order polynomial fits used to calculate using Mie theory.

together with values for S_A and S_P are summarised in Table A.1. The scattering parameters were estimated for both phantoms according to Mie theory using Equation 2.4 for the least squared first order polynomial fit to $(ln(\mu_s')$ against λ, as shown in Figure A.3.

Phantom	μ_a (630nm)	μ_a (710nm)	μ_a (730nm)	μ_a (830nm)	μ_a (930nm)	S_A	S_P
Cuboid	0.0216	0.0195	0.0189	0.0165	0.0224	0.94	0.20
Cylinder	0.0105	0.0097	0.0096	0.0086	0.0114*	1.70	0.17

Table A.1: Absorption at the wavelengths of interest and scattering properties calculated using Mie theory, used for either phantom during system characterisation. *Estimated value by extrapolation of the spectral response of the cylindrical phantom based on the cuboid.

A.1.2 Reflectance Standards

Four diffuse reflectance standards (Spectralon, Labsphere, North Sutton, USA) as shown in Figure A.4 were used for multiple experiments including for system calibration or characterisation. The standards were coated in barium sulphate to produce a spatially flat ($\pm$ 4%) and spectrally flat ($\pm$ 1%) highly Lambertian reflector over the 300 - 2400nm range, with reflectances specified as either 99% , 50%, 25% or 2% respectively. By illuminating

Figure A.4: Diffuse reflectance standards with either 99%, 50%, 25% or 2% from left to right.

these using the halogen light source placed at a sufficient distance, they were used to create a reflectance signal with a spectral response equivalent to the light source that could be imaged using the CCD camera.

A.2 Camera Parameters

The total noise N_T in each pixel of the image for a CCD camera is a combination of undesirable signal resulting from the cameras electronic components, including both read noise σ_r and dark noise σ_d, and the physical variation of incident photon flux due called shot noise σ_s, defined by:

$$N_T = \sqrt{\sigma_r^2 + \sigma_d^2 + \sigma_s^2}, \tag{A.1}$$

It is important to carefully characterise and control these noise contributions to enable adequate signal to noise levels such that image information accurately reflects the incident flux on the chip. This is done through a combination of selecting optimum modes of camera operation and setting sufficient exposure times.

A.2.1 Shot noise

Shot noise is the natural statistical variation in flux incident on the chip, due to the inherent quantization of light. The number of incident photons follows a Poisson distribution resulting in fluctuations in the number of photoelectrons at a given pixel,

$$\sigma_s^2 = Q_E S, \tag{A.2}$$

where Q_E is the camera quantum efficiency and S is the signal.

A.2.2 Dark noise

The rate of generation of thermally generated e^- within the silicon structure is called dark current. The term dark noise refers to the statistical variation in the number of thermally induced e^- during the exposure and follows a Poisson relationship with the dark current (D),

$$\sigma_d^2 = t_{exp} D, \tag{A.3}$$

where t_{exp} is the exposure time. In high-performance scientific cameras such as the one used in this work, the dark current is dramatically reduced by significantly cooling the chip. To measure the dark current two images were taken, one at exposure time of 1s and one at 101s, in dark conditions with the lens cap on and at the same acquisition settings as used during optical images in joint studies, in high precision readout mode. The average difference between these images was divided by 100 and multiplied to the gain transfer coefficient, to give 0.0082 e^-/pixel/s, which was only slightly higher than the nominal value of 0.0065 e^-/pixel/s at -65 ° C, such that the associated dark noise was expected to be negligible at typical exposure times. It must be noted that when left for over 2 hours, the minimum camera temperature only ever reached -42 ° C, a discrepancy which may contribute to this elevated dark noise and be deterioration in Peltier cooling due to the age of the camera.

A.2.3 Readout noise

Readout noise is the inherent noise resulting from the CCD system components when both converting charge carrier numbers to voltages and then analogue signal to digital during image formation, with the on-chip pre-amplifier commonly the most significant source. A dependency on the pixel clock rate means a quicker readout will result in greater readout noise, meaning in practical terms the noise will only depend on the selected readout mode and is added to every pixel uniformly,

$$\sigma_r, \tag{A.4}$$

This high-performance scientific camera incorporates design enhancements to reduce the readout noise dramatically, with a nominal readout noise from the manufacture is stated as typically 6 e^- r.m.s. or a minimum of 4 e^- r.m.s. for high-precision readout mode. An alternative high-speed read out mode was available for this CCD camera, but was not considered in this work due to its inferior read noise characteristics and its reduced precision, with digital data output only available in 12-bit for this mode.

A.2.4 Pixel Binning

On-chip binning is when the electric charges of adjacent arrays of pixels (either 2×2, 4×4, or 8×8) are read out simultaneously. The total frame time ($Tf(s)$) for the CCD camera in high precision readout mode can be calculated in seconds as,

$$Tf(s) = (6 \times BH_n + 387.2 \times V_n + 10536.8) \times 10^{-6} + Texp(s) \tag{A.5}$$

where B is the on-chip binning number, 1, 2, 4 or 8, H_n is the number of readout pixels and V_n is the number of readout lines. The impact of on-chip binning is to improve sensitivity, meaning shorter exposure times can be used to achieve the same SNR, and also reduce readout time according to Equation A.5, as effectively fewer pixels are readout.

Post-acquisition binning of pixels in software is also possible to increase SNR, but this approach will not impact readout times. Drawbacks of on-chip binning are increased readout noise and reduced image resolution. To quantify the impact of on-chip binning on readout noise, two images were taken at the minimum exposure time of 0.02s in dark conditions with the lens cap on. The standard deviation of the difference between these images was calculated, which was divided by $\sqrt{2}$ and multiplied by the amp gain transfer coefficient, which was $1.26e^{-}$/ADcounts at 16-bit in super high dynamic range mode. This was repeated 10 times for each of the 4 on-chip binning modes and the corresponding frame times were also measured.

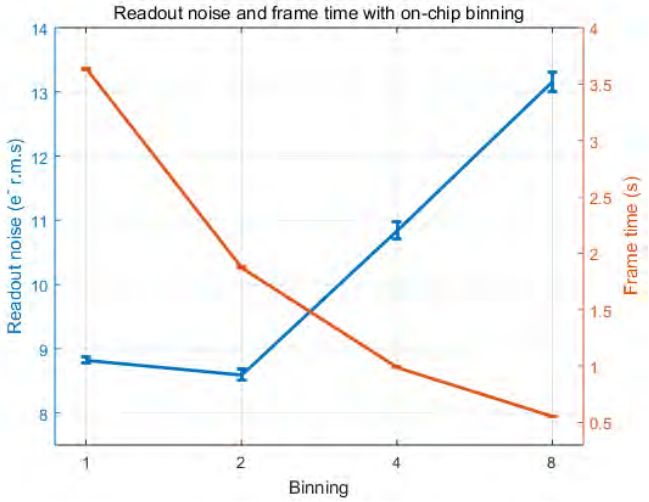

Figure A.5: Variation in measured readout noise (blue) or total acquisition frame time (red) as binning settings were changed.

The measured value for 1×1 binning is around 50% higher than the nominal readout noise, stated as 6 e^{-} r.m.s. This may be a result deterioration of the on-board electronics due to the age of the camera and amount of usage it has experienced. Additionally, as binning increased above 2×2, the readout noise also increased. Even at 13 e^{-} r.m.s., these values are still relatively low, corresponding to around 10 counts. Provided good signal of at least 5000 counts is acquired in images, data would still be expected to be shot noise dominated. A substantial reduction of around ×7 in frame time, which for 0.02s exposure is effectively readout time, was seen by increasing the binning from 1×1 to 8×8. The resulting read out times are also plotted in Figure A.5, illustrating the trade-off between

readout times and noise.

A.2.5 Signal-to-Noise Ratio

Signal-to-noise ratio (SNR) indicates the measurement quality, therefore a higher SNR is always desirable. For a CCD camera, the SNR in an image is the relative magnitude of the signal compared to the uncertainty in the measurement due to total noise, defined as

$$SNR = \frac{S}{N_T}. \tag{A.6}$$

As images contained measurements from a an pixel array of discrete physical locations, the SNR was calculated on a per-pixel basis. For the presented system, due to a combination of a highly cooled chip and efficient electronics and by only considering pixels with sufficient signal, the SNR could be assumed to be shot noise dominated, where read and dark noise contributions become negligible, as shown in Section 4.2.2.

$$SNR = \frac{S}{\sigma_s} = \frac{S}{\sqrt{Q_E S}} \propto \sqrt{S}, \tag{A.7}$$

A.3 System Characterisation Tests

A.3.1 Linearity of Signal With Fluence

Digital counts are commonly used in the literature in place of photons, but this relies on the assumption that the relationship between digital signal measured by the CCD camera and the number of incident photons maintains linearity within the dynamic range utilised. For implementation of an autoexposure routine, it was necessary to validate that signal response of the CCD camera with exposure time was linear across the well depth of the chip up to the maximum used of 50,000 counts. The 99% reflectance phantom was imaged at exposures times between 0.02s and 0.2s in 0.02s intervals, with 5 repeats taken at each

exposure time. This was repeated for all five wavelengths, each time adjusting the light source strength so that good signal was measured for 0.2s exposure.

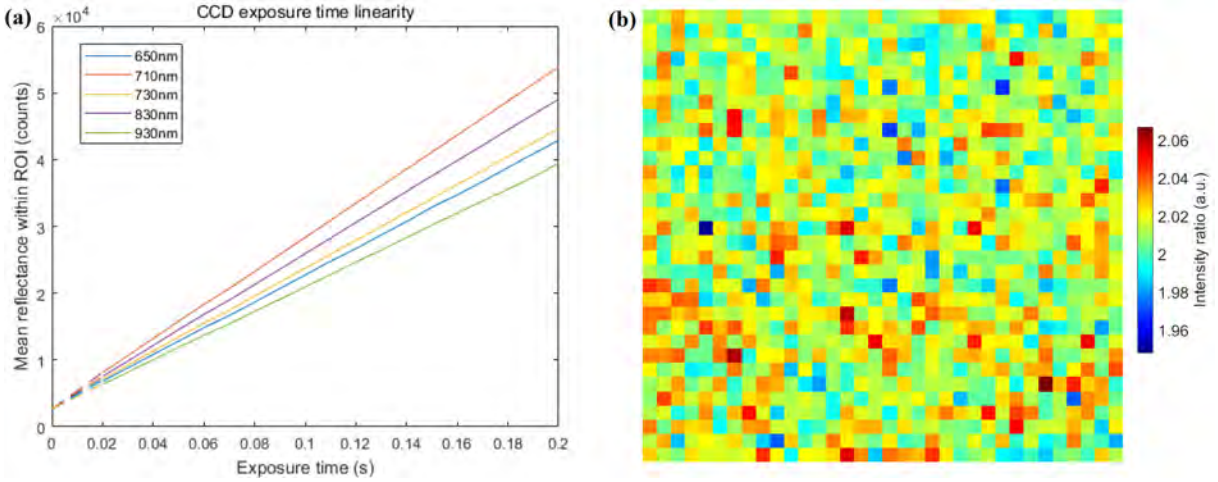

Figure A.6: (a) Plots demonstrating the linearity of the CCD response with exposure time, for different wavelengths. (b) Images indicating the spatial homogeneity of this linearity, with the ratio of images of the reflectance standard acquired at 0.2s and 0.1s

As expected, the signal response of the output counts is clearly linear with exposure time. Extrapolation of this line to no exposure intercepted the y axis at around 2050 counts, closely matching to the digitiser offset previously assessed. To ensure that there was no significant bias spatially across the chip in the observed linearity, the mean image at 0.2s exposure was divided by the equivalent for 0.1s exposure. The resulting image of the intensity ratio demonstrated only speckle noise with no drastic bias over this ROI and with a mean value of 2.014 ± 0.0145.

To assess the linearity further by varying the photon fluence, each of the four reflectance standards, with either 2%, 50%, 75% or 99% reflectance were placed on the platform in the same position. The optic fibre coupled to the light source was setup such that the standards were illuminated evenly and each standard was imaged with 20 repeats, providing a controlled way to vary the incident flux on the chip. The mean value for a by pixel ROI. A high degree of linearity ($R^2 \approx 1$) can be seen up to 50,000 counts, which was the maximum used during optical imaging, an unsurprising result for this high specification camera.

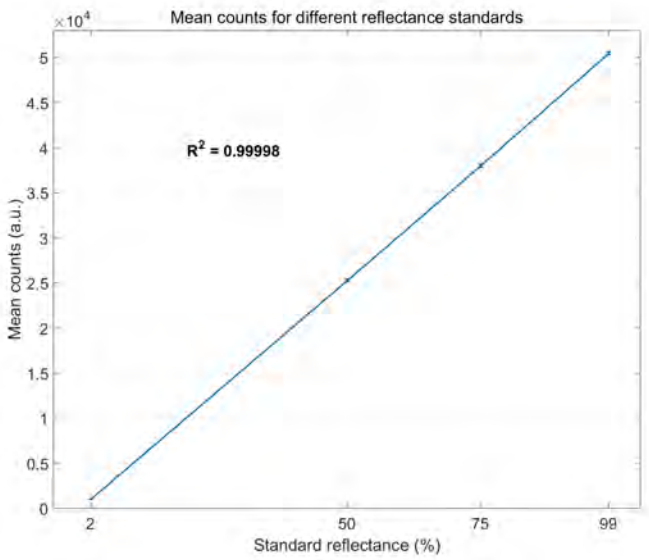

Figure A.7: Plot illustrating the linearity of the CCD response with incident flux up to 50,000 counts, demonstrated by varying the reflectivity of the reflectance standard when the ND filter was set. Error bars are included at each measurement, but are too small to visualise.

A.3.2 Ambient Lighting Assessment

The high dynamic range and sensitivity of the scientific grade CCD increased the potential for detecting signal originating from external ambient light sources. To minimise any cross talk with the touch screen monitor, its settings were adjusted to dim the brightness and display in only blue or green. An experiment to assess the impact of ambient lighting on the signal was carried out, in which the 99% reflective standard was imaged with 50 repeats and camera settings set to be identical to those used during joint imaging. Ambient conditions were altered to be either (1) dark, with all room lights and screens switched off, (2) only the patient visualisation monitor switched on, (3) only the SI units switched on and set to project an array of 0 counts in dark mode identical optical transmission imaging settings, or (4) with only room lights in the clinical unit turned on. These tests were repeated for all wavelengths of interest, 650, 710, 730, 830 and 930nm, with integration times set at either 0.5, 0.1, 0.1, 0.1 or 1s respectively, chosen based on approximately the longest typically exposures reached when imaging joints.

Detection of fluence originating from the visualisation screen was deemed to be negligible,

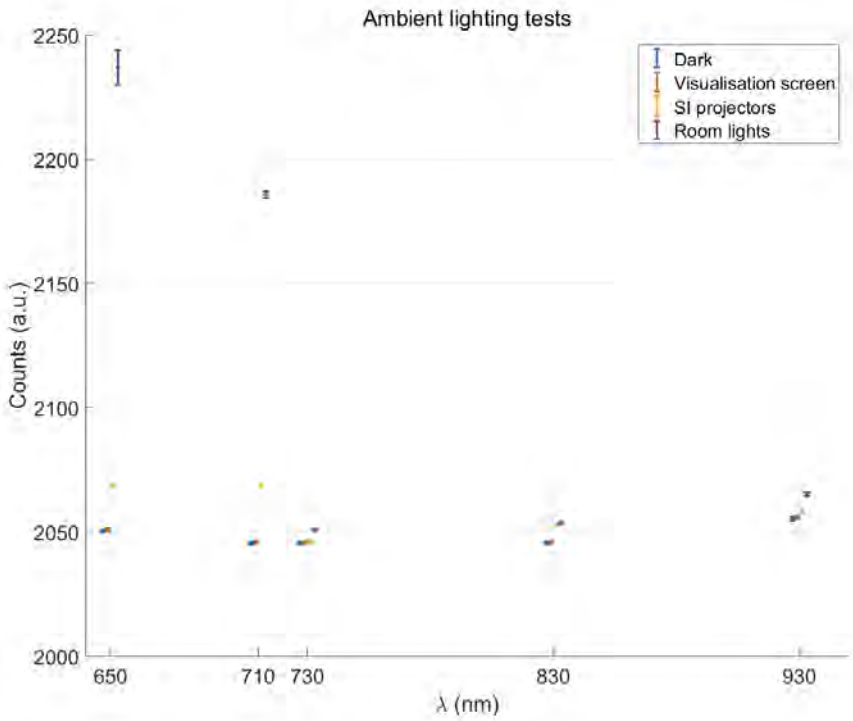

Figure A.8: Variation in mean counts for 99% reflectance standard in different ambient conditions. Error bars are included, but are too small to see for a majority of points.

with a slight increase of around 1 count across all wavelengths when the monitor was switched on. It was decided that it was preferable to turn off room lights during joint imaging protocols once the patients were safely seated for acquisition, due to the drastic cross talk of up to 100 counts observed in Figure A.8 at 650 and 710nm. There was also a degree of cross talk between with the SI projectors at these wavelengths (≈10 counts) that was unavoidable without unplugging the SI units, which would have been highly impractical between imaging different joints. To ensure this crosstalk was kept to a minimum, dark images acquired at equivalent exposure times were subtracted at each wavelength, as outlined in Section 3.6. It must be noted elevated values for ambient signal were conservatively measured as the standards reflectivity would have been significantly higher than patients skin.

A.4 Prevalence of inflammation in RA joints

Results of US and CE data for all hand joints from 80 patients diagnosed with RA taken from historical subset of BEACON cohort. The prevalence of scores greater than zero for each feature are shown in Figure A.4. These distributions of prevalence are useful for indicating features most commonly seen in RA patients to be used as ground truth references and for choosing an optimal subset of joints during optical scanning studies.

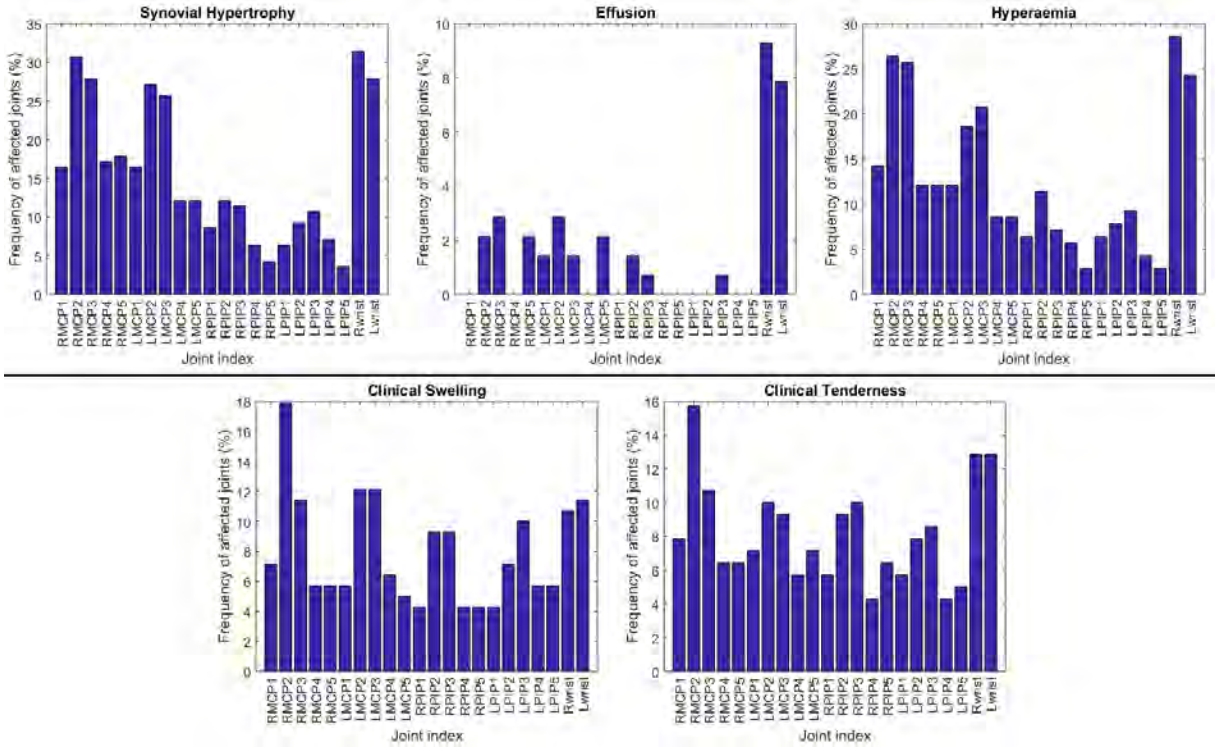

Figure A.9: Bar charts indicating the prevalence of US scores across all hand joints from 80 patient sample within Beacon cohort.

Synovial hypertrophy and hyperaemia are more prevalent US features in RA joints than than effusion. These US scores are also more commonly seen than CE scores of swelling and tenderness, indicative of the greater sensitivity of semi-quantitative US scoring system. It is also evident in all US and CE features that inflammation is more prevalent in the MCP joints than the PIP joints, and most commonly seen in the 2nd and 3rd joints in RA.

A.5 Standardised Circular Model

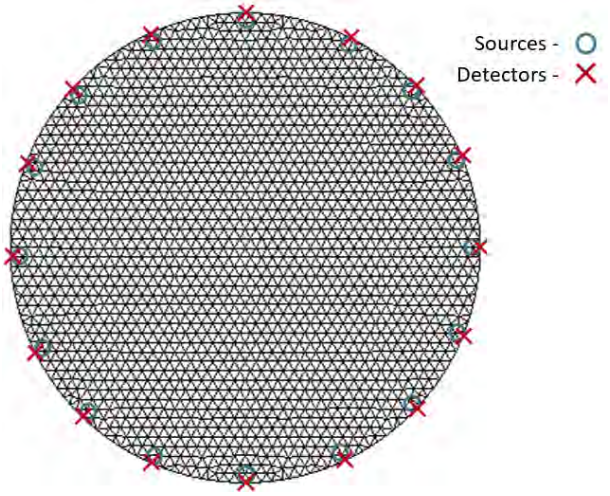

Figure A.10: Example of a circular surface discretized into a FEM mesh consisting of 3418 elements and 1785 nodes.

A 43mm radius circle was discretized into an FEM mesh composed of 1785 nodes and 3418 linear triangular elements used as a basis for the forward problem, while a regular grid of 648 nodes and 1230 linear triangular elements was used as a basis for the inverse problem. Sixteen co-located sources and detectors were placed equidistantly along the circle boundary, as shown in Fig. A.10, with each source illuminated individually, whilst the remaining 15 optodes were used as detectors, resulting in 240 individual source-detector pair measurements per wavelength. This combination of reflectance and transmittance measurements provides a high quality reconstruction of anomalies, making it useful as a standardised model to quantitatively assess and compare the performance of an algorithms such as with different wavelength combinations.

A.6 Commercialisation

Potential commercialisation is an important factor in development of medical imaging systems to ultimately facilitate the translation of the imaging technology into clinic practice. Improvements required for the realisation of this with the DOT hand imaging system presented include; lower total cost, more compact with miniaturisation of optical systems a

topic of wide investigation currently in biomedical optics, and more robust and user friendly software for acquisition and data processing. A key advantage of CW data acquisition over FD or TD alternatives is that it is generally cheaper to implement. To provide a perspective on the financial costs to build the prototype system presented in this work, an itemised list of all components and their prices are outlined in table A.2.

Component	Manufacturer	Model	Cost (£)	Quantity
Filter wheel	Thorlabs	FW102C	857	1
Galvanometer	Thorlabs	GVSM002/M	1,902	1
CCD camera	Hamamatsu Photonics	C4742 - 98	≈22,000	1
Webcam	Logitech	C920	65	2
Halogen light source	Ocean Optics	HL2000-FHSA	1,213	1
Personal computer	Stone	N/A	≈1000	1
DAQ device	National Instruments	USB-6002	176	1
Pocket projector	Texas Instruments	DLP LightCrafter EVM	583	2
Docking Station	Startech	USB3SDOCKHD	111	1
Touchscreen Monitor	Beetronics	10TS2W	265	1
Monitor	Ilyama	Prolite B2280WSD	150	1
Optical Fibre	Ocean Optics	QP1000-2-VIS-BX	348	1
Aluminium frame	RS Components		≈200	N/A
Plastic Casing	plasticsheets.com	N/A	130	N/A
Lenses	Thorlabs			1
Bandpass filters	Thorlabs	FB(λ) - 10	66	5
ND Filter	Thorlabs	ND20A	53	1
Connecting components	Thorlabs	N/A	≈300	N/A
TOTAL COST				30,461

Table A.2: Itemised components list with corresponding costs incurred during construction.

The CCD camera incurred the majority of the total system cost, however this was purchased in 2012 during a previous PhD project, 3 years before system construction. Progress in camera electronics mean that scientific CMOS are now comparable in specifications to CCD camera at significantly lower cost. The ORCA Flash 4.0 V3 (Hamamatsu Photonics, Welwyn Garden City, UK) is just one example of such cameras with higher frame rate, a comparable spectral sensitivity profile, better dynamic range and more convenient control via USB 3.0, currently available on the market at around £7500 - 10,000. These new sCMOS cameras are also smaller with more lightweight casing, and don't require a separate power unit, which is useful for miniaturisation. Furthermore, investigation into

whether lower quality, even cheaper cameras are sufficient for these imaging applications is required. Additionally, as the source positions utilised for were a linear array, it would be feasible to install a 1D galvanometer, reducing cost and complexity further. Nevertheless, for perspective the Xiralite and Hemics Handscan joint imaging systems cost prices are ≈£200,000 and ≈£115,000 respectively, so a £30,000 build price for a medical imaging device should be commercially viable.

LIST OF REFERENCES

[1] D Golovko, R Meier, E Rummeny, and H Daldrup-Link. Optical imaging of rheumatoid arthritis. *International journal of clinical rheumatology*, 6(1):67–75, 2011.

[2] S Glinton, A J Naylor, and E Claridge. Diagnosing hypoxia in murine models of rheumatoid arthritis from reflectance multispectral images. In *European Conference on Biomedical Optics*, page 1041109. Optical Society of America, 2017.

[3] Z Yuan, Q Zhang, E Sobel, and H Jiang. Three-dimensional diffuse optical tomography of osteoarthritis: initial results in the finger joints. *Journal of Biomedical Optics*, 12(3):034001–034001, 2007.

[4] A H Hielscher, H K Kim, L D Montejo, S Blaschke, U J Netz, P A Zwaka, G Illing, G A Muller, and J Beuthan. Frequency-domain optical tomographic imaging of arthritic finger joints. *IEEE transactions on medical imaging*, 30(10):1725–1736, 2011.

[5] E Suresh. Diagnosis of early rheumatoid arthritis: what the non-specialist needs to know. *Journal of the Royal Society of Medicine*, 97(9):421–424, 2004.

[6] E M Barrett, D G I Scott, N J Wiles, and D P M Symmons. The impact of rheumatoid arthritis on employment status in the early years of disease: a uk community-based study. *Rheumatology*, 39(12):1403–1409, 2000.

[7] National Audit Office. Services for people with rheumatoid arthritis. *National Audit Office*, 823:1–37, 2009.

[8] M van Onna and A Boonen. The challenging interplay between rheumatoid arthritis, ageing and comorbidities. *BMC musculoskeletal disorders*, 17(1):1, 2016.

[9] C Turesson, W M O'fallon, C S Crowson, S E Gabriel, and E L Matteson. Extra-articular disease manifestations in rheumatoid arthritis: incidence trends and risk factors over 46 years. *Annals of the rheumatic diseases*, 62(8):722–727, 2003.

[10] A J MacGregor, H Snieder, A S Rigby, M Koskenvuo, J Kaprio, K Aho, A J Silman, et al. Characterizing the quantitative genetic contribution to rheumatoid arthritis using data from twins. *Arthritis & Rheumatism*, 43(1):30, 2000.

[11] R F van Vollenhoven. Sex differences in rheumatoid arthritis: more than meets the eye... *BMC medicine*, 7(1):12, 2009.

[12] Y Koumantaki, E Giziaki, A Linos, A Kontomerkos, P Kaklamanis, G Vaiopoulos, J Mandas, and E Kaklamani. Family history as a risk factor for rheumatoid arthritis: a case-control study. *The Journal of rheumatology*, 24(8):1522–1526, 1997.

[13] K Kim, S Bang, H Lee, and S Bae. Update on the genetic architecture of rheumatoid arthritis. *Nature Reviews Rheumatology*, 13(1):13, 2017.

[14] X Zhang, D Zhang, H Jia, Q Feng, D Wang, D Liang, X Wu, J Li, L Tang, Y Li, et al. The oral and gut microbiomes are perturbed in rheumatoid arthritis and partly normalized after treatment. *Nature medicine*, 21(8):895, 2015.

[15] T R Mikuls, J B Payne, F Yu, G M Thiele, R J Reynolds, G W Cannon, J Markt, D McGowan, G S Kerr, R S Redman, et al. Periodontitis and porphyromonas gingivalis in patients with rheumatoid arthritis. *Arthritis & rheumatology*, 66(5):1090–1100, 2014.

[16] L Klareskog, P Stolt, K Lundberg, H Källberg, C Bengtsson, J Grunewald, J Rönnelid, H Erlandsson Harris, A Ulfgren, S Rantapää-Dahlqvist, et al. A new model for an etiology of rheumatoid arthritis: smoking may trigger hla–dr (shared epitope)–restricted immune reactions to autoantigens modified by citrullination. *Arthritis & Rheumatism: Official Journal of the American College of Rheumatology*, 54(1):38–46, 2006.

[17] I B McInnes and G Schett. The pathogenesis of rheumatoid arthritis. *New England Journal of Medicine*, 365(23):2205–2219, 2011.

[18] C Orr, E Vieira-Sousa, D L Boyle, M H Buch, C D Buckley, J D Cañete, A I Catrina, E H S Choy, P Emery, E Fearon, et al. Synovial tissue research: a state-of-the-art review. *Nature Reviews Rheumatology*, 13(8):463–475, 2017.

[19] D Scott, F Wolfe, and T Huizinga. Rheumatoid arthritis. *The Lancet*, 376(9746):1094–1108, 2010.

[20] B Bartok and G S Firestein. Fibroblast-like synoviocytes: key effector cells in rheumatoid arthritis. *Immunological reviews*, 233(1):233–255, 2010.

[21] V Strand, R Kimberly, and J D Isaacs. Biologic therapies in rheumatology: lessons learned, future directions. *Nature Reviews Drug Discovery*, 6(1):75–92, 2007.

[22] D L Scott, B L Coulton, and A J Popert. Long term progression of joint damage in rheumatoid arthritis. *Annals of the Rheumatic Diseases*, 45(5):373, 1986.

[23] C T Ng, M Biniecka, A Kennedy, J McCormick, O Fitzgerald, B Bresnihan, D Buggy, C T Taylor, J O'sullivan, U Fearon, et al. Synovial tissue hypoxia and inflammation in vivo. *Annals of the rheumatic diseases*, page 1389âĂŞ1395, 2010.

[24] K Lund-Olesen. Oxygen tension in synovial fluids. *Arthritis & Rheumatism*, 13(6):769–776, 1970.

[25] S Konisti, S Kiriakidis, and E M Paleolog. Hypoxia-a key regulator of angiogenesis and inflammation in rheumatoid arthritis. *Nature Reviews Rheumatology*, 8(3):153–162, 2012.

[26] M A Akhavani, L Madden, I Buysschaert, B Sivakumar, N Kang, and E M Paleolog. Hypoxia upregulates angiogenesis and synovial cell migration in rheumatoid arthritis. *Arthritis research & therapy*, 11(3):1, 2009.

[27] K H Falchuk, E J Goetzl, and J P Kulka. Respiratory gases of synovial fluids: an approach to synovial tissue circulatory-metabolic imbalance in rheumatoid arthritis. *The American journal of medicine*, 49(2):223–231, 1970.

[28] H Mohamed-Ali, R W Hauer, and H Sörensen. [morphology and growth behavior of synovial cells in monolayer culture]. *Zeitschrift fur Rheumatologie*, 50(2):74–81, 1990.

[29] L Dahlberg, L Ryd, D Heinegård, and L S Lohmander. Proteoglycan fragments in joint fluid: influence of arthrosis and inflammation. *Acta Orthopaedica Scandinavica*, 63(4):417–423, 1992.

[30] J Collins, A Rudenski, J Gibson, L Howard, and R O'Driscoll. Relating oxygen partial pressure, saturation and content: the haemoglobin–oxygen dissociation curve. *Breathe*, 11(3):194, 2015.

[31] H D El-Gabalawy and P E Lipsky. Why do we not have a cure for rheumatoid arthritis? *Arthritis Research & Therapy*, 4(3):S297, 2002.

[32] J S Smolen, R Landewé, F C Breedveld, M Dougados, P Emery, C Gaujoux-Viala, S Gorter, R Knevel, J Nam, M Schoels, et al. Eular recommendations for the management of rheumatoid arthritis with synthetic and biological disease-modifying antirheumatic drugs. *Annals of the rheumatic diseases*, pages 964–975, 2010.

[33] D M Gerlag, K Raza, L G M van Baarsen, E Brouwer, C D Buckley, G R Burmester, C Gabay, A I Catrina, A P Cope, F Cornelis, et al. Eular recommendations for terminology and research in individuals at risk of rheumatoid arthritis: report from the study group for risk factors for rheumatoid arthritis. *Annals of the rheumatic diseases*, pages 638–641, 2012.

[34] F C Arnett, S M Edworthy, D A Bloch, D J Mcshane, J F Fries, N S Cooper, L A Healey, S R Kaplan, M H Liang, H S Luthra, et al. The american rheumatism association 1987 revised criteria for the classification of rheumatoid arthritis. *Arthritis & Rheumatology*, 31(3):315–324, 1988.

[35] P Santos-Moreno, O Andrade, W Chona, L Amador, L Villarreal, A Urbina, M Cubides, and J Bello. Osteoarthritis as a frequent cause of misdiagnosis of rheumathoid arthritis and how to perform correct diagnosis. *Osteoarthritis and Cartilage*, 20:S165, 2012.

[36] S L Hider, S Muller, T Helliwell, J A Prior, I Scott, S A Lawton, I Zwierska, D van Schaardenburg, A van der Helm-van Mil, K Raza, et al. Symptoms associated with inflammatory arthritis are common in the primary care population: results from the joint symptoms survey. *Rheumatology*, 2019.

[37] F Banal, M Dougados, C Combescure, and L Gossec. Sensitivity and specificity of the american college of rheumatology 1987 criteria for the diagnosis of rheumatoid arthritis according to disease duration: a systematic literature review and meta-analysis. *Annals of the rheumatic diseases*, 67(7):1184–1191, 2008.

[38] D Aletaha, T Neogi, A J Silman, J Funovits, D T Felson, C O Bingham, N S Birnbaum, G R Burmester, V P Bykerk, M D Cohen, et al. 2010 rheumatoid arthritis classification criteria: an american college of rheumatology/european league against rheumatism collaborative initiative. *Arthritis & Rheumatology*, 62(9):2569–2581, 2010.

[39] J Bluett, I Ibrahim, D Plant, K L Hyrich, A W Morgan, A G Wilson, J D Isaacs, H Gaston, D Mulherin, T Price, et al. Association of a complement receptor 1 gene

variant with baseline erythrocyte sedimentation rate levels in patients starting anti-tnf therapy in a uk rheumatoid arthritis cohort: results from the biologics in rheumatoid arthritis genetics and genomics study syndicate cohort. *The pharmacogenomics journal*, 14(2):171–175, 2014.

[40] V P K Nell, K P Machold, G Eberl, T A Stamm, M Uffmann, and J S Smolen. Benefit of very early referral and very early therapy with disease-modifying anti-rheumatic drugs in patients with early rheumatoid arthritis. *Rheumatology*, 43(7):906–914, 2004.

[41] R Landewé, M Boers, A C Verhoeven, R Westhovens, M AFJ van de Laar, H M Markusse, J C van Denderen, M L Westedt, A J Peeters, B A C Dijkmans, et al. Cobra combination therapy in patients with early rheumatoid arthritis: long-term structural benefits of a brief intervention. *Arthritis & Rheumatism*, 46(2):347–356, 2002.

[42] M P M van der Linden, S Le Cessie, K Raza, D van der Woude, R Knevel, T W J Huizinga, A van der Helm-van Mil, et al. Long-term impact of delay in assessment of patients with early arthritis. *Arthritis & Rheumatism*, 62(12):3537–3546, 2010.

[43] K Raza, F Falciani, S J Curnow, E J Ross, C Lee, A N Akbar, J M Lord, C Gordon, C D Buckley, and M Salmon. Early rheumatoid arthritis is characterized by a distinct and transient synovial fluid cytokine profile of t cell and stromal cell origin. *Arthritis research & therapy*, 7(4):1, 2005.

[44] R J Stack, P Nightingale, C Jinks, K Shaw, S Herron-Marx, R Horne, C Deighton, P Kiely, C Mallen, and K Raza. Delays between the onset of symptoms and first rheumatology consultation in patients with rheumatoid arthritis in the uk: an observational study. *BMJ open*, 9(3):e024361, 2019.

[45] A Barton and C Pitzalis. Stratified medicine in rheumatoid arthritis-the matura programme: Targeted treatment for patients, 2016.

[46] P Barrera, A van Der Maas, A E Van Ede, B A L M Kiemeney, R F J M Laan, L B A van de Putte, and P L C M van Riel. Drug survival, efficacy and toxicity of monotherapy with a fully human anti-tumour necrosis factor-α antibody compared with methotrexate in long-standing rheumatoid arthritis. *Rheumatology*, 41(4):430–439, 2002.

[47] K L Hyrich, K D Watson, A J Silman, and D P M Symmons. Predictors of response to anti-tnf-α therapy among patients with rheumatoid arthritis: results from the british society for rheumatology biologics register. *Rheumatology*, 45(12):1558–1565, 2006.

[48] M M Soliman, D M Ashcroft, K D Watson, M Lunt, D P M Symmons, K L Hyrich, British Society for Rheumatology Biologics Register, et al. Impact of concomitant use of dmards on the persistence with anti-tnf therapies in patients with rheumatoid arthritis: results from the british society for rheumatology biologics register. *Annals of the rheumatic diseases*, page annrheumdis139774, 2011.

[49] D M F M van der Heijde. Plain x-rays in rheumatoid arthritis: overview of scoring methods, their reliability and applicability. *Bailliere's clinical rheumatology*, 10(3):435–453, 1996.

[50] J A Jacobson, G Girish, Y Jiang, and D Resnick. Radiographic evaluation of arthritis: Inflammatory conditions 1. *Radiology*, 248(2):378–389, 2008.

[51] M Backhaus, T H Kamradt, D Sandrock, D Loreck, J Fritz, K J Wolf, H Raber, B Hamm, G-R Burmester, and M Bollow. Arthritis of the finger joints: a comprehensive approach comparing conventional radiography, scintigraphy, ultrasound, and contrast-enhanced magnetic resonance imaging. *Arthritis & Rheumatism: Official Journal of the American College of Rheumatology*, 42(6):1232–1245, 1999.

[52] R J Wakefield, M J Green, H Marzo-Ortega, P G Conaghan, W W Gibbon, D McGonagle, S Proudman, and P Emery. Should oligoarthritis be reclassified? ultrasound reveals a high prevalence of subclinical disease. *Annals of the Rheumatic Diseases*, 63(4):382–385, 2004.

[53] A K Scheel, K G A Hermann, S Ohrndorf, C Werner, C Schirmer, J Detert, M Bollow, B Hamm, G A Müller, G R Burmester, et al. Prospective 7 year follow up imaging study comparing radiography, ultrasonography, and magnetic resonance imaging in rheumatoid arthritis finger joints. *Annals of the rheumatic diseases*, 65(5):595–600, 2006.

[54] E Naredo, G Bonilla, F Gamero, J Uson, L Carmona, and A Laffon. Assessment of inflammatory activity in rheumatoid arthritis: a comparative study of clinical evaluation with grey scale and power doppler ultrasonography. *Annals of the rheumatic diseases*, 64(3):375–381, 2005.

[55] A K Brown, P G Conaghan, Z Karim, M A Quinn, K Ikeda, C G Peterfy, E Hensor, R J Wakefield, P J O'Connor, and P Emery. An explanation for the apparent dissociation between clinical remission and continued structural deterioration in rheumatoid arthritis. *Arthritis & Rheumatism*, 58(10):2958–2967, 2008.

[56] V Foltz, F Gandjbakhch, F Etchepare, C Rosenberg, M L Tanguy, S Rozenberg, P Bourgeois, and B Fautrel. Power doppler ultrasound, but not low-field magnetic resonance imaging, predicts relapse and radiographic disease progression in rheumatoid arthritis patients with low levels of disease activity. *Arthritis & Rheumatology*, 64(1):67–76, 2012.

[57] M Szkudlarek, M Court-Payen, C Strandberg, M Klarlund, T Klausen, and M Østergaard. Power doppler ultrasonography for assessment of synovitis in the metacarpophalangeal joints of patients with rheumatoid arthritis: a comparison with dynamic magnetic resonance imaging. *Arthritis & Rheumatology*, 44(9):2018–2023, 2001.

[58] A Filer, P de Pablo, G Allen, P Nightingale, A Jordan, P Jobanputra, S Bowman, C D Buckley, and K Raza. Utility of ultrasound joint counts in the prediction of rheumatoid arthritis in patients with very early synovitis. *Annals of the rheumatic diseases*, 70(3):500–507, 2011.

[59] E Naredo, I Möller, C Moragues, J J De Agustín, A K Scheel, W Grassi, E de Miguel, M Backhaus, P Balint, G A W Bruyn, et al. Interobserver reliability in musculoskeletal ultrasonography: results from a "teach the teachers" rheumatologist course. *Annals of the rheumatic diseases*, 65(1):14–19, 2006.

[60] I Sudoł-Szopińska, E Kontny, W Maśliński, Mika Prochorec-Sobieszek, A Warczyńska, and B Kwiatkowska. Significance of bone marrow edema in pathogenesis of rheumatoid arthritis. *Polish journal of radiology*, 78(1):57, 2013.

[61] M W Chan, G Nathanael, A Kis, A Amirabadi, A Zhong, T Rayner, R Weiss, G Detzler, R Jong, H Gahunia, et al. Systematic protocol for assessment of the validity of bold mri in a rabbit model of inflammatory arthritis at 1.5 tesla. *Pediatric radiology*, 44(5):566–575, 2014.

[62] O C Nasui, M W Chan, G Nathanael, A Crawley, E Miller, J Belik, H-L Cheng, A Kassner, T Rayner, R Weiss, G Detzler, A Zhong, R Moineddin, R Jong, M Rogers, and A S Doria. Physiologic characterization of inflammatory arthritis in a rabbit model with bold and dce mri at 1.5 tesla. *European Radiology*, 24(11):2766–2778, Nov 2014.

[63] R J Hodgson, P O'Connor, and R Moots. Mri of rheumatoid arthritis-image quantitation for the assessment of disease activity, progression and response to therapy. *Rheumatology*, 47(1):13–21, 2008.

[64] P Conaghan, P Bird, B Ejbjerg, P O'connor, C Peterfy, F McQueen, M Lassere, P Emery, R Shnier, J Edmonds, et al. The eular–omeract rheumatoid arthritis mri reference image atlas: the metacarpophalangeal joints. *Annals of the rheumatic diseases*, 64(suppl 1):i11–i21, 2005.

[65] D A Long. *Raman spectroscopy*, volume 276. McGraw-Hill New York, 1977.

[66] J R Mourant, N Canpolat, C Brocker, O Esponda-Ramos, T M Johnson, A Matanock, K Stetter, and J P Freyer. Light scattering from cells: the contribution of the nucleus and the effects of proliferative status. *Journal of biomedical optics*, 5(2):131–138, 2000.

[67] B Beauvoit, T Kitai, and B Chance. Contribution of the mitochondrial compartment to the optical properties of the rat liver: a theoretical and practical approach. *Biophysical Journal*, 67(6):2501–2510, 1994.

[68] O C Marina, C K Sanders, and J R Mourant. Correlating light scattering with internal cellular structures. *Biomedical optics express*, 3(2):296–312, 2012.

[69] W-F Cheong, S A Prahl, and A J Welch. A review of the optical properties of biological tissues. *IEEE journal of quantum electronics*, 26(12):2166–2185, 1990.

[70] H J Van Staveren, C J M Moes, J van Marie, S A Prahl, and M J C Van Gemert. Light scattering in lntralipid-10% in the wavelength range of 400–1100 nm. *Applied optics*, 30(31):4507–4514, 1991.

[71] J R Mourant, T Fuselier, J Boyer, T M Johnson, and I J Bigio. Predictions and measurements of scattering and absorption over broad wavelength ranges in tissue phantoms. *Applied optics*, 36(4):949–957, 1997.

[72] H Dehghani, M E Eames, P K Yalavarthy, S C Davis, Sra Srinivasan, C M Carpenter, B W Pogue, and K D Paulsen. Near infrared optical tomography using nirfast: Algorithm for numerical model and image reconstruction. *Communications in numerical methods in engineering*, 25(6):711–732, 2009.

[73] S L Jacques. Optical properties of biological tissues: a review. *Physics in medicine and biology*, 58(11):R37, 2013.

[74] M G L Gustafsson. Surpassing the lateral resolution limit by a factor of two using structured illumination microscopy. *Journal of microscopy*, 198(2):82–87, 2000.

[75] M J Rust, M Bates, and X Zhuang. Sub-diffraction-limit imaging by stochastic optical reconstruction microscopy (storm). *Nature methods*, 3(10):793–796, 2006.

[76] F F Jobsis. Noninvasive, infrared monitoring of cerebral and myocardial oxygen sufficiency and circulatory parameters. *Science*, 198(4323):1264–1267, 1977.

[77] T G Phan and A Bullen. Practical intravital two-photon microscopy for immunological research: faster, brighter, deeper. *Immunology and cell biology*, 88(4):438–444, 2010.

[78] A L Harris. Hypoxia-a key regulatory factor in tumour growth. *Nature Reviews Cancer*, 2(1):38, 2002.

[79] D A Boas, A M Dale, and M A Franceschini. Diffuse optical imaging of brain activation: approaches to optimizing image sensitivity, resolution, and accuracy. *Neuroimage*, 23:S275–S288, 2004.

[80] A T Eggebrecht, B R White, S L Ferradal, C Chen, Y Zhan, A Z Snyder, H Dehghani, and J P Culver. A quantitative spatial comparison of high-density diffuse optical tomography and fmri cortical mapping. *Neuroimage*, 61(4):1120–1128, 2012.

[81] S Srinivasan, B W Pogue, S Jiang, H Dehghani, C Kogel, S Soho, J J Gibson, T D Tosteson, S P Poplack, and K D Paulsen. Interpreting hemoglobin and water concentration, oxygen saturation, and scattering measured in vivo by near-infrared breast tomography. *Proceedings of the National Academy of Sciences*, 100(21):12349–12354, 2003.

[82] C M Carpenter, B W Pogue, S Jiang, H Dehghani, X Wang, K D Paulsen, W A Wells, J Forero, C Kogel, J B Weaver, et al. Image-guided optical spectroscopy provides molecular-specific information in vivo: Mri-guided spectroscopy of breast cancer hemoglobin, water, and scatterer size. *Optics letters*, 32(8):933–935, 2007.

[83] Y Xu, N Iftimia, H Jiang, L Key, and M Bolster. Imaging of in vitro and in vivo bones and joints with continuous-wave diffuse optical tomography. *Optics Express*, 8(7):447–451, 2001.

[84] J C Hebden, H Veenstra, H Dehghani, E MC Hillman, M Schweiger, S R Arridge, and Dd T Delpy. Three-dimensional time-resolved optical tomography of a conical breast phantom. *Applied Optics*, 40(19):3278–3287, 2001.

[85] S Lighter, J Hughes, I Styles, A Filer, and H Dehghani. Multispectral, non-contact diffuse optical tomography of healthy human finger joints. *Biomedical optics express*, 9(4):1445–1460, 2018.

[86] A K Scheel, A Krause, I Mesecke-von Rheinbaben, G Metzger, H Rost, V Tresp, P Mayer, M Reuss-Borst, and G A Müller. Assessment of proximal finger joint inflammation in patients with rheumatoid arthritis, using a novel laser-based imaging technique. *Arthritis & Rheumatism*, 46(5):1177–1184, 2002.

[87] A Schwaighofer, V Tresp, P Mayer, A Krause, J Beuthan, H Rost, G Metzger, G A Muller, and A K Scheel. Classification of rheumatoid joint inflammation based on laser imaging. *IEEE Transactions on Biomedical Engineering*, 50(3):375–382, 2003.

[88] L D Montejo, J Jia, H K Kim, U J Netz, S Blaschke, G A Müller, and A H Hielscher. Computer-aided diagnosis of rheumatoid arthritis with optical tomography, part 2: image classification. *Journal of biomedical optics*, 18(7):076002–076002, 2013.

[89] M Rupawala, H Dehghani, S J E Lucas, P Tino, and D Cruse. Shining a light on awareness: A review of functional near-infrared spectroscopy for prolonged disorders of consciousness. *Frontiers in neurology*, 9, 2018.

[90] A T Eggebrecht, S L Ferradal, A Robichaux-Viehoever, M S Hassanpour, H Dehghani, A Z Snyder, T Hershey, and J P Culver. Mapping distributed brain function and networks with diffuse optical tomography. *Nature photonics*, 8(6):448–454, 2014.

[91] A H Hielscher, A D Klose, A K Scheel, B Moa-Anderson, M Backhaus, U Netz, and J Beuthan. Sagittal laser optical tomography for imaging of rheumatoid finger joints. *Physics in medicine and biology*, 49(7):1147, 2004.

[92] J W Hoi, H K Kim, C J Fong, L Zweck, and A H Hielscher. Non-contact dynamic diffuse optical tomography imaging system for evaluating lower extremity vasculature. *Biomedical optics express*, 9(11):5597–5614, 2018.

[93] J A Guggenheim, H R A Basevi, J Frampton, I B Styles, and H Dehghani. Multi-modal molecular diffuse optical tomography system for small animal imaging. *Measurement Science and Technology*, 24(10):105405, 2013.

[94] M D Reisman, Z E Markow, A Q Bauer, and J P Culver. Structured illumination diffuse optical tomography for noninvasive functional neuroimaging in mice. *Neurophotonics*, 4(2):021102, 2017.

[95] H Y Wu, A Filer, I Styles, and H Dehghani. Development of a multi-wavelength diffuse optical tomography system for early diagnosis of rheumatoid arthritis: simulation, phantoms and healthy human studies. *Biomedical Optics Express*, 7(11):4769–4786, 2016.

[96] S L Taylor, P N Newsome, and H Dehghani. Development of a multi-modal optical imaging system. In *Optical Tomography and Spectroscopy*, pages OTu2C–2. Optical Society of America, 2016.

[97] D Lighter, A Filer, and H Dehghani. Multispectral diffuse optical tomography of finger joints. In *European Conference on Biomedical Optics*, page 104120N. Optical Society of America, 2017.

[98] J Ren, S Han, A R Proctor, D S Benoit, and R Choe. Non-contact scanning diffuse optical tomography for three-dimensional vascular imaging in a murine bone graft model. In *Optical Tomography and Spectroscopy*, pages JM3A–7. Optical Society of America, 2016.

[99] S Han, J Johansson, M Mireles, A R Proctor, M D Hoffman, J B Vella, D S W Benoit, T Durduran, and R Choe. Non-contact scanning diffuse correlation tomography system for three-dimensional blood flow imaging in a murine bone graft model. *Biomedical optics express*, 6(7):2695–2712, 2015.

[100] S Bélanger, M Abran, X Intes, C Casanova, and F Lesage. Real-time diffuse optical tomography based on structured illumination. *Journal of biomedical optics*, 15(1):016006, 2010.

[101] J Ripoll. Derivation of the scalar radiative transfer equation from energy conservation of maxwell's equations in the far field. *Journal of the Optical Society of America A*, 28(8):1765–1775, 2011.

[102] S T Flock, M S Patterson, B C Wilson, and D R Wyman. Monte carlo modeling of light propagation in highly scattering tissues. i. model predictions and comparison with diffusion theory. *IEEE Transactions on biomedical Engineering*, 36(12):1162–1168, 1989.

[103] E D Aydin, C R E De Oliveira, and A J H Goddard. A comparison between transport and diffusion calculations using a finite element-spherical harmonics radiation transport method. *Medical physics*, 29(9):2013–2023, 2002.

[104] A H Hielscher, R E Alcouffe, and R L Barbour. Comparison of finite-difference transport and diffusion calculations for photon migration in homogeneous and heterogeneous tissues. *Physics in Medicine & Biology*, 43(5):1285, 1998.

[105] A D Klose and E W Larsen. Light transport in biological tissue based on the simplified spherical harmonics equations. *Journal of Computational Physics*, 220(1):441–470, 2006.

[106] M Chu, K Vishwanath, A D Klose, and H Dehghani. Light transport in biological tissue using three-dimensional frequency-domain simplified spherical harmonics equations. *Physics in Medicine & Biology*, 54(8):2493, 2009.

[107] M Chu and H Dehghani. Image reconstruction in diffuse optical tomography based on simplified spherical harmonics approximation. *Optics express*, 17(26):24208–24223, 2009.

[108] J B Fishkin, E Gratton, W W Mantulin, et al. Diffusion of intensity-modulated near-infrared light in turbid media. In *Time-Resolved Spectroscopy and Imaging of Tissues*, volume 1431, pages 122–136. International Society for Optics and Photonics, 1991.

[109] M S Patterson, E Schwartz, and B C Wilson. Quantitative reflectance spectrophotometry for the noninvasive measurement of photosensitizer concentration in tissue during photodynamic therapy. In *Photodynamic Therapy: Mechanisms*, volume 1065, pages 115–123. International Society for Optics and Photonics, 1989.

[110] K D Paulsen and H Jiang. Spatially varying optical property reconstruction using a finite element diffusion equation approximation. *Medical Physics*, 22(6):691–701, 1995.

[111] S R Arridge, M Schweiger, M Hiraoka, and D T Delpy. A finite element approach for modeling photon transport in tissue. *Medical physics*, 20(2):299–309, 1993.

[112] M Schweiger, S R Arridge, M Hiraoka, and D T Delpy. The finite element method for the propagation of light in scattering media: boundary and source conditions. *Medical physics*, 22(11):1779–1792, 1995.

[113] H Dehghani, B Brooksby, K Vishwanath, B W Pogue, and K D Paulsen. The effects of internal refractive index variation in near-infrared optical tomography: a finite element modelling approach. *Physics in Medicine & Biology*, 48(16):2713, 2003.

[114] H Dehghani, D T Delpy, and S R Arridge. Photon migration in non-scattering tissue and the effects on image reconstruction. *Physics in medicine & biology*, 44(12):2897, 1999.

[115] H Dehghani, B W Pogue, S P Poplack, and K D Paulsen. Multiwavelength three-dimensional near-infrared tomography of the breast: initial simulation, phantom, and clinical results. *Applied Optics*, 42(1):135–145, 2003.

[116] M Doulgerakis, A Eggebrecht, J Culver, and H Dehghani. Towards real-time functional human brain imaging with diffuse optical tomography. In *European Conference on Biomedical Optics*, page 1041209. Optical Society of America, 2017.

[117] S R Arridge and M Schweiger. A gradient-based optimisation scheme for optical tomography. *Optics Express*, 2(6):213–226, 1998.

[118] A H Hielscher, A D Klose, and K M Hanson. Gradient-based iterative image reconstruction scheme for time-resolved optical tomography. *IEEE Transactions on medical imaging*, 18(3):262–271, 1999.

[119] H Jiang, K D Paulsen, U L Osterberg, B W Pogue, and M S Patterson. Optical image reconstruction using frequency-domain data: simulations and experiments. *JOSA A*, 13(2):253–266, 1996.

[120] R Penrose. A generalized inverse for matrices. In *Mathematical proceedings of the Cambridge philosophical society*, volume 51, pages 406–413. Cambridge Univ Press, 1955.

[121] S R Arridge. Optical tomography in medical imaging. *Inverse problems*, 15(2):R41, 1999.

[122] S R Arridge and M Schweiger. Photon-measurement density functions. part 2: Finite-element-method calculations. *Applied Optics*, 34(34):8026–8037, 1995.

[123] A Nch Tikhonov, A V Goncharsky, V V Stepanov, and A G Yagola. *Numerical methods for the solution of ill-posed problems*, volume 328. Springer Science & Business Media, 2013.

[124] W Lu, D Lighter, and I B Styles. L 1-norm based nonlinear reconstruction improves quantitative accuracy of spectral diffuse optical tomography. *Biomedical optics express*, 9(4):1423–1444, 2018.

[125] S Srinivasan, B W Pogue, S Jiang, H Dehghani, and K D Paulsen. Validation of hemoglobin and water molar absorption spectra in near-infrared diffuse optical tomography. In *Optical Tomography and Spectroscopy of Tissue V*, volume 4955, pages 407–416. International Society for Optics and Photonics, 2003.

[126] S Srinivasan, B W Pogue, S Jiang, H Dehghani, and K D Paulsen. Spectrally constrained chromophore and scattering near-infrared tomography provides quantitative and robust reconstruction. *Applied optics*, 44(10):1858–1869, 2005.

[127] B Brooksby, S Srinivasan, S Jiang, H Dehghani, B W Pogue, K D Paulsen, J Weaver, C Kogel, and S P Poplack. Spectral priors improve near-infrared diffuse tomography more than spatial priors. *Optics letters*, 30(15):1968–1970, 2005.

[128] D A Boas, T Gaudette, and S R Arridge. Simultaneous imaging and optode calibration with diffuse optical tomography. *Optics express*, 8(5):263–270, 2001.

[129] S R Arridge and W R B Lionheart. Nonuniqueness in diffusion-based optical tomography. *Optics letters*, 23(11):882–884, 1998.

[130] A Corlu, R Choe, T Durduran, K Lee, M Schweiger, S R Arridge, E M C Hillman, and A G Yodh. Diffuse optical tomography with spectral constraints and wavelength optimization. *Applied optics*, 44(11):2082–2093, 2005.

[131] M E Eames, J Wang, B W Pogue, and H Dehghani. Wavelength band optimization in spectral near-infrared optical tomography improves accuracy while reducing data acquisition and computational burden. *Journal of biomedical optics*, 13(5):054037–054037, 2008.

[132] J Beuthan, U Zabarylo, A Krause, M Taupitz, and O Minet. Ra diagnostics using laser-optical images and conventional x-rays (fused imaging). *Medical Laser Application*, 22(2):127–133, 2007.

[133] O Minet, H Gajewski, J A Griepentrog, and J Beuthan. The analysis of laser light scattering during rheumatoid arthritis by image segmentation. *Laser Physics Letters*, 4(8):604, 2007.

[134] A J L Meier, W HJ Rensen, P K de Bokx, and R N J de Nijs. Potential of optical spectral transmission measurements for joint inflammation measurements in rheumatoid arthritis patients. *Journal of biomedical optics*, 17(8):0814201–0814206, 2012.

[135] E D Harris. Clinical features of rheumatoid arthritis. *Kelley's textbook of rheumatology*, pages 1043–1078, 2005.

[136] V Prapavat, R Schuetz, W Runge, J Beuthan, and G J Mueller. Evaluation of scattered light distributions of cw-transillumination for functional diagnostic of rheumatic disorders in interphalangeal joints. In *BiOS Europe'95*, pages 121–129. International Society for Optics and Photonics, 1995.

[137] V Prapavat, J Mans, R Schuetz, G Regling, J Beuthan, and G J Mueller. In-vivo investigations on the detection of chronical polyarthritis (cp) using a cw-transillumination method at interphalangeal joints. In *BiOS Europe'95*, pages 360–366. International Society for Optics and Photonics, 1995.

[138] V Prapavat, W Runge, J Mans, A Krause, J Beuthan, and G Mueller. Determination of optical tissue parameters of joint system at an early stage of rheumatoid arthritis (in vitro). *Minimal Invasive Medizin*, 8(1-2):7–16, 1997.

[139] V Prapavat, W Runge, J Mans, A Krause, J Beuthan, and G Müller. The development of a finger joint phantom for the optical simulation of early inflammatory rheumatic changes. *Biomedizinische Technik. Biomedical engineering*, 42(11):319–326, 1997.

[140] J Beuthan, V Prapavat, R-D Naber, O Minet, and G J Mueller. Diagnosis of inflammatory rheumatic diseases with photon density waves. In *Photonics West'96*, pages 43–53. International Society for Optics and Photonics, 1996.

[141] J Beuthan, U Netz, O Minet, Annerose D Klose, A H Hielscher, A Scheel, J Henniger, and G Müller. Light scattering study of rheumatoid arthritis. *Quantum Electronics*, 32(11):945–952, 2002.

[142] A Schwaighofer, V Tresp, P Mayer, S K Scheel, and G A Müller. The ra scanner: Prediction of rheumatoid joint inflammation based on laser imaging. In *Advances in Neural Information Processing Systems*, pages 1433–1440, 2003.

[143] O Minet, U Zabarylo, and J Beuthan. Deconvolution of laser based images for monitoring rheumatoid arthritis. *Laser Physics Letters*, 2(11):556, 2005.

[144] O Minet, P Scheibe, and U J Zabarylo. Diagnosis of rheumatoid arthritis using light: correction of motion artefacts and color visualization of multispectral images. *Journal of biophotonics*, 3(3):130–137, 2010.

[145] I Amitai, S Werner, B Schicke, G-R Burmester, O Minet, U Zabaryło, M Backhaus, and S Ohrndorf. Comparison of photo optical imaging with musculoskeletal ultrasound and clinical examination in the assessment of inflammatory activity in proximal interphalangeal joints in rheumatoid arthritis and osteoarthritis. *The Journal of rheumatology*, 42(9):1595–1602, 2015.

[146] A D Klose, A H Hielscher, K M Hanson, and J Beuthan. Two-and three-dimensional optical tomography of finger joints for diagnostics of rheumatoid arthritis. In *BiOS Europe'98*, pages 151–160. International Society for Optics and Photonics, 1998.

[147] U Netz, J Beuthan, H-J Cappius, H-C Koch, A D Klose, and A H Hielscher. Imaging of rheumatoid arthritis in finger joints by sagittal optical tomography. *Medical Laser Application*, 16(4):306–310, 2001.

[148] U J Netz, J Beuthan, and A H Hielscher. Multipixel system for gigahertz frequency-domain optical imaging of finger joints. *Review of Scientific Instruments*, 79(3):034301, 2008.

[149] L D Montejo, J Jia, H K Kim, U J Netz, S Blaschke, G A Müller, and A H Hielscher. Computer-aided diagnosis of rheumatoid arthritis with optical tomography, part 1: feature extraction. *Journal of biomedical optics*, 18(7):076001–076001, 2013.

[150] M B Goldring and M Otero. Inflammation in osteoarthritis. *Current opinion in rheumatology*, 23(5):471, 2011.

[151] Y Xu, N Iftimia, H Jiang, L L Key, and M B Bolster. Three-dimensional diffuse optical tomography of bones and joints. *Journal of biomedical optics*, 7(1):88–92, 2002.

[152] Q Zhang and H Jiang. Three-dimensional diffuse optical tomography of simulated hand joints with a 64× 64-channel photodiodes-based optical system. *Journal of Optics A: Pure and Applied Optics*, 7(5):224, 2005.

[153] Z Yuan, Q Zhang, E S Sobel, and H Jiang. Image-guided optical spectroscopy in diagnosis of osteoarthritis: a clinical study. *Biomedical optics express*, 1(1):74–86, 2010.

[154] B A Brooksby, H Dehghani, B W Pogue, and K D Paulsen. Near-infrared (nir) tomography breast image reconstruction with a priori structural information from mri: algorithm development for reconstructing heterogeneities. *IEEE Journal of selected topics in quantum electronics*, 9(2):199–209, 2003.

[155] B Brooksby, S Jiang, H Dehghani, B W Pogue, K D Paulsen, J Weaver, C Kogel, and S P Poplack. Combining near-infrared tomography and magnetic resonance imaging to study in vivo breast tissue: implementation of a laplacian-type regularization to

incorporate magnetic resonance structure. *Journal of biomedical optics*, 10(5):051504–051504, 2005.

[156] Z Yuan, Q Zhang, E S Sobel, and H Jiang. Tomographic x-ray–guided three-dimensional diffuse optical tomography of osteoarthritis in the finger joints. *Journal of biomedical optics*, 13(4):044006–044006, 2008.

[157] J Lasker, D Ginat, E Dwyer, and A Hielscher. Comparison of static and dynamic optical tomographic imaging of rheumatoid joints. In *Biomedical Topical Meeting*, page SC10. Optical Society of America, 2006.

[158] J M Lasker, C J Fong, D T Ginat, E Dwyer, and A H Hielscher. Dynamic optical imaging of vascular and metabolic reactivity in rheumatoid joints. *Journal of biomedical optics*, 12(5):052001–052001, 2007.

[159] M van Onna, D F Ten Cate, K L Tsoi, A J L Meier, J W G Jacobs, A A A Westgeest, P B L Meijer, M C van Beek, W H J Rensen, and J W J Bijlsma. Assessment of disease activity in patients with rheumatoid arthritis using optical spectral transmission measurements, a non-invasive imaging technique. *Annals of the rheumatic diseases*, 75(3):511–518, 2016.

[160] N J Besselink, P van der Meijde, W H J Rensen, P B L Meijer, A C A Marijnissen, J M van Laar, F P J G Lafeber, and J W G Jacobs. Optical spectral transmission to assess inflammation in hand and wrist joints of rheumatoid arthritis patients. *Rheumatology*, 2018.

[161] Z Yuan, Q Zhang, E Sobel, and H Jiang. Comparison of diffusion approximation and higher order diffusion equations for optical tomography of osteoarthritis. *Journal of biomedical optics*, 14(5):054013–054013, 2009.

[162] L Montejo. Computational methods for the diagnosis of rheumatoid arthritis with diffuse optical tomography. 2014.

[163] X Wang, D L Chamberland, P L Carson, J B Fowlkes, R O Bude, D A Jamadar, and B J Roessler. Imaging of joints with laser-based photoacoustic tomography: an animal study. *Medical physics*, 33(8):2691–2697, 2006.

[164] Y Sun and H Jiang. Quantitative three-dimensional photoacoustic tomography of the finger joints: phantom studies in a spherical scanning geometry. *Physics in medicine and biology*, 54(18):5457, 2009.

[165] Y Sun, E Sobel, and H Jiang. Quantitative three-dimensional photoacoustic tomography of the finger joints: an in vivo study. *Journal of biomedical optics*, 14(6):064002–064002, 2009.

[166] Z Deng and C Li. Noninvasively measuring oxygen saturation of human finger-joint vessels by multi-transducer functional photoacoustic tomography. *Journal of biomedical optics*, 21(6):061009–061009, 2016.

[167] J Jo, G Xu, A Marquardt, G Girish, and X Wang. Photoacoustic evaluation of human inflammatory arthritis in human joints. In *Photons Plus Ultrasound: Imaging and Sensing 2017*, volume 10064, page 1006409. International Society for Optics and Photonics, 2017.

[168] J Jo, G Xu, M Cao, A Marquardt, S Francis, G Gandikota, and X Wang. A functional study of human inflammatory arthritis using photoacoustic imaging. *Scientific reports*, 7(1):15026, 2017.

[169] W-T Chen, U Mahmood, R Weissleder, and C-H Tung. Arthritis imaging using a near-infrared fluorescence folate-targeted probe. *Arthritis research & therapy*, 7(2):R310, 2005.

[170] S G Werner, H-E Langer, S Ohrndorf, M Bahner, P Schott, C Schwenke, M Schirner, H Bastian, G Lind-Albrecht, B Kurtz, et al. Inflammation assessment in patients with arthritis using a novel in vivo fluorescence optical imaging technology. *Annals of the rheumatic diseases*, 71(4):504–510, 2012.

[171] V S Schäfer, W Hartung, P Hoffstetter, J Berger, C Stroszczynski, M Müller, M Fleck, and B Ehrenstein. Quantitative assessment of synovitis in patients with rheumatoid arthritis using fluorescence optical imaging. *Arthritis research & therapy*, 15(5):R124, 2013.

[172] P Mohajerani, M Koch, K Thürmel, B Haller, E J Rummeny, V Ntziachristos, and R Meier. Fluorescence-aided tomographic imaging of synovitis in the human finger. *Radiology*, 272(3):865–874, 2014.

[173] D Lighter, M Clancy, D Davies, G M Balanos, S J Lucas, and H Dehghani. Assessing the quantitative accuracy of continuous wave and frequency domain near infrared spectroscopy for detecting hypoxia in patients with traumatic brain injury. In *Clinical and Translational Biophotonics*, pages JW3A–44. Optical Society of America, 2016.

[174] S A Prahl. Tabulated molar extinction coefficient for hemoglobin in water. *http://omlc. ogi. edu/spectra/hemoglobin/summary. html*, 1999.

[175] G M Hale and M R Querry. Optical constants of water in the 200-nm to 200-μm wavelength region. *Applied optics*, 12(3):555–563, 1973.

[176] J Geng. Structured-light 3d surface imaging: a tutorial. *Advances in Optics and Photonics*, 3(2):128–160, 2011.

[177] V Srinivasan, H-C Liu, and M Halioua. Automated phase-measuring profilometry of 3-d diffuse objects. *Applied optics*, 23(18):3105–3108, 1984.

[178] H R A Basevi, J A Guggenheim, H Dehghani, and I B Styles. Simultaneous multiple view high resolution surface geometry acquisition using structured light and mirrors. *Optics express*, 21(6):7222–7239, 2013.

[179] I Sahbudin, J Bell, K Kumar, K Raza, and A Filer. Observing real-time images during ultrasound-guided procedures improves patients' experience. *Rheumatology*, 55(3):585–586, 2015.

[180] Em-ccd. technical note. 2009.

[181] S Audet and M Okutomi. A user-friendly method to geometrically calibrate projector-camera systems. In *Computer Vision and Pattern Recognition Workshops, 2009. CVPR Workshops 2009. IEEE Computer Society Conference on*, pages 47–54. IEEE, 2009.

[182] The CGAL Project. *CGAL User and Reference Manual*. CGAL Editorial Board, 4.12 edition, 2018.

[183] M Jermyn, H Ghadyani, M A Mastanduno, W Turner, S C Davis, H Dehghani, and B W Pogue. Fast segmentation and high-quality three-dimensional volume mesh creation from medical images for diffuse optical tomography. *Journal of biomedical optics*, 18(8):086007–086007, 2013.

[184] Visual Computing Lab ISTI CNR. Meshlab. http://meshlab.sourceforge.net/.

[185] J A Guggenheim. *Multi-modal diffuse optical tomography and bioluminescence tomography system for preclinical imaging*. PhD thesis, University of Birmingham, 2014.

[186] S L Taylor. *Quantitative bioluminescence tomography: hardware and software development for a multi-modal imaging system*. PhD thesis, University of Birmingham, 2018.

[187] X Wu, A T Eggebrecht, S L Ferradal, J P Culver, and H Dehghani. Fast and efficient image reconstruction for high density diffuse optical imaging of the human brain. *Biomedical optics express*, 6(11):4567–4584, 2015.

[188] M E Eames, B W Pogue, P K Yalavarthy, and H Dehghani. An efficient jacobian reduction method for image reconstruction using diffuse optical tomography. In *Biomedical Optics*, page BSuE35. Optical Society of America, 2008.

[189] G Alexandrakis, F R Rannou, and A F Chatziioannou. Tomographic bioluminescence imaging by use of a combined optical-pet (opet) system: a computer simulation feasibility study. *Physics in medicine and biology*, 50(17):4225, 2005.

[190] B Caprile and V Torre. Using vanishing points for camera calibration. *International journal of computer vision*, 4(2):127–139, 1990.

[191] M Warren, D McKinnon, and B Upcroft. Online Calibration of Stereo Rigs for Long-Term Autonomy. In *International Conference on Robotics and Automation (ICRA)*, Karlsruhe, 2013.

[192] Z Zhang. A flexible new technique for camera calibration. *IEEE Transactions on pattern analysis and machine intelligence*, 22(11):1330–1334, 2000.

[193] Y Chen and G Medioni. Object modelling by registration of multiple range images. *Image and vision computing*, 10(3):145–155, 1992.

[194] J A Guggenheim, I Bargigia, A Farina, A Pifferi, and H Dehghani. Time resolved diffuse optical spectroscopy with geometrically accurate models for bulk parameter recovery. *Biomedical Optics Express*, 7(9):3784–3794, 2016.

[195] T O McBride, B W Pogue, U L Österberg, and K D Paulsen. Strategies for absolute calibration of near infrared tomographic tissue imaging. In *Oxygen Transport to Tissue XXIV*, pages 85–99. Springer, 2003.

[196] W Lu, J Duan, D Orive-Miguel, L Herve, and I B Styles. Graph-and finite element-based total variation models for the inverse problem in diffuse optical tomography. *arXiv preprint arXiv:1901.01969*, 2019.

[197] L A Dempsey, M Persad, S Powell, D Chitnis, and J C Hebden. Geometrically complex 3d-printed phantoms for diffuse optical imaging. *Biomedical optics express*, 8(3):1754–1762, 2017.

[198] F Ayers, A Grant, D Kuo, D J Cuccia, and A J Durkin. Fabrication and characterization of silicone-based tissue phantoms with tunable optical properties in the visible and near infrared domain. In *Design and Performance Validation of Phantoms Used in Conjunction with Optical Measurements of Tissue*, volume 6870, page 687007. International Society for Optics and Photonics, 2008.

[199] T O McBride, B W Pogue, E D Gerety, S B Poplack, U L Österberg, and K D Paulsen. Spectroscopic diffuse optical tomography for the quantitative assessment of hemoglobin concentration and oxygen saturation in breast tissue. *Applied optics*, 38(25):5480–5490, 1999.

[200] J F Barrett and N Keat. Artifacts in ct: recognition and avoidance. *Radiographics*, 24(6):1679–1691, 2004.

[201] M Reuter, M D Tisdall, A Qureshi, R L Buckner, A J W van der Kouwe, and B Fischl. Head motion during mri acquisition reduces gray matter volume and thickness estimates. *Neuroimage*, 107:107–115, 2015.

[202] R Cooper, J Selb, L Gagnon, D Phillip, H W Schytz, H K Iversen, M Ashina, and D A Boas. A systematic comparison of motion artifact correction techniques for functional near-infrared spectroscopy. *Frontiers in neuroscience*, 6:147, 2012.

[203] N U F Dosenbach, J M Koller, E A Earl, O Miranda-Dominguez, R L Klein, A N Van, A Z Snyder, B J Nagel, J T Nigg, A L Nguyen, et al. Real-time motion analytics during brain mri improve data quality and reduce costs. *Neuroimage*, 161:80–93, 2017.

[204] L Haywood and D A Walsh. Vasculature of the normal and arthritic synovial joint. *Histology and histopathology*, 16(1):277–284, 2001.

[205] D G Altman. *Practical statistics for medical research*. CRC press, 1990.

[206] N Shah, A Cerussi, C Eker, J Espinoza, J Butler, J Fishkin, R Hornung, and B Tromberg. Noninvasive functional optical spectroscopy of human breast tissue. *Proceedings of the National Academy of Sciences*, 98(8):4420–4425, 2001.

[207] R Cubeddu, C D'Andrea, A Pifferi, P Taroni, A Torricelli, and G Valentini. Effects of the menstrual cycle on the red and near-infrared optical properties of the human breast. *Photochemistry and photobiology*, 72(3):383–391, 2000.

[208] J F Brun, C Bouchahda, D Chaze, A Aïssa Benhaddad, J P Micallef, and J Mercier. The paradox of hematocrit in exercise physiology: which is the âĂIJnormalâĂİ range from an hemorheologist's viewpoint? *Clinical hemorheology and microcirculation*, 22(4):287–303, 2000.

[209] L Gao, C E Elwell, M Kohl-Bareis, M Gramer, C E Cooper, T S Leung, and I Tachtsidis. Effects of assuming constant optical scattering on haemoglobin concentration measurements using nirs during a valsalva manoeuvre. *Advances in experimental medicine and biology*, 701:15–20, 2011.

[210] F Jennings, E Lambert, and M Fredericson. Rheumatic diseases presenting as sports-related injuries. *Sports Medicine*, 38(11):917–930, 2008.

[211] G Zonios, J Bykowski, and N Kollias. Skin melanin, hemoglobin, and light scattering properties can be quantitatively assessed in vivo using diffuse reflectance spectroscopy. *Journal of Investigative Dermatology*, 117(6):1452–1457, 2001.

[212] L Terslev, E Naredo, P Aegerter, R J Wakefield, M Backhaus, P Balint, G A W Bruyn, A Iagnocco, S Jousse-Joulin, W A Schmidt, et al. Scoring ultrasound synovitis in rheumatoid arthritis: a eular-omeract ultrasound taskforce-part 2: reliability and application to multiple joints of a standardised consensus-based scoring system. *RMD open*, 3(1):e000427, 2017.

[213] M-A D'Agostino, L Terslev, P Aegerter, M Backhaus, P Balint, G A Bruyn, E Filippucci, W Grassi, A Iagnocco, S Jousse-Joulin, et al. Scoring ultrasound synovitis in rheumatoid arthritis: a eular-omeract ultrasound taskforce-part 1: definition and development of a standardised, consensus-based scoring system. *RMD open*, 3(1):e000428, 2017.

[214] R S Galan and S R Gambino. Beyond normality-the predictive value and efficiency of medical diagnosis, 1975.

[215] W J Youden. Index for rating diagnostic tests. *Cancer*, 3(1):32–35, 1950.

[216] A H Hielscher, A D Klose, A K Scheel, M Backhaus, U J Netz, and J Beuthan. Assessment of finger joint inflammation by diffuse optical tomography. In *European Conference on Biomedical Optics*, page 5138_46. Optical Society of America, 2003.

[217] V Prapavat, T Luhmann, A Krause, M Backhaus, J Beuthan, and G J Mueller. Evaluation of early rheumatic disorders in pip joints using a cw-transillumination method: first clinical results. In *BiOS Europe'97*, pages 71–78. International Society for Optics and Photonics, 1998.

[218] A K Scheel, U J Netz, K-G A Hermann, A H Hielscher, A D Klose, V Tresp, A Schwaighofer, G A Müller, G-R Burmester, and M Backhaus. Laser imaging techniques for follow-up analysis of joint inflammation in patients with rheumatoid arthritis. *Medical Laser Application*, 18(3):198–205, 2003.

[219] M W Seymour, S Kelly, C R Beals, M-P Malice, J A Bolognese, B J Dardzinski, A S Cheng, C E Cummings, S S Smugar, C McClinton, et al. Ultrasound of metacarpophalangeal joints is a sensitive and reliable endpoint for drug therapies in rheumatoid arthritis: results of a randomized, two-center placebo-controlled study. *Arthritis research & therapy*, 14(5):R198, 2012.

[220] M N Witt, F Mueller, P Weinert, A P Nigg, C S Reindl, F Proft, H Schulze-Koops, and M Grunke. Ultrasound of synovitis in rheumatoid arthritis: advantages of the dorsal over the palmar approach to finger joints. *The Journal of rheumatology*, pages jrheum–131027, 2014.

[221] M Østergaard, C Peterfy, P Conaghan, F McQueen, P Bird, B Ejbjerg, R Shnier, P O'Connor, M Klarlund, P Emery, et al. Omeract rheumatoid arthritis magnetic resonance imaging studies. core set of mri acquisitions, joint pathology definitions, and the omeract ra-mri scoring system. *The Journal of rheumatology*, 30(6):1385–1386, 2003.

[222] H Soliman, A Gunasekara, M Rycroft, J Zubovits, R Dent, J Spayne, M J Yaffe, and G J Czarnota. Functional imaging using diffuse optical spectroscopy of neoadjuvant chemotherapy response in women with locally advanced breast cancer. *Clinical cancer research*, 16(9):2605–2614, 2010.

[223] A Cerussi, D Hsiang, N Shah, R Mehta, A Durkin, J Butler, and B J Tromberg. Predicting response to breast cancer neoadjuvant chemotherapy using diffuse optical spectroscopy. *Proceedings of the National Academy of Sciences*, 104(10):4014–4019, 2007.

[224] J M Cochran, D R Busch, A Leproux, Z Zhang, T D O'Sullivan, A E Cerussi, P M Carpenter, R S Mehta, D Roblyer, W Yang, et al. Tissue oxygen saturation predicts response to breast cancer neoadjuvant chemotherapy within 10 days of treatment. *Journal of biomedical optics*, 24(2):021202, 2018.

[225] D Roblyer, S Ueda, A Cerussi, W Tanamai, A Durkin, R Mehta, D Hsiang, J A Butler, S McLaren, W-P Chen, et al. Optical imaging of breast cancer oxyhemoglobin flare correlates with neoadjuvant chemotherapy response one day after starting treatment. *Proceedings of the National Academy of Sciences*, 108(35):14626–14631, 2011.

[226] K P Murphy. *Machine learning: a probabilistic perspective*. MIT press, 2012.

[227] C Fedorow and H P Grocott. Cerebral monitoring to optimize outcomes after cardiac surgery. *Current Opinion in Anesthesiology*, 23(1):89–94, 2010.

[228] D J Davies, M Clancy, D Lighter, G M Balanos, S J e Lucas, H Dehghani, Z Su, M Forcione, and A Belli. Frequency-domain vs continuous-wave near-infrared spectroscopy devices: a comparison of clinically viable monitors in controlled hypoxia. *Journal of clinical monitoring and computing*, 31(5):967–974, 2017.

[229] H Dehghani, Y Feng, D Lighter, L Zhang, and Y Wang. Deep neural networks improve diagnostic accuracy of rheumatoid arthritis using diffuse optical tomography. In *Diffuse Optical Spectroscopy and Imaging VII*, volume 11074, page 110741I. International Society for Optics and Photonics, 2019.

[230] Y Feng, D Lighter, L Zhang, Y Wang, and H Dehghani. Application of deep neural networks to improve diagnostic accuracy of rheumatoid arthritis using diffuse optical tomography. *Quantum Electronics*, 50(1):21, 2020.

[231] L A Dempsey, R J Cooper, T Roque, T Correia, E Magee, S Powell, A P Gibson, and J Hebden. Data-driven approach to optimum wavelength selection for diffuse optical imaging. *Journal of biomedical optics*, 20(1):016003, 2015.

[232] S J Woltman, G D Jay, and G P Crawford. Liquid-crystal materials find a new order in biomedical applications. *Nature materials*, 6(12):929, 2007.

[233] Q Li, X He, Y Wang, H Liu, D Xu, and F Guo. Review of spectral imaging technology in biomedical engineering: achievements and challenges. *Journal of biomedical optics*, 18(10):100901–100901, 2013.

[234] J E Gibbs and D W Ray. The role of the circadian clock in rheumatoid arthritis. *Arthritis research & therapy*, 15(1):205, 2013.